ORNL-TM-3797

FUELS AND MATERIALS DEVELOPMENT PROGRAM

QUARTERLY PROGRESS REPORT

FOR PERIOD ENDING MARCH 31, 1972

P. Patriarca

OAK RIDGE NATIONAL LABORATORY
OPERATED BY UNION CARBIDE CORPORATION • FOR THE U.S. ATOMIC ENERGY COMMISSION

ORNL-TM-3797

Contract No. W-7405-eng-26

METALS AND CERAMICS DIVISION

FUELS AND MATERIALS DEVELOPMENT PROGRAM QUARTERLY PROGRESS REPORT FOR PERIOD ENDING MARCH 31, 1972

P. Patriarca

JUNE 1972

OAK RIDGE NATIONAL LABORATORY
Oak Ridge, Tennessee 37830
operated by
UNION CARBIDE CORPORATION
for the
U.S. ATOMIC ENERGY COMMISSION

HIGHLIGHTS

PART I. FAST REACTOR TECHNOLOGY

FUELS

Mixed oxide pellets have been prepared for fuel dissolution studies, a vented fuel pin capsule, and replacement pins for the F-1 experiment in EBR-II. (p. 4)

Three EBR-II encapsulated pins containing Sphere-Pac $(U,Pu)O_2$ fuel have attained a calculated peak burnup of 8% FIMA. (p. 5)

The lead $(U,Pu)O_2$ fuel pin in the 37-pin EBR-II subassembly has attained a peak burnup of 3.9% FIMA. (p. 7)

The first capsule (MINT-1) to measure the effect of power cycling on axial extension of fuel and cladding and on fission gas release has been operated to 14 kW/ft with simulated reactor scrams each day. The fuel column expansion supports the theory that with dished pellets the outer pellet temperature is controlling. The pressure changes observed confirms the thoery that fission gas release is promoted by thermal cycling. (p. 14)

A detailed fuel-cladding gap conductance model, which accounts for the type of gap, has been developed and incorporated into the FMØDEL fuel performance code. (p. 25)

One of the two capsules, each containing four (U,Pu)N pins, being irradiated was removed from testing in January 1972, and shipped to Los Alamos Scientific Laboratory for postirradiation examination. The second capsule continues in irradiation testing. Peak burnup at present is 6% FIMA. (p. 40)

A process was developed for conditioning pyrophoric (U,Pu)N powders prior to shipment for recovery at Hanford or Savannah River. Nitric acid dissolution was chosen over controlled oxidation. (p. 41)

ABSORBERS

Metallographic examination of irradiated boron carbide from the EBR-II Higher Worth Control Rod, which had received about 1.5% burnup of ^{10}B at temperatures below about 500°C revealed only a very few small cracks located primarily at the interface between graphite particles and along adjacent grain boundaries. Electrolytic etching could not be carried out on this material due to the extremely high electrical resistance in the as-irradiated condition. Annealing at temperatures to about 1600°C reduced the resistance to about the unirradiated value. (p. 43)

Lattice parameter measurements indicate a volume increase of about 0.3% on irradiation. Again, annealing to about 1300°C resulted in a return to the original cell volume. Gas release was estimated to be $8.1 \pm 4.6\%$. (p. 45)

Neutron radiography of capsules removed from EBR-II experiment subassembly X099 has revealed more swelling than anticipated and some pellets showed extensive cracking and fragmentation. The higher temperature pellets exhibited more cracking and of these the high-density and high boron-to-carbon ratio pellets cracked the most. (p. 52)

Capsules containing tantalum alloys have been delivered to EBR-II to fill out subassembly X099A. Tantalum borides and stainless steel vent assemblies have been successfully fabricated for testing in EBR-II test 2α. Fabrication of capsules for test 2α and 2β is partially completed and scheduled for delivery to EBR-II on June 1, 1972, and August 1, 1972, respectively. (p. 56).

X-ray lattice and density information on boron carbide single crystals indicates that significant numbers of interstitial atoms, presumably boron, are present in material with boron contents greater than $B_{13}C_2$. Such materials might be expected to exhibit a significantly different irradiation behavior. (p. 55)

As part of the Modeling Task, a host of boron carbide thermal irradiation data have been collected and analyzed. These show that (1) gas release decreases with increasing burnup at low temperatures but increases slightly at high temperatures, (2) porosity has little effect on gas release at low temperatures but does increase gas release at high temperatures, and (3) powders generally release more gas than pellets. (p. 63)

CLADDINGS

Two of seven elements have been removed from EBR-II subassembly X100. These elements are being disassembled and evaluation will begin shortly. (p. 73)

The effects of preirradiation heat treatment and alloy composition on irradiation induced swelling and mechanical property changes are being investigated. (p. 75)

Microstructural studies and evaluation of the creep-rupture properties of annealed and 20% cold-worked type 316 stainless steel irradiated in EBR-II subassembly X034A at 450 to 800°C to fluences up to 2.7×10^{22} neutrons/cm^2 (>0.1 MeV) have been completed. The void, dislocation, and precipitate structures have been characterized in detail. (p. 89)

Results of creep-rupture tests and metallographic examination on thermal control specimens (annealed and 20% cold-worked type 316 stainless steel aged 4000 hr at 550 and 650°C) are reported. Extensive changes in microstructure as well as strength occurred as a result of the thermal aging. (p. 92)

The room temperature tensile properties and fracture behavior of annealed type 304 stainless steel irradiated to about 1.7×10^{23} neutrons/cm^2 (>0.1 MeV) are presented and discussed. (p. 98)

The results of creep-rupture testing and some scanning electron microscopy observations on irradiated 8001, 6061, and 5052 aluminum are reported for neutron fluences up to 1.6×10^{22} neutrons/cm^2 (>0.8 MeV) and for irradiation temperatures ranging from 50 to about 175°C. Irradiation-induced strengthening occurs in 8001 and 6061 aluminum as a result of the formation of silicon precipitates and dislocation networks; thse obstacles to deformation became coarser and less effective barriers to deformation with increasing irradiation temperature. The creep ductilities of these materials always exceed 2 or 3%. The magnesium solid solution strengthened 5052 alloy forms uniformly distributed Mg_2Si β' precipitates during irradiation which causes the irradiated alloy to be about as strong as the 6061 alloy. However, postirradiation creep ductilities as low as 1% have been measured for the 5052 alloy at 50°C. (p. 105)

Specimens of 20% cold-worked type 316 stainless steel tubing of FFTF fuel cladding dimensions having sharp "altered" longitudinal notches (approx 0.0001 in. wide) and control specimens have been tested at 650°C under biaxial stress-rupture conditions. The notches cause premature failure, and there is metallographic evidence that more rapid local deformation occurs at the notches than that which occurs in the remainder of the tube. (p. 121)

FABRICATION DEVELOPMENT OF LMFBR COMPONENTS

Fabrication of the Inconel 625 steam corrosion loop for investigating stress corrosion cracking with caustic additions has been initiated. Pipe and fittings of 9 Cr–1 Mo steel have been received for construction of a replacement for the Incoloy 800 chloride loop which will probably be taken out of service due to cracking. An environmental analysis of moisture and chloride contents in various parts of this Incoloy 800 loop has been completed. The eighth run in this loop is now under way with 20 ppm O and 10 ppm NaCl as the contaminants. (p. 129)

Posttest examination of the Alco/BLH steam generator is continuing. The proximity of stress-corrosion cracks in a failed tube to the original tube-to-tube sheet weld (this weld was machined away during the plugging operation) provides a plausible failure mechanism; steam leaking through the weld into the sodium-filled tube crevice would set up conditions conducive to caustic stress-corrosion cracking. Metallographic examinations of failed steam-side thermocouples has revealed cracks in the sheaths as a consequence of the poor joint design used in welding the sheaths to pads. (p. 137)

For use in obtaining high-temperature design data, the procurement of 64 weld test plates using the filler metal and welding procedures used on the FFTF vessel has been completed. Several experimental batches of improved filler metals for welding piping have been prepared commercially and at ORNL, and they have been welded into test plates for weldability and mechanical properties evaluations. Creep-rupture tests on an electroslag weld showed it to be slightly weaker but of greater ductility than submerged-arc welds. (p. 148)

A small-rod-anode x-ray unit for radiography of bore-side tube-to-tube sheet welds has been borrowed and techniques are being developed for optimum focusing. We demonstrated that indications of visible dye penetrant can be viewed through a borescope and closed circuit television system. Design calculations on a new type of reflection encircling coil for the phase-sensitive eddy current instrument indicate the potential to monitor both size and position of a discontinuity (relative to the surface) within a tubular specimen. An ultrasonic scanning system is being prepared for welded joints that will allow simultaneous recording of amplitude and x and y positions of a discontinuity. (p. 180)

We are developing techniques for determining weld metal segregation with ^{63}Ni-tagged filler metal. A great deal of heterogeneity is evident in multipass welds, and severe impoverishment of filler metal in the root pass was evident. (p. 156)

Weldability studies on various steam generator materials are being conducted. By using an experimental Incoloy 800 weld metal with a controlled chemical analysis, we are able to produce a finer grain size in the weld deposit than is obtained with prior Incoloy 800 compositions. We believe this is an important factor in decreasing the crack susceptibility of Incoloy 800 welds. Welds in niobium-stabilized 2 1/4 Cr— 1 Mo steel exhibit excellent Charpy-V notch toughness at 5°C (40°F). A double-torch welding technique has been developed for simulating conditions at the overlap region of bore-side tube-to-tube sheet welds. (p. 164)

Heat to heat variation in type 304 stainless steel properties is in progress. For short-time tensile properties the inelastic behavior up to the 0.2% yield stress varies significantly between 17 heats. In short-time creep tests, the time to 0.5% creep strain at 17,000 psi (593°C) varies over an order of magnitude for the 12 heats examined to date. (p. 185)

The problems of creep data representation are being examined. A polynomial equation fits the creep data better than an exponential creep-type equation. (p. 197)

The longitudinal tensile properties of type 308 stainless steel weld metal from the FFTF vessel test welds have been evaluated at 25, 482, 565, and 649°C (75, 900, and 1200°F, respectively). There is no

effect of strain rate at 25 and 482°C, but property variations with strain rate were found at 565 and 649°C. The tensile specimens from the center of the weld were generally stronger and less ductile than specimens from near the surface of the weld. The yield strength of the weld metal is greater at all temperatures than the minimum yield strength for type 304 stainless steel base metal taken from the ASME Boiler and Pressure Vessel Case 1331-5. The total elongations for the weld metal always exceeded 22%. (p. 210)

Transverse specimens that included base metal, fusion zones, and weld metal in the gage length were tested in tension at room temperature. These specimens failed at the center of the weld metal. (p. 229)

Computer studies of eddy current measurement of thickness have led to simple guidelines for design of optimum coils and techniques for more accurate results and minimized errors. Significant improvements were made in decreasing the drift in response due to variation in temperature of the coil to a value approximately 1% of that normally encountered. (p. 172)

The ultrasonic frequency analysis system was modified into a mobile system increasing its flexibility and utility. Excellent results were obtained in experimental determination of size of reflectors with irregular shape and contours. (p. 175)

Improvements to the closed circuit television system for radiographs allowed display of a break in a single 30-μm-diam wire in a mesh. (p. 179)

PART II. SPACE POWER TECHNOLOGY

Six refractory metal-clad UN pins and three UO_2 pins continue to operate satisfactorily in the ORR under space reactor conditions. (p. 253)

Additional creep data obtained at low stresses at 1650°C show a large decrease in the strength of CVD tungsten containing 20 ppm F compared to material having a fluorine content of 6 ppm. However, annealing at 1800°C before testing at 1650°C and 2000 psi decreases the minimum creep rate of the high fluorine material to one-tenth of that of the low fluorine material. (p. 258)

Irradiation of our high-temperature tungsten experiment in EBR-II has been completed after receiving a peak fluence of 8×10^{21} neutrons/cm^2 ($E > 0.1$ MeV). (p. 265)

Much higher oxygen levels can be tolerated by T-111 without embrittlement at temperatures higher than present Pioneer operating temperatures. T-111 embrittled by oxygen contaminants at 825°C can be ductilized by a heat pulse equivalent to that received by a Pioneer heat source upon reentry into the earth's atmosphere. (p. 269)

Molybdenum alloys and coatings on T-111 continue to show relative insensitivity to contaminating environments. (p. 278)

The Pt-Rh-W alloys were found to be relatively insensitive to atmosphere contaminants such as those found in radioisotope thermoelectric generators. Hemispheres of Pt—26% Rh—8% W and Pt—30% Rh—8% W—0.25% Hf—0.1% Ti have been successfully fabricated. (p. 283)

Iridium has been zone refined into single-crystal bar which can be cold swagged 40% without cracking. (p. 289)

CONTENTS

PART I. FAST REACTOR TECHNOLOGY

FUELS

1. DEVELOPMENT OF FBR OXIDE FUELS

P. Patriarca A. L. Lotts F. J. Homan

The purpose of this program is to advance the technology of $(U,Pu)O_2$ as a fuel for the LMFBR. The oxide fuels studied in this program are derived from coprecipitation, mechanical blending, and sol-gel processes and are fabricated by cold pressing and sintering and Sphere-Pac. We emphasize determination of the properties and performance of oxide fuels derived from the sol-gel process and fabricated by Sphere-Pac techniques, but we also compare these fuels with those fabricated by other processes. The main objectives of the program are (1) to establish the performance characteristics and limitations of $(U,Pu)O_2$ fuel fabricated by the different processes, (2) to obtain a fundamental understanding of the mechanisms that are involved in the behavior of fuel elements under irradiation, (3) to develop fabrication techniques that provide both economy and a product with optimized performance, and (4) to develop analytical methods sufficiently accurate to optimize experimental design and to predict the response of fuel elements to LMFBR service conditions.

Fabrication of $(U,Pu)O_2$ Fuels

J. D. Sease R. A. Bradley

The objective of our $(U,Pu)O_2$ fabrication program is to develop processes by which mixed oxide fuel of controlled density and stoichiometry can be fabricated for irradiation tests. A large portion of this program has been the development of Sphere-Pac and sol-gel pellet fabrication techniques.

During this report period we fabricated the fuel pins for a capsule to be irradiated in the ETR to provide fuel for reprocessing dissolution studies. We also completed fabrication of the GB-10 capsule and continued work on the replacement fuel pins for the F-1 experiment on the Gas-Cooled Fast Breeder Reactor program.

Fuel Reprocessing Fuel Pins (R. A. Bradley)

We fabricated four fuel pins to be inserted in capsule 43-123 for irradiation in the ETR. After irradiation the fuel will be used for fuel reprocessing dissolution studies. Each fuel pin contains about 3 in. of 94% dense $(U_{0.75},Pu_{0.25})O_{1.97}$ pellets fabricated by Westinghouse-Hanford from mechanically mixed oxides (batch FS018A1B1C5). This particular batch of fuel was selected because preliminary dissolution tests showed that its dissolubility was much greater than mechanically mixed oxides used in previous irradiation experiments in this series.

The fuel pellets were heat treated in our laboratory to reduce the sorbed gas to the specified limit. After heat treatment the sorbed gas, H_2O content, and oxygen-to-metal ratio were within specification. The fluorine content was 22 ppm, which was greater than the specified limit of 10 ppm, but it was decided to use the fuel rather than delay the experiment.

GB-10 Fuel Pin (R. A. Bradley)

The fuel pin for the GB-10 capsule to be irradiated in the ORR on the Gas-Cooled Fast Breeder Reactor program required about 8.8 in. of nominally 87.5% dense dished-end $(U_{0.88},Pu_{0.12})O_{1.97}$ pellets with the uranium containing 9% ^{235}U. During this report period we performed sintering tests to establish the pressing and sintering conditions required to yield the desired pellet density and oxygen-to-metal ratio and then fabricated sufficient pellets for loading GB-10. The fuel was completely characterized and then loaded into the preassembled fuel pin provided by Gulf General Atomic. The closure weld was made and inspected and the fuel pin was transferred to the Irradiation Engineering Group of the Reactor Division for encapsulation.

Replacement Fuel for the F-1 Experiment (R. A. Bradley)

Eight fuel pins containing $(U,Pu)O_2$ pellets were fabricated previously for the GCFR F-1 irradiation experiment in collaboration with Gulf General

Atomic.[1] We have been requested to prepare the fuel for five additional pins that will be used in replacement capsules. The fuel requirements and the preparation of the fuel were discussed previously.[2]

All of the cladding hardware has been received from GGA and initial welds have been made satisfactorily. The charcoal traps are presently being loaded. We expect to load the fuel pins during the next report period.

Irradiation Testing of $(U,Pu)O_2$ Fuels

F. J. Homan T. N. Washburn

The performance characteristics of mixed $(U,Pu)O_2$ fuels are being evaluated in a variety of irradiation tests for potential application in an LMFBR. We are now concentrating on comparative tests of fuel fabricated as pellets or as microspheres loaded by the Sphere-Pac technique. The program includes thermal-flux experiments, which permit use of instrumented capsules and continuously controlled heat rates, and fast flux experiments, in which the fission rate distribution and radiation effects on the cladding are more typical of those for operating conditions anticipated in an LMFBR.

Fast Flux Irradiation Tests (A. R. Olsen)

The fast flux irradiation tests in the EBR-II are designed to approximate conditions to be encountered in a commercial-scale LMFBR. The objective of these tests is to establish the effects of fuel fabrication form (Sphere-Pac or pellet), void distribution, and stoichiometry on the swelling of the fuel, mechanical and chemical interactions of fuel and cladding, release of fission gas, and distribution of fission

---

[1] T. N. Washburn, J. D. Sease, R. A. Bradley, E. J. Manthos, and M. K. Preston, LMFBR Fuel Cycle Studies Progr. Rept. May 1970, No. 15, ORNL-TM-3018, pp. 57–58.

[2] J. D. Sease and R. A. Bradley, Fuels and Materials Development Program Quart. Progr. Rept. September 30, 1971, ORNL-TM-3550, pp. 4–6.

products in a $(U,Pu)O_2$ fuel operating at typical heat rates to design levels of burnup.

The five Series I encapsulated tests all contain Sphere-Pac fuels. Two of the capsules, S-1-A and S-1-E, were returned to ORNL after the initial period of irradiation in subassembly X050 which was discharged from the EBR-II at the end of run 42 on May 18, 1970. The other three capsules are continuing under irradiation to a scheduled average burnup of 10.5% FIMA. On January 14, 1972, subassembly X119A in which these pins were being irradiated was discharged from the reactor for interim examination of all capsules and replacement of some capsules being irradiated by other AEC sites. At the time of discharge the calculated burnup on our three capsules for the combined exposure in subassemblies X050 and X119A was approximately 8% FIMA. The interim nondestructive examination is incomplete but the results of gamma scanning and neutron radiography indicate no failures or other abnormalities. Therefore, the current plans are to incorporate all three capsules in a reconstituted subassembly for continued irradiation starting with EBR-II run 56 in July 1972. Details of the subassembly loading configuration and selection of the reactor core location have not yet been defined.

The postirradiation examination of pins S-1-A and S-1-E is continuing with all effort now being directed toward establishing the radial distribution of fission products. Satisfactory nonaqueous polishing of selected sections was completed this report period. The microprobe analysis is currently under way. The results of the routine postirradiation examination reported in previous reports of this series have been summarized.[3]

The Series II tests are with unencapsulated pins in a 37-pin subassembly. Details of the testing program and the individual pin operating conditions are reported in the data package.[4] The Babcock and Wilcox Company fabricated 18 of the first 37 pins to be irradiated

---

[3]A. R. Olsen, "Sol-Gel Sphere-Pac $(U,Pu)O_2$ Fuel Performance in EBR-II Irradiation Tests," Trans. Am. Nucl. Soc. 14(2), 596–97 (Oct. 1971).

[4]A. R. Olsen et al., Preirradiation Data for ORNL Series II and B&W Oxide Fuels Tests in EBR-II, ORNL-TM-3446 (Nov. 1971).

in subassembly X112 and 16 pins for replacement of pins removed at the scheduled burnup levels. On July 1, we assumed responsibility for the entire irradiation program and postirradiation examination. The first incremental irradiation is being done in subassembly X112.

At the start of run 49, subassembly X112 was inserted in EBR-II grid position 6B2 but it was moved to the requested higher flux position 6E3 before the start of run 50. The irradiation is now approved through the current run (55) which is scheduled for termination on April 8, 1972. At that time the calculated burnup for the lead pin will be approximately 3.9% FIMA.

The scheduled installation of a stainless steel reflector in the EBR-II between runs 55 and 56 will require the relocation of this test group from the current row 6 to a row 7 position to maintain the desired fission rates. No row 7 position is adjacent to a control or safety rod thimble so the peak permissible plenum pressure for unencapsulated fuel pins in an N37 type subassembly is 1000 psi instead of the 450 psi for row 6 locations. With this relaxation in the plenum pressure limit available we have submitted a request to the EBR-II project to extend the irradiation of subassembly X112 to a calculated peak burnup of 6.1% FIMA for the lead pin as requested in the original data package. We have also requested an increase in flux to provide higher fission rates. The higher fission rates are to accommodate both the effects of fissile depletion and the lower coolant temperatures resulting from the actual measured subassembly coolant flow rate being approximately 10% higher than requested. The adjustment will return the prime operating parameter of peak cladding temperature to the desired 650°C without significantly affecting other operating parameters.

Uninstrumented Thermal Flux Irradiation Tests (A. R. Olsen)

A series of uninstrumented capsules is being irradiated in the X-basket facilities of the ETR. Each capsule contains four test pins arranged in tandem. The initial objective of these tests was to investigate at extended burnup the effects of fabrication form on release of fission gas, migration of fission products, and swelling of the fuel. The

capsules now being irradiated are to provide short-cooled irradiated fuel for LMFBR reprocessing studies. The current status of these tests is given in Table 1.1. The results of low and intermediate burnup level tests have been presented.[5,6]

During the report period we were informed of the probable change in operating mode for the ETR starting January 1, 1973. Consequently, the operating conditions for capsule 43-123 were reviewed with the group doing fuel recycle studies. As a result of these discussions the principal objective for this capsule was altered. Originally it was designed to investigate the effect of lowering the linear heat rate on fuel dissolution characteristics and was to contain the same fuel as capsules 43-117 through 43-119. Since the test space may not be available long enough to obtain a significant burnup level at the lower fission rate the capsule will be irradiated at the linear heat rate at which 43-117 through 43-119 have been operating (14 to 16 kW/ft). The test will now provide data on the effect of irradiation on the dissolution characteristics of a mechanically blended UO_2-PuO_2 pellet fuel which is essentially completely soluble in HNO_3 before irradiation. These data will then be compared with the data from the other tests which contained similar fuel in which approximately 15% of the PuO_2 was insoluble in HNO_3 before irradiation.

ETR Instrumented Tests (A. R. Olsen and R. A. Buhl)

The ETR instrumented tests are designed to determine the performance of mixed oxide fuel under simulated LMFBR design operating conditions.

Series I consists of two capsules, 43-120 and 43-121. Each capsule contains four fuel pins with two thermocouples to measure cladding temperature at the fuel axial midplane of each pin. These tests are designed to investigate fuel swelling and fuel-cladding chemical interactions of Sphere-Pac and pelletized $(U,Pu)O_2$ fuels over a wide range of cladding temperatures up to a maximum of 650°C.

---

[5]A. R. Olsen, C. M. Cox, and R. B. Fitts, "Low Burnup Irradiation Tests of Sphere-Pac Sol-Gel $(U,Pu)O_2$ Fuels," Trans. Am. Nucl. Soc. 12, 605–606 (1969).

[6]A. R. Olsen,"Intermediate-Burnup Irradiation Tests of Sphere-Pac Sol-Gel $(U,Pu)O_2$ Fuels," Trans. Am. Nucl. Soc. 13, 32–33 (1970).

Table 1.1. Noninstrumented Thermal Flux Tests of $(U,Pu)O_2$ Fuels

Experiment Number	Fuel		Number of Rods	Peak Burnup (% FIMA)[a]	Peak Linear Heat Rate (W/cm)	Peak Cladding Inner Surface Temperature (°C)	Status March 1972
	Form	Composition					
43-99	Sphere-Pac	$(^{235}U_{0.80},Pu_{0.20})O_{2.00}$	2	1.5[b]	1640[b]	1000	Examined
43-100	Sphere-Pac	$(^{235}U_{0.80},Pu_{0.20})O_{2.00}$	2	1.4[b]	1470[b]	900	Examined
43-103	Sphere-Pac Pellet	$UO_{2.02}$(20% ^{235}U) $UO_{2.00}$(20% ^{235}U)	3 1	5	690	530	Examined
43-112	Sphere-Pac	$(^{238}U_{0.85},Pu_{0.15})O_{1.97}$ $UO_{2.02}$(20% ^{235}U)	3 1	0.7	500	360	Examined
43-113	Sphere-Pac	$(^{238}U_{0.85},Pu_{0.15})O_{1.97}$ $UO_{2.02}$(20% ^{235}U)	3 1	10[c]	500[c]	380[c]	Being examined
43-115	Sphere-Pac	$(^{238}U_{0.85},Pu_{0.15})O_{1.97}$ $UO_{2.02}$(20% ^{235}U)	3 1	6.5	600	460	Examined
43-116	Sphere-Pac	$(^{238}U_{0.85},Pu_{0.15})_{01.97}$	4	1.5[c]	600[c]	460[c]	Processed
43-117	FTR Pellets	$(^{238}U_{0.75},Pu_{0.25})O_{1.98}$	4	1.5[c]	430[c]	360[c]	Being examined
43-118	FTR Pellets	$(^{238}U_{0.75},Pu_{0.25})O_{1.98}$	4	8.0[c]	430[c]	360[c]	In-reactor ≈7.3% FIMA
43-119	FTR Pellets	$(^{238}U_{0.75},Pu_{0.25})O_{1.98}$	4	10.0[c]	430[c]	360[c]	In-reactor ≈7.0% FIMA
43-123	FTR Pellets	$(^{238}U_{0.75},Pu_{0.25})O_{1.98}$	4	4.0	430[c]	360[c]	In preparation

[a] FIMA is fissions per initial actinide metal atom.

[b] Rods failed in reactor from overpowering.

[c] These are target design values.

Capsule 43-121 was discharged from the reactor on January 10, 1972, and capsule 43-120 was moved to a higher flux position. Both capsules at that time had been irradiated for 335 effective full power days and the estimated peak burnup for 43-121 was 7.6% FIMA. A detailed history of the irradiation conditions for each pin in each capsule has been prepared using a computer program which utilizes the thermocouple data and reactor operating history to calculate cladding temperatures, linear heat rate, and burnup. Figures 1.1 and 1.2 show such histories for the highest heat rate pin in each capsule. The computer program does not currently take into account gamma heating so the burnup level plotted is higher than the actual expected value. However, the other features including cladding temperature and linear heat rate are accurate.

Capsule 43-121 was discharged because the fuel cladding temperatures could not be brought back to the desired levels.[7,8] Capsule 43-120 was moved to a higher flux which was expected to bring the peak cladding inner surface temperature up to approximately 625°C. This transfer apparently did not provide as large a step in fission rate as the available data on unperturbed flux levels had indicated. In fact the apparent change in peak linear heat rate was from 12.1 to 13.8 kW/ft, an increase of only 14%. Based on the unperturbed flux ratio of the two positions, we had anticipated an increase of greater than 50%. The calculated peak cladding inner surface temperature, based on thermocouple readings, was 470°C prior to the change in position and 525°C after the change. The peak cladding temperature on the top pin did rise during the final few days of cycle 114 to approximately 600°C. This is an effect of extreme flux distribution changes and only lasts for a very short time at the end of an extended ETR cycle. At the end of cycle 114 on February 13, 1972, capsule 43-120 had been irradiated

---

[7]A. R. Olsen and R. A. Buhl, Fuels and Materials Development Program Quart. Progr. Rept. Sept. 30, 1971, ORNL-TM-3550, pp. 15–17.

[8]A. R. Olsen and R. A. Buhl, Fuels and Materials Development Program Quart. Progr. Rept. Dec. 31, 1971, ORNL-TM-3703, pp. 10–11.

Fig. 1.1. Capsule No. ORNL-43-120, Fuel Pin No. 2.

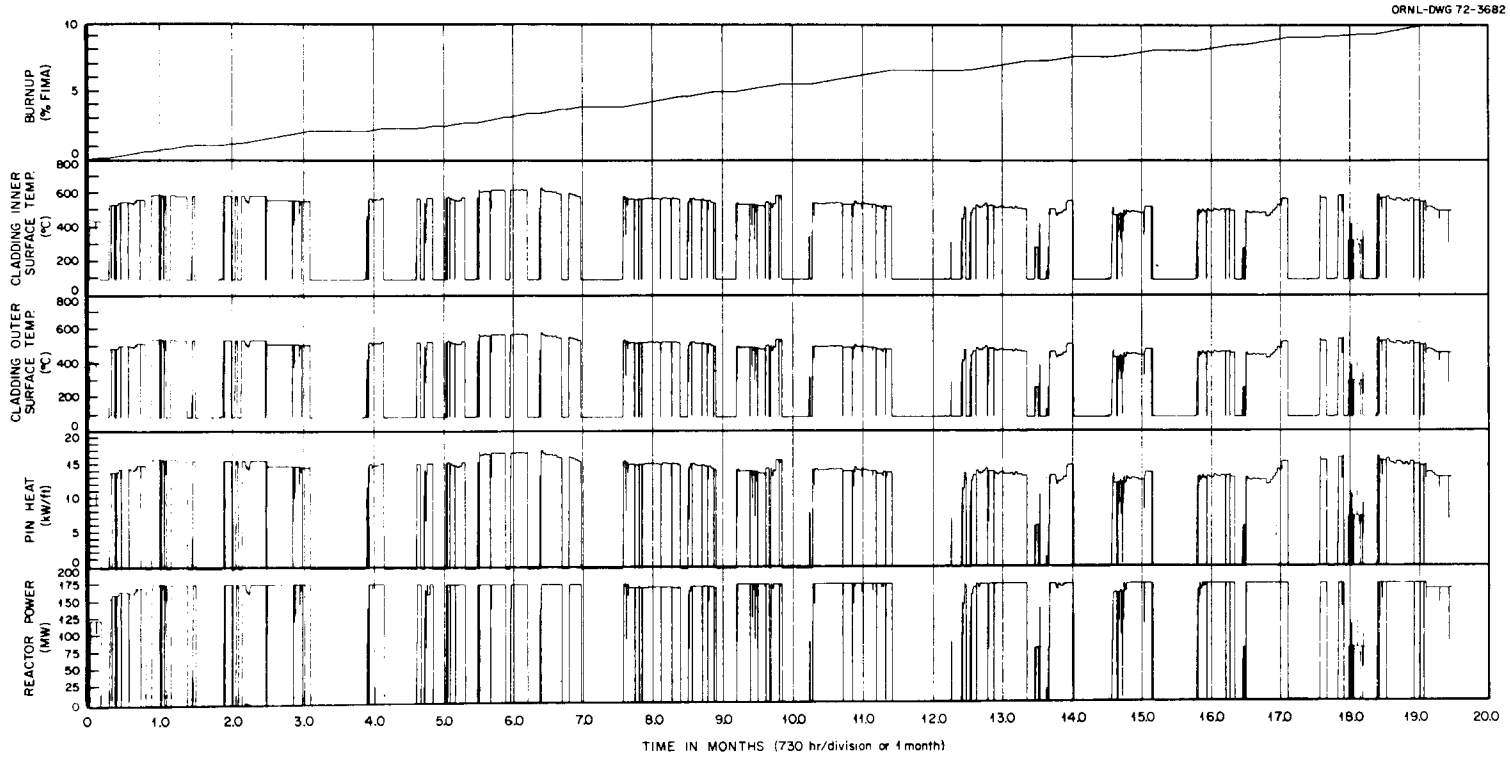

Fig. 1.2. Capsule No. ORNL-43-121, Fuel Pin No. 2.

for 351 EFPD to a peak calculated burnup of approximately 8% FIMA. We plan to remove this capsule after one more cycle of irradiation.

The Series II tests will consist of three instrumented capsules. These capsules will each contain a single fuel pin with a 20-in.-long fuel column. Each pin is instrumented with a pressure transducer to measure gas pressure in the plenum region during irradiation, and nine thermocouples to measure cladding temperatures at selected axial locations along the fuel column and in the gas plenum region.

One capsule will contain FTR type pellets of the highest permissible density (94% of theoretical), the second will contain FTR pellets of the lowest permissible density (88% of theoretical), and the third will contain a packed bed of Sphere-Pac U-Fines[9] fuel. In the latter fuel, all the plutonium is contained in the coarse fraction (~400 μm diam) microspheres and a fine fraction (<44 μm diam) of depleted UO_2 is infiltrated into the coarse bed.

The two capsules containing the low density FTR pellets and the Sphere-Pac fuel are currently under construction. We have begun the preparation of the safety analysis for these two capsules. This analysis indicates a peak unperturbed flux of 1.0 to 1.1 × 10^{14} neutrons/cm^2-sec (2200 m/sec) will be required to achieve the required operating conditions. The Aerojet Nuclear Corporation personnel inserted flux monitors in selected positions during cycle 115 to update the information on available fluxes. These measurements should minimize the possibility of improper test conditions such as we have encountered with the Series I tests.

Tests of Mechanical Interaction of Fuel and Cladding (B. Fleischer, R. B. Fitts, and R. L. Senn[10])

The intent of our program is to measure in-reactor the axial extension of both the fuel column and cladding and also the fuel pin

---

[9]J. D. Sease, C. R. Reese, R. A. Bradley, and W. H. Pechin, "U-Fine Process," pp. 329–331 in Symposium on Sol-Gel Processes and Reactor Fuel Cycles, Gatlinburg, Tennessee, May 4–7, 1970, CONF-700502.

[10]Reactor Division.

internal gas pressure during operation of prototypic LMFBR fuel pins under carefully controlled conditions. These include programmed power cycles and an occasional overpower cycle. The irradiation capsules are designed so that the fuel pin operates in the ORR Poolside irradiation facility at LMFBR prototypic power and temperature conditions. The irradiation tests are planned for one to two years and will give burnup levels of 5 to 9%. As described previously,[11] the first in-reactor power cycling capsule (MINT-1) contains a prototype Fast Test Reactor (FTR) fuel pin. The MINT-1 capsule was installed in the ORR during the November 16 shutdown. A summary of the operating history since that time is presented in Table 1.2. We achieved nominal operating conditions of approximately 14 kW/ft on March 9, and have been performing simulated reactor scrams as practical each day.

Preliminary analysis of a portion of the data collected during March 1972 reveals detail behavior patterns of the fuel column height and the internal pressure. The fuel column height as compared to the height at the start of the test is plotted versus time, starting March 14, 1972, in Fig. 1.3. At the beginning of this report period the fuel column was approximately 40 mils shorter than the initial height. Each increase in power to approximately 14 kW/ft causes an expansion of about 60 mils. This amount of expansion is consistent with that expected if the temperature near the fuel pellet outer surface is controlling. This is expected in this test since the pellets are dished at both ends. At this power level we estimate that the fuel surface temperature increases about 800°C. Assuming an expansion coefficient of about 8×10^{-6} in./in.-°C for the $(U_{0.8},Pu_{0.2})O_2$ fuel pellets, the 9.6-in. fuel column should expand about 61 mils. This reasonable agreement between measured and predicted values supports expectations and supports the value of dished pellets in minimizing fuel column expansion.

The internal pressure history of the fuel element is presented in Fig. 1.4. The salient features of these data are the systematic

---

[11]R. B. Fitts, R. L. Senn, J. G. Morgan, and J. D. Jenkins, Fuels and Materials Development Program Quart. Progr. Rept. June 30, 1970, ORNL-4600, pp. 58–63.

Table 1.2 Summary of Operating History

Power Level (kW/ft)	Time at Power[a] (hr)	Number of Cycles
2	24	Startup Phase of Operation
4	254	
6	77	
8	21	
10	24	
14	24	
14	412	12[b]
16	20	
Total	856	

[a]Through March 31, 1972.

[b]Typical transient: 60°C/hr heatup, average cooling rate to 100°C ≃400°C/min., and maximum cooling rate ≃480°C/min.

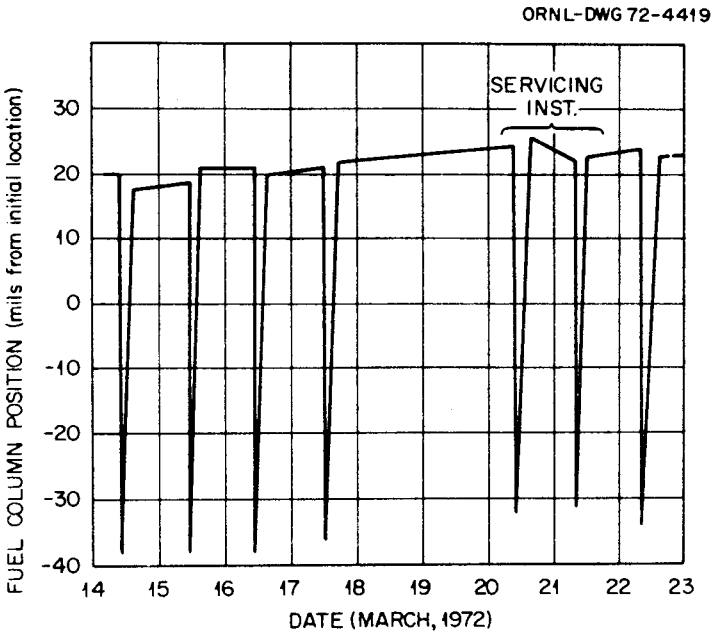

Fig. 1.3. MINT-1 Fuel Column Behavior.

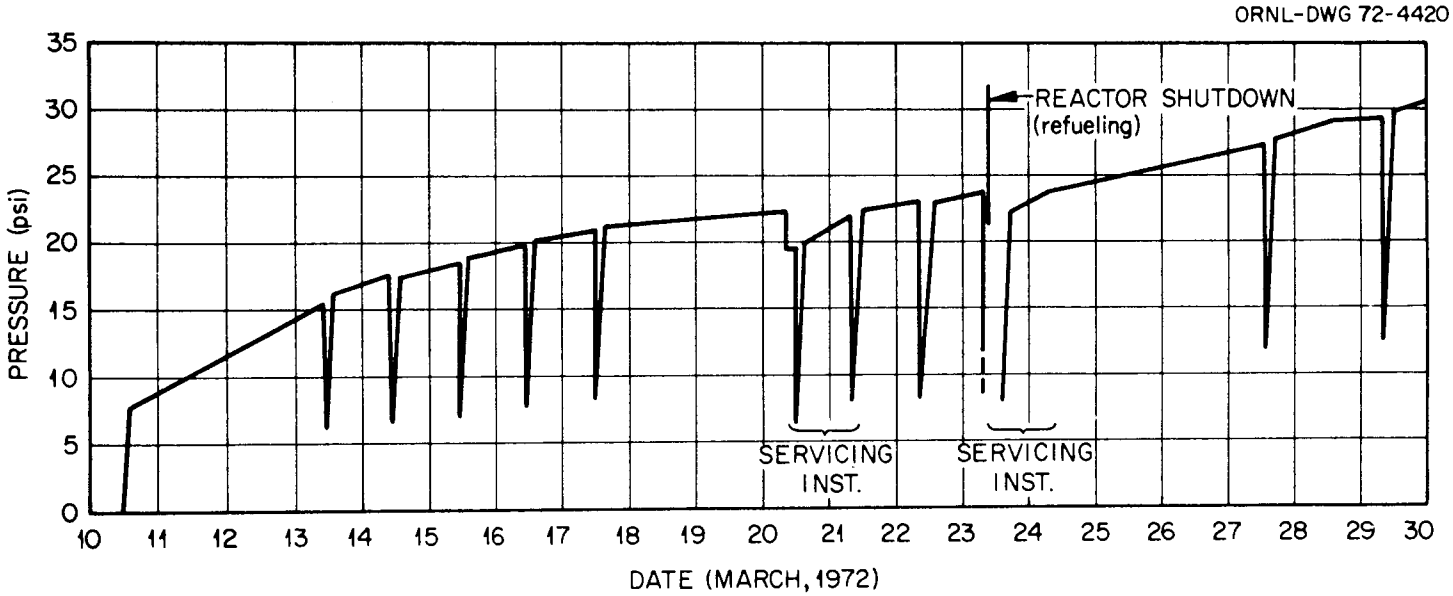

Fig. 1.4. MINT-1 Fuel Element Internal Pressure.

pressure changes as a function of burnup, and the small step changes in pressure after each cooldown and return to power. The incremental pressure change (∿0.5 psi) confirms the theory that fission gas release is promoted by thermal cycling. The data show that the pressure has slowly increased from about 0 to 12 psi during approximately 400 hr at 14 kW/ft.

Analysis of Fuel Element Performance

F. J. Homan

The objectives of this work are a fundamental understanding of the behavior of LMFBR fuel elements and the development of analytical models to describe their performance and probability of their failure under various operating conditions. Special emphasis is given to modeling fuel-cladding mechanical interactions and to characterizing irradiated $(U,Pu)O_2$ fuels. This work is an integral part of the irradiation testing program, providing design methods and evaluation of the tests.

Analysis of Oxide Fuel-Cladding Chemical Attack (J. M. Leitnaker)

The Rand-Roberts-Markin theory[12,13] has been advanced to describe the control of fuel stoichiometry across the strong temperature gradient of an oxide fuel pin. We have previously reported calculations which indicate this theory is probably not correct.[14] During the report period we refined and extended those calculations. The results have strengthened our belief that, while the Rand-Roberts-Markin theory was a useful approximation, it is not in fact correct. The calculations show that both oxygen transport gas species, CO_2 and H_2O, are reduced to very low values. The CO_2 is removed via reaction of the CO_2 with the clad to form the $M_{23}C_6$ phase, while H_2O is removed via diffusion of H_2 through the clad.

---

[12]M. H. Rand and L.E.J. Roberts, "Thermodynamics and Nuclear Engineering," pp. 3–31 in Thermodynamics, Vol. I, IAEA, Vienna, 1966.

[13]M. H. Rand and T. L. Markin, "Some Thermodynamic Aspects of $(U,Pu)O_2$ Solid Solutions and Their Use as Nuclear Fuels," pp. 637–50 in Thermodynamics of Nuclear Fuels, IAEA, Vienna, 1968.

[14]J. M. Leitnaker, Fuels and Materials Development Program Quart. Progr. Rept. Dec. 31, 1971, ORNL-TM-3703, pp. 13–14.

Removal of CO_2 from the Fuel - For clarity we briefly review the previous calculation, combining that with our present extension.

The thermodynamic basis for the Rand theory is the equilibria which would be imposed by the existence of a constant ratio of CO_2 and CO gas across a fuel pin. The important equation to be considered is

$$CO(g) + 1/2\ O_2(g) = CO_2(g) \quad . \tag{1}$$

The standard free energy for Reaction (1), $\Delta G°(1)$, is well known[15] and the oxygen potential at each point in the fuel is assumed by the theory to be determined by the relationship

$$RT\ \ell n\ P_{O_2} = 2\Delta G°(1) + 2RT\ \ell n \frac{P_{CO_2}}{P_{CO}} \quad . \tag{2}$$

Another reaction is important within the system, however. This is

$$2\ CO(g) = CO_2(g) + C(\text{graphite}) \tag{3}$$

for which $\Delta G°(3)$ is given by

$$\Delta G°(3) = -40{,}800 + 41.7\ T\ (\text{calories}) \quad , \tag{4}$$

from appropriate data in Kubaschewski et al.[15] Equation (4) reveals that at equilibrium Reaction (3) tends to proceed to the right at low temperatures and to the left at high temperatures. At 978 K, $\Delta G°(3)$ is zero; thus with a fuel in equilibrium with graphite whose overall oxygen potential would correspond to a $\frac{P_{CO_2}}{P_{CO}}$ ratio of unity, the P_{CO} would also be unity, and sufficient gas could be assumed to be present to transport oxygen within the fuel.

Because of the arrangement of a typical sodium-cooled reactor, a significant axial gradient exists along the fuel rod. Thus, the

---

[15] O. Kubaschewski, E. Ll. Evans, and C. B. Alcock, Metallurgical Thermochemistry, 4th ed., Pergamon Press, New York, 1967.

end of the rod at which sodium enters the core will be more than 200° colder than the hottest portion of the rod. With current design criteria, significant portions of cladding interior surfaces could be 750 K or colder. At 750 K, $\Delta G°(3) = -9{,}525$ cal, or log K = 2.775. Since for Reaction (3) the equilibrium constant, K, is

$$K = \frac{P_{CO_2} a_C}{(P_{CO})^2} \quad , \tag{5}$$

with an oxygen potential fixed by the fuel surface, the equilibrium pressure of CO_2 and CO is fixed by the activity of carbon.

The activity of carbon in type 316 stainless steel is reduced, relative to graphite, by formation of the $M_{23}C_6$ phase. We approximate this reduction in carbon activity as follows. The solubility limit of carbon in stainless steel, in equilibrium with $M_{23}C_6$, is given by Weiss and Stickler[16] as 0.029 wt % at 1650°F (1172 K) and 0.015 wt % at 1500°F (1089 K). A plot of log (wt % C) versus $\frac{1}{T}$ yields the solubility limit of 2.24×10^{-4} wt % C at 750 K. The activity of carbon in austenite at this composition can be obtained by extrapolating the data of Smith[17] on the activity of carbon in pure austenite. An activity of carbon relative to graphite of 1.82×10^{-3} at 750 K is obtained.

The carbon activity can also be computed from consideration of the equation

$$1/6\ Cr_{23}C_6(s) = 23/6\ Cr(s) + C(\text{graphite}) \tag{6}$$

for which the standard free energy change $\Delta G°(6)$ is given by[15]

$$\Delta G° = 16{,}380 + 1.54\ T \quad . \tag{7}$$

---

[16]B. Weiss and R. Stickler, Phase Instabilities During High Temperature Exposure of 316 Austenitic Stainless Steel, Scientific Paper 70-1D4-STABL-P1 (July 9, 1970).

[17]R. P. Smith, "Equilibrium of Iron-Carbon Alloys with Mixtures of $CO-CO_2$ and CH_4-H_2," J. Am. Chem. Soc. 48, 1163 (1946).

By assuming the activity of Cr is 0.2 and that of $Cr_{23}C_6$ is 0.7, which is the mole fraction of $Cr_{23}C_6$ in $M_{23}C_6$, (Ref. 16) we obtain an equilibrium carbon activity of 3.5 ± 10^{-3}. The agreement within a factor of 2 between the two independent calculations reinforces the confidence in value of the carbon activity.

Quite recently, Tuma et al.[18] has measured the activity of carbon in stainless steel by equilibrating such steels with pure iron containing known activities of carbon. The results led to activities much lower than those calculated here. He found for the mole fraction solubility of carbon, Nc, in stainless steel not differing significantly from type 316, that

$$\log_{10} Nc = -6120/T + 2.363 \quad , \tag{8}$$

and that the activity coefficient, γc, is given by

$$\log_{10} \gamma c = 741/T - 0.1206 \quad . \tag{9}$$

We compute an activity of carbon of 1.2×10^{-5}. This disagreement indicates the thermodynamic data for $Cr_{23}C_6$ are uncertain by several kilocalories, and we have not assessed the reason for this. For this presentation we choose to use the higher calculated carbon activity. Use of the lower activity would increase the deviation calculated from the Rand-Roberts-Markin theory.

Thus, at 750 K equilibrium with type 316 stainless steel containing the $M_{23}C_6$ phase should be established when

$$\log \frac{P_{CO_2}}{P_{CO}} - \log P_{CO} = 5.515 \quad . \tag{10}$$

---

[18] R. Tuma et al., "Activity and Solubility of Carbon in Stainless Chromium-Nickel Steel with Approximately 18% Cr and 8% Ni," Arch. Eisenhuettenw. (Duesseldorf) 40(No. 9), 727–731 (1969). [NLL-CE-Trans-5635-(9022.09)].

If $\frac{P_{CO_2}}{P_{CO}}$ is taken as fixed at unity by the fuel near the cladding, which corresponds to a stoichiometric $(U,Pu)O_2$ fuel and an oxygen potential greater than that to oxidize Mo to MoO_2, then P_{CO} is 3.0×10^{-6} atm, which also equals P_{CO_2} for this case.

This calculation is important for the following reason: Transport of oxygen within a fuel might take place either by gas phase movement or by solid-state diffusion, or a combination of both. Rand and Markin[13] believed 10 ppm C from the fuel converted to a $CO-CO_2$ mixture would provide enough pressure of CO and CO_2 to transport the oxygen by a gas phase mechanism. If one assumes an 85% smear density for the fuel, an effective temperature of 1200°C, 10 ppm C could produce a pressure of about 6 atm or 6 orders of magnitude greater than that in equilibrium with $M_{23}C_6$ in the clad at 750 K. In fact, carbides of the $M_{23}C_6$ type are seen concentrated near the inner cladding surface of stainless steel clad oxide fuel rods.[19]

Elimination of H_2O From the Fuel - We also calculated previously the rate of transport of H_2 through the cladding.[14] This calculation has been refined to take into account the change in diffusion rate of the H_2 at low pressures. For calculational purposes a 0.25-in.-diam (0.635 cm) fuel rod, clad in 0.015-in. (0.0381 cm) 316 stainless steel, of 85% smear density $(U,Pu)O_2$, and a fractional gas release of 0.09 cm^3 (STP) per gram of fuel, all assumed to be H_2, was considered. The calculation considers a centimeter length of rod. The free volume is thus 0.0368 cm^3 and the gas release is 0.204 cm^3 (STP). We have used the study by Randall and Salmon[20] on type 347 stainless steel to approximate type 316 stainless steel. The rate of H_2 diffusion from the fuel pin, R_o, in cm^3 (STP)/hr is given by

$$R_o = \alpha \sqrt{P} \frac{A}{d} \left[\frac{\beta d \sqrt{P}}{1 + \beta d \sqrt{P}} \right] , \qquad (11)$$

---

[19]B. F. Rubin, Summary of $(U,Pu)O_2$ Properties and Fabrication Methods, GEAP-13582, p. 55 (Nov. 1970).

[20]D. Randall and O. N. Salmon, Diffusion Studies I — The Permeability of Type 347 Stainless Steel to Hydrogen and Tritium, KAPL-904 (March 1953).

in which P is the pressure in cm of Hg; A is the area in cm^2, 1.755; d is the thickness in mm, −0.381; α is given by

$$\alpha = \alpha^\circ e^{\frac{-E}{2RT}} \ (cm^2\text{-}torr^{-1/2}\text{-}hr^{-1}) \quad . \tag{12}$$

β is γ/α, where γ is given by

$$\gamma = \gamma^\circ e^{\frac{-E'}{RT}} \ (cm/hr) \quad . \tag{13}$$

Units of E and E' are cal/mole; those of R are $cal/mole^{-1}\text{-}K^{-1}$, and T in K. Values of constants are: $\alpha^\circ = 105.6$, $E = 33.01 \times 10^3$, $\gamma = 616.0$, and $E' = 16.86 \times 10^3$. The pressure, P, of Eq. (9) was always calculated via the ideal gas law assuming an effective gas temperature of 1073 K. At a given pressure, the amount of H_2 lost by diffusion in incremental time was calculated. Then the amount of gas present was adjusted and the calculation repeated for a second increment, and the two results were averaged to yield a better approximation for the first increment. The calculation was repeated until the pressure of H_2 was reduced below 7.6×10^{-8} torr. The time increment size was reduced by a factor of 10 during calculation if the calculated loss was greater than the amount of H_2 present. Initial increments of 0.01 and 0.001 hr gave the same results within 0.6%. The time required to reduce the H_2 pressure to 1×10^{-9} atm was 0.33 hr at 873 K, and was 1.56 hr at 750 K.

The above calculation indicates that any H_2 initially present will rapidly be eliminated from the fuel-cladding system by diffusion through the cladding. Since P_{H_2O} near the fuel will be fixed by the oxygen potential of the fuel and P_{H_2}, P_{H_2O} can be calculated and must also be very low.

Aitken et al.[21,22] have performed transport experiments in a temperature gradient out-of-pile which relate to this problem. They

---

[21] E. A. Aitken, M. G. Adamson, S. K. Evans, and T. E. Ludlow, A Thermodynamic Data Program Involving Plutonia and Urania at High Temperatures, Quarterly Rept. No. 15, GEAP-12210 (April 1971).

[22] S. K. Evans, E. A. Aitken, and C. N. Craig, "Effect of a Temperature Gradient on the Stoichiometry of Urania-Plutonia Fuel," J. Nucl. Mater. 30, 57–61 (1969).

show that for $(U_{0.8},Pu_{0.2})O_{1.94}$ heated 15 hr in a gradient between 2000 and 1250°C, the heat of transport, Q*, is −7.1 kcal/mole down to about 1500 K. This value is interpreted as indicating that oxygen transport does not take place via an H_2-H_2O mechanism. Since the molybdenum capsule used for the experiments was surrounded with N_2—6% H_2, one should expect that the inside of the tube also contained H_2 at approximately 0.06 atm pressure. For the reaction

$$H_2(g) + 1/2\ O_2(g) = H_2O(g) \quad , \tag{14}$$

the standard free-energy change is given by[15]

$$\Delta G^\circ = -58{,}900 + 13.1\ T = RT\ \ell n \frac{P_{H_2}}{P_{H_2O}} + 1/2\ RT\ \ell n\ P_{O_2} \quad . \tag{15}$$

For $(U_{0.8},Pu_{0.2})O_{1.94}$, from Rand and Markin,[13] at 1500 K, $RT\ \ell n\ P_{O_2}$ = −142,000 cal. Using 0.06 atm as P_{H_2} we compute P_{H_2O} as 1.4×10^{-6} atm. Hence, at 1500 K with the material used for the experiment, transport by H_2O at 1.4×10^{-6} atm is slower than some other as yet unspecified mechanism.

The 15-hr experiment[22] described above used short pellets which were observed to be bonded together in the high temperature region. Another experiment used long pellets of $(U_{0.75},Pu_{0.25})O_{1.956}$ over the range 1445 to 1005°C for 2000 hr.[21] Two ranges of behavior were observed: 1445 to 1070°C in which a heat of transport, Q*, of −10.2 kcal/mole was observed, and 1070 to 1005°C in which Q* was −26 kcal/mole. The lower temperature region has a Q* which is significantly different from that corresponding to transport by H_2-H_2O ($\sim$ −45 kcal/mole). But even if they were the same, one can assume that at approximately 1400 K, H_2-H_2O transport no longer dominates because of the greatly reduced Q* above this point. Using the same data sources as before, we calculate $P_{H_2O} = 3.1 \times 10^{-6}$ atm at P_{H_2} = 0.06 atm and T = 1400 K.

Calculations presented above show that for near stoichiometric fuel the pressure of the oxygen-carrying species in a typical fuel pin will be approximately 3×10^{-6} atm in the case of CO_2, when equilibrium

is established with the clad, and will be much less than this in the case of H_2O because of loss of H_2 through the clad. The data obtained by Aitken allow us to conclude that transport of oxygen by gases at these pressures is slower than bulk transport processes within the oxide. This statement is true for the out-of-pile experiments. It seems to us that in the reactor the defects produced by irradiation would allow even faster bulk migration of oxygen.

Equation (10) reveals that as the CO_2-CO ratio increases by a factor of 10, P_{CO_2} increases by a factor of 100; Eq. (2) reveals that a corresponding increase then occurs in the oxygen potential. If such a high oxygen potential could be maintained within a fuel pin, it would seem that at some point control of oxygen distribution might indeed be controlled by a CO_2-CO mechanism. At present it seems more likely that the cladding itself will buffer any oxygen buildup above that corresponding to a CO_2-CO ratio of unity and that the CO_2-CO control mechanism will not be observed in reactor operation except for relatively short times.

From the above discussion it seems clear that after carbon is removed from the fuel the transport of oxygen in the bulk of a $(U,Pu)O_2$ fuel in-reactor must take place by some process(es) other than the CO-CO_2 transport process postulated by the Rand-Roberts-Markin theory. Measurement of the oxygen potential across a fuel pin would not only help establish the oxygen transport mechanism but would also help elucidate the fuel-clad interaction.

In principle, the oxygen activity could be measured indirectly by making use of fission products in a fuel element. Experiments have already been carried out at Argonne National Laboratory demonstrating that such a measurement is practical,[23,24] although the actual application

---

[23]C. E. Crouthamel and C. E. Johnson, "Chemistry of Irradiated Fuel Materials," Reactor Development Progress Report, ANL-7753, pp. 118–120 (1970).

[24]C. E. Crouthamel and C. E. Johnson, "Chemistry of Irradiated Fuel Materials," Reactor Development Progress Report, ANL-7887, pp. 5.31–5.33 (1971).

has not been made. The method involves measuring the distribution of Mo and MoO_2 across an irradiated fuel element. From the equation

$$Mo(s) + O_2(g) = MoO_2(s) \quad , \tag{16}$$

one sees that the oxygen potential can be obtained from the relationship

$$RT \ \ell n \ P_{O_2} = \Delta G^\circ(16) + RT \ \ell n \ k \frac{[MoO_2]}{[Mo]} \quad , \tag{17}$$

where k is the ratio of the activity coefficients of MoO_2 in the oxide phase and Mo in the metallic inclusion phase. Crouthamel and Johnson[23] have measured the concentration of Mo, Tc, Ru, Rh, Pd, and Fe in the metallic inclusions across several fuel sections with an electron microprobe and have also measured[24] the MoO_2 concentration in the oxide matrix, unfortunately on different pins. All that is lacking is the auxiliary thermodynamic data to be able to give a measurement of the oxygen potential.

Description of Fuel to Cladding Gap Conductance

C. M. Cox,[25] F. J. Homan, and R. L. Diamond[26]

Early versions of the FMØDEL code required that the fuel-cladding gap conductance be input. This simplification was adequate temporarily as other aspects of the code were developed, but is not acceptable in the final version of the code because of its serious limitations. For example, gap conductance increases with decreasing gap size (and thus changes with pin power) and decreases with increasing fission gas content (burnup). Thus to treat it as a constant is a poor assumption. Since the calculated fuel temperature profile depends upon the calculated surface temperature, and the surface temperature is in turn calculated from the

---

[25]Present address: Hanford Engineering Development Laboratory, Richland, Washington.

[26]ORAU summer student (Summer 1971).

cladding temperature and the gap conductance, the importance of this parameter for good analytical analysis is obvious. Many of the fuel performance characteristics are strongly temperature dependent, and predictions of fuel performance are adversely affected if calculated temperatures are in error due to an inadequate gap conductance model.

The gap conductance model presently incorporated in FMØDEL consists of two components. For large gaps where there is no solid-solid contact between fuel and cladding heat is conducted across the gap primarily by the gas present in the gap (a mixture of helium fill gas plus xenon and krypton fission gases). Should the fuel-cladding gap close due to differential thermal expansion or fuel swelling, there would be contact between the peaks of the fuel outer surface and inner cladding surface. Spaces between the points of contact would be filled with gas and conduction would occur both through the points of contact and across the gas pockets. Accommodation effects and surface roughness of fuel and cladding are important in the latter case.

Heat Transfer Across a Gas Gap - When gap conduction is due to heat transfer across a gas phase only, we begin with the Fourier equation of heat conduction.[27]

$$q = -k\ A \frac{dT}{dr} \tag{16}$$

where q = the rate of heat flow per unit length at radius r (W/cm),

k = the thermal conductivity of the gas at radius r (W/cm°C),

A = the surface area per unit length of a right cylinder of radius r (cm^2/cm),

$= 2\Pi r$, and

dT/dr = the radial temperature gradient at radius r (°C/cm).

---

[27]Warren M. Rohsenow and Harry Choi, Heat, Mass and Momentum Transfer, Prentice-Hall, Inc., Englewood Cliffs, New Jersey, 1961.

Now, under steady-state condition no heat is generated or absorbed in the fuel-cladding gap so q is a constant with r and k as a function of temperature. Thus Eq. (16) can be rewritten as

$$k(T)dT = -q \frac{dr}{A}$$

$$\text{or} \quad \int_{T_c}^{T_f} k(T)dT = \frac{-q}{2\Pi} \int_{r_c}^{r_f} \frac{dr}{r} = \frac{q}{2\Pi} \ln \frac{r_c}{r_f} \tag{17}$$

where T_f = the temperature at the fuel surface (°C),
T_c = the temperature at the cladding inner surface (°C),
r_c = the radius of the cladding inner surface (cm), and
r_f = the radius of the fuel outer surface (cm).

T_c is known, so if k(T) is also known, Eq. (17) can be solved for T_f. We assume that the gas in the fuel-cladding gap is a mixture of fission gas (krypton and xenon) and helium fill gas. The relative amounts of each will change with burnup. Brokaw's equation[28] is used to calculate the thermal conductivity of a mixture of monotomic gases. This equation is given below.

$$k_{mix} = 0.5 \left[\sum_{i=1}^{n} X_i k_i + \frac{1}{\sum_{i=1}^{n} \frac{X_i}{k_i}} \right] \tag{18}$$

where k_{mix} = the thermal conductivity of the gas mixture at a given temperature (W/cm°C),
X_i = the mole fraction of the ith gas in the mixture, and
k_i = the thermal conductivity of the ith gas at the given temperature.

---

[28]R. S. Brokaw, "Estimating Thermal Conductivities for non-Polar Mixtures: Simple Empirical Method," Ind. Eng. Chem. 47(11), 2398–2400 (1955).

Expressions for $k_i(T)$, the thermal conductivity functions for the three gases considered (He, Xe, Kr) were developed by fitting data from the literature[29-31] to an expression of the following form.

$$k_i(T) = A_i + B_i T + C_i T^2 \quad . \tag{19}$$

Values for A_i, B_i, and C_i for the three gases considered are tabulated below.

	He	Xe	Kr
A	1.31×10^{-3}	5.74×10^{-5}	9.56×10^{-5}
B	3.70×10^{-6}	1.45×10^{-7}	2.14×10^{-7}
C	-5.85×10^{-10}	-2.32×10^{-11}	3.51×10^{-11}

Equation (17) then becomes

$$\phi_1 + \phi_2 + \phi_3 + \phi_4 - \frac{q}{\Pi} \ell n \frac{r_c}{r_f} = 0 \tag{20}$$

where $\phi_1 = X_{He} \int_{T_c}^{T_f} k_{He}(T)dT,$

$$\phi_2 = X_{Xe} \int_{T_c}^{T_f} k_{Xe}(T)dT,$$

$$\phi_3 = X_{Kr} \int_{T_c}^{T_f} k_{Kr}(T)dT, \text{ and}$$

$$\phi_4 = \int_{T_c}^{T_f} \frac{dT}{\left(\frac{X_{Ke}}{k_{He}(T)} + \frac{X_{Xe}}{k_{Xe}(T)} + \frac{X_{Kr}}{k_{Kr}(T)}\right)} \quad .$$

---

[29]J. H. Dymond, "High Temperature Transport Coefficients for the Rare Gases Neon to Xenon," p. 624 in J. Phys. B: Atom, Molec. Phys.,Vol. 4 (1971).

[30]R. W. Powell, C. Y. Ho, and P. E. Liley, Thermal Conductivity of Selected Materials, National Standard Reference Data Series, National Bureau of Standards, 8, p. 149 (1966).

[31]G. V. Massey, The Thermal Properties of Gases for Use in Reactor Heat-Transfer Calculations, DEG Report 14 (D), UKAEA, Risley, Warrington, Lancashire (1960).

The mole fractions of the three gases are calculated from the known burnups and fission product yields of the fissile species, and the available models for fission gas release. Since ϕ_1, ϕ_2, and ϕ_3 are simply the mole fractions of He, Xe, and Kr respectively, multiplied by the integral of a polynominal representation of the gas thermal conductivity as a function of temperature, values can be obtained in closed form. For ϕ_4, however, integration cannot be accomplished in closed form, so a numerical procedure using Simpson's rule is employed. Thus, to solve Eq. (17) for T_f, Newton's method is used whereby

$$(T_f)_{i+1} = (T_f)_i - \frac{f\left[(T_f)_i\right]}{f'\left[(T_f)_i\right]} \tag{21}$$

where $(T_f)_{i+1}$ = value of T_f for iteration i+1,

$(T_f)_i$ = value of T_f for iteration i, and

$$f\left[(T_f)_i\right] = \int_{T_c}^{(T_f)_i} k_{mix}\,(T_f)\,d(T_f)_i - \frac{q}{2\Pi}\,\ell n\left(\frac{r_c}{r_f}\right) .$$

$$f'\left[(T_f)_i\right] = k_{mix}\,(T_f)_i . \tag{22}$$

Equation (22) results from the theorem

$$\frac{d}{dx}\left[\int_{g(x)}^{h(x)} f(x)dx\right] = f[h(x)]\,h'(x) - f[g(x)]g'(x) .$$

Equation (21) is iterated until T_{i+1} and T_i are within some user specified number of degrees of each other.

After convergence has been achieved with respect to the fuel surface temperature, the temperature distribution throughout the rest of the fuel is calculated using methods already described.[32] Expansion of the fuel is

[32] C. M. Cox and F. J. Homan, PRØFIL — A One-Dimensional FORTRAN IV Program for Computer Steady-State Temperature Distributions in Cylindrical Ceramic Fuels, ORNL-TM-2443 (March 1969) and Addendum (August 1969).

then calculated, employing a simple model[33] to account for the fuel cracking which occurs to relieve the stresses caused by the high temperature gradients in oxide fuels. Since the fuel thermal expansion will change the value of the $\ell n(r_c/r_f)$ term in Eq. (17) the entire calculational procedure is repeated again and the new value for fuel central temperature compared to the one calculated previously. Iteration is continued until consecutive center temperatures agree to within some user specified error.

Heat Transfer Across a Closed Gap - In an operating fuel pin the gap between the fuel and cladding becomes smaller during power increases due to differential thermal expansion between the fuel and cladding. As burnup increases the fuel swells due to accumulation of fission products, further reducing the gap. If Eq. (17) remains valid as the gap closes it can be seen that

$$\lim_{r_f \to r_c} \ell n \frac{r_c}{r_f} = 0$$

$$\text{so } T_f \to T_c \text{ as } r_f \to r_c$$

implying that the heat transfer coefficient across the gap approaches infinity as the gap closes. This, however, is not the case.

The fuel and cladding surfaces are not perfectly smooth, but are made up of peaks and valleys. As the gap closes the peaks on the fuel surface come into contact with the peaks on the cladding surface, and heat is transferred both through the points of solid-solid contact and through the pockets of gas phase in between the points of contact. As the contact pressure between the fuel and cladding increases, the points of contact become enlarged due to localized plastic deformation in both fuel and cladding, and the component of heat transfer from solid to solid will increase.

---

[33]F. J. Homan, A Parametric Analysis of Fuel-Cladding Mechanical Interactions, ORNL-TM-3508 (August 1971).

Ross and Stoute[34] have suggested an equation to describe the heat transfer across a closed fuel cladding gap.

$$h = h_s + h_f \quad , \tag{23}$$

$$h_s = \frac{k_m P}{A_o R^{1/2} H} \quad , \tag{24}$$

$$h_f = \frac{k_f}{c(R_1+R_2) + (g_1+ g_2)} \quad , \tag{25}$$

where h_s = component of heat coefficient by conduction through the solid-solid contact spots ($W/cm^2-°C$),

$k_m = \frac{2(k_1\ k_2)}{k_1 + k_2}$ ($W/cm-°C$) ,

k_1 = the thermal conductivity of the fuel at the outer surface ($W/cm-°C$)

k_2 = the thermal conductivity of the cladding at the inner surface ($W/cm-°C$),

P = the contact pressure between fuel and cladding, normal to the interface (kg/cm^2),

a_o = a constant ($cm^{1/2}$),

$R = \left[\frac{R_1^2 + R_2^2}{2}\right]^{1/2}$ (cm),

R_1 = the root mean square roughness of the fuel (cm),

R_2 = the root mean square roughness of the cladding (cm),

H = the Meyer hardness number of the softer material (fuel or cladding) (kg/cm^2),

h_f = the component of heat transfer coefficient due to conduction through the gas occupying the void spaces between spots of solid-solid contact ($W/cm^2-°C$),

k_f = the thermal conductivity of the gas occupying the void spaces between spots of solid-solid contact, at the average temperature of the void spaces ($W/cm-°C$),

c = a dimensionless constant,

g_1 = the average temperature jump distance for the gas at the fuel surface (cm), and

g_2 = the average temperature jump distance for the gas at the cladding surface (cm).

---

[34]A. M. Ross and R. L. Stoute, Heat Transfer Coefficient Between UO_2 and Zircaloy-2, AECL-1552 (June 1962).

Of the terms used in Eqs. (23) through (25) and defined above, several need additional description. In calculating the temperature distribution in a fuel pin, the steady-state temperature at the cladding inside diameter can be determined without knowledge of the gap conductance but from geometry and heat generation rates alone. Therefore, k_2 can be considered known. However, without knowing the gap conductance, the temperature of the fuel surface is not known and therefore k_1 is not known. Therefore, a temperature must be estimated to calculate a value for k_1, then a gap conductance determined from Eq. (23), a temperature at the fuel surface calculated, resulting in a new value for k_1. This process is iterated until convergence is achieved.

The contact pressure between fuel and cladding is usually not known either and must be calculated. A description of the procedures used here is beyond the scope of this work but may be found in our publications[33] related to work done with the FMØDEL fuel performance code.

The constant a_o was used by Ross and Stoute[34] to fit their gap conductance data generated in a vacuum to an equation of the form of Eq. (24). In a vacuum there would be no gas phase heat transfer. For the heat transfer between UO_2 fuel and zircaloy cladding, a value of $a_o = 1/2\ cm^{1/2}$ gave the best fit of the data.

The Meyer Hardness Number (H) used in Eq. (24) is an indication of the hardness, or resistance to deformation, of the softer material. By comparing creep strengths of UO_2 and stainless steel it is easily verified that at the temperatures typical of the fuel-cladding gap, stainless steel is the softer material. As the contact pressure between two surfaces increases, the points of contact become enlarged due to localized plastic deformation and solid-solid conductance is improved. The harder the materials in contact (large H) the more resistant they are to plastic deformation and subsequent improvement in conductance, as predicted by Eq. (24). The Meyer Hardness Number is a measure of indentation hardness and is defined as the load applied during a static ball test divided by the projected cross sectional area of the indentation. Meyer's work was proceeded by the work of Brinell, who defined indentation hardness as the load applied during a static ball test to the surface area of the

indentation. Meyer and others were able to point out some shortcomings in Brinell's technique of comparing the hardness of different materials and recommended changing the basis of the hardness number to the projected area of the indentation rather than the surface area, but by that time there had accumulated a large body of data based on Brinell's technique and there was considerable oppositon to altering a well-established scale of values.[35] Since Brinell hardness values are much more readily available in the literature, we have used this scale in our work. The difference between the two hardness scales is quite small for stainless steel,[36] with the Meyer number being slightly larger because the projected area of the indentation is smaller than the indentation surface area. It will be shown later that h_f is substantially larger than h_s, making this simplification of even smaller consequence. Unfortunately, hardness data only at room temperature is readily available in handbooks. Ross and Stoute[34] suggested that the hardness of a materials is proportional to the yield strength, and using this assumption a curve of hardness versus temperature has been developed. A Brinell Hardness Number of 150 kg/mm^2 at room temperature[37] and a yield relationship of 42.5 ksi at room temperature[38] were used to normalize the relationship, which is shown in Fig. 1.5.

---

[35]Hugh O'Neill, Hardness Measurement of Metals and Alloys, Chapman and Hall Ltd., London, 1934.

[36]Vincent E. Lysaght, Indentation Hardness Testing, Reinhold Publishing Co., 1949.

[37]Metals Handbook, Vol. 1, Properties and Selection of Metals, 8th ed., p. 414 (1961).

[38]J. B. Conway, J. T. Berling, R. H. Stentz, and D. G. Salyards, Stress-Strain Behavior of Several Stainless Steel to Elevated Temperatures, GEMP 686, p. 157 (May 1969).

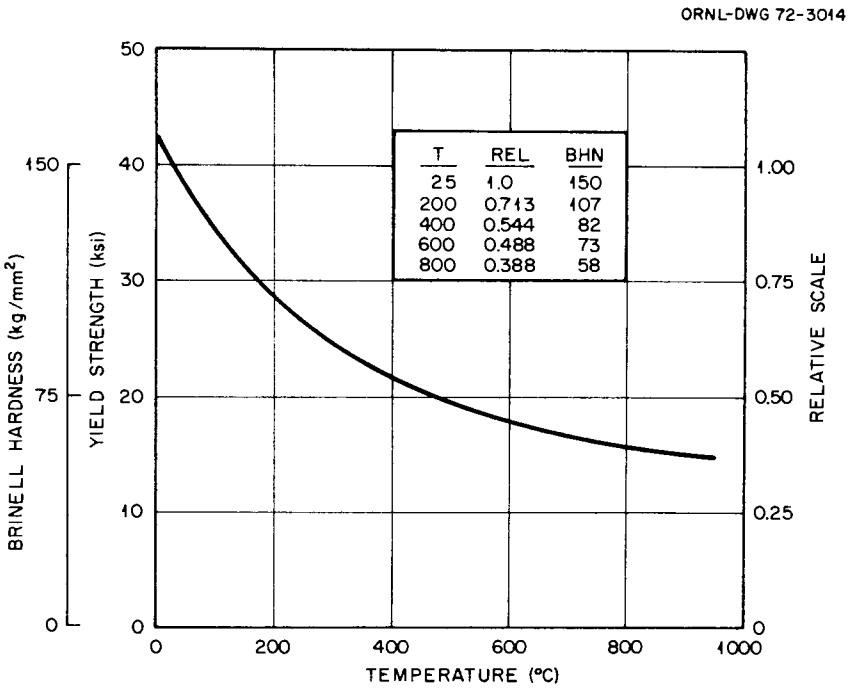

Fig. 1.5. Yield Strength vs Temperature for Type 316 Stainless Steel.

The dimensionless constant c in Eq. (25) is used to describe the effective width of the gas gap between the two surfaces in contact. The denominator in Eq. (25) is the effective width of the gas gap and is composed of terms reflecting the surface roughness of the fuel and cladding materials and the temperature jump distances. If Eq. (25) were to be rewritten in the form of Eq. (26)

$$t = \frac{k_f}{H_f} = c(R_1+R_2) + (g_1+g_2) \qquad (26)$$

and if values of k_f/h_f obtained from experimental data such as Ross' and Stoute's[34] are plotted against (R_1+R_2) at constant interfacial pressure, the resulting curve should be a straight line with slope c and y axis intercept (g_1+g_2). Upon performing this exercise, Ross and Stoute found that c had a value of about 2.5 for an interfacial

pressure of 100 kg/cm^2 (1422 psi) and this decreased to about 1.5 at 500 kg/cm^2 (7110 psi). Cursory analysis of the contribution of surface roughness to effective width of the gas gap would probably result in the expectation that c should be unity. That it is larger is most likely due to the "waviness" and "error of form" of the two surfaces in contact. That is, in addition to the separation of the two surfaces in contact by the peaks present on each surface there is an additional component of separation due to a deviation from cylindrical form inherent in each surface. That this deviation decreases with increasing pressure (evidenced by the value of c decreasing from 2.5 to 1.5 in going from 100 to 500 kg/cm^2) is expected, as the waviness and error of form of the softer material are forced by the high pressure to assume the waviness and error of form of the harder material. In our model the value of c is determined by linear interpolation and extrapolation of the values reported by Ross and Stoute.

Besides surface roughness, the temperature jump distances at the gap boundaries (g_1+g_2) contribute to the effective width of the gas gap. The geometrical interpretation of the temperature jump distances is shown schematically in Fig. 1.6. As shown in the figure, the temperature

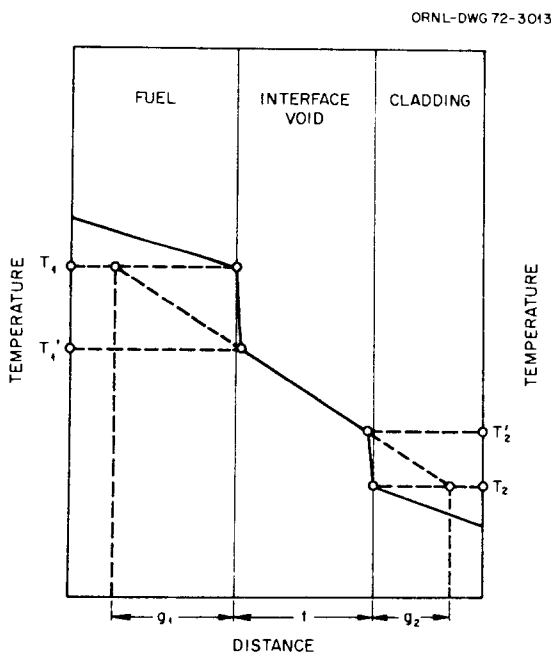

Fig. 1.6. Schematic Temperature Distribution Across a Void in the Interface Between Two Solids, A and B.

gradient across the gap is linear, except in the regions immediately adjacent to the fuel and cladding where there is a sharp departure from linearity. The departure is due to the difficulty with which gas atoms and atoms at the surface of the solids exchange energy. For example, a hot gas atom strikes the cooler cladding surface and is reflected back into the gap, having given up only a fraction of its energy to the cladding surface. If the linear temperature gradient in the gap were extended beyond the boundaries of the fuel and cladding, as shown in Fig. 1.6, a new "effective" gap is defined by the end points of the linear temperature gradient. The size of this effective gas is (g_1+g_2+t) where t is the actual distance separating the two solid surfaces. The temperature jump distance at a given solid surface is defined[39] by the following expression

$$T_k - T_w = g \frac{\partial T}{\partial n} \tag{27}$$

where T_k = the temperature that the gas adjacent to the surface would be if the temperature gradient of the gas continued without change right up to the surface itself (represented by T_1' and T_2' in Fig. 1.6),

T_w = the wall temperature (T_1 and T_2) in Fig. 1.6,

g = the temperature jump distance, and

$\frac{\partial T}{\partial n}$ = the temperature gradient in the gas ($\frac{T_1' - T_2'}{t}$ in Fig. 1.6).

The temperature jump distance has been shown[39] by kinetic theory to be directly proportional to the mean free path of the gas occupying the gap. In developing the theory related to the temperature jump distance, it is convenient to introduce a constant describing the extent to which an interchange of energy takes place when a gas atom or molecule strikes a solid surface. This constant, called the accommodation coefficient, is defined as the fractional extent to which those gas molecules or atoms that fall on a surface and are reflected from it have their mean energy adjusted or "accommodated" toward what their mean energy would be if they

---

[39]Earle H. Kennard, Kinetic Theory of Gases, McGraw-Hill Book Co., Inc., New York, p. 311 (1938).

were issued as a stream of gas out of a mass at the same temperature as the surface. The absolute value of the accommodation coefficient depends upon the gas species, the surface, and the temperature of the interface. The temperature jump distance can now be expressed[39] in terms of the accommodation coefficient

$$g = \frac{2 - \alpha}{\alpha} \quad (2\Pi RT)^{1/2} \frac{k}{(\gamma + 1)C_V P} \tag{28}$$

where g = the temperature jump distance (cm),

α = the accommodation coefficient (dimensionless),

R = the gas constant (joules/g°C),

T = the surface temperature (°K),

γ = the ratio $\frac{C_P}{C_V}$,

C_V = specific heat at constant volume (cal/g°C),

C_P = specific heat at constant pressure (cal/g°C),

k = the gas thermal conductivity (cal/sec cm °C), and

P = the pressure of the gas (dynes/cm^2).

Since the gas in the gap between the fuel and cladding is usually a mixture of fill gas and fission gases, several of the terms used in Eq. (28) must be weighted averages. Accordingly, Table 1.3 reflects the values used for He, Xe, and Kr, which are the primary constituents of the gas in the gap. The weighted averages of the gas properties contained in Table 1.3 were obtained through application of the "law of mixtures,[40]" which states that the contribution of a given gas species in a mixture of gases is according to the weight of that species.

---

[40]Earle H. Kennard, Kinetic Theory of Gases, McGraw-Hill Book Co., Inc., New York, p. 266 (1938).

Table 1.3. Properties of Helium, Xenon, and Krypton Gases

	Helium	Xenon	Krypton
(g/mole)	4.003	131.30	83.80
$R \frac{\text{joules}}{g°K}$	2.007	0.0633	0.0993
$C_v \frac{cal}{g°C}$ (Ref. a)	0.747	0.0226	0.0347
γ (Ref. b)	1.659	1.66	1.68
α	0.4[c]	1.0	1.0
λ (cm) (Ref. c,d)	18.62×10^{-6}	3.76×10^{-6}	5.12×10^{-6}

[a] G. V. Massey, The Thermal Properties of Gases for Use in Reactor Heat Transfer Calculations, DEG Report 14(D), UKAEA, Risley, 1960. Tables XVI and XIX.

[b] Kennard, p. 252.

[c] Kennard, p. 323.

[d] λ is the mean free path.

2. ADVANCED FAST BREEDER REACTOR FUELS DEVELOPMENT

J. L. Scott P. Patriarca

The goals of this program are to investigate the properties and behavior of those uranium- and plutonium-base ceramic fuels that we term conductors such as the mononitrides, carbonitrides, and monocarbides (LMFBR) fuel with that of $(U,Pu)O_2$, which by comparison is an insulator. Since the thermal conductivity of the ceramic conductors is about ten times that of $(U,Pu)O_2$, one could theoretically operate a conductor at ten times the power density with the same central temperature. In practice, heat transfer limitations, thermal stresses in the cladding, and high rates of swelling at high temperatures limit the power density to about two or three times that of $(U,Pu)O_2$ – still a challenging improvement. Additionally, the margins for transient overpower are much higher in the ceramic conductors than in $(U,Pu)O_2$.

In spite of the potential benefits of advanced LMFBR fuels, the level of effort is being reduced because of the budget limitations. For this reason this program is being phased out at ORNL and the work reported here represents an orderly phaseout.

Other work on nitride fuels is reported in Chapter 10.

Irradiation Testing

T. N. Washburn

Thermal Flux Tests

Two noninstrumented capsules of four pins were irradiated in the ETR. These "scanning" tests were to determine the performance of high purity (U,Pu)N. The peak linear heat rating was 30 kW/ft and peak burnup was about 5% FIMA for one capsule and will be about 8% FIMA for the second capsule. The fuel is cold-pressed pellets with densities from 86 to 91% of theoretical, and the fuel pins have a 0.010-in. radial gap between the fuel pellet and cladding, filled with NaK-19 to enhance heat transfer.

Capsules 43-N1 and 43-N2 were inserted into the ETR during the cycle 110 shutdown and the reactor went to full power on December 9, 1970. Capsule 43-N2 was removed from the reactor in January 1972 during the midcycle shutdown of cycle 114 and shipped to LASL for postirradiation examination. This capsule is approximately 5% FIMA. Capsule 43-N1 will remain in the reactor until the end of FY 1972.

Synthesis, Fabrication, and Characterization of Advanced FBR Fuels

E. S. Bomar

We found variation in the stability of nitride powders which had been oxidized then exposed to air. During this quarter we evaluated a procedure for nitric acid dissolution instead.

Passivation Treatment of Residual Nitride Fuels

The experimental treatments, described in the last quarterly progress report,[1] to convert our residual nitride materials to a stable form were continued.

We found a variation in the behavior of different batches of nitride powders in contact with water wet mixtures of argon plus air or oxygen and at a temperature of 500°C. Some powders were completely converted to the oxide, as indicated by weight change; others showed superficial weight increases, à behavior also observed earlier.

A test, by exposing a small sample in an air atmosphere box, of the stability of one batch of powder which showed a small weight increase during oxidation resulted in a flash burning of the sample. This occurred even though the powder had been heated for several hours in an oxidizing atmosphere.

---

[1]E. S. Bomar, Fuels and Materials Development Program Quart. Progr. Rept. Dec. 31, 1971, ORNL-TM-3703, pp. 35–37.

We concluded that the available furnacing equipment would not assure that a stable oxidized powder would be formed. We, therefore, examined nitric acid dissolution as an alternate method of treatment.

The glove boxes in which we have done the nitride work and their off-gas system are not designed for wet chemical operation. We, therefore, assembled a gettering column to condition the gaseous products of dissolution prior to releasing them into the glove box atmosphere. Initially, the column contained three layers composed of Ascarite, Dri-Rite, and charcoal. A small squirrel-cage blower capable of static negative pressure of about 1 in. w.g. was attached to the getter column. This was sufficient to provide a slow flow of argon from the box atmosphere through the flask and getter column when one of the two necks on the flask was uncovered.

We had assumed that the rate of powder addition for dissolution would be limited due to heating during dissolution. In practice, the limit was set by burning portions of the nitride powder as the concentration of nitrogen oxides in the flask reaches a level sufficient to cause ignition of the nitride powder as it fell through the atmosphere above the acid. The pyrotechnics were disconcerting but were controlled by stopping the feed until the flask had purged a bit. This resulted in a slow rate of treatment of powder.

Early in the dissolution work we found that the Ascarite loaded column quickly choked off due to formation of a wet layer of reaction product. Diluting the Ascarite with about 50% of Dri-Rite tempered but did not eliminate the problem. We subsequently replaced the Ascarite, Dri-Rite, and charcoal column with two pint jars containing sodium hydroxide pellets. The reactive gases were removed in the first jar; the sodium hydroxide in the second jar remained unaffected. We could dissolve an average of about 100 g of nitride a day in a 1-liter dissolver flask equipped with getter jars containing sodium hydroxide pellets.

3. DEVELOPMENT OF FBR NEUTRON-ABSORBER MATERIALS

R. G. Donnelly J. L. Scott G. M. Adamson, Jr.

The objective of our work is to characterize boron carbide sufficiently to provide measurable control parameters to properly evaluate fabrication techniques and the effects of irradiation. The irradiation studies emphasize effects of materials variables in fast-reactor environments. Concurrently, we are evaluating tantalum alloys and tantalum borides as potential alternates to boron carbide. Helium vents are also being developed for absorber rods.

Irradiation Behavior of Boron Carbide

Supplemental Evaluation of Powders from HEDL Experiment X042 (G. L. Copeland)

The results reported in the previous quarterly report essentially completed our supplemental evaluation of these powders, which were irradiated by HEDL as vibratorily compacted capsules in the EBR-II. These results have been summarized in a report.[1] During this quarter we have performed a vacuum fusion of these powders for a retained gas content determination. The values obtained are listed in Table 3.1. These results compare very well with the capsule puncture and vacuum fusion results of HEDL.

Gas Release and Solid Swelling of Irradiated B_4C from EBR-II Higher Worth Control Rods (G. L. Copeland)

We are evaluating pellets from capsules G and H from the ANL Higher Worth Control Rod, Assembly L-4008S, from the EBR-II. In the previous quarterly we reported the results of the (1) plenum gas analysis, (2) visual examination, (3) length, diameter, and weight measurements, (4) transmission electron microscopy, and (5) scanning electron microscopy of fractured surfaces. During this quarter we have obtained metallography, x-ray diffraction measurements of lattice parameters,

---

[1] G. L. Copeland, H. L. Yakel, and C.K.H. DuBose, Evaluation of Fast-Reactor-Irradiated Boron Carbide Powders, ORNL-TM-3729 (in press).

Table 3.1. Retained Helium Analysis by Vacuum Fusion

Sample	Burnup		Helium, cm^3/g		Helium Released[d] (%)
	% of ^{10}B[a]	n,α/cm^3[b]	Generated[b]	Retained[c]	
		$\times 10^{20}$			
BC-2	4.8	9.98	14.735	11.82±0.59	19.9±4.0
BC-8	3.7	7.69	11.354	6.54±0.33	42.2±2.9

[a]Based on $^{10}B/^{11}B$ determined by HEDL.

[b]Based on 208 $\times 10^{20}$ $^{10}B/cm^3$ B_4C.

[c]Accuracy based on a reasonable guess that retained helium can be measured with ±5% accuracy; more experience needed to determine accuracy.

[d]Compares to gas release determined by puncturing capsules after irradiation of 17% for BC-2 and 48% for BC-8. Vacuum fusion at HEDL indicated 22% and 49% gas release for BC-2 and BC-8, respectively.

burnup analysis, and have initiated measurements to determine retained gas by vacuum fusion analysis.

Burnup Analysis. – Samples of three pellets from each capsule were analyzed for burnup by mass spectrographic analysis for $^{10}B/^{11}B$ ratio. The results of these analyses are shown in Table 3.2. These values are plotted as a function of position in the capsule in Fig. 3.1. Values from the capsules being evaluated by ANL and HEDL are shown for comparison.[2] The burnup value obtained for sample G-9 appears to be out of line with the rest of the samples and this value is being rechecked.

Metallography. – The microstructure of the unirradiated control sample is shown in Fig. 3.2. The microstructure is typical of carbon-rich hot-pressed B_4C with some free graphite in the grain boundaries, a typical amount of twinning, some metallic appearing impurities, some intergranular porosity, and a small amount of intragranular porosity. The samples appeared to be in good condition after irradiation. A very few small cracks such as shown in Fig. 3.3 were observed which were

[2]L. C. Walters, ANL, personal communication, March 2, 1972.

Table 3.2. Burnup Analysis of EBR-II Higher Worth Control Rod Capsules G and H

Sample	Total Boron, at. %		Calculated Burnup (% of ^{10}B)
	^{10}B	^{11}B	
Unirradiated Control A-6	19.81	80.19	
G-4	19.61	80.39	1.26
G-9	19.67	80.33	0.86
G-13-T-2	19.54	80.46	
G-13-B-2	19.52	80.48	1.72
G-13-T-1	19.56	80.44	
H-2	19.61	80.39	1.26
H-7	19.57	80.43	1.51
H-14	19.55	80.45	1.62

primarily located in the interface between graphite particles and along adjacent grain boundaries.

We were unable to etch the as-irradiated sample because of its not conducting current during the electrolytic etching. However, a sample which had been annealed did etch satisfactorily. We used an ohmmeter to obtain a rough estimate of the electrical resistance of some samples that had been annealed for hardness testing. The sharp points of the ohmmeter contacts were pressed onto the polished sample surface 1/4 in. apart. The results are in Table 3.3. The as-irradiated and 700°C annealed samples did not etch at all. The 1150 and 1600°C annealed samples etched satisfactorily, but not uniformly. A uniformly good etch was obtained on the unirradiated sample. The etchant used was 10% chromic acid in water at about 0.1 A for 30 sec. We do not have an explanation for this electrical conductivity behavior, nor do we know how typical it is. Boron carbon has previously been electrolytically etched after irradiation in a thermal spectrum reactor using a solution of 10 g Na_2CO_3 + 10 g $NaNO_3$ + 80 cm^3 of water.[3]

[3]R. G. Gray and L. R. Lynam, Irradiation Behavior of Bulk B_4C and B_4C + SiC Burnable Poison Plates, WAPD-261 (October 1963).

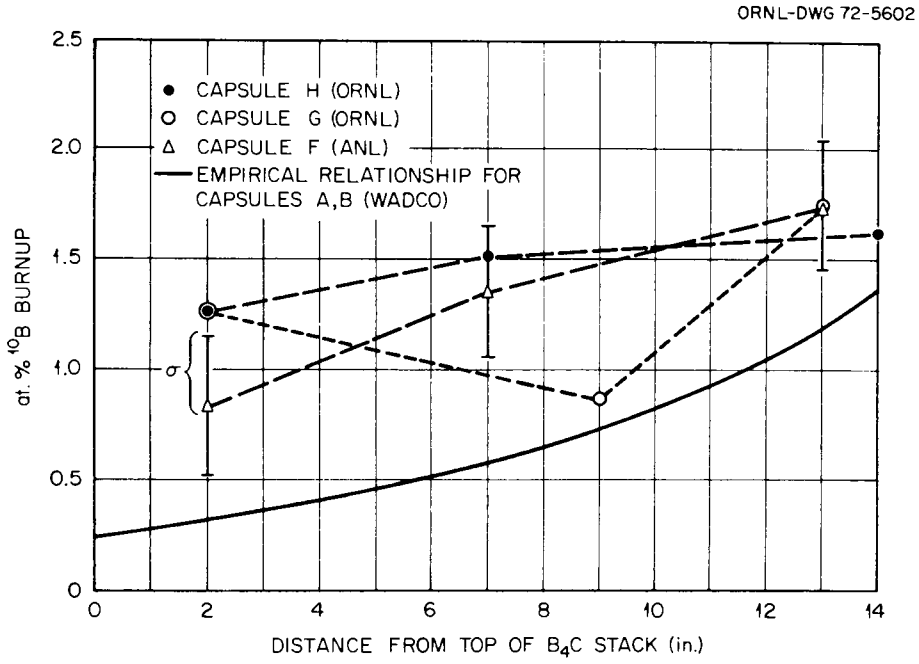

Fig. 3.1. ^{10}B Burnup Analyses Results on B_4C Pellets from Higher Worth Control Rod L-4008S.

The purpose of annealing these samples was to conduct microhardness tests on them. Samples which had been annealed cut and broke differently than the as-irradiated samples. However, we were unable to obtain hardness readings because of fracturing of the samples. The anneal did not affect the microstructure in the as-polished condition as shown in Figs. 3.4(a) and 3.5(a). One difference noted in the etched samples is the apparent lack of twinning as shown in Figs. 3.4(b) and 3.5(b). Twins are observed in transmission electron microscopy, both as irradiated and after annealing. The spots in the grain boundaries after the 1600°C anneal [Fig. 3.5(b)] are apparently an etching effect since they are not observed as polished and no bubbles are observed on the grain boundaries by transmission electron microscopy.

Lattice Parameter Measurements. – Portions of three pellets from each capsule were annealed at temperatures from 400 to 1900°C in graphite boats. A portion of each piece was crushed to –325 mesh powder and

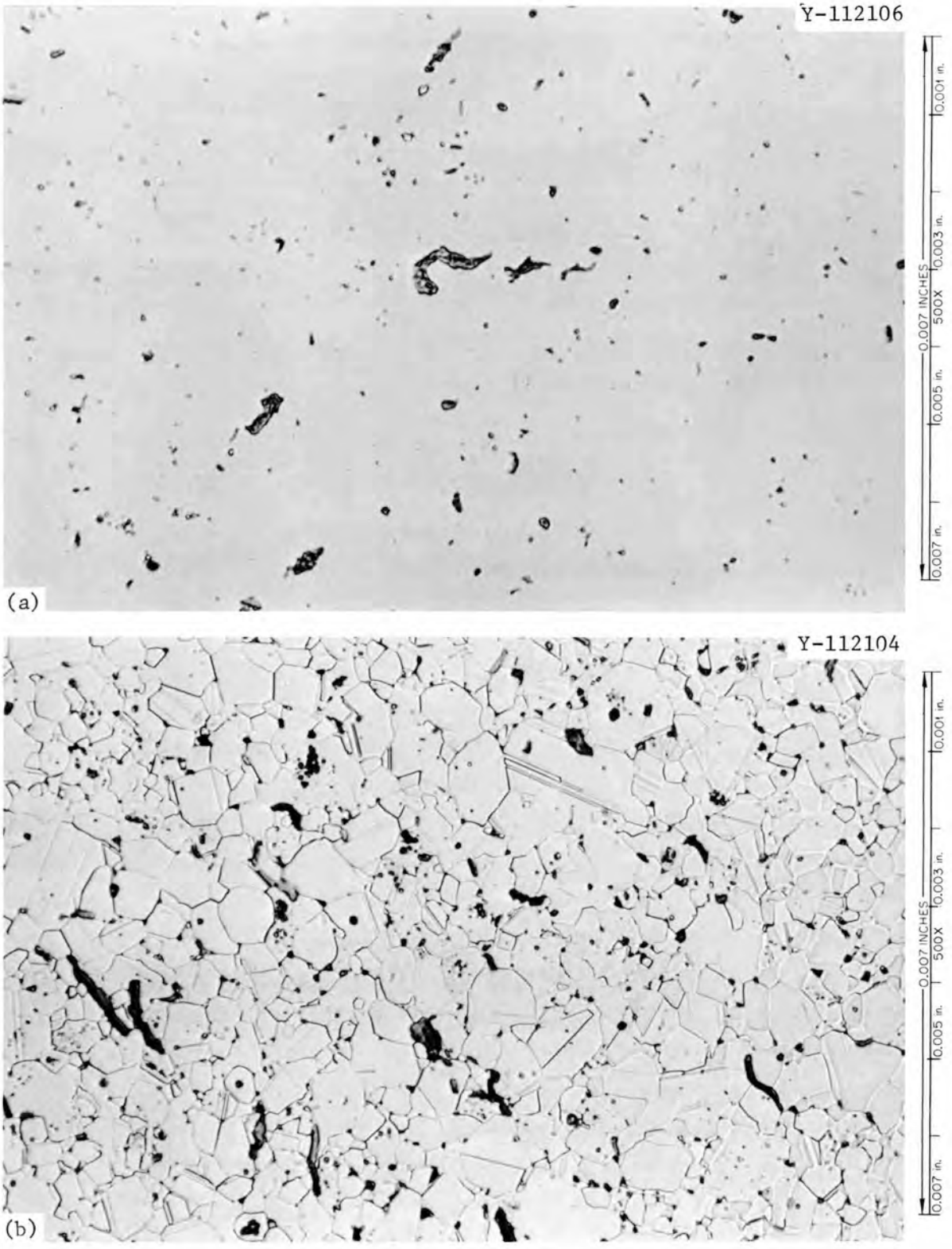

Fig. 3.2. Microstructure of EBR-II Higher Worth Control Rod Unirradiated Control Pellet A-6. (a) As polished. (b) Electrolytically etched with 10% chromic acid.

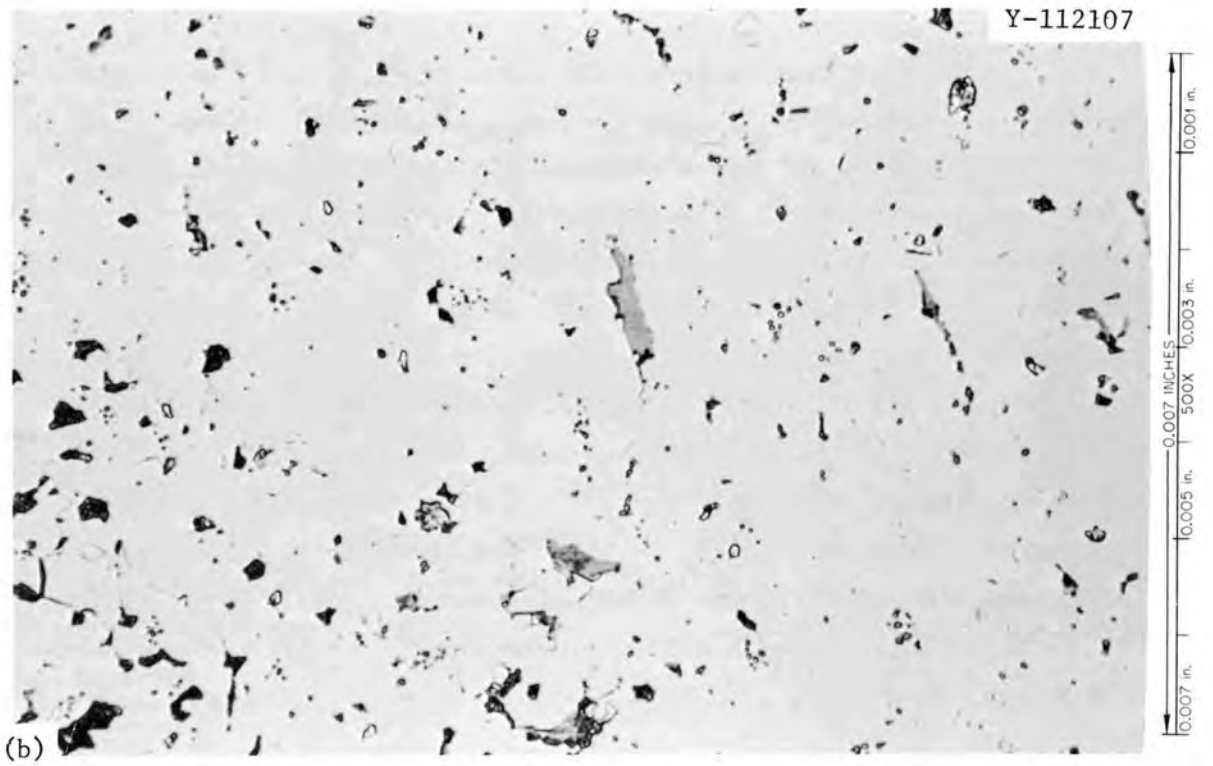

Fig. 3.3. Microstructure of EBR-II Higher Worth Control Rod Pellet H-13, As Irradiated. As polished. (a) 100×. (b) 500×.

Table 3.3. Electrical Resistance of Irradiated Boron Carbide Pellets

Sample	Electrical Resistance[a] (ohm)
H-13, as irradiated	70,000,000
H-13, irradiated, annealed at 700°C	20,000,000
H-13, irradiated, annealed at 1150°C	2,500
H-13, irradiated, annealed at 1600°C	250
A-6, unirradiated control	150

[a]Crude measure of electrical resistance between two sharp probes pressed onto metallographically polished surface 1/4 in. apart.

loaded into capillaries for Debye-Scherrer x-ray powder patterns. Chromium Kα (V-filtered) x radiation was used. Lattice parameters calculated from these patterns are shown in Figs. 3.6 through 3.8 plotted as a function of annealing temperature. The as-irradiated values are plotted at 500°C (estimate of maximum irradiation temperature) and the values from the unirradiated control sample (pellet A-6) are shown at the right of Figs. 3.6 and 3.7. The as-irradiated lattice parameters show a unit cell volume increase of about 0.3% through an increase in the rhomobohedral $\underline{a}$ parameter and a slight decrease in the angle α. This is in contrast to the X042 powders, which showed a decrease in the unit cell volume (a decrease in $\underline{a}$ and no change in α). These pellets were operated at a lower temperature in reactor than the X042 powders. Thermal irradiations of B_4C at temperatures of less than 500°C have generally shown unit cell volume increases. The behavior of the lattice parameters during annealing was similar for these pellets as for the X042 powders. The $\underline{a}$ parameter first increased, then decreased with increasing annealing temperature. The angle α first showed a marked decrease and then a rapid increase with annealing temperature. The volume again changed uniformly with annealing temperature and returned to about the unirradiated value around 1300°C.

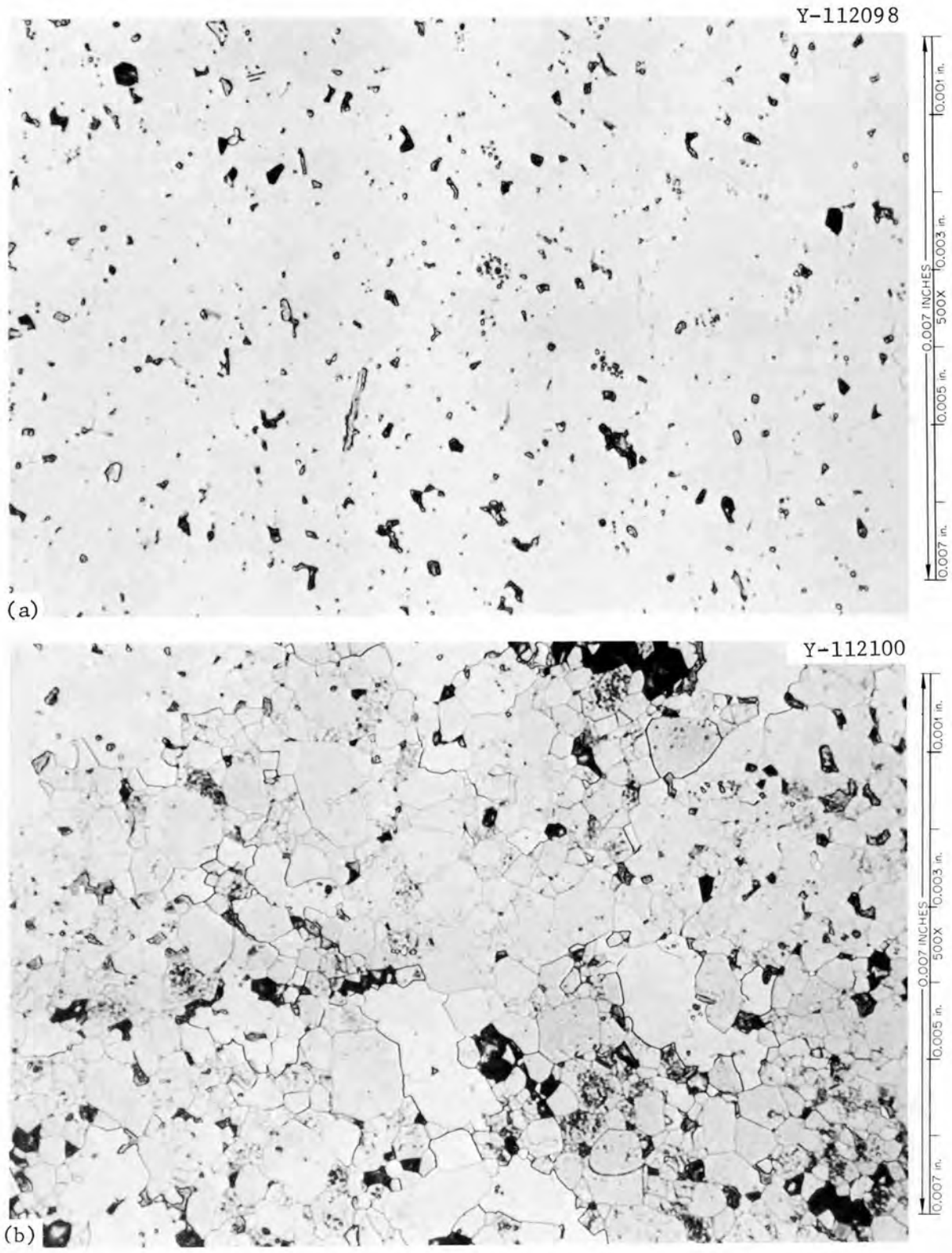

Fig. 3.4. Microstructure of EBR-II Higher Worth Control Rod Pellet H-13, Irradiated and Annealed at 1150°C for 1 hr. (a) As polished. (b) Electrolytically etched with 10% chromic acid.

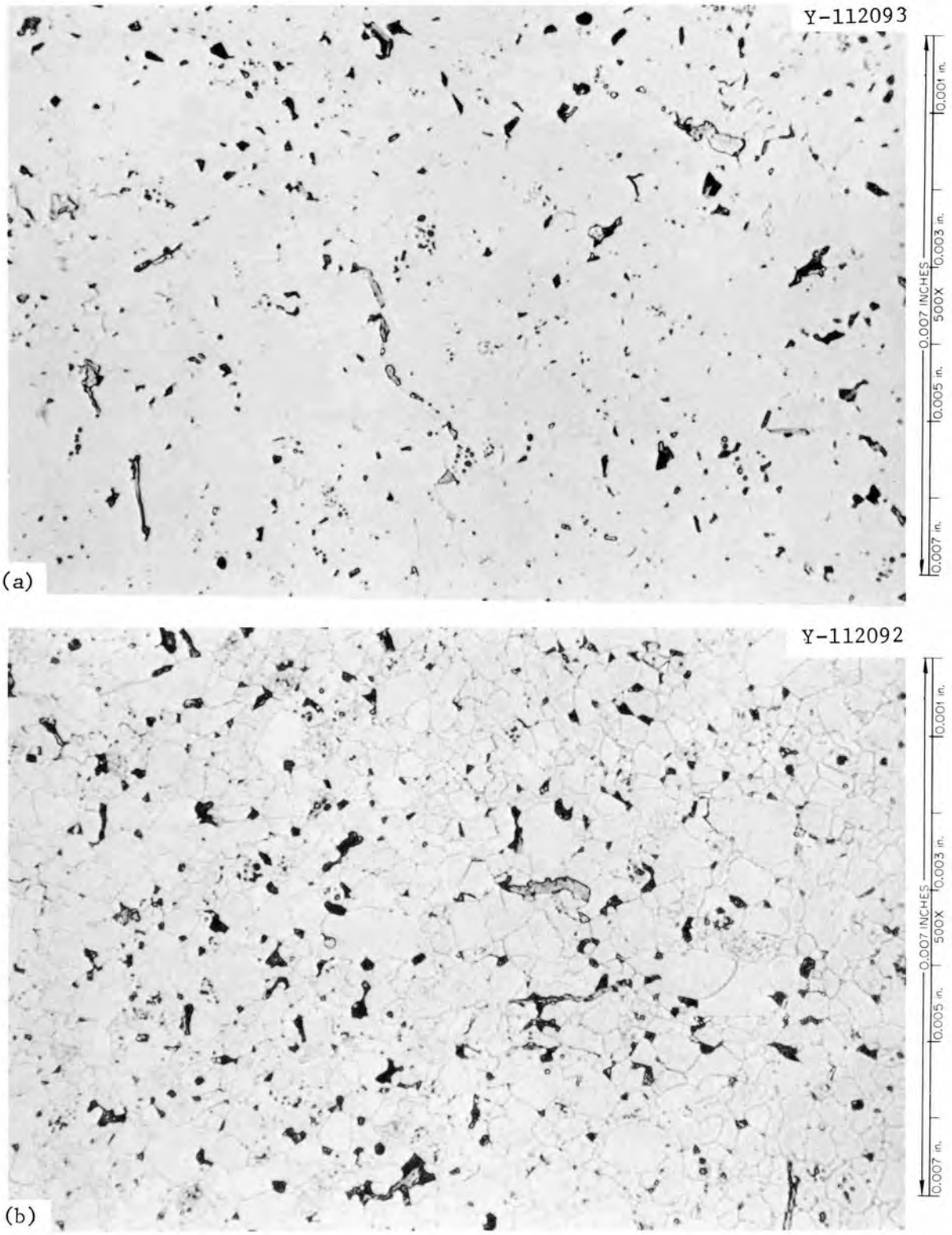

Fig. 3.5. Microstructure of EBR-II Higher Worth Control Rod Pellet H-13, Irradiated and Annealed at 1600°C for 1 hr. (a) As polished. (b) Electrolytically etched with 10% chromic acid.

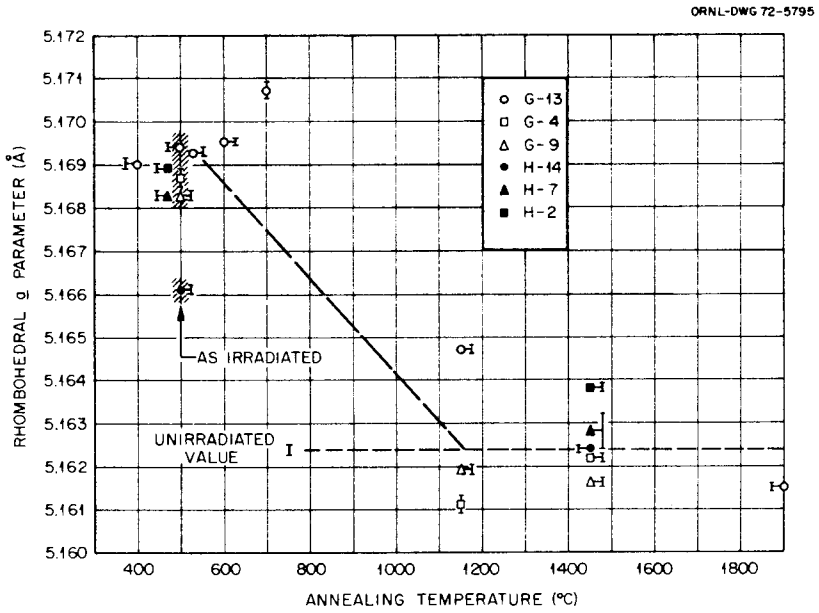

Fig. 3.6. Rhombohedral a Parameter of EBR-II Higher Worth Control Rod Boron Carbide Pellets.

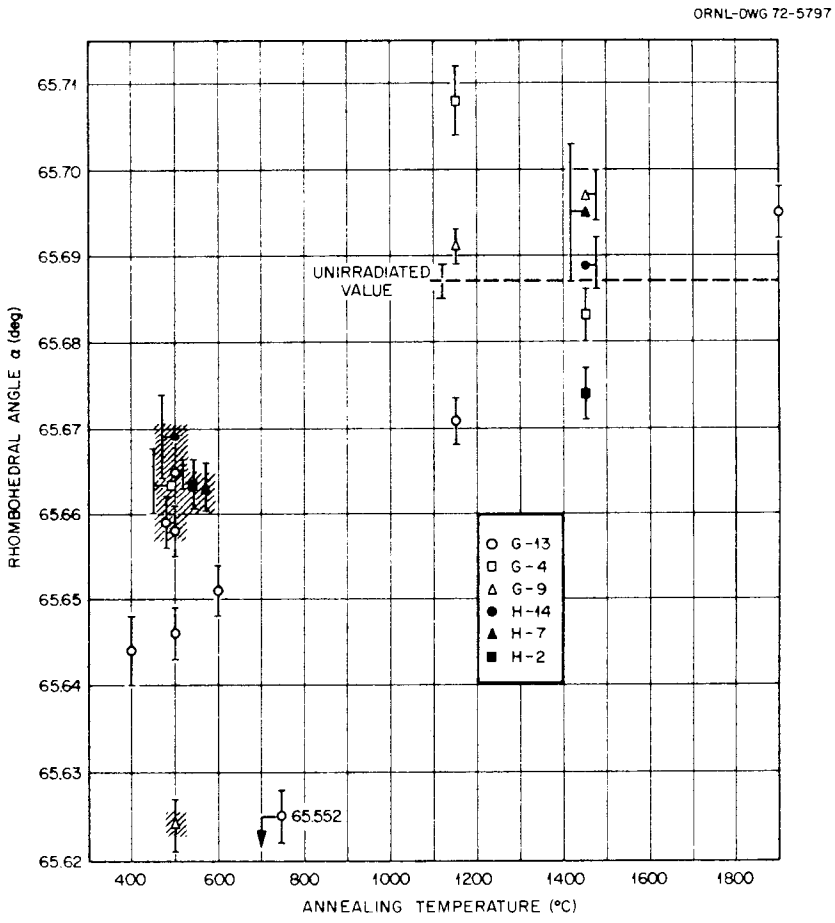

Fig. 3.7. Rhombohedral Angle α of EBR-II Higher Worth Control Rod Boron Carbide Pellets.

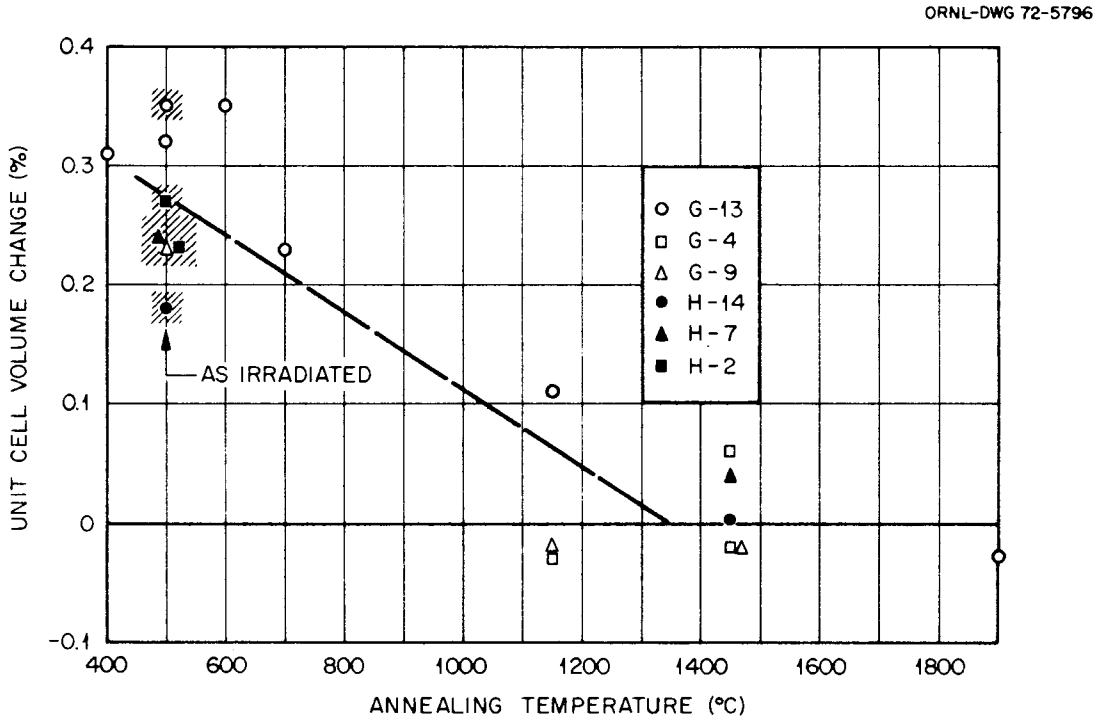

Fig. 3.8. Unit Cell Volume Change of EBR-II Higher Worth Control Rod Boron Carbide Pellets.

Vacuum Fusion. — Results are available for the retained gas analysis by vacuum fusion for pellet H-14. This pellet analyzed 1.62% burnup of ^{10}B which would generate 4.97 cm^3 He/g B_4C. The vacuum fusion analysis indicated 4.57 cm^3 He/g B_4C retained in the pellet. This indicates that 8.1 $\pm$ 4.6% of the gas generated was released during irradiation (accuracy based on estimate of helium content determination accuracy of $\pm$5%). This is in reasonable agreement with the capsule puncture which indicated 1.65% He release for the entire rod based on an average burnup of 1.2% of ^{10}B. Further analyses of pellets from these capsules are in progress.

Evaluation of EBR-II Experiment X099 (G. L. Copeland)

Capsules 0-5, 0-9, and 0-10 from EBR-II experiment X099 have been returned to ORNL for evaluation. We plan to completely evaluate capsules 0-5 and 0-9. Most of the pellets from capsule 0-10 are to be reencapsulated and receive further irradiation. The remaining X099 capsules 0-6, 0-7, and 0-8 are being reconstituted for further irradiation.

Thus far, we have neutron radiographed capsules 0-5, 0-9, and 0-10. The pellets appear to have swelled more than anticipated and at least some of the pellets show extensive cracking and fragmentation. The high-temperature pellets in 0-9 and 0-10 show more cracking. In these, the high-density pellets and the higher B/C ratio pellets show more cracking. The centering devices on the pins appear to have functioned properly. Some of the centering pins appear to be bent somewhat, but the pins are centered in the capsules. Capsule 0-9 is bowed about 3/8 in. in the center. The pins in this capsule are naturally closer on one side; however, they do not appear to touch the capsule wall. These comments are a result of a rather cursory look at the radiographs, and a more detailed study is under way. The capsules are now in the process of disassembly.

Thermal Reactor Irradiations (G. L. Copeland)

Nine capsules were irradiated for six weeks in the ORR during this quarter. These contain boron carbide at higher temperatures as well as some TaB_2 and TaB. These capsules are currently being evaluated.

Fabrication of EBR-II Absorber Experiments (E. J. Manthos, J. W. Woods)

Engineering drawings for capsules (see Table 3.4) 0-14, -15, -16, -17, -18, -19, -20, and -23 have been reviewed and issued. Preliminary drawings for 0-21 and -22 have been reviewed and the final drawings are being completed. Capsule 0-14 has been completed and the bottom pin for capsule 0-18 has been completed.

All the components for capsules 0-15, -16, -17, -18, and -20 have been fabricated. Pellets to complete loading of 0-15, -16, -17, -18, -19, and -20 were received. Loading of the pins for 0-15, -16, -18, and -20 has started (each capsule contains two pins). Fabrication and loading of the two pins for 0-17 will start as soon as the Nb–1% Zr qualification welds have been examined metallographically. Component fabrication for 0-19 is not complete because it is different from the other capsules since the 0 specimens in the pins are sodium bonded. As soon as component fabrication is complete, determination of the weld parameters will commence.

Table 3.4. Status of ORNL EBR-II Neutron Absorber Experiments

Capsule Number	Control Material[a]	Schedule			Comments
		Ship	EBR-II Start	EBR-II Complete	
			Subassembly X099		
0-5	BC		2/25/71	1/14/72	At ORNL for evaluation
0-6	BC		2/25/71	1/14/72	Reconstitute for X099A
0-7	BC		2/25/71	1/14/72	Reconstitute for X099A
0-8	BC		2/25/71	1/14/72	Reconstitute for X099A
0-9	BC		2/25/71	1/14/72	At ORNL for evaluation
0-10	BC		2/25/71	1/14/72	At ORNL for interim examination and reconstitution
			Subassembly X099A		
0-6	BC		7/1/72	7/1/73	At EBR-II
0-7	BC		7/1/72	7/1/73	At EBR-II
0-8	BC		7/1/72	7/1/73	At EBR-II
0-12	TA		7/1/72	7/1/73	At EBR-II
0-13	TA		7/1/72	7/1/73	At EBR-II
BTA-7	TA		7/1/72	7/1/73	At EBR-II
BTA-8	TA		7/1/72	7/1/73	At EBR-II
			Subassembly 2α		
0-14	BC	6/1/72	8/1/72	8/1/73	
0-15	BC	6/1/72	8/1/72	8/1/73	
0-16	BC	6/1/72	8/1/72	8/1/73	
0-17	BC	6/1/72	8/1/72	8/1/73	
0-18	BC + TB	6/1/72	8/1/72	8/1/73	
0-20	TB	6/1/72	8/1/72	8/1/73	
B-58	TA	6/1/72	8/1/72	8/1/73	
			Subassembly 2β		
0-10	BC	9/1/72	11/1/72	11/1/73	
0-19	BC + V	9/1/72	11/1/72	11/1/73	
0-21	BC	9/1/72	11/1/72	1/1/74	
0-22	BC	9/1/72	11/1/72	11/1/73	
0-23 (NASA)	BC	9/1/72	11/1/72	1/1/74	

[a] BC = boron carbide; TA = tantalum and tantalum alloys; TB = tantalum borides; V = vent materials.

Capsule O-23 will contain six separate pins, each with its own helium collector chamber. The specimen holders will be fabricated from T-111 alloy and the helium collector chamber from stainless steel. Fabrication of the stainless steel components is complete. The T-111 components are being fabricated out-of-plant and completion is expected early in April. Qualification of the stainless steel welds has begun and qualification of the T-111 welds and a T-111-to-stainless-steel braze joint will begin as soon as the components are delivered.

Tantalum absorber capsules O-12 and -13 were completed and delivered to the EBR-II for inclusion in subassembly X099A. Arrangements were also made to include capsules BTA-7 and -8, originally fabricated by HEDL, into the ORNL absorber test program and irradiations in subassembly X099A.

Boron Carbide

Structure of Hyperstoichiometric Boron Carbide (H. L. Yakel)

X-ray lattice parameter and density data for 15 unirradiated single crystals from boron carbide batch M-103 were obtained. If the lattice parameter versus composition results from De Luca's recent experiments[4] are correct, the lattice parameters of these crystals suggest carbon contents ranging from 14 to 16 at. % C, placing them just on the high-boron side of the $B_{13}C_2$ composition. The experimentally determined mass within a primitive rhombohedral unit cell was, with only one exception, consistently larger by about 2 amu than the mass of 13 boron and 2 carbon atoms. This strongly suggests that significant numbers of interstitial atoms (about 0.2 per rhombohedral cell) must be present in the crystals.

---

[4] J. P. De Luca, Fuels and Materials Development Program Quart. Progr. Rept. Dec. 31, 1971, ORNL-TM-3703, pp. 38–42.

Alternate Absorber Materials

Fabrication of Tantalum Borides (M. M. Martin)

Our objective is to evaluate the general applicability of borides other than boron carbide and other potential absorber materials to both the FTR and LMFBR plants. To date, work has been concentrated on the tantalum borides. This study includes fabrication of Ta_2B and TaB_2 pellets, the irradiation of these materials in Series II Neutron Absorber Experiment in EBR-II, and their postirradiation examination to determine dimensional stability and *in situ* helium retention. The latter two phases of the study will be completed in FY 1973.

Considerable progress has been made this quarter. To prepare the tantalum boride powders, we used the borothermic reduction of Ta_2O_5 oxide under vacuum for TaB_2 and direct thermal interaction between tantalum and boron under vacuum for Ta_2B:

$$Ta_2O_5(s) + 9B(s) \xrightarrow[\text{vacuum}]{1650°C - 1\ hr} 2TaB_2(s) + 5BO(g) , \qquad (1)$$

$$2Ta(s) + B(s) \xrightarrow[\text{vacuum}]{1650°C - 1\ hr} Ta_2B(s) . \qquad (2)$$

In Eq. (2) the elemental boron was enriched to 40 wt % in isotope ^{10}B. Each set of reactants were blended obliquely for 45 min in glass jars containing 60 to 70 vol % mixing space, and then immediately consolidated into 1-in.-diam by 1-in.-high, 70%-dense pellets, at 25 tsi using double-action floating die compaction.

From temperature and/or system pressure observation during heating of groups of the pellets, we believe that both reactions indicated by Eqs. (1) and (2) began at about 1000°C. Near this temperature in the case of Ta_2B preparation, rapid heat generation occurred and the temperature exceeded 2000°C in a few seconds but returned to about 1200°C in less than 1 min. After an additional 2 to 3 min, the system pressure returned to less than 1×10^{-3} torr. Although not observed, we believe that the reaction of Eq. (1) is also highly exothermic with most of the

gaseous product being released between 1000 and 1200°C. We continued to heat both types of pellets at a rate of about 500°C/hr to 1650°C and then allowed the furnace to cool under vacuum to room temperature.

The solid products of Eqs. (1) and (2) were crushed in a diamond mortar and pestle to pass a 60-mesh screen for the Ta_2B and a 100-mesh screen for the TaB_2 materials. Because of the extreme toughness of the Ta_2B product in comparison to TaB_2, the former was magnetically cleaned after the crushing operation to reduce abraded contaminants from the diamond mortar and pestle. Tables 3.5 and 3.6 present some physical and chemical attributes of all reactants and crushed and cleaned products as used and prepared by Eqs. (1) and (2).

Pellets for 0-18-T, 0-20-T, and 0-20-B pins for ORNL Series II Neutron Absorber Experiment in EBR-II were also produced this quarter from the materials described in Tables 3.5 and 3.6. They were hot pressed for 1 hr at 2000°C and 5000 psi using graphite dies and punches. Since Ta_2B is not compatible with graphite, the die cavities and ends of the punches for these pellets were lined with two layers of 0.001-in.-thick tantalum foil to minimize carbon contamination. One set of TaB_2 pellets, made from powder blend PB-45, was sintered for 35 hr at 1900°C and less than 1×10^{-3} torr. This operation increased their density from 92 to greater than 95% of theoretical. The Ta_2B pellets were not sintered since the hot-pressing operation produced cylinders of greater than 95% of theoretical density. All were ground to a final size of 0.375-in.-diam by 0.375-in. high without difficulty, and those selected to accept centrally located silicon carbide monitors were electrodischarge machined to produce a 0.125-in.-diam axial hole. To complete their fabrication, the pellets were cleaned by heating to 1000°C at less than 1×10^{-3} torr and stored in plastic vials.

Pellets selected for irradiation are now being placed in sub-assemblies for shipment to the EBR-II site.

Table 3.5. Some Physical and Chemical Properties of Powder Materials Used in Manufacture of TaB_2 and Ta_2B Pellets for Series IIα Neutron Absorber Experiment in EBR-II

Absorber Pin Designation	Identification of Process Powders	Toluene Density (g/cm^3)	Surface Area (m^2/g)	Selected Chemical Analyses, wt %			
				Boron	Oxygen	Carbon	Nitrogen
O-18-T	PB-48: Tantalum pentoxide reactant	7.888	0.61	a	18.4	0.004	a
	PB-49: Boron (19.8% ^{10}B) reactant	2.219	13.0	94.0	3.03	0.55	0.050
	PB-50: Tantalum diboride product	11.255	0.81	11.1	0.41	0.006	0.009
O-20-T	PWD-148: Tantalum reactant	16.486	0.06	a	0.11	a	a
	PB-44: Boron (41.4% ^{10}B) reactant	2.304	0.63	97.8	0.01	0.97	0.004
	PB-46: Ditantalum monoboride product	14.810	0.08	3.5	0.20	0.053	
O-20-B	PB-42: Tantalum pentoxide reactant	8.513	1.40	a	17.7	0.011	a
	PB-43: Boron (19.8% ^{10}B) reactant	2.203	11.8	92.3	2.97	0.72	0.092
	PB-45: Tantalum diboride product	11.159	0.80	10.9	0.38	0.009	0.005

[a]Not determined.

Table 3.6. Spectrographic Analysis of Powder Materials Used in Manufacture of TaB_2 and Ta_2B Pellets for Series II Neutron Absorber Experiment in EBR-II[a]

Absorber Pin Designation	Identification of Process Powders	Impurities (by Weight) (Greater than 0.1%)	Impurities (by Weight) (0.01 to 0.10%)
O-18-T	PB-48: Tantalum pentoxide reactant	None	Cb, Cu
	PB-49: Boron (19.8% ^{10}B) reactant	Ca, K, Mg, Mn, S	Al, Cu, Fe, P, Pb, Si
	PB-50: Tantalum diboride product	Ca	Co, Cr, Fe, Mn, Ni, Si
O-20-T	PWD-148: Tantalum reactant	None	Fe, Cb, Si
	PB-44: (Boron (41.4% ^{10}B) reactant	Fe, Si	Al, Ca, Cr, Mn, Zr
	PB-46: Ditantalum monoboride product	None	Ca, Cb, Cu, Fe
O-20-B	PB-42: Tantalum pentoxide reactant	None	Al, Cb, K, Si
	PB-43: Boron (19.8% ^{10}B) reactant	Ca, Fe, K, Mg, Mn, Si	Al, Cu, Ni, P, S
	PB-45: Tantalum diboride product	Al	Ca, Fe, Mg, Mn

[a]All process powders contained numerous trace impurities of less than 0.01% by weight.

Helium Vents for Absorber Rods

J. I. Federer

The purpose of this task is to develop a venting device which will release helium gas from FTR/LMFBR absorber elements, thereby preventing damaging pressure increases. The basic requirements of helium vents in this application are: (1) provide a helium release rate proportional to the generation rate so as to minimize differential pressure across the vent; (2) compatibility with sodium; (3) prevent intrusion of sodium into the element due to hydraulic and capillary forces. Our approach to the problem is the use of porous disks bonded to holders which, in turn, would be bonded to the element. Important elements of this task

are fabrication of porous disks, bonding of disks to holders, and characterization of vent assemblies. These are necessary steps to our immediate goal of installing vent assemblies in the EBR-II for irradiation testing and a longer range goal of optimizing vent properties by optimizing materials and fabrication techniques.

Porous disks are being fabricated of types 304 and 316 stainless steel, molybdenum, stainless steel-ZrO_2, and molybdenum-ZrO_2. The fabrication technique presently consists only of cold pressing followed by sintering; we also plan to utilize hot pressing for some materials. Stainless steel disks can be welded to stainless steel holders, but molybdenum and cermet disks appear to require brazing. Another possibility we are considering for a molybdenum disk would involve welding to a molybdenum holder, then brazing the holder to the absorber element.

The vent holder designed for the EBR-II irradiation experiment was illustrated previously.[5] Twenty-four holders have been machined from type 304 stainless steel. Fourteen holders are needed for the experiment, and the remainder are being used for joining studies and spare parts. With these holders two joints are required to make a vent assembly. A 0.375-in.-diam by 0.063-in.-thick porous disk and a 0.063-in.-OD tube must be bonded to the holder. We previously reported that three type 304 stainless steel disks were electron beam welded to holders, but the disks then had much smaller than expected leak rates.[5] We have since determined that the leak rates of these three disks prior to welding were actually much lower than indicated. The discrepancy was due to an inadequate seal in the device used to make the measurements. A new device for holding the disks during preweld leak testing employs an O-ring seal, and was found to be satisfactory.

An overall view of one of the EBR-II-type vent assemblies discussed above is shown in cross section in Fig. 3.9(a). The electron beam weld which joined the disk to the holder is shown in Fig. 3.9(b). The small fusion zone would allow a short circuit path from the surface to the

---

[5]J. I. Federer, Fuels and Materials Development Program Quart. Progr. Rept. Dec. 31, 1971, ORNL-TM-3703, pp. 74–78.

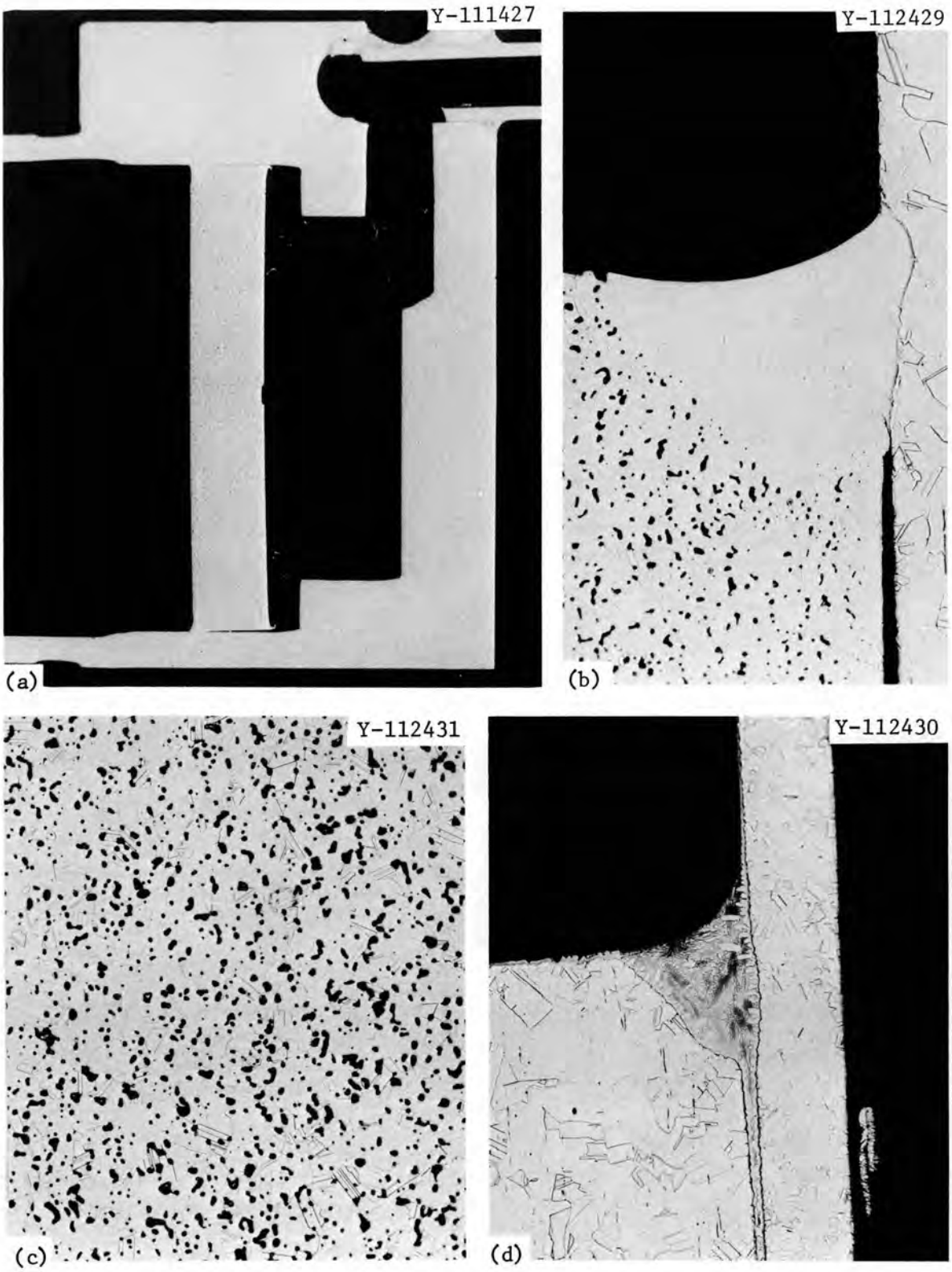

Fig. 3.9. EBR-II Vent Assembly. (a) Overall cross-sectional view, ~ 7×, (b) electron beam weld of porous disk to holder, 100×, (c) grain and pore structure in the disk, 100×, and (d) braze joint between 0.063-in.-OD tube and holder, 50×.

edge of the disk. In future welds of this type we will strive for complete penetration to bond the disk to the machined ledge on the side opposite the weld. The disk was supposed to be in contact with the ledge when the weld shown in Fig. 3.9(b) was made. Figure 3.9(c) shows the porosity in the sintered disk, which in this case was only slightly interconnected since the leak rate through the disk was only about 4×10^{-8} cm^3/sec. The braze joint which joined the 0.063-in.-OD tube to the holder is shown in Fig. 3.9(d). This joint is always made and leak tested before the disk is welded in place. The braze alloy is Nicrobraz 50, a 77% Ni–13% Cr–10% P alloy.

Stainless steel disks have been fabricated by cold pressing −325 mesh powder in a 0.406-in.-ID die at 46 tsi followed by sintering in hydrogen at 1200°C for a time sufficient to produce the desired leak rate. A nominal leak rate for FTR/LMFBR absorber elements is 10^{-4} cm^3/sec. In the case of type 304 stainless steel disks the leak rate was still in excess of 10^{-3} cm^3/sec after sintering for 19 hr, and we estimated that a total of 40 hr would be required to achieve a leak rate of 10^{-4} cm^3/sec. On the other hand, leak rates in the range of 2 to 8×10^{-4} cm^3/sec were obtained in type 316 stainless steel disks after only 15 hr. Molybdenum disks were also cold pressed at 46 tsi, then sintered at 1600°C in vacuum. A leak rate of about 10^{-4} cm^3/sec appears to be attainable in these disks after sintering for 5 to 7 hr.

The primary method for joining stainless steel disks to stainless steel holders is electron beam welding. Disks have been welded into 0.375-in.-ID tubes which served as stand-ins for more expensive machined holders of the EBR-II-type discussed previously. Solid nonleaking disks were welded first to establish welding parameters. The joints were leak-tight after welding and after thermal cycling five times between 25 and 1200°C. Disks with known leak rates have also been welded without substantially affecting the leak rates. The narrow fusion and heat-affected zone of electron beam welds minimizes changes in the pore structure of porous disks. Brazing the disks to holders is an alternate joining technique. Our attempts to braze stainless steel disks so far have produced erratic results including poor wetting in the joint and spreading of braze alloy on the face of the disks.

Performance Modeling Boron Carbide Absorber Rods

F. J. Homan

A previous progress report[6] pointed out the importance of the analytical treatment of helium gas release from boron carbide under irradiation in predicting the buildup of gas pressure within absorber rods. In that report some calculations of helium pressure buildup with time were presented for different ^{10}B enrichments, assuming that the design equation[7] for helium release was valid. The design equation indicates that helium gas release is exponential in temperature and linearly related to buildup.

During this reporting period some helium release data from thermal irradiations were examined in an effort to improve the gas release correlations. Sixty-seven data points were included in the study, 65 of them[8] covering a range of operating temperatures of about 300 to 650°C, a burnup range of 7 to 26 $\times 10^{20}$ captures/cm^3, and including both pellets (65, 80, and 99% of theoretical density) and powders (65 and 80% of theoretical density). The remaining two points[9] were for a 40% theoretically dense powder operated at 400°C to 1.29 $\times 10^{22}$ captures/cm^3, and a 100%-dense pellet operated at 250°C to 8.25 $\times 10^{21}$ captures/cm^3.

A plot of the raw data is shown in Fig. 3.10. Gas release is plotted against temperature. The considerable scatter shown in the figure is probably due in part to uncertainty about the operating temperatures in these thermal flux experiments, where most of the captures (and hence, most of the gas generation) occur close to the pellet or powder surface.

---

[6]F. J. Homan, Fuels and Materials Development Program Quart. Progr. Rept. Sept. 30, 1971, ORNL-TM-3550, pp. 58–70.

[7]L. E. Strawbridge, Manager, Nuclear Design, FFTF Project, letter FRP-294, dated September 2, 1970, p. 21.

[8]A. L. Pitner and G. E. Russcher, Irradiation of Boron Carbide Pellets and Powders in Hanford Thermal Reactors, WHAN-FR-24 (December 1970).

[9]E. W. Hoyt and D. L. Zimmerman, Radiation Effects in Borides, Part I – Helium Release and Swelling in Irradiated Borides, GEAP-3743 (Pt. 1) (February 1962).

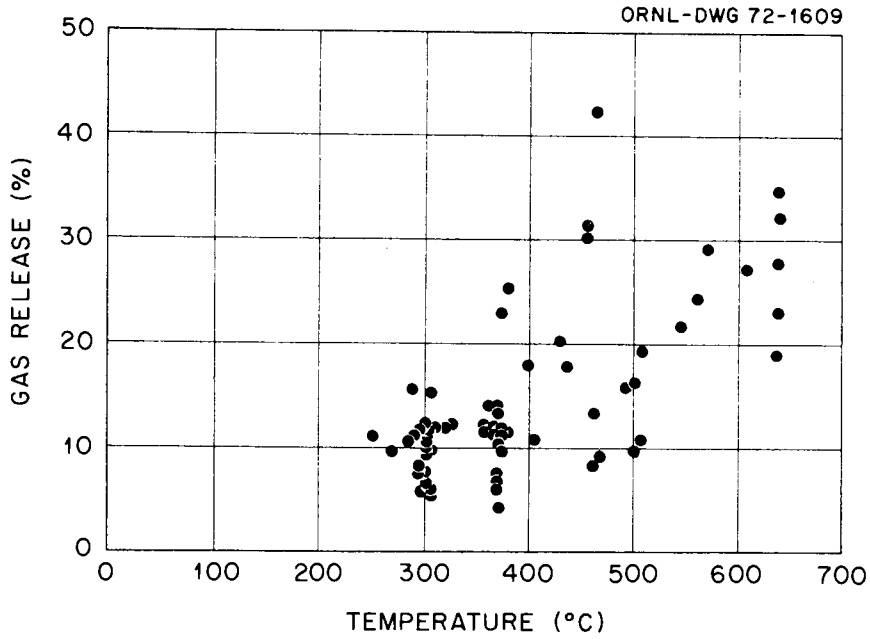

Fig. 3.10. Influence of Temperature on Gas Release from Irradiated B_4C.

It is also expected that other variables (porosity, burnup, material form) may be influencing gas release.

To evaluate the influence of these other variables, the data shown in Fig. 3.10 has been replotted several ways. Figures 3.11 through 3.15 show percent gas release plotted against captures per cubic centimeter for 65- and 80%-dense B_4C powders, and 65, 80, and 99% theoretically dense B_4C pellets, respectively. Because of the substantial scatter in the data, nothing really conclusive can be drawn from these plots. However, it appears that gas release may decrease slightly with increasing burnup for the low-temperature (below 400°C) irradiations, whereas for the higher temperature data gas release appears to increase slightly with burnup. Figure 3.16 is a plot of percent gas release versus percent theoretical density. All 67 data points are shown in the figure. Again, the scatter in the data is considerable, but some definite trends can be observed. At low temperatures there appears to be very little dependence of gas release upon porosity, while at higher temperatures (above 350°C) gas release appears to decrease with increasing density. Figure 3.17 is a plot of percent gas release versus temperature for the 65 and 80% theoretically dense material in both pellet and powder form.

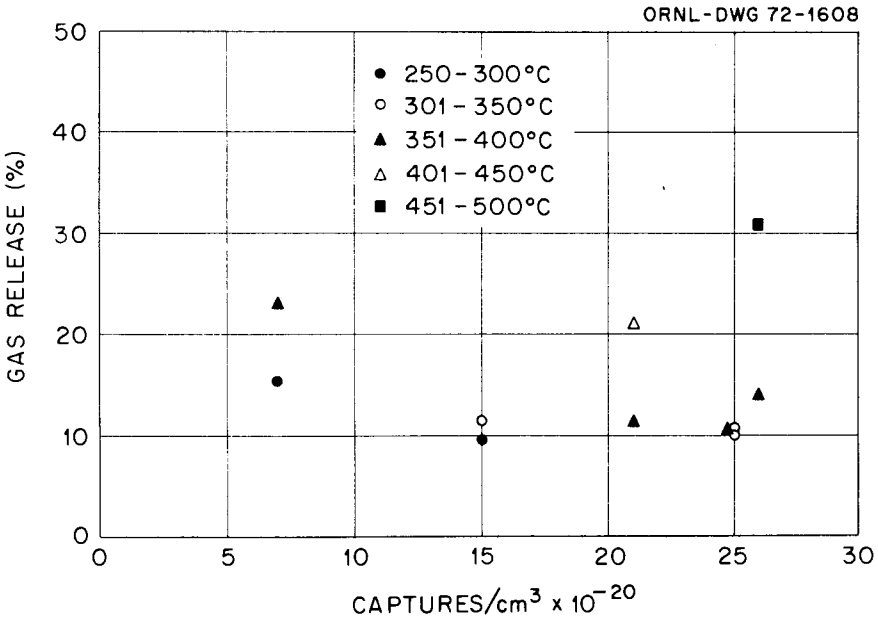

Fig. 3.11. Influence of Burnup on Gas Release in 65% Theoretically Dense B_4C Powders.

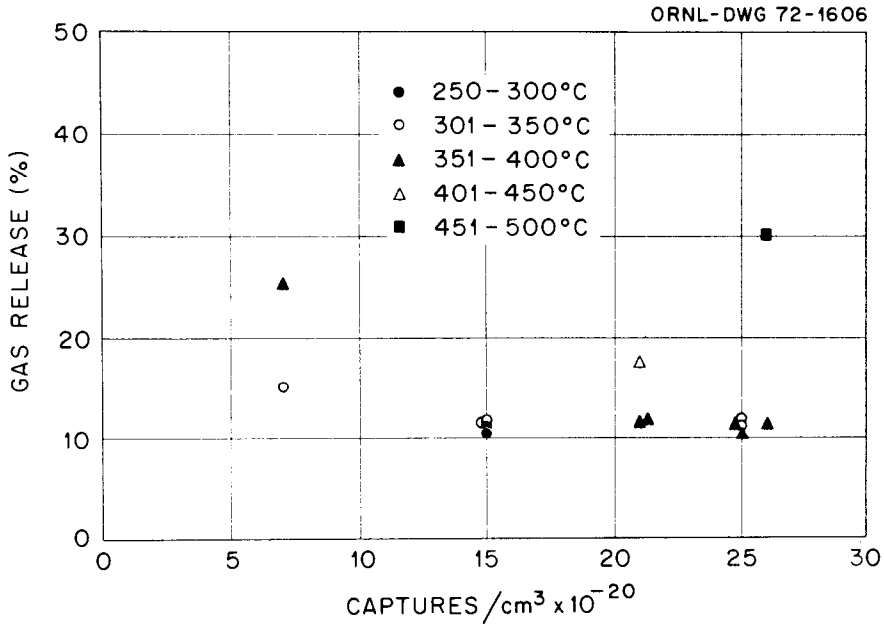

Fig. 3.12. Influence of Burnup on Gas Release in 80% Theoretically Dense B_4C Powders.

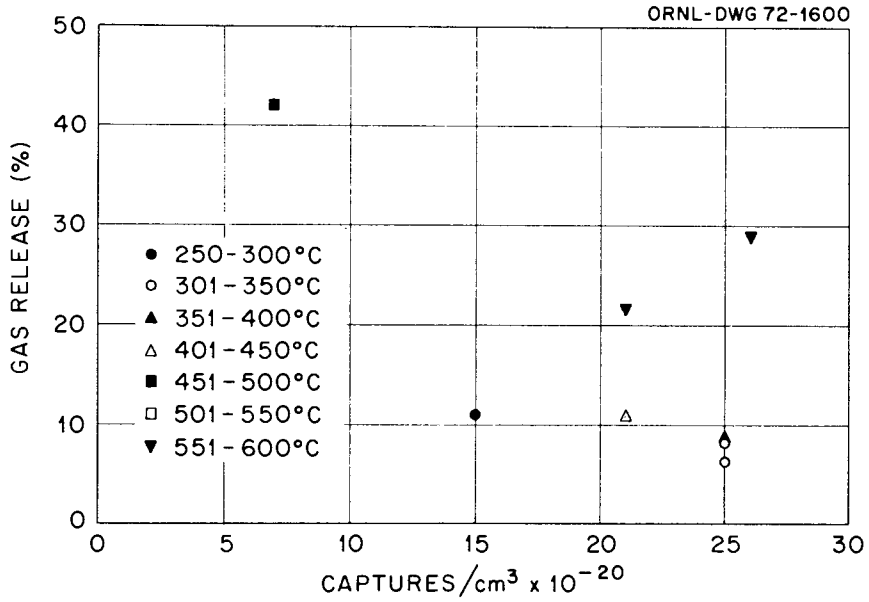

Fig. 3.13. Influence of Burnup on Gas Release in 65% Theoretically Dense B_4C Pellets.

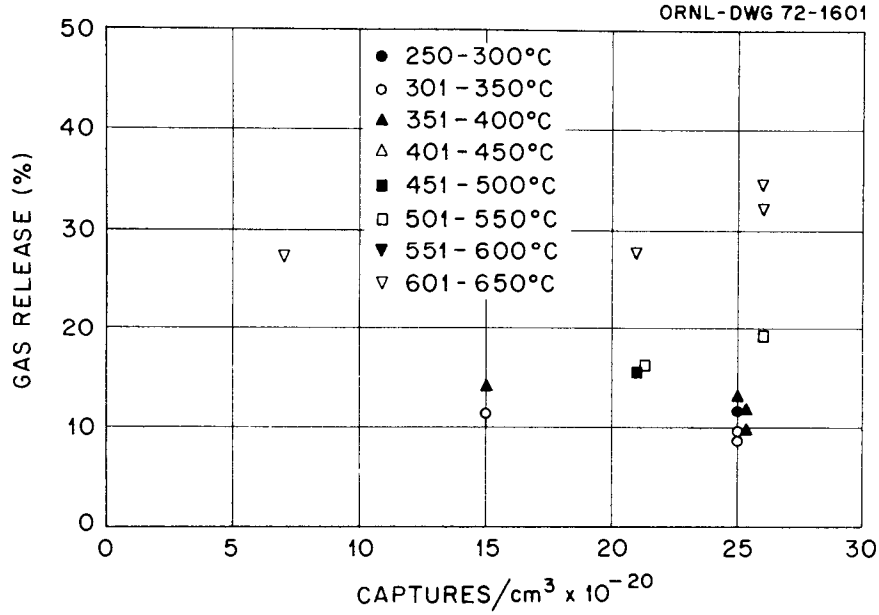

Fig. 3.14. Influence of Burnup on Gas Release in 80% Theoretically Dense B_4C Pellets.

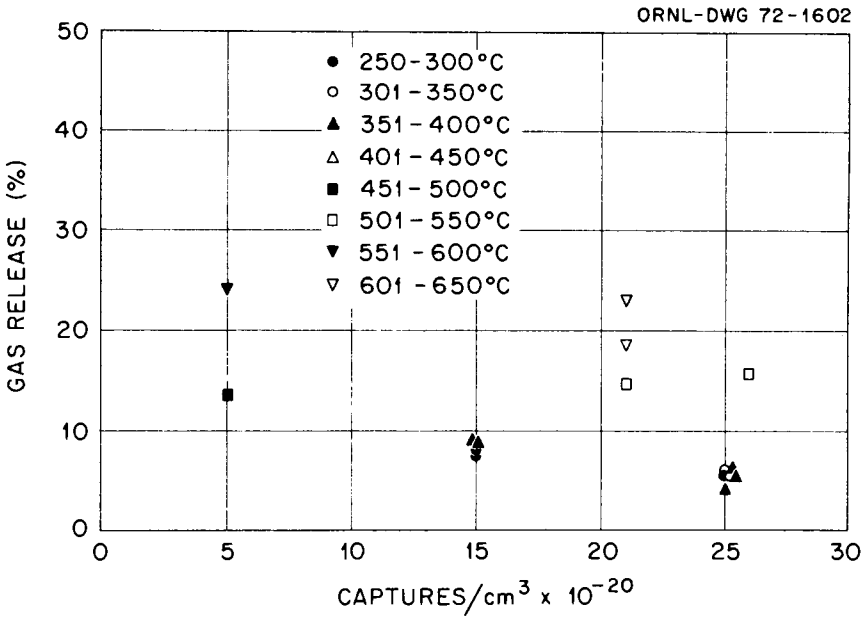

Fig. 3.15. Influence of Burnup on Gas Release in 99% Theoretically Dense B_4C Pellets.

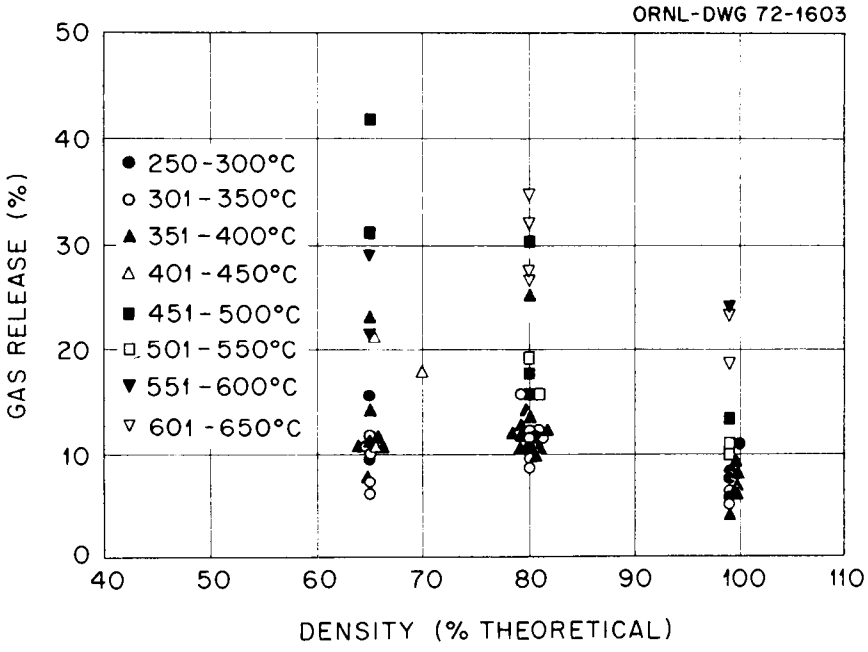

Fig. 3.16. Influence of Porosity on Gas Release in Irradiated B_4C.

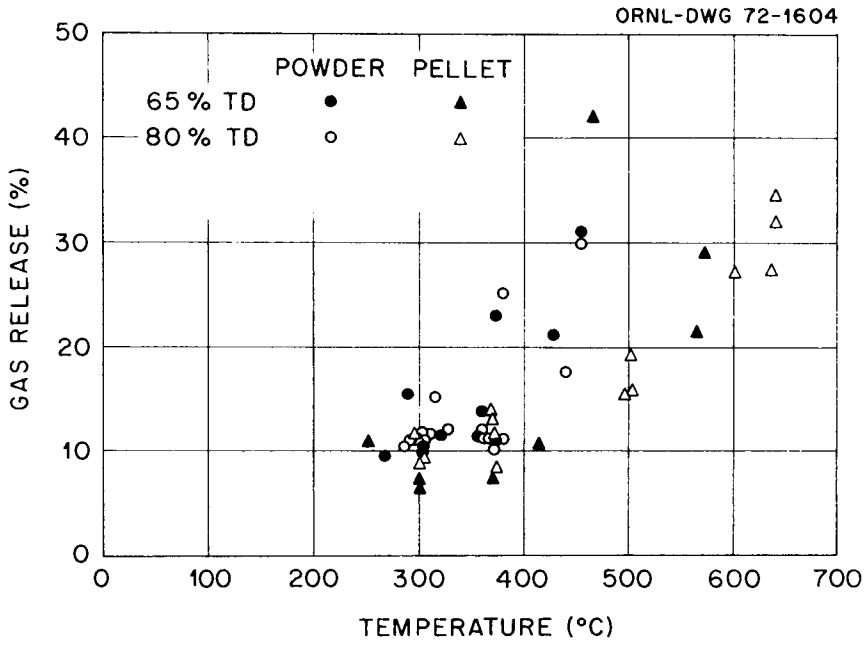

Fig. 3.17. Influence of Material Form on Gas Release in Irradiated B_4C.

Different symbols are used so that the effect of both density and form can be determined. From this figure it can be seen that gas release from powders is generally higher than from pellets (circles generally higher on the plot than triangles). Also the observation that the open triangles are above the closed triangles at low temperatures supports the observation made earlier regarding the porosity plot. At higher temperatures there are not enough closed triangles to make such an observation.

In order to fit the 67 data points discussed here to some sort of useful equation, the data were plotted again as shown in Fig. 3.18, with LOG_e (percent helium release) versus reciprocal temperature. Then each of the five cases (65%-dense powder, 80%-dense powder, 65-, 80-, and 99%-dense pellets) were fit to a straight line using the method of least squares. With the exception of the line representing data for 80%-dense powder, the lines had slopes matching the general line of the data points, with intercepts increasing with decreasing porosity. From this we assumed that the same mechanism was operating in all cases to release gas, and that the activation energy of this process is given by the

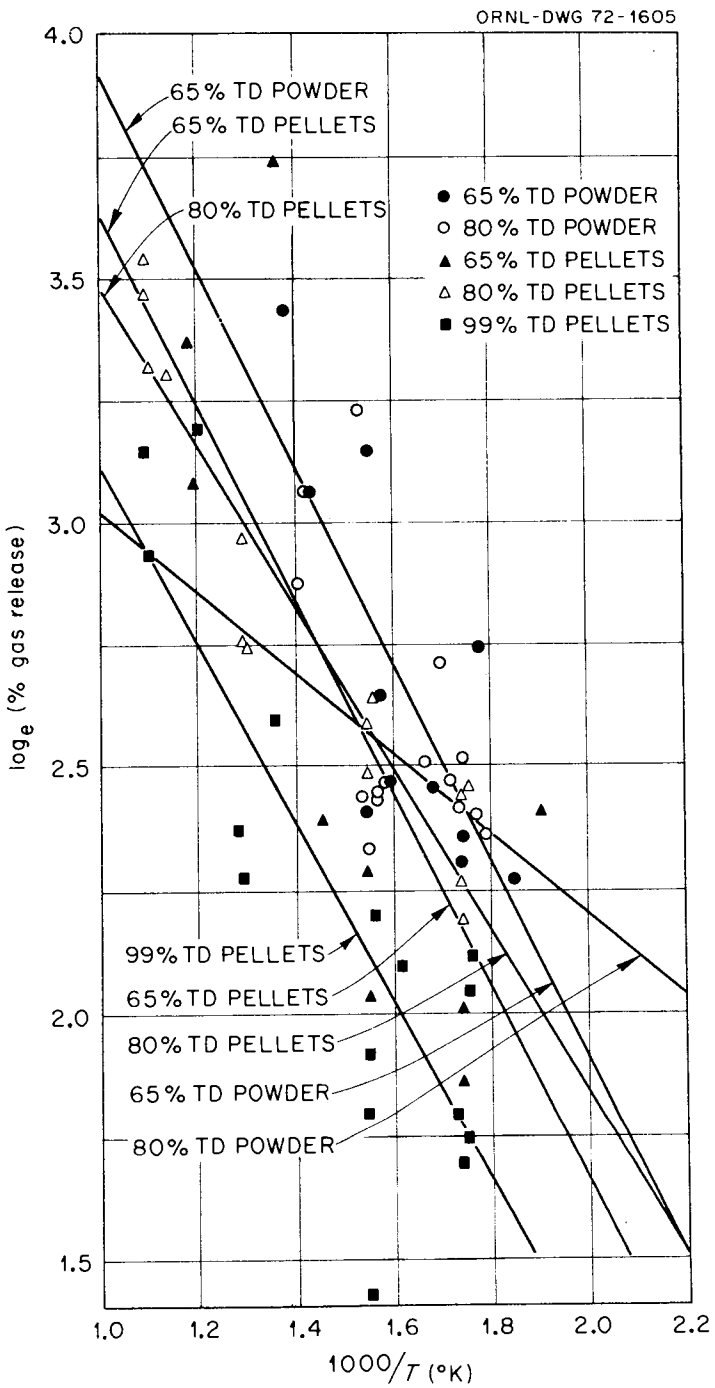

Fig. 3.18. Plot of LOG_e (Helium Release) Versus Reciprocal Temperature for B_4C Powders and Pellets.

average of the four slopes (excluding the slope of the 80%-dense powder data). A summary of slopes and intercepts is given below.

	1.986 (slope)	Intercept
65% theoretically dense powder	4000	5.93
80% theoretically dense powder	1628	3.84
65% theoretically dense pellets	3878	5.57
80% theoretically dense pellets	3246	5.10
99% theoretically dense pellets	3641	4.94

To introduce the influence of porosity into the correlation, the intercepts were plotted against fractional density for the three pellet densities being studied. This plot is shown in Fig. 3.19. In view of

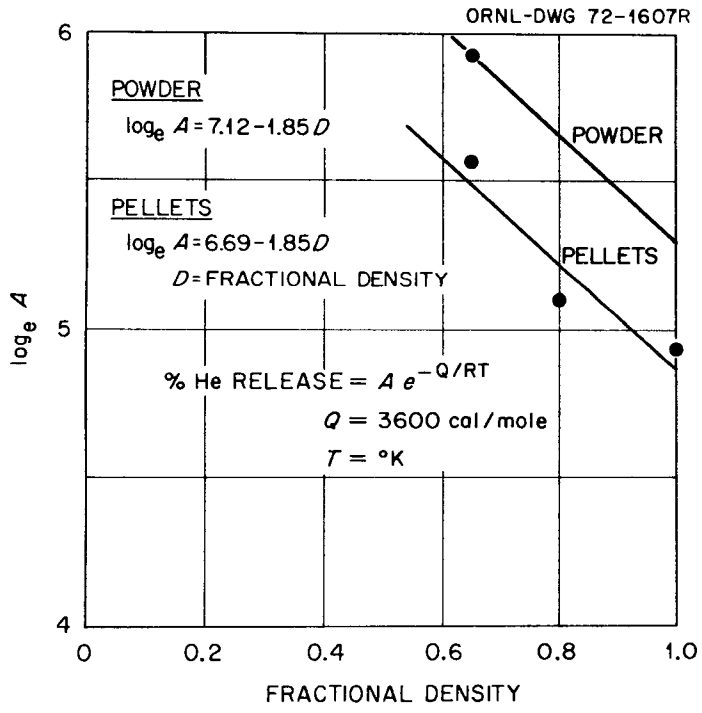

Fig. 3.19. LOG_eA Versus Density for B_4C Powder and Pellets.

the substantial scatter in the data observed earlier, these three points can be fit to a straight line over the density range of interest without significant loss of accuracy. The equation for helium gas release as a function of temperature and density then becomes

$$\% \text{ He release} = \exp\left(C - 1.850 - \frac{C_v}{RT}\right)$$

where

D = fractional density,

T = °K,

C = 6.69 for pellets, and

C = 7.12 for powders

It should be noted that because the least-squares fit for 80%-dense powder shown in Fig. 3.18 was eliminated from consideration, there is only one intercept point to be plotted in Fig. 3.19 for the powdered boron carbide. Thus, the curve representing $LOG_e A$ versus density for the powders has been drawn through that point, and parallel to the similar curve for pellets.

4. MECHANICAL PROPERTIES OF ALLOYS IN REACTOR ENVIRONMENTS AND DEVELOPMENT OF LMFBR CLADDING AND STRUCTURAL MATERIALS

J. R. Weir, Jr. W. R. Martin E. E. Bloom

The main emphasis of this program is on austenitic stainless steels. Included in our work are types 304 and 316 stainless steel and titanium-modified 304 and 316 stainless steel. Types 318, 19-9-D1, and 12R72HV stainless steel have also been included in recent experiments inserted into the Experimental Breeder Reactor-II (EBR-II). The irradiation effects are determined by measurements of swelling and mechanical properties after irradiation. Experiments are run in three reactors: the EBR-II, the Oak Ridge Research Reactor (ORR), and the High-Flux Isotope Reactor (HFIR). Comparative results should reveal any effects of flux and reactor spectrum. Specimens of each material are irradiated in a variety of conditions so that the effects of irradiation temperature, fluence, and metallurgical condition can be evaluated.

Some work on aluminum-base alloys is also described in this section, although this work is supported by the Division of Research. This work is important for several reasons: (1) since several reactors now in operation use aluminum as a structural material, any limits on their period of operation must be determined; (2) irradiation damage to aluminum alloys parallels in many ways that observed in austenitic stainless steels; and (3) since the fluence required to initiate swelling in pure aluminum is relatively low, fluences that produce large amounts of swelling can be obtained in short periods of time. This last characteristic makes it possible to observe the variation of swelling with fluence over a wide range of variables.

AUSTENITIC STAINLESS STEELS

Status of Irradiation Experiments

E. E. Bloom A. F. Zulliger J. W. Woods

Subassembly X100 was removed from Row 2 of the EBR-II after accumulating an exposure of 11,457 MWd. Capsules A and B were removed from the subassembly and shipped to ORNL for evaluation. These capsules contain approximately 170 samples for density, transmission electron microscopy, and mechanical property testing. The primary objective of this experiment is to establish the effects of preirradiation heat treatment (and thus preirradiation microstructure) on the swelling resistance and post-irradiation mechanical properties of standard type 316 stainless steel and titanium-modified type 316 stainless steel. Other objectives of the experiment are (1) investigation of the effects of certain compositional variations on the swelling and postirradiation mechanical properties of type 316 stainless steel including variations, in molybdenum (0.0 — 5.0%), titanium (0.0 — 0.6%), and carbon (0.02 and 0.06%); and (2) determination of the effects of irradiation on the mechanical properties of type 304 stainless steel weldments.

Disassembly of the capsules is under way. Removal of holders from the capsules was accomplished with no trouble and all holders appeared normal. Dimensions of the individual holders are being determined prior to opening since this information is required for calculation of end-of-life irradiation temperatures.

Calculation of end-of-life temperatures for Subassembly X035 is in progress. This subassembly was inserted into the EBR-II at the beginning of Run 27F and was removed at the end of Run 45B with an accumulated exposure of 22,435 MWd. The majority of this exposure was accumulated in reactor grid positions 7B3 and 7B4. Table 4.1 shows the initial and end-of-life calculated temperatures for those specimen holders which contained silicon carbide (SiC) temperature monitors and were located in the central

Table 4.1. Irradiation Temperatures in EBR-II Subassembly X035

Position Number and Distance From Midplane (in.)	Initial Temperature at 45 MW Reactor Power, °C	End-of-Life Temperature at 50 MW Reactor Power Using Swollen Capsule and Specimen Holders, °C	Temperature Determined From SiC Lattice Parameter Measurements, °C
K8[a] +10.125	770	780	740
K11 +3.75	600	620	670
K17 -10.125	650	665	660
K19 -14.625	425	430	450

[a]Tungsten specimen holder, all other holders were stainless steel.

pin (K) of the 7 pin subassembly. The end-of-life temperatures were calculated using previously described procedures[1] and gamma heating rates which were determined in a calibration experiment[2] and which are in close agreement with values published in Fig. C-18, p. C-29 of the "Guide for Irradiation Experiments in EBR-II," for the grid and pin position in question. An increase in irradiation temperature occurred during the life of the experiment as a result of differential swelling between the containment tube and the specimen holders. Irradiation temperatures determined from lattice parameter measurements on the SiC monitors are shown for comparison.

Calculations have also been completed for Pin J which was the pin closest to the core centerline. Figure C-13 (p. C-22) of the "Guide for Irradiation Experiments in EBR-II," shows a gamma heating rate in stainless steel at this radial position which is about 2.1 times higher than

[1]E. E. Bloom and A. F. Zulliger, Fuels and Materials Development Program Quart. Progr. Rept. March 31, 1971, ORNL-TM-3416, p. 94.

[2]E. E. Bloom and A. F. Zulliger, Fuels and Materials Development Program Quart. Progr. Rept. December 31, 1967, ORNL-TM-2090, pp. 45-49.

in the central pin of the subassembly. Using this factor to adjust the gamma heating rate which was used for the central pin (K) and using the end-of-life dimensions, it is calculated that the end-of-life temperature in position J-15 (5.675 in. below the midplane) was 887°C. The SiC monitor indicated the end-of-life temperature was about 730°C. A possible explanation for this discrepancy is that the gamma heating rate in this grid position does not decrease as rapidly with radial distance as indicated by the guide.

Defect Structures in Irradiated Type 316 Stainless Steel

J. O. Stiegler E. E. Bloom

Microstructural analysis has been completed of the defect structures and precipitate particles formed in type 316 stainless steel irradiated in EBR-II to fluences of about 2×10^{22} neutrons/cm^2 (> 0.1 MeV) at temperatures ranging from 455 to 790°C. The results are qualitatively similar to those produced in type 304 stainless steel in that void and dislocation structures form and precipitation reactions are modified and enhanced. Special care was taken in the present work to obtain more quantitative descriptions of the defect populations, especially the dislocation structure. Foil thicknesses were measured by stereomicroscopy techniques. For loop and dislocation counts, both micrographs of the stereo pair were made in the same reflection (usually [200]), and an image of the same area in a second reflection (usually [020]) was obtained to ensure that all dislocations were being observed. Measurements were made on composite micrographs constructed to show all the dislocations or allowance was made for invisible dislocations by assuming all Burgers vectors were equally probable. No evidence was obtained to dispute this. Statistics describing the various defect configurations measured in this study are summarized in Table 4.2.

For irradiation at 455°C to a fluence of 1.9×10^{22} neutrons/cm^2 the microstructure was dominated by the faulted dislocation loops which were present in a concentration of at least 1×10^{15}/cm^2 (Fig. 4.1).

Table 4.2. Defect Statistics in Irradiated Type 316 Stainless Steel

Irradiation Temperature (°C)	Fluence Neutrons/cm^2 (E > 0.1 MeV)	Dislocation Structures			Voids		$\frac{\Delta V}{V}$	Precipitates	
		Loops		Dislocation Density (cm/cm^3)	Concentration (voids/cm^3)	Mean Diameter (Å)	Calc (%)	Type	Concentration (cm^{-3})
		Concentration (voids/cm^3)	Size						
455	1.9×10^{22}	1×10^{15}	< 100Å min 1700Å max		6.9×10^{13}	236	0.06		
510	1.5×10^{22}	5.2×10^{14}	125Å min 2100Å max		1.8×10^{13}	337	0.05		
580	1.9×10^{22}	4.8×10^{12}	870Å min 1700Å ave 3500Å max	4×10^{9}	1×10^{13}	666	0.2	$M_{23}C_6$ Ribbon-like	1.3×10^{12} 3.6×10^{13}
675/715	1.9×10^{22}			9.8×10^{8}	7.7×10^{12}[a]			$M_{23}C_6$ Rod-like	1.8×10^{12} 1.6×10^{11}

[a] Helium bubbles.

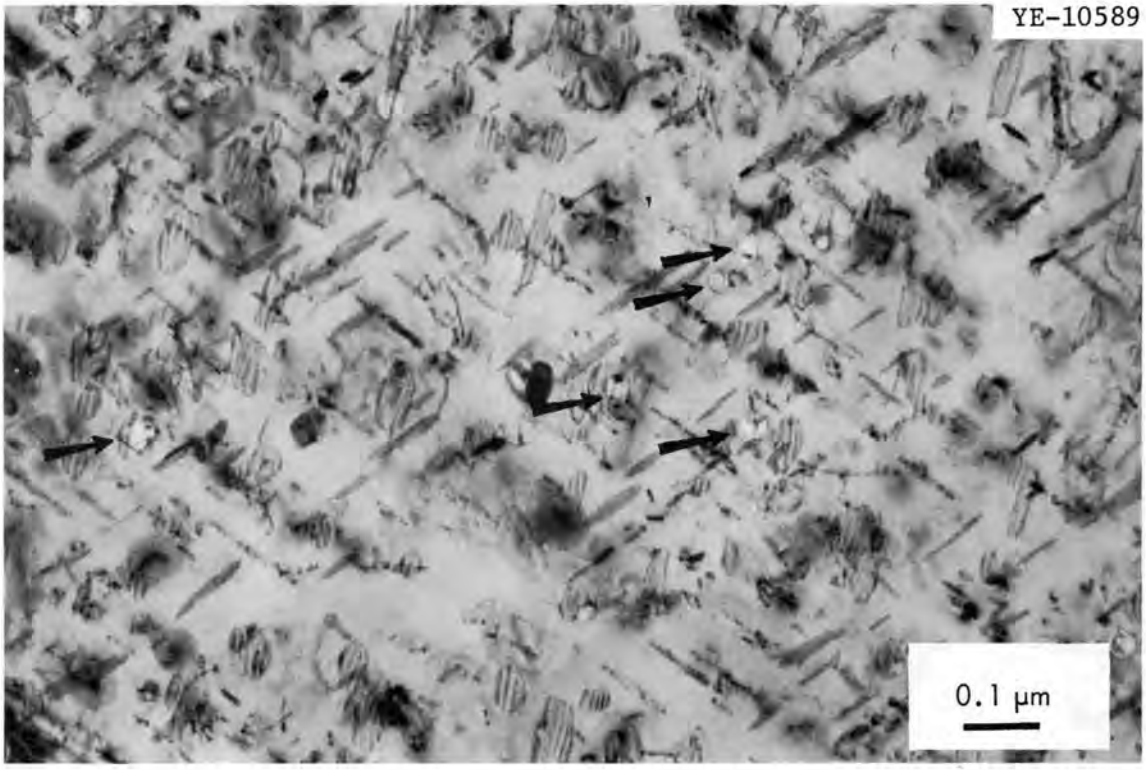

Fig. 4.1. Dislocation Loops and Voids (at ends of arrows) Formed in Type 316 Stainless Steel Irradiated to a Fluence of 1.9×10^{22} neutrons/cm^2 at 455°C.

The loops were irregularly shaped often with reentrant sides resembling pieces of a jigsaw puzzle. Because of this it was impossible to estimate an average size, but loops ranging between 50 and 1700 Å across were found. In some grains enhanced loop formation was noted in regions adjacent to grain boundaries. Voids averaging 236 Å in diam were present in a concentration of 6.9×10^{15}/cm^3. As in type 304 stainless steel the voids were polyhedral, no two possessed the same external shape. Occasional blocky $M_{23}C_6$ precipitate particles were found in grain boundaries. Little, if any, precipitation was noted within the grains.

Similar features were found for irradiation at 510°C to a fluence of 1.5×10^{22} neutrons/cm^2. Both loops and voids were larger on the average and present in lower concentrations than at 455°C.

For irradiation at 580°C to a fluence of 1.9×10^{22} neutrons/cm^2 a mixture of faulted and unfaulted dislocation loops and dislocation lines was observed as shown in Fig. 4.2. There were about 4.8×10^{12} faulted loops/cm^3 that were generally circular and ranged between 870 and 3500 Å in diam with an average of about 1700 Å. It was not possible to characterize the distribution of unfaulted loops and they were included in the count of dislocation lines which yielded a dislocation density of

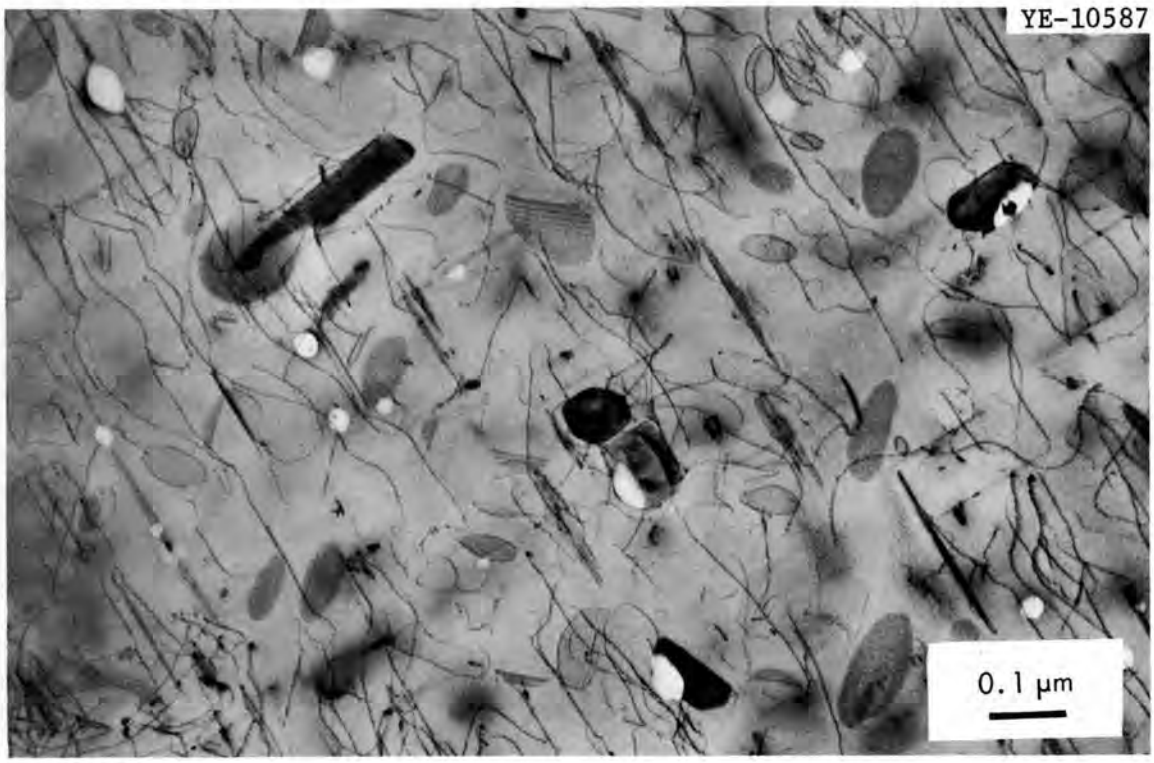

Fig. 4.2. Dislocation Lines and Loops, Voids and Precipitate Particles Formed in Type 316 Stainless Steel Irradiated to a Fluence of 1.9×10^{22} neutrons/cm^2 at 580°C.

4×10^9 cm/cm^3. Most of the voids found in this specimen were associated with precipitate particles. Not all precipitates had voids attached, however. Two types of precipitate particles were present, the blocky $M_{23}C_6$ particles shown in Fig. 4.2, and some needle or more properly ribbon-like particles shown in Fig. 4.3. Although selected area diffraction patterns have been obtained from the latter, it has been impossible

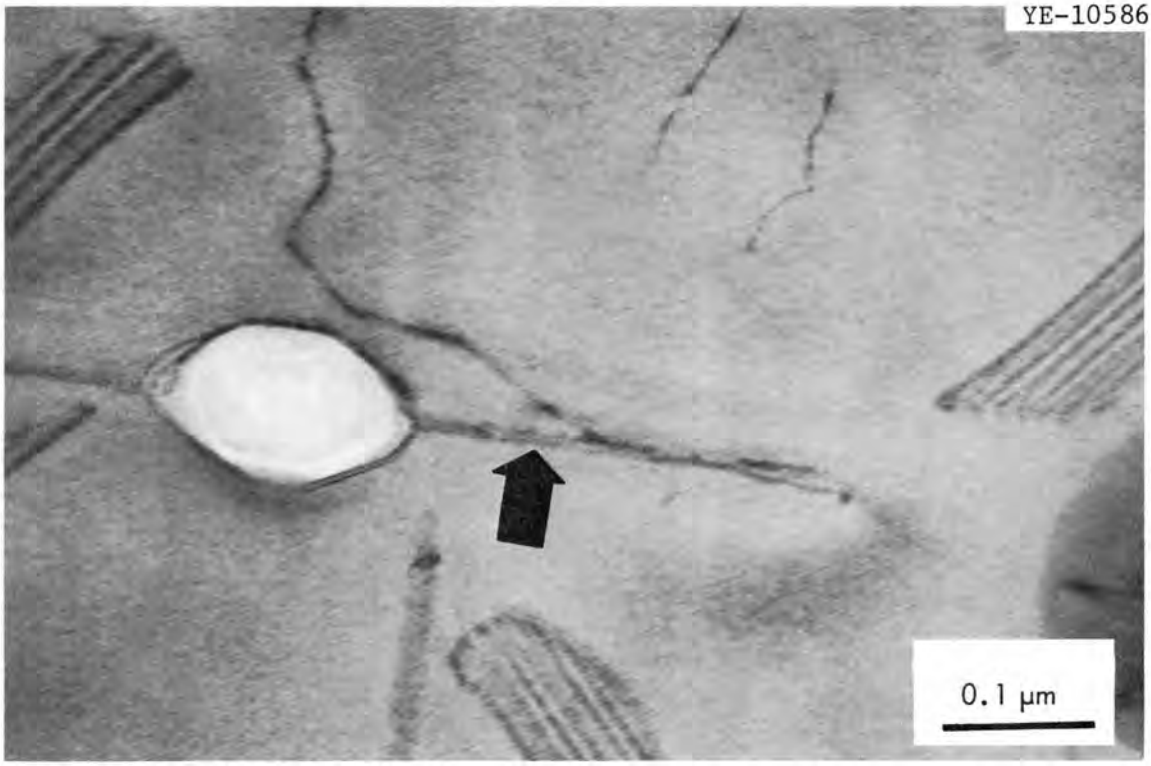

Fig. 4.3. Ribbon-Like Precipitate Intersecting a Void in a Specimen of Type 316 Stainless Steel Irradiated to a Fluence of 1.9×10^{22} neutrons/cm^2 at 580°C.

to match them with any of the known phases in this system; namely, $M_{23}C_6$, M_6C, MC, Laves, Chi or Sigma. It is possible that it is a variant of one of these phases having a composition and lattice parameter different from that usually found. Alternatively, it may be a new phase not formed by conventional thermal treatments. The ribbon-like precipitates run in (100) directions. It has not been possible to specify their habit plane, but from a comparison with stacking fault fringes Bisson and Vouillon[3] concluded that they lay on (110) planes. In their case these precipitates disappeared on annealing at temperatures above 600°C. Here

[3]Andre Bisson and Michel Vouillon, Electron Microscope Study of Needle-Shaped Precipitates in Irradiated Austenitic Steels, EURFNR-891, September 1970.

they were found for irradiations at temperatures as high as 630°C. Figure 4.2 does not give a fair representation of the concentration of the ribbon-like precipitates since they are not imaged well under diffraction conditions. They were present in a concentration of $3.6 \times 10^{13}/cm^3$ in contrast to 1.3×10^{12} carbides/cm^3. For comparison there were about 1×10^{13} voids/cm^3. Every carbide had a void attached as did about a quarter of the ribbon-like precipitates. In some cases voids were found at the center of three mutually perpendicular ribbon-like precipitates, and in a few instances several voids were distributed along a single precipitate. A nearly continuous distribution of $M_{23}C_6$ particles was found along the grain boundaries in this specimen.

For irradiation in the temperature range 675 to 715°C to a fluence of 1.9×10^{22} neutrons/cm^2 a dual cavity structure was observed, small cavities ranging up to 300 Å in diam usually, although not always, associated with plate-like $M_{23}C_6$ particles (Fig. 4.4) and large cavities up to 1000 Å in diam on angular precipitates, probably also carbides. Because of their small size the former are believed to be equilibrium helium bubbles. The latter, which were extremely rare, may be voids. Grain boundaries displayed an almost continuous layer of small $M_{23}C_6$ particles, shown in Fig. 4.5. No dislocation loops were found in this specimen, but a general dislocation density of 9.8×10^8 cm/cm^3 was measured. In some cases loops were observed around large precipitate particles that evidently had been punched out during cooling, but these were isolated and not included in the dislocation count.

Cold-Worked Material

Deformation of 20% by cold-working produced significant modifications in the microstructures of type 316 stainless steel for the fluence levels studied here by suppressing the formation of voids except in isolated recovered areas of a specimen irradiated at 580°C, by eliminating the formation of dislocation loops under all conditions, and by altering the type, amount and distribution of precipitate particles.

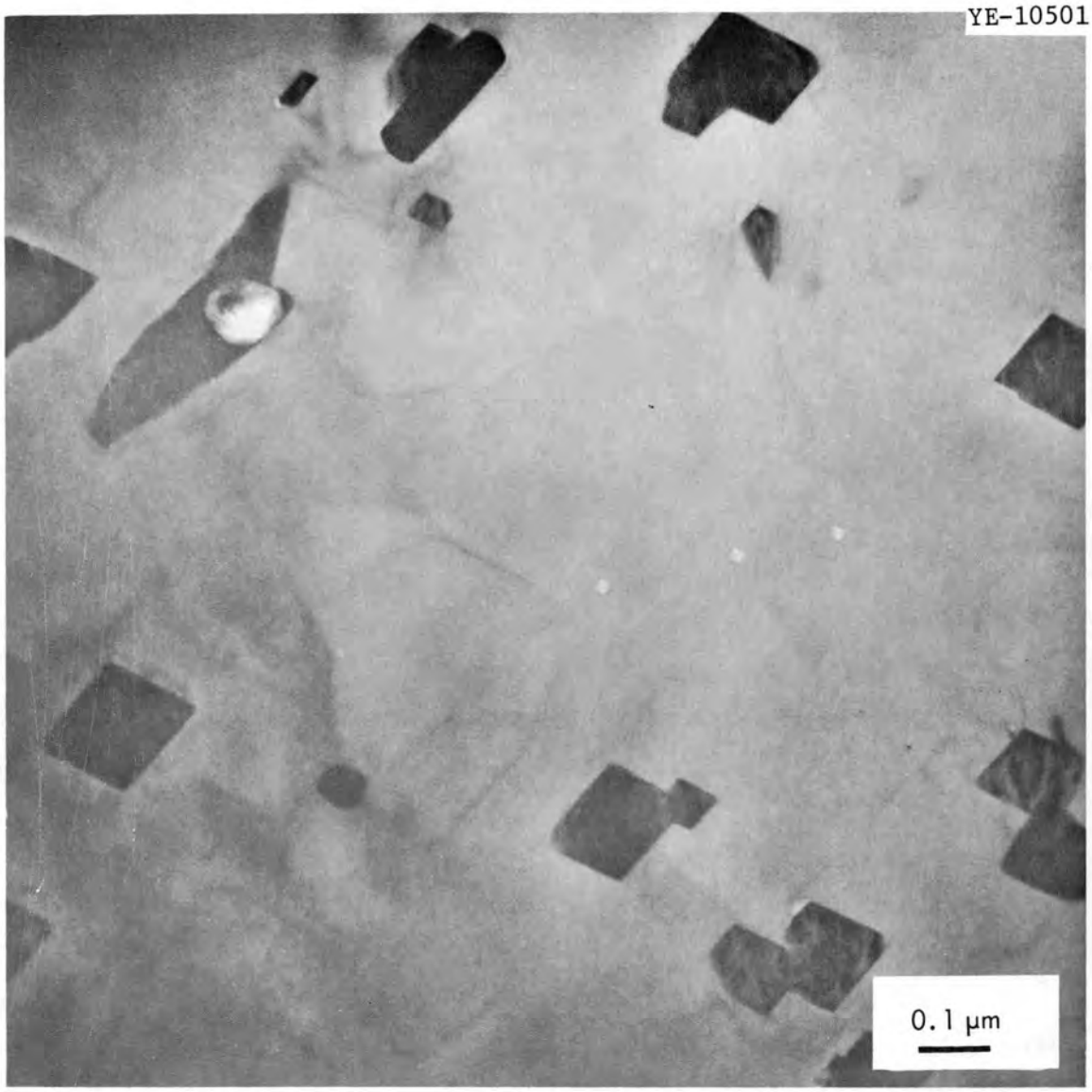

Fig. 4.4. Cavities and $M_{23}C_6$ Precipitates Formed in Type 316 Stainless Steel Irradiated to a Fluence of 1.9×10^{22} neutrons/cm^2 at 675/715°C.

It was not possible to detect any microstructural change in a specimen irradiated at 450°C to a fluence of 1.9×10^{22} neutrons/cm^2. It was somewhat easier to image the microstructure, but this cannot be taken as evidence for recovery. No precipitate particles were observed either on grain boundaries or within grains.

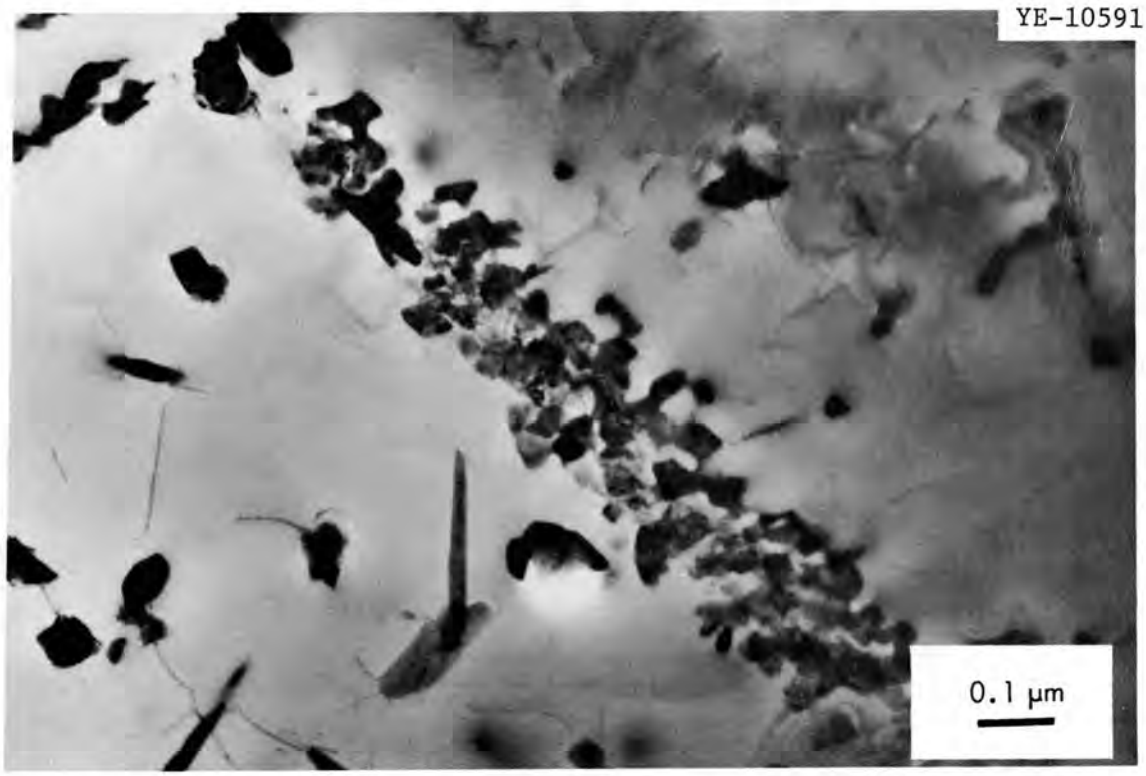

Fig. 4.5. $M_{23}C_6$ Particles on a Grain Boundary of Type 316 Stainless Steel Irradiated to a Fluence of 1.9×10^{22} neutrons/cm^2 at 675/715°C.

For irradiation at 510°C to a fluence of 1.2×10^{22} some recovery clearly had taken place in the dislocation structure. In addition, sheet of $M_{23}C_6$ formed on the stacking fault bands (Fig. 4.6) and some elongated Laves phase particles on or near the bands (Fig. 4.7). Isolated $M_{23}C_6$ particles were also located along the grain boundaries.

More extensive carbide and Laves phase precipitation in the same morphologies was present in the specimen irradiated at 580°C to a fluence of 2.7×10^{22}. In addition, more extensive recovery had occurred, and in regions of relatively low dislocation density some voids were found (Fig. 4.8). No loops were evident anywhere. There were such extreme variations in dislocation void and precipitate densities that no meaningful number could be extracted to describe the specimen.

Fig. 4.6. Sheets of $M_{23}C_6$ on a Stacking Fault Band and a Laves Phase Particle (arrow) in Type 316 Stainless Steel Cold-Worked 20% Prior to Irradiation to a Fluence of 1.2×10^{22} neutrons/cm^2 at 510°C.

Fig. 4.7. Voids in a Recovered Area of Type 316 Stainless Steel Cold-Worked 20% Prior to Irradiation to a Fluence of 2.7×10^{22} neutrons/cm^2 at 580°C.

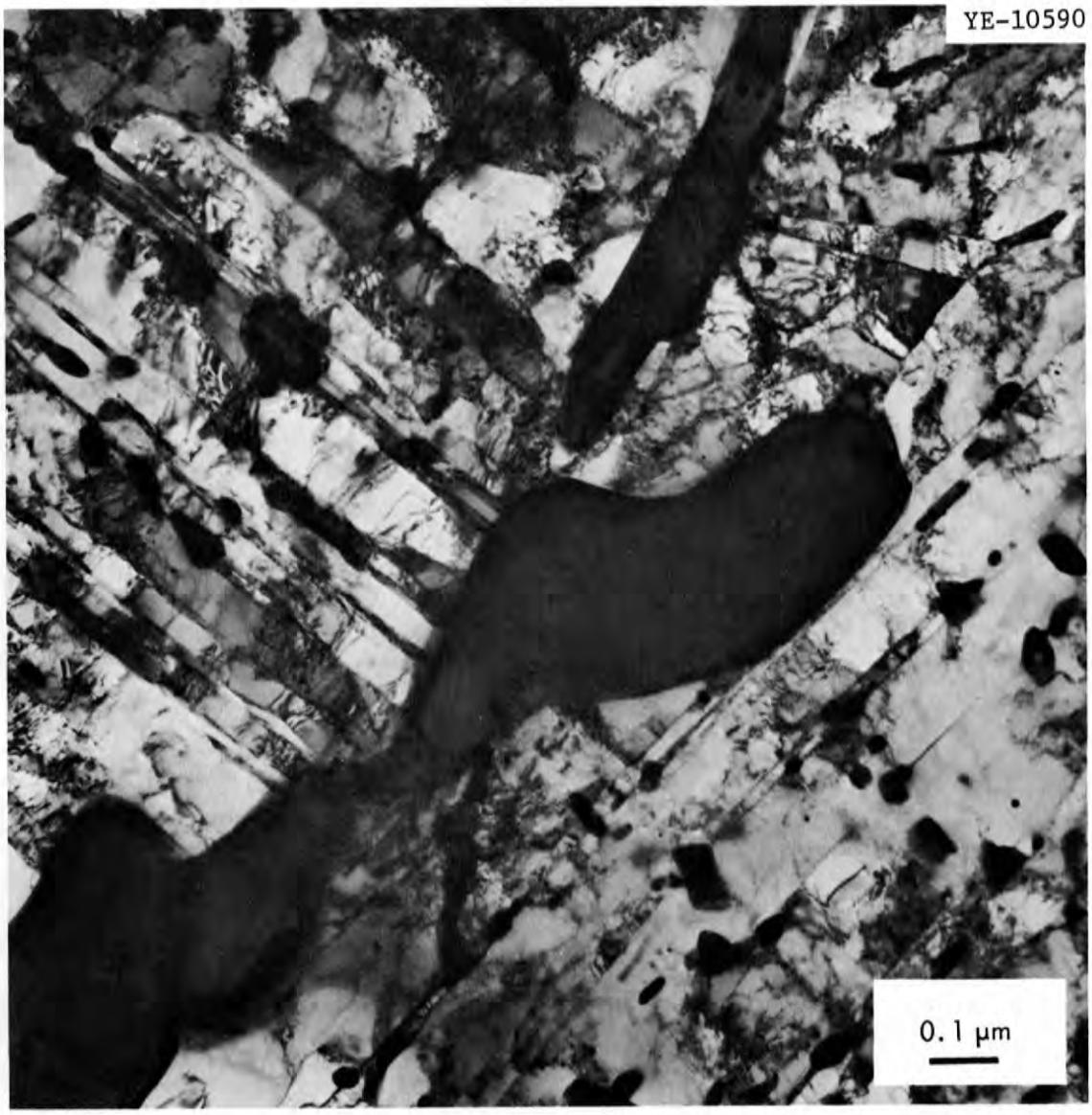

Fig. 4.8. Sigma Phase Grains and Precipitates of Laves Phase in Recovered Areas of a Specimen of Type 316 Stainless Steel Cold Worked 20% Prior to Irradiation to a Fluence of 2.3×10^{22} neutrons/cm^2 at 680/725°C.

For irradiation to a fluence of 2.3×10^{22} in the temperature range 680–725°C more extensive recovery, some recrystallization and precipitation of large sigma phase particles occurred. No cavities were found in any of the recrystallized grains, but the amount of recrystallization was significantly less than in control specimens held 4000 hr at 650°C.

Figure 4.9 illustrates the appearance of grains of sigma phase in a matrix of recovered material containing elongated Laves phase particles. The sigma particles formed at triple grain junctions and within grains in regions at the intersection of different deformation substructure. Usually only one or two sets of stacking fault bands are found in an area of a grain, but other sets may occur in other parts of that grain. It is at the intersection between these different regions that the sigma phase nucleates.

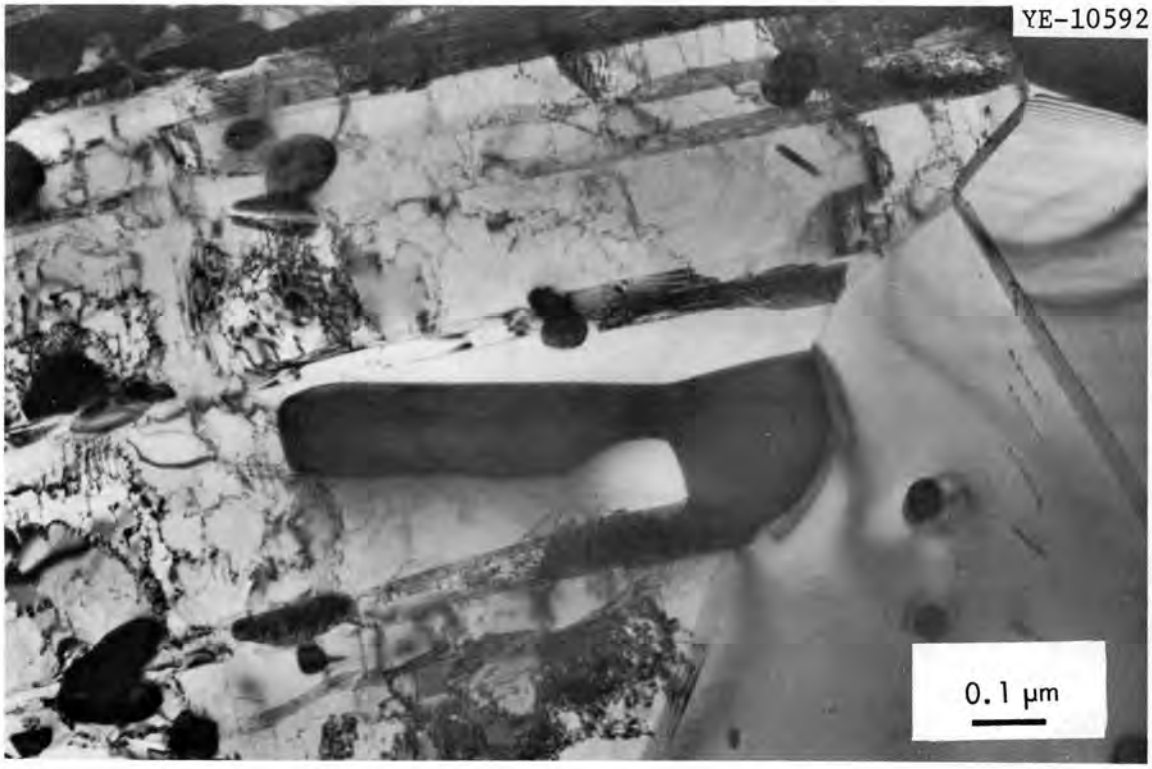

Fig. 4.9. Laves Phase Precipitates in Recrystallized and Recovered Areas of a Specimen of Type 316 Stainless Steel Irradiated to a Fluence of 2.7×10^{22} neutrons/cm^2 at 735/795°C.

Recrystallization was not complete in a specimen irradiated to a fluence of 2.7×10^{22} at a temperature that ranged between 735°C at the start of the irradiation and 795°C at the finish. A control specimen

showed essentially complete recrystallization in 10 hr at 750°C.[4] Bubbles were noted in the recrystallized grains and especially in the interface between recovered and recrystallized material (Fig. 4.10).

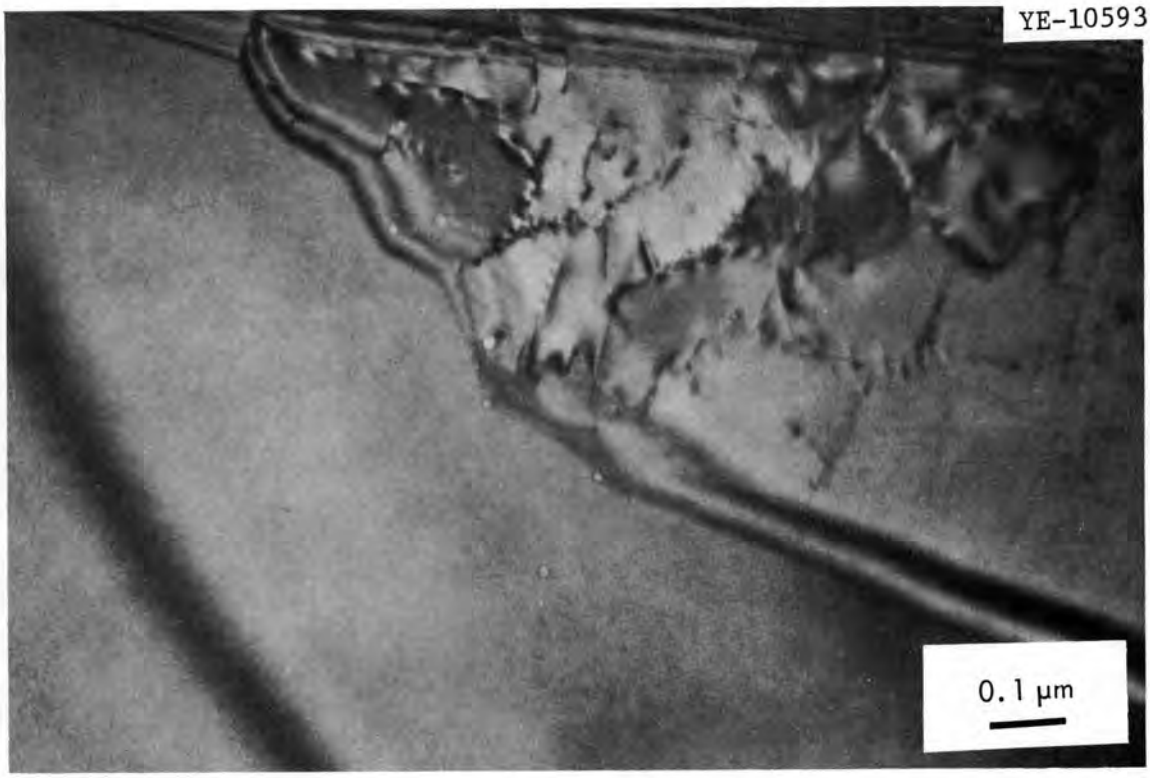

Fig. 4.10. Helium Bubbles Within a Grain and on the Interface Between a Recovered Area and a Recrystallized Grain in 316 Stainless Steel Irradiated to a Fluence of 2.7×10^{22} neutrons/cm^2 at 735/795°C.

Laves phase particles were also found in both areas; in recovered regions they were elongated as described previously and in recrystallized areas they were equiaxed (Fig. 4.9). This suppression of recrystallization suggests that the actual irradiation temperatures may have been somewhat less than the values quoted above. It is unlikely, however, that the final temperature was much below 750°C. The presence of the bubbles

[4]Dieter Fahr, Oak Ridge National Laboratory, private communication, 1972.

suggests that recrystallization may have been retarded, in part at least, by transmutation produced helium as has been found in an aluminum-nickel alloy.[5] Not enough helium or other damage could be accumulated in the first few hours of irradiation to produce this effect, so the initial irradiation temperature must have been below 735°C.

Two other levels of cold work were examined in this study: 10% irradiated to a fluence of 2.3×10^{22} neutrons/cm^2 at 565–610°C and 50% irradiated to a fluence of 1.5×10^{22} neutrons/cm^2 at 630–650°C. In neither case were voids or a radiation-induced dislocation structure found. Precipitation was more extensive in the more lightly deformed material with $M_{23}C_6$ sheets occurring on the stacking fault bands and Laves phase in the recovered regions. More massive precipitates, presently unidentified, formed in the more highly cold-worked specimen.

Comparison with Type 304 Stainless Steel

Detailed studies of the entire defect microstructure have never been made on type 304 stainless steel, but extensive measurements of void concentrations, sizes and swelling have been obtained and reduced to an empirical expression.[6] In Table 4.3 void statistics from the type 316 stainless steel studied here are compared with the calculated values for type 304 stainless steel. In the type 316 stainless steel void concentrations are at least an order of magnitude lower than in type 304. This is compensated for to some extent by larger void diameters, but the overall volume change is lower in 316 than 304. The difference decreases with increasing irradiation temperature, and at 580°C the difference is barely significant. It appears from these limited observations that the temperature for maximum swelling occurs at a higher temperature in 316 than 304 stainless steel.

---

[5]K. Farrell, Oak Ridge National Laboratory, private communication, 1972.

[6]H. R. Brager, J. L. Straalsund, J. J. Holmes, and J. F. Bates, "Irradiation Produced Defects in Austenitic Stainless Steel," Met. Trans. 2, 1893 (1971).

Table 4.3. Comparison of Void Populations in Types 316 and 304 Stainless Steels[a]

Irradiation Temperature (°C)	Fluence (neutrons/cm^2) > 0.1 MeV	Void Concentration (cm^{-3})		Mean Void Diameter (Å)		ΔV/V (%)	
		316	304	316	304	316	304
450	1.9×10^{22}	6.9×10^{13}	1.3×10^{15}	236	178	0.058	0.54
510	1.5×10^{22}	1.8×10^{13}	4.0×10^{14}	337	212	0.05	0.28
580	1.9×10^{22}	1×10^{13}	1.7×10^{14}	666	258	0.21	0.26

[a]Values for 304 stainless steel were calculated using the empirical correlations of H. R. Brager, J. L. Straalsund, J. J. Holmes, and J. F. Bates, "Irradiation Produced Defects in Austenitic Stainless Steel," Met. Trans. 2, 1893 (1971).

Mechanical Properties of Type 316 Stainless Steel

E. E. Bloom J. O. Stiegler

Creep-rupture testing of type 316 stainless steel specimens which were irradiated in EBR-II Subassembly X100 in the annealed, 20% and 50% cold-worked conditions to peak fluences of 2.7×10^{22} neutrons/cm^2 (> 0.1 MeV) is complete and results have been reported in previous progress reports.[7] A final topical report has been drafted.

To investigate and to separate the effects of thermal history from effects due to irradiation per se we are examining the microstructure and creep-rupture properties of "thermal control" specimens which have been aged in the annealed and 20% cold-worked conditions for 4000 hr at 550 and 650°C. Creep-rupture properties at test temperatures of 550 and 650°C are shown in Figs. 4.11 and 4.12. Aging annealed specimens at 550°C had no effect on rupture life, creep rate, or ductility. Aging at 650°C caused a slight reduction in rupture life and an increase in the creep rate by about a factor of 3. For the 20% cold-worked condition aging at 550 and at 650°C caused a decrease in rupture life and an increase in creep rate with the fractional changes being much greater at 650 than at 550°C. The ductility in the cold-worked and aged condition (both 550 and 650°C) was approximately the same as that of annealed material.

Transmission electron microscopy has shown[8] that aging in the annealed condition for 4,000 hr at 550°C formed grain boundary precipitates which have been identified by electron diffraction as $M_{23}C_6$ carbides. In the 20% cold-worked condition some precipitation on deformation bands as well as at grain boundaries was observed. At 650°C

---

[7]E. E. Bloom and J. O. Stiegler, Fuels and Materials Development Program Quart. Progr. Rept. December 31, 1971, ORNL-TM-3703, pp. 79–89.

[8]D. Fahr, Fuels and Materials Development Program Quart. Progr. Rept. December 31, 1971, ORNL-TM-3703, pp. 97–132.

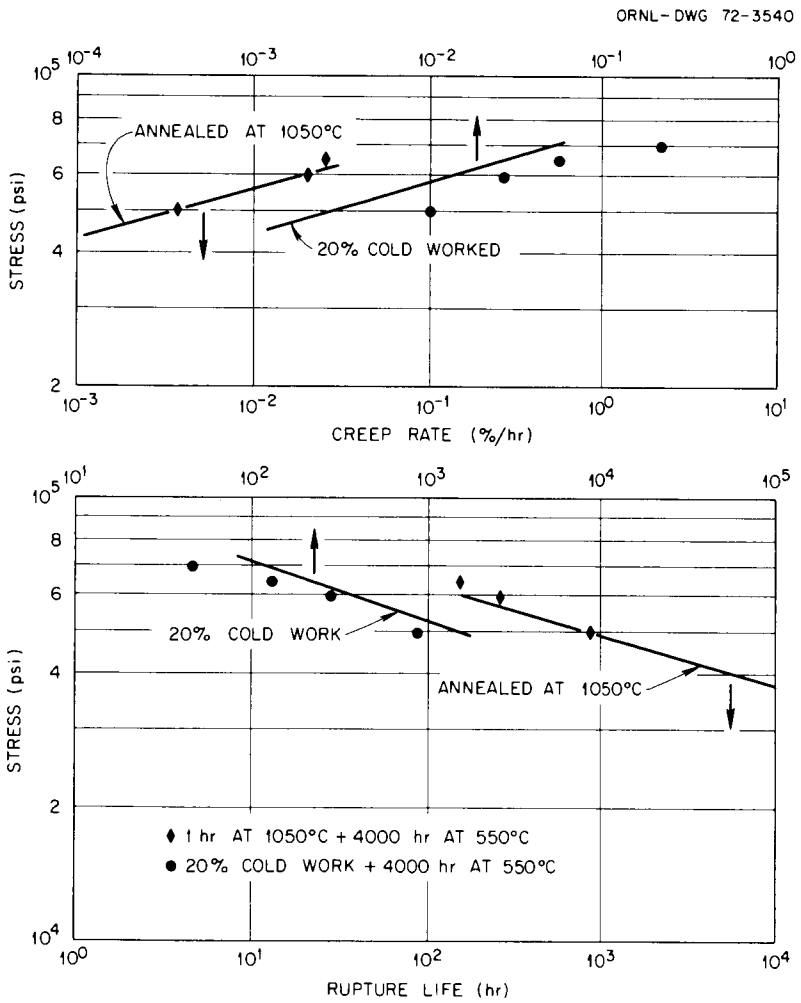

Fig. 4.11. Effect of Aging 4,000 hr at 550°C on the Creep-Rupture Properties of Annealed and 20% Cold-Worked Type 316 Stainless Steel.

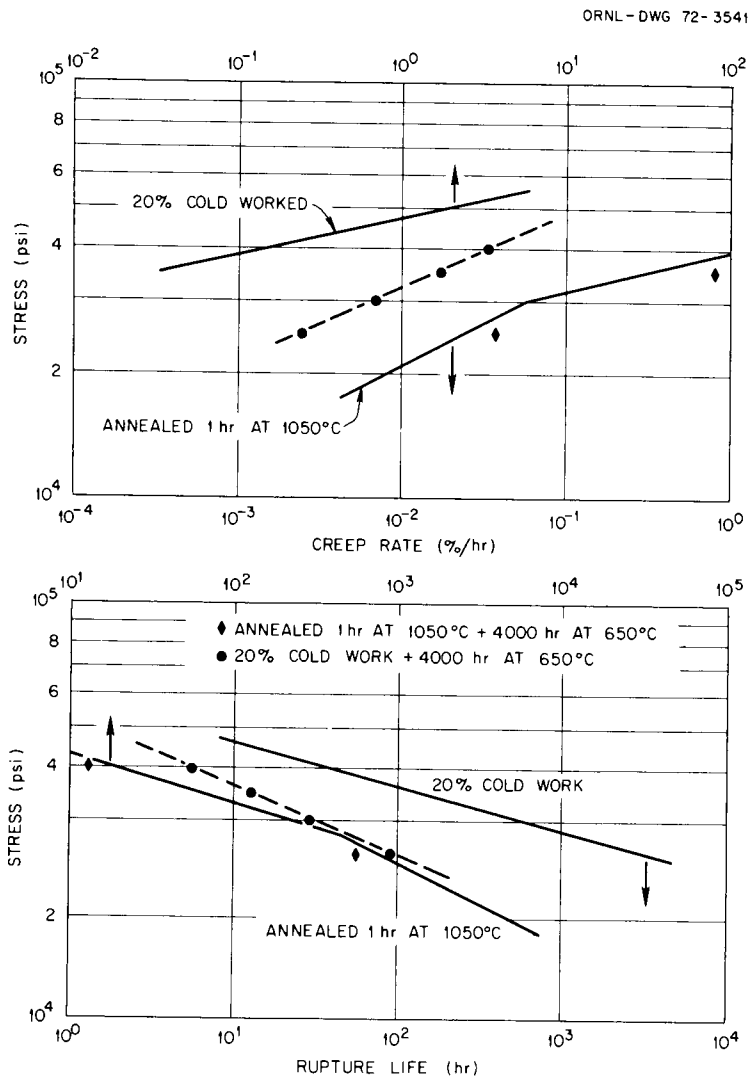

Fig. 4.12. Effect of Aging 4,000 hr at 650°C on the Creep-Rupture Properties of Annealed and 20% Cold-Worked Type 316 Stainless Steel.

extensive matrix and grain boundary precipitation of $M_{23}C_6$ carbides occurred in the annealed specimens while recovery, recrystallization, $M_{23}C_6$ carbide, and sigma phase precipitation occurred in the cold worked structure. The decreased strength due to aging of annealed specimens at 650°C apparently resulted from removal of carbon from solution. This was not compensated for by strengthening from the precipitation which occurred in the matrix. For the cold worked specimens decreased strength probably resulted from both the removal of carbon from solution and recovery of the dislocation structure. To further examine the role of carbon on the strength of the cold-worked structure samples were machined from rod which had been annealed 1 hr at 1050°C then aged 100 hr at 800°C prior to cold working 20% by swaging. The 800°C aging treatment should have removed much of the carbon from solution as large $M_{23}C_6$ precipitates,[9,10] primarily at grain boundaries. Table 4.4 compares the 600°C creep-rupture properties of material having the above mentioned heat treatment to the properties of material in the annealed and the 20% cold-worked conditions. The strength in the aged and then cold-worked condition falls between that of the annealed and the 20% cold-worked condition. At the present time the dislocation structure in the material which was cold worked after aging at 800°C has not been examined. If this structure is the same or similar to that of material which was cold worked after the 1050°C solution treatment, then these results show that carbon in solution has a pronounced effect on the strength in the cold-worked as well as the annealed conditions.

---

[9]B. Weiss and R. Stickler, Phase Instabilities During High Temperature Exposure of 316 Austenitic Stainless Steel, Scientific Paper 70-104-STABL-P1, July 9, 1970, Westinghouse Research Laboratories, Pittsburgh, Pennsylvania.

[10]J. T. Barnby, JISI 204, 23 (1966).

Table 4.4. Effect of Thermal-Mechanical Treatment on the Creep-Rupture Properties of Type 316 Stainless Steel at 600°C

Stress (psi)	1 hr at 1050°C		1 hr at 1050 + 20% cold work		1 hr at 1050 + 100 hr at 800°C + 20% cold work	
	t_R (hr)	$\dot{\varepsilon}$ (%/hr)	t_R (hr)	$\dot{\varepsilon}$ (%/hr)	t_R (hr)	$\dot{\varepsilon}$ (%/hr)
60,000	6.1	0.22	115	0.033	24.0	-
55,000	-	-	229	0.013	56.9	0.056
45,000	98	0.096	1856	0.00034	349.3	0.0075

The potent effects of the microstructural changes which occur during thermal aging on the mechanical properties of austenitic stainless steels are apparent from these results and are also well documented in the literature.[10,11] These changes occur in the temperature range in which the alloy will be used in LMFBR applications. The necessity for investigating the precipitation kinetics and phase stability is thus obvious. It is also apparent that care must be taken in areas such as analysis of fuel pin performance, fuel element modeling, and core component design since mechanical properties can be significantly altered by precipitation which occurs during service. Adjustment of adjustable parameters using as-heat-treated mechanical properties or even low fluence postirradiation results may lead to significant errors in predicting long-term behavior.

Effect of Chromium Concentration on the Formation of Sigma Phase in Type 316 Stainless Steel

J. M. Leitnaker Helen Mateer

Examination of a 20% cold-worked and aged specimen of type 316 stainless steel revealed a large (about 20%) volume concentration of sigma phase and a surface zone denuded of the sigma phase. Measurements

[11] J. T. Barnby, JISI 203, 392 (1965).

of the chromium concentration yielded substantially the same value in the bulk matrix as in the denuded zone suggesting that the formation of sigma phase was promoted by a surplus of chromium in the steel.

The stainless steel specimen, D2-77, had been annealed 1 hr at 1050°C and quenched by pulling to a cold zone of the furnace. After swaging to obtain 20% reduction in area, it was machined to a suitable tensile test specimen and heat treated 4000 hr at 650°C in argon. Finally, it was tensile tested in air at 650°C which involved several hours at temperature. A bulk chemical analysis is given in Table 4.5. The gage portion of the specimen was cut longitudinally and mounted for metallographic examination. The specimen was etched electrolytically with $(NH_4)_2SO_4$ solution (5 g in 100 cm^3 H_2O) at 1100 MV. Photomicrograph

Table 4.5. Composition of Type 316 Stainless Steel

Element	Weight Percent
C	0.05
Cr	17.5
Ni	13.0
Mo	2.6
Mn	1.9
Si	0.8
Ti	0.05
P	0.013
S	0.016

of the sample are shown in Figs. 4.13 and 4.14. X-ray analysis of precipitates which were removed electrolytically in 10% HCl-methanol indicated that 90 vol % were sigma phase; $M_{23}C_6$ made up about 7 vol %, and Laves phase about 2%. We conclude that the large, blackly outlined precipitates are sigma because of the relatively large quantity of them as revealed in the x-ray examination. The smaller precipitates are largely carbide, $M_{23}C_6$.

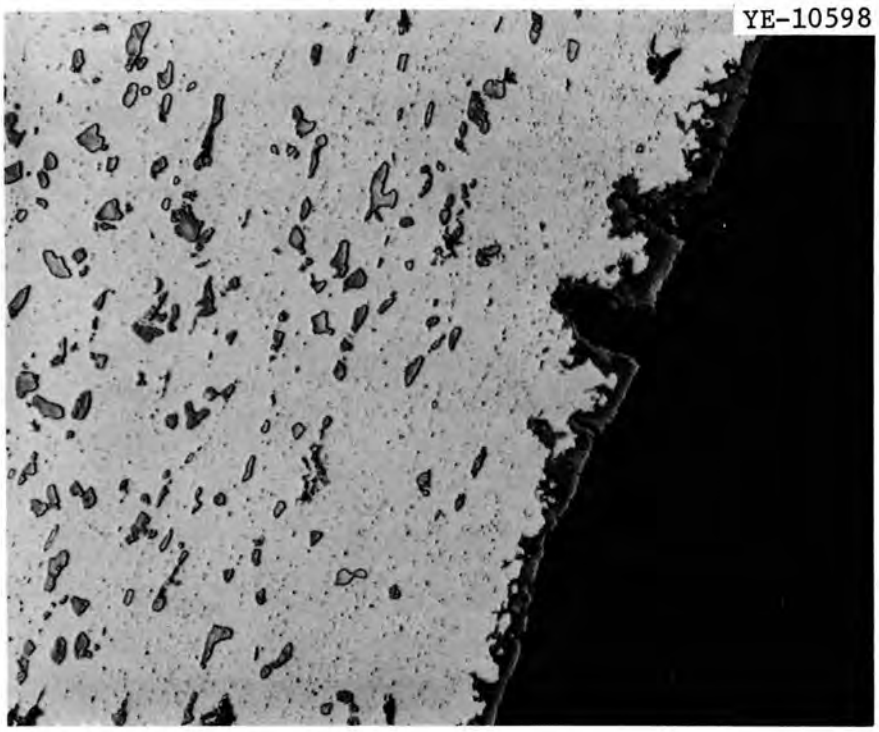

Fig. 4.13. Specimen D2-77 (Gage). Electrolytically etched with $(NH_4)_2SO_4$. 1000×.

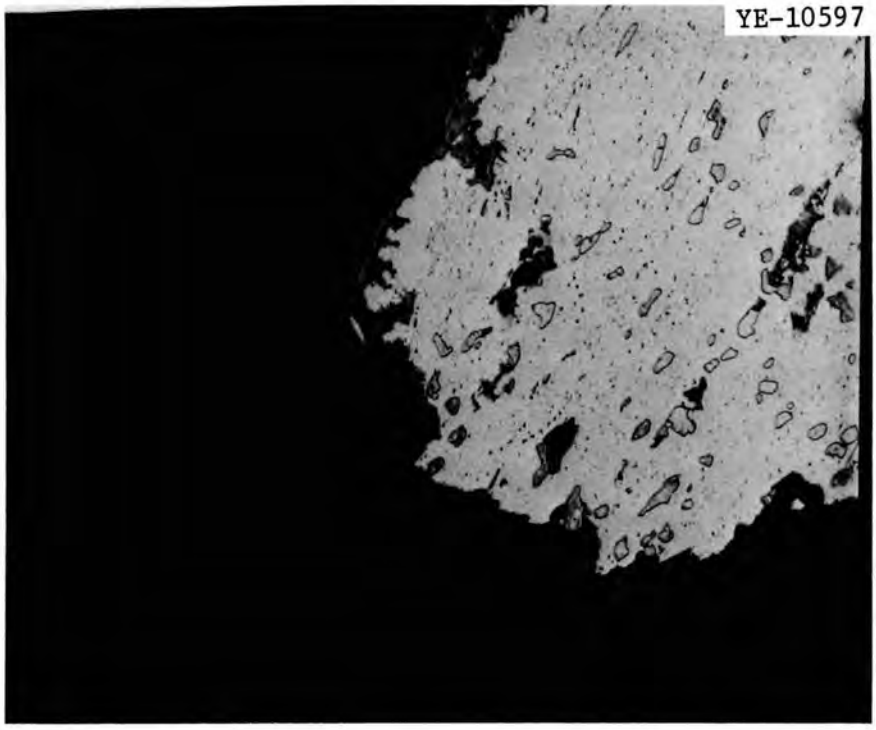

Fig. 4.14. Broken End of Specimen D2-77 (Gage). Electrolytically etched with $(NH_4)_2SO_4$. 1000×.

One sees several important features in the photomicrographs. The most striking is about 20 vol % sigma phase with a smaller amount of carbides and Laves phase. A layer denuded in sigma of about 2.5×10^{-3} cm width is seen on the outside surface. Nearer the surface a zone about 5×10^{-3} cm width in which carbides are absent is present. In Fig. 4.14 it is apparent that the cracks tend to develop at the sigma austenite interface. Within the sample, near the fracture surface, tearing always appeared associated with sigma phase. One also sees an oxide layer along the surface and extending into the cracks which penetrate a distance of about 2.5×10^{-3} cm into the sample.

Microprobe examination of the sample revealed the information shown in Fig. 4.15. Chromium concentration is nearly the same in the matrix as in the denuded layer on the outside of the sample. There is also a further depletion of the chromium at the outer surface of the specimen.

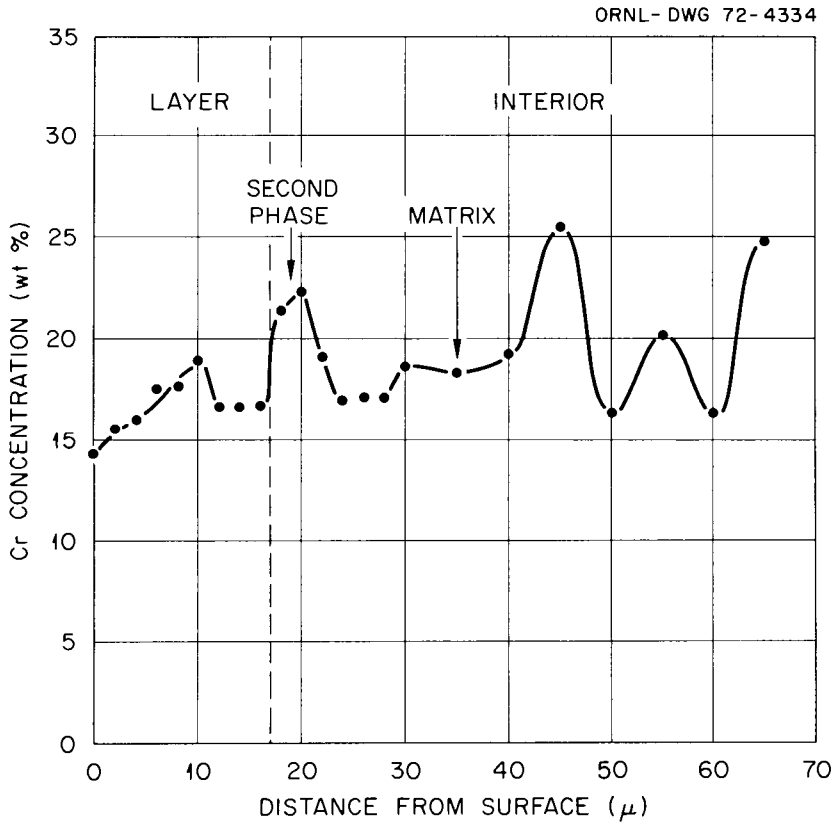

Fig. 4.15. Microprobe Examination of Specimen of Type 316 Stainless Steel Which was Annealed at 1050°C, Cold Worked 20%, Aged 4000 hr at 650°C, Then Tensile Tested at 650°C.

Sigma phase in 316 stainless steel is reported by Weiss and Stickler[12] to have the composition (wt %) of Mo, 11%; Cr, 29%; Fe, 55%; and Ni 5%. Our finding, Fig. 4.15, that the chromium concentration is only about 26% probably represents a contribution of the matrix to the analysis of the sigma phase, rather than a disagreement with the previous work.

It appears from these observations that the formation of sigma phase depletes the chromium concentration in the matrix to a level of about 17% and that in areas of the specimen having a concentration below this level the formation of sigma is suppressed.

Figure 4.14 shows that tearing or cracking of the specimen in the tensile test occurred at or near sigma particles. If this is true, removing the sigma phase should be beneficial to the alloy's ductility and rupture life. Furthermore, since the volume of the stainless steel decreases because of the formation of the denser sigma phase, a stress could be placed on cladding in addition to that imposed by the swelling of the oxide fuel. Again, removal of sigma phase should be beneficial. Since corrosion protection of the steel by chromium has been reduced to the amount imparted by the chromium concentration of the bulk matrix, nominal reduction of chromium in the steel would not only prevent formation of sigma phase, it would also provide the same corrosion protection as the composition now used. Thus, there appears to be little, if any, advantage in using a steel in which sigma phase forms during aging. To determine the chromium level above which sigma forms, it is important to know the composition of the matrix of the aged specimen, which should represent a close approximation to the gamma/(gamma plus sigma) boundary.

At present it is not clear whether the depletion of chromium in the outer layer took place during the testing of the specimen in air or during the 4000 hr anneal in argon, although we suspect the latter. The absence of carbide precipitates near the surface is probably related to oxidation of the carbon. Experiments which are indicated include: (1) examination of a specimen which has been heat treated but not tested, and (2) careful analysis of the matrix to determine the composition.

---

[12]B. Weiss and R. Stickler, Phase Instabilities During High Temperature Exposure of 316 Austenitic Stainless Steel, Scientific Paper 70-1D4-STABL-P1, July 9, 1970.

Simultaneous Imaging of Voids and Dislocation Loops in the Electron Microscope

J. O. Stiegler

Examination of several irradiated stainless steel specimens in the high voltage electron microscope have shown conditions for greatly improving the quality of the images of the dislocation loops and for simultaneously imaging the loops and voids. Our knowledge of the dislocation structure in irradiated stainless steels is extremely meager on account of the difficulty in obtaining clear images of the loops. This arises because the loops are present in such high concentrations that considerable image overlap and interaction occur when the strong diffraction conditions necessary for imaging the loops are obtained. In general, the loop and void structures are imaged separately because under normal operating conditions one is invisible under the best conditions for imaging the other.

We have found that these disadvantages can be overcome and that high quality images of both voids and dislocation loops can be obtained by exciting a high index reflection of a systemmatic set (for example, see Figs. 4.1 and 4.2). The width of dislocation images decreases by a factor of about 3 over that formed by a low index reflection of the set. In addition, the contrast decreases with a higher index reflection allowing the voids to be observed.

This is a multi-beam effect; improved image quality occurs only when a systemmatic set of reflections is used. Improved resolution using these conditions was predicted by Bell and Thomas[13] from 12 beam calculations and verified by Osiecki and Thomas[14], in a study of dislocation images in Gallium Arsenide. The results here are more striking, and the ability to image voids and loops simultaneously is an added bonus.

---

[13]W. L. Bell and G. Thomas, Proceedings of the 27th EMSA Meeting, 1969, Claitor's Publishing Division (Baton Rouge, Louisiana), p. 156.

[14]R. Osiecki and G. Thomas, Proceedings of the 29th EMSA Meeting, 1971, Claitor's Publishing Division (Baton Rouge, Louisiana) p. 178.

In principle the technique can be applied at lower accelerating voltages,[15] although it is usually more difficult to obtain a set of systematic reflections. This technique should prove useful in irradiation damage studies using the electron microscope. By exciting the (600) reflection of the (200) set, all loops as well as the voids will be visible. The improved resolution of the technique also can be used to advantage in deformation studies in cases where specimens containing high dislocation densities must be examined.

Fast Neutron Irradiation of 304 Stainless Steel to a Fluence Level of 1.37×10^{23} Neutrons/cm^2: Some Room-Temperature Tensile Test Observations

D. Fahr

An EBR-II safety rod thimble (3A1) specimen, irradiated at 420°C to a peak fluence of 13.7×10^{22} neutrons/cm^2 was tested at room temperature using a crosshead speed of 0.002 in./min. The engineering stress-strain curve is shown in Fig. 4.16 with a yield point at 100,100 psi, 3.9% elongation, and a fracture stress of 132,400 psi.

Figure 4.17 shows the void structure of the above specimen after testing at room temperature. The density decrease was measured to be 11%. We are presently investigating the possibility that the high concentration of voids is responsible for the development of a state of multiaxial tension during the test and thus a decrease in the shear stress and an increase in elastic strain energy. If such a stress state is produced then a high void density could explain the high yield point and low ductility observed.

True cleavage does not occur in fcc metals or alloys, and no evidence of cleavage-type, brittle fracture has been found. However, some intergranular fracture has been observed (Figs. 4.18 and 4.19).

---

[15] W. L. Bell and G. Thomas, Electron Microscopy and Structure of Materials, G. Thomas, editor, p. 23, University of California Press, Berkeley (1972).

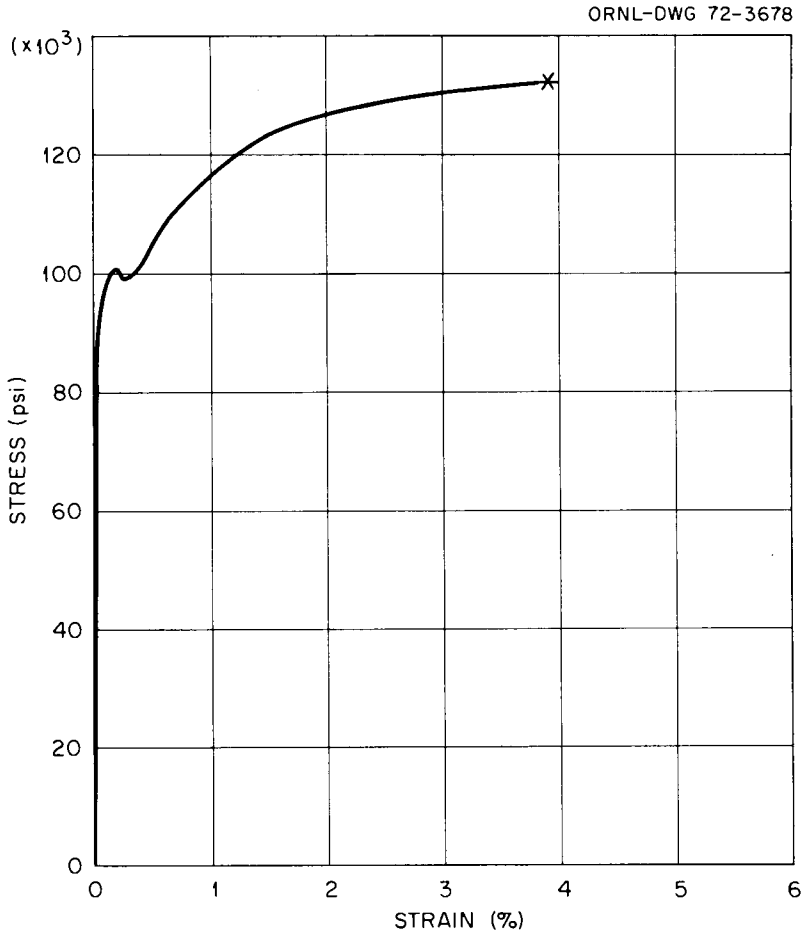

Fig. 4.16. Room-Temperature Engineering Stress-Strain Curve of 304 Stainless Steel Irradiated at 420°C to a Peak Fluence of 13.7×10^{22} neutrons/cm^2. Crosshead speed: 0.002 in./min.

Figure 4.20(a) and (b) show the effect of irradiation on the precipitates at grain and twin boundaries, respectively. Cohesion between precipitates and the matrix appears to be drastically reduced and some carbide particles have fallen out of the foil.

Brittle fracture can occur by separation along grain boundaries, i.e., intergranular fracture. One usually distinguishes between two types of such failures: one in which a film of a brittle phase separates at the grain boundaries, e.g., austenitic chromium-nickel steels embrittled by intergranular carbide precipitation,[16] and the other in which

[16]J. Plateau, G. Henry, and C. Crussard, Rev. Met. 54, 200 (1957).

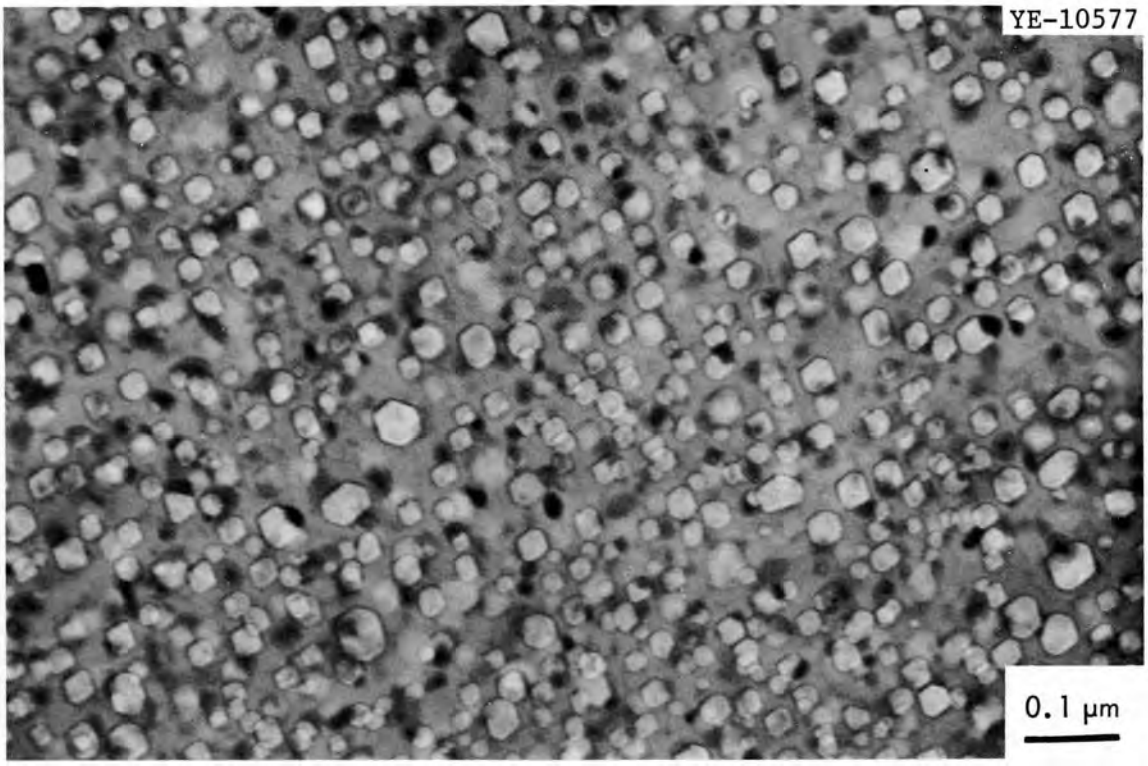

Fig. 4.17. Electron Micrograph of the Void Structure of 304 Stainless Steel Irradiated at 420°C to a Peak Fluence of 13.7×10^{22} neutrons/cm^2.

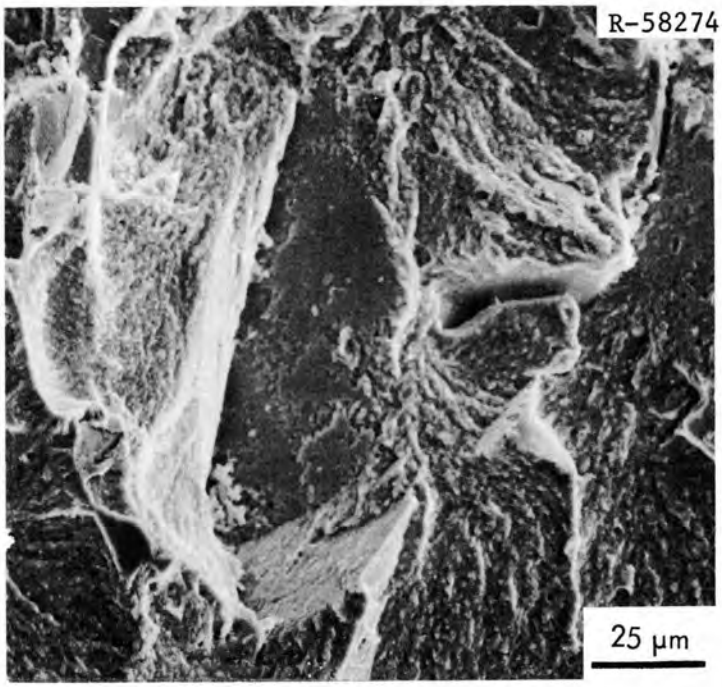

Fig. 4.18. Scanning Electron Micrograph of the Fracture Surface of 304 Stainless Steel Irradiated at 420°C to a Peak-Fluence of 13.7×10^{22} neutrons/cm^2 Showing Intergranular Fracture at Room Temperature.

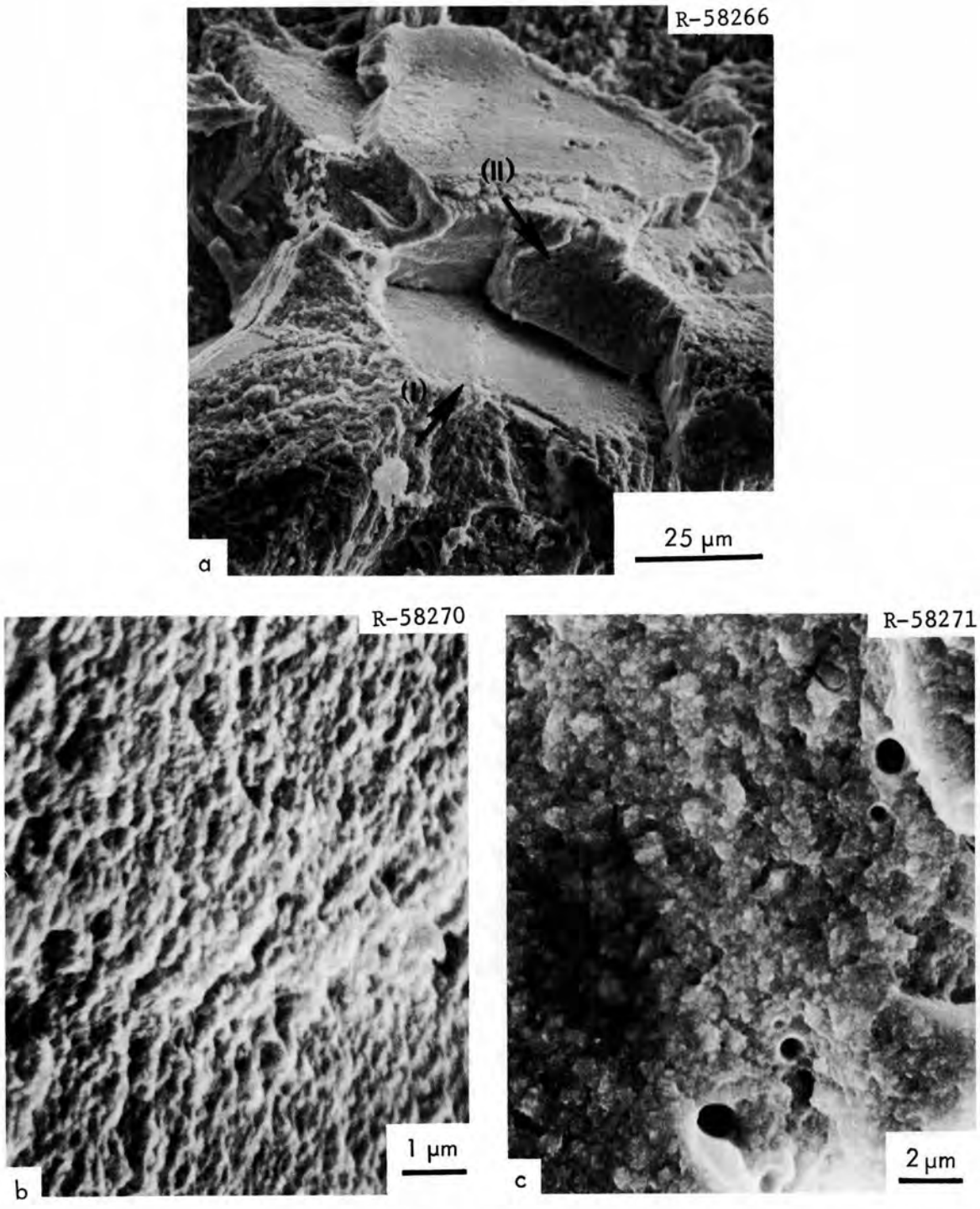

Fig. 4.19. Scanning Electron Micrographs of the Fracture Surface of 304 Stainless Steel Irradiated at 420°C to a Peak Fluence of 13.7×10^{22} neutrons/cm^2 Showing (a) Intergranular Fracture at Room Temperature, (b) a Close-Up of a Fracture Surface Approximately Perpendicular to the Direction of the Applied Stress (I), and (c) a Fracture Surface Approximately Parallel to the Direction of the Applied Stress (II).

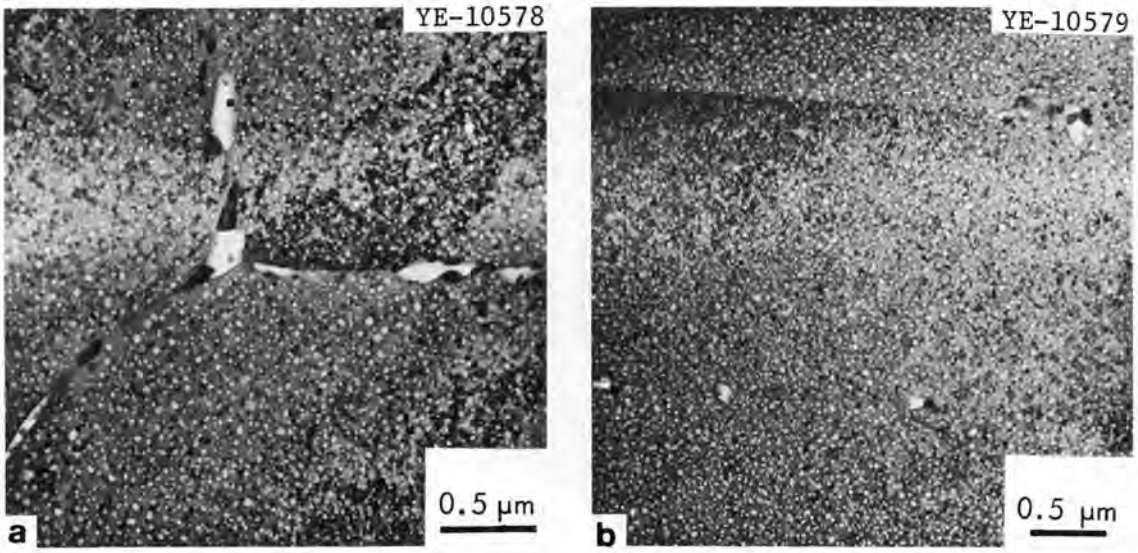

Fig. 4.20. Electron Micrographs of (a) Grain Boundaries and (b) Twin Boundaries in a 304 Stainless Steel Irradiated at 420°C to a Peak Fluence of 13.7×10^{22} neutrons/cm^2.

the grain boundary is embrittled presumably by impurity segregation alone, without the appearance of a separate phase, e.g., copper embrittled by antimony,[17] and iron embrittled by oxygen.[18] A third type seems to be responsible for intergranular fracture in the above specimen. Fracture does not occur because the grain boundary precipitates fail in a brittle manner by cleavage, but because of lack of cohesion or the weakness of the bond between precipitate and matrix. Figure 4.21 clearly shows, especially at higher magnification [Fig. 4.21(b)], the areas on which carbides had formed and from which they have been lifted without any tearing or any traces of plastic deformation. Some precipitate particles which could not be pulled out without deformation of the surrounding matrix fractured [Fig. 4.21(b)]. Irradiation-produced helium may reduce the strength of grain boundaries by weakening the grain-boundary

[17]D. McLean, J. Inst. Metals, 81, 121 (1952-1953).

[18]W. P. Rees and B. E. Hopkins, J. Iron Steel Inst., 172, 403 (1952).

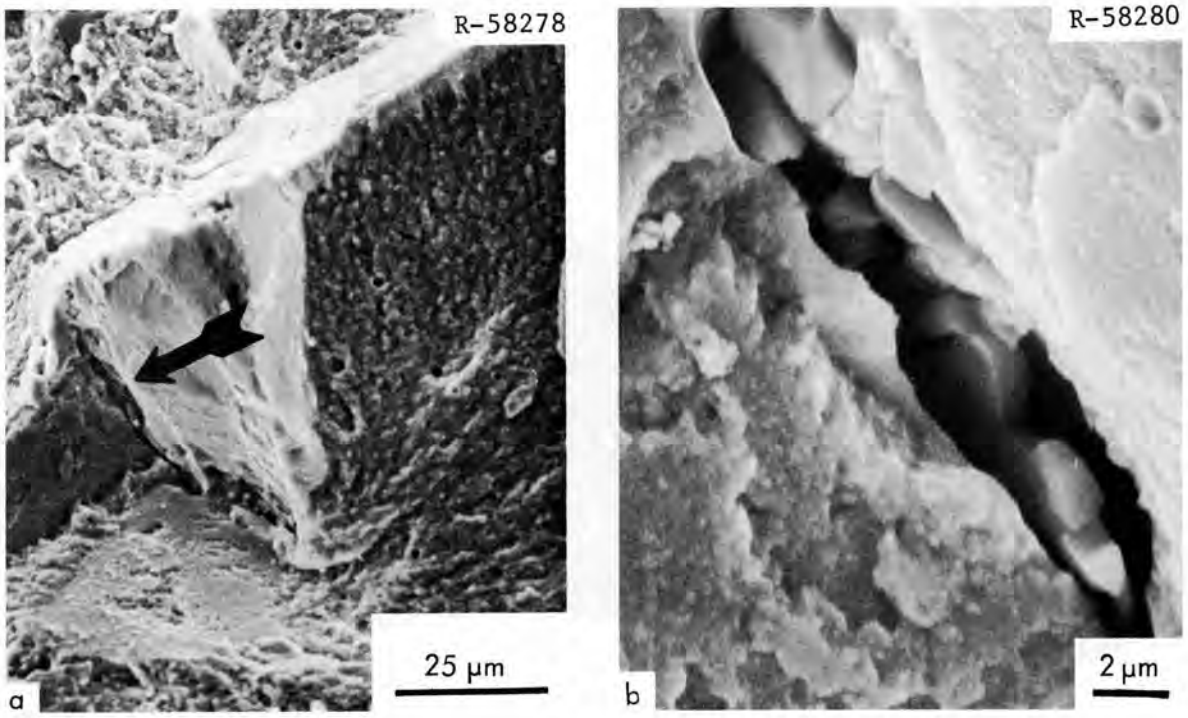

Fig. 4.21. Scanning Electron Micrographs of Carbide Precipitation Sites at a Grain Boundary of 304 Stainless Steel Irradiated at 420°C to a Peak Fluence of 13.7×10^{22} neutrons/cm^2. "Clean" separation of precipitate particles from the matrix during fractures at room temperature shown (a) at low, and (b) at higher magnification.

precipitate — matrix interface in such a way that grain boundary separation is initiated not by fracture of the precipitate particle itself or the adjacent matrix but by the lack of cohesion between the two phases.

Holes which must have contained and some which still contain parts of precipitate particles are seen in Fig. 4.19(c). While it is impossible to determine whether the above precipitate particles were spheres or rods [Fig. 4.19(c)], Fig. 4.22(a and b) clearly show a rod extending from the fracture surface, and holes shown in Fig. 4.22(c) may have been caused by similar rods pulled out of that half of the specimen during fracture.

No chemical analysis has been carried out as yet to determine the composition of the rod, and thus one can only speculate as to its origin. Rod-shaped, second phases or rod-like particles such as shown in Fig. 4.22(b) are not unusual in liquid-solid transformations under conditions pertaining

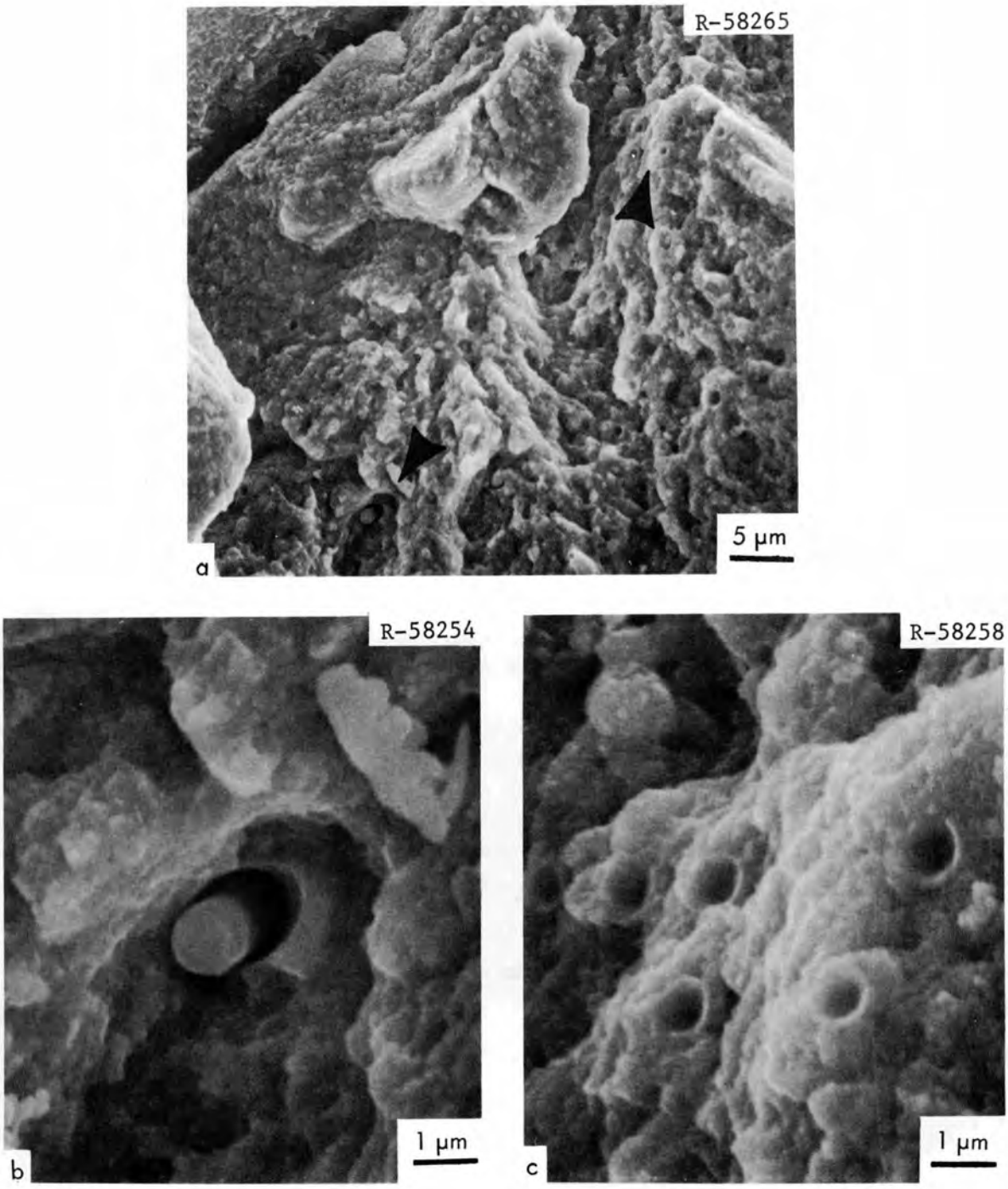

Fig. 4.22. Scanning Electron Micrographs of the Fracture Surface of 304 Stainless Steel Irradiated at 420°C to a Peak Fluence of 13.7×10^{22} neutrons/cm^2 and Tested at Room Temperature Showing (a) a General Area, (b) a Rod, and (c) Holes That May Be Due to Rods.

to unidirectional solidification of eutectics or eutectic-like systems. However, there is virtually no evidence of uniform rods forming as a result of a solid-solid-phase transformation beside the spontaneous growth of whiskers from plated substrates and alloys.[19] The theory of solid-state whisker growth requires dislocations in the substrate which meet the free surface with a component of the Burgers vector perpendicular to the surface. Moreover, a mechanism for the generation of vacancies at the base and transport of vacancies from the base to a sink is required. For such a transport to work, a driving force has to be provided.

It is very unlikely that any rod that may have formed during solidification of the steel may have survived all the deformation processes necessary to produce a safety rod thimble. On the other hand, vacancies necessary for the transport of substitutionally dissolved atoms to the base of the rod are abundantly generated during irradiation. Voids and dislocations surrounding the rod act as sinks for vacancies and may be responsible for a vacancy concentration gradient between them and the base of a rod, thus supplying the driving force necessary to keep the rod growing.

ALUMINUM IRRADIATION DAMAGE

R. T. King A. E. Richt

Because of the wide-spread use of aluminum and aluminum alloys in water-cooled test and isotope production reactors, the effects of neutron irradiation on aluminum alloys continue to be studied. Early work focused attention on tensile properties and the effects of irradiation and postirradiation annealing on the structure and properties of both high-purity aluminum and commercial aluminum alloys used in reactors. Although such work is of fundamental interest, it is necessary for reactor safety analyses and for materials usage in future reactors to understand the effects of irradiation over a range of temperatures on the properties and structures of promising alloys.

---

[19]R. V. Coleman, Met. Reviews, 9, No. 35, 261 (1964).

It is also necessary to characterize the slow strain-rate deformation properties of irradiated aluminum. Presently we cannot creep test a large number of specimens in the reactor, so as a useful alternative we are investigating the postirradiation creep-rupture properties of aluminum alloys. This irradiation and test schedule is most applicable to transient loading conditions for reactor components. A series of experiments has been designed and built, and specimens have been irradiated and evaluated for this purpose. We report here a compilation of the significant creep-rupture results obtained to date from these experiments. Results are presented for the 6061-T6, 5052-0, 8001-0 aluminum alloys irradiated at temperatures ranging from 50 to about 175°C and then tested at 50, 100, or 150°C. The neutron fluences for irradiated specimens range from 0.38 to 1.6 $\times$ 10^{22} neutrons/cm (> 0.82 MeV).

In general, the irradiation-induced strengthening that occurs under these conditions can be attributed to precipitate particles involving transmutation-produced silicon with an unknown contribution arising from the irradiation-induced changes in dislocation structures. At present, the losses of ductility that occur in 8001-0 and 6061-T6 aluminum under these conditions are felt to be largely associated with the strengthening processes. However, the irradiated 5052-0 aluminum specimen that has been tested exhibited very low ductility, and its fracture probably initiated as an intergranular fracture process. This unexpected result casts some doubt on the previous observations that most aluminum alloys were affected by irradiation in similar manners and the matter requires further investigation.

The Effect of Irradiation on the Creep-Rupture Behavior of 5052-0 Aluminum at 50°C

R. T. King D. R. Cuneo A. Jostsons

Irradiation damage in the 5052-0 aluminum alloy (nominally Al—2.5% Mg) is of interest for both engineering and scientific reasons. The alloy is presently in service as a major component of the Oak Ridge Research Reactor (ORR) tank. It is also of interest because, even though magnesium in the

primary aluminum solid solution is supersaturated at low temperatures, the alloy is essentially a solid-solution-hardened alloy with most of the magnesium in solid solution.[20] We were interested in discovering whether the transmutation-produced silicon precipitates out as β-silicon as it does in other aluminum alloys,[21] or whether it combines with the magnesium available in solid solution to form Mg_2Si precipitate particles. The latter has proven to be true.

The chemical analysis of the lot of 5052-0 aluminum used in this experimental program is given in Table 4.6. Standard buttonhead tensile specimens having a 1-in.-long × 0.125-in.-diam gage section were

Table 4.6. Chemical Analysis of 5052-0 Aluminum

Element	Weight Percent
Cr	0.20
Ni	< 0.3
Fe	0.18
Mo	< 0.02
Mn	0.017
V	< 0.01
Ti	0.02
Cu	0.02
Al	Major
Mg	2.2
Pb	< 0.01
Zr	< 0.07
Si	< 0.098

[20] Metals Handbook, 1948 ed., American Society for Metals, Cleveland, Ohio, pp. 820 and 1163.

[21] R. T. King, K. Farrell, and A. Jostsons, Fuels and Materials Development Program Quart. Progr. Rept. June 30, 1971, ORNL-TM-3540, pp. 134–135.

fabricated and annealed to the "0" temper.[22] A set of these specimens was then tested in uniaxial creep-rupture at 50°C. A second set of the specimens was irradiated in the High Flux Isotope Reactor (HFIR) in the aluminum experiment 5 in contact with water at calculated temperatures between 52 and 60°C. The specimens received neutron fluences ranging from 0.52 to 1.33 × 10^{22} neutrons/cm^2 (> 1 MeV). One of the specimens that was irradiated to 0.52 × 10^{22} neutrons/cm^2 at 52°C and tested at 50°C has been examined in detail.

The results of the creep-rupture tests on control specimens are given in Table 4.7. Testing at 25,000 psi stress produced 941.4 and 1966.7 hr rupture times, while testing at 30,000 psi stress caused almost immediate failure. All control specimens exhibited total strains to failure greater than 35%, although much of the strain did occur on loading and during first-stage creep. We have examined the fracture surface of specimen 51-46, which failed after 315.9 hr at 28,000 psi stress, using scanning electron microscopy techniques; it is shown in Fig. 4.23. The fractured end is the "cone" half of a cup-cone fracture, with an 87% reduction of area. The entire surface has the dimple pattern characteristic of transgranular ductile fracture. A stereo light microscope comparison of the fracture surfaces of the other unirradiated specimens with this fracture surface leads to the conclusion that all of the unirradiated specimens failed in essentially the same manner.

The irradiated specimen, on the other hand, was subjected to a series of increasing stresses which caused 0.4% strain and then was allowed to fracture at 52,000 psi in 166.1 hr. The total strain exhibited by the irradiated specimen was 1.15% as measured from the loading train. A strain of 2.4% was measured by fitting the specimen halves together after the test. No measurable reduction of area occurred. This specimen was also examined by scanning electron microscopy techniques, and the results are shown in Figs. 4.24 and 4.25. Fracture appears to have

---

[22] Aluminum Standards and Data, The Aluminum Association, New York, 1968, p. 51.

Table 4.7. Stress-Rupture Properties of 5052-0 Aluminum Alloy at 50°C

Applied Stress (psi)	Minimum Strain Rate (%/hr)	Stage I Creep Strain (%)	Stage II Creep Strain (%)	Stage III Creep Strain (%)	Stage I Creep Time (hr)	Stage II Creep Time (hr)	Stage III Creep Time (hr)	Total Strain to Failure (%)	Total Time to Failure (hr)
20,000								> .87	> 20.2
Raised to 30,000								> 27.9	> 0.1
30,000								28.47	< 0.01
28,000	0.053	23	9.75	12.0	75.0	185	55.9	44.8	315.9
25,000	0.015	17.5	16.0	25.9	150	950	957	59.4	1966.7
25,000	0.023	< 31	18.5		25	810	~100	49.16	941.4
57,000	0.0022	0.4[a]	0.4	0.35	~0	145	21.1	1.15[b]	166.1

[a] Total accummulated during preloading and Stage I creep.

[b] 2.4% measured after test.

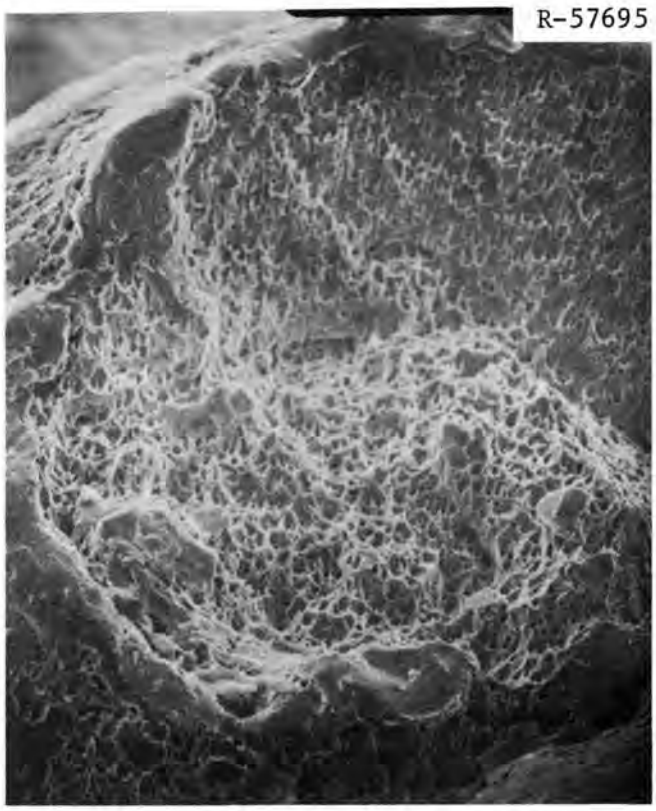

Fig. 4.23. Creep-Rupture Fracture Surface of Unirradiated 5052-0 Aluminum Tested at 50°C. 100×.

initiated near the surface of the specimen and proceeded in an intergranular mode to a depth of perhaps 0.02 in. beneath the surface. The remainder of the fracture is a shear cup-cone fracture exhibiting the characteristic ductile shear dimples, and this portion of the fracture presumably occurred relatively rapidly under the higher stress caused by the reduction of the load-bearing cross section. The result may indicate a transition from intergranular fracture at slow strain rates to transgranular fracture at rapid strain rates under these irradiation and testing conditions for this alloy.

This is the first observation of intergranular fracture in any irradiated aluminum alloy at 50°C and it is significant because it may alter our present picture of irradiation damage to aluminum alloys. We had previously observed the consistent pattern for the 1100, 6061,

Fig. 4.24. Creep-Rupture Fracture Surface of 5052-0 Aluminum Irradiated to 0.52×10^{22} neutrons/cm^2 (> 1 MeV) at 50°C and Tested at 50°C. The fracture is predominantly intergranular near the outside surface of the specimen (upper left) and predominantly a transgranular fracture near the center (lower right). 100×.

and 8001 aluminum alloys that irradiation-induced strengthening was responsible for ductility losses observed below about half the absolute melting point of aluminum (about 200°C) and that the fractures in this range were always ductile and transgranular. At higher temperatures helium embrittlement was thought to be responsible for ductility losses by causing premature intergranular fracture. This result for irradiated 5052-0 aluminum clearly does not fit that established pattern. We will pursue the matter by further testing of irradiated specimens and by optical and electron microscopy of the fractured specimens. Initial transmission electron microscopy performed on the unstressed portion of the irradiated specimen has revealed the presence of a fine uniformly distributed β' Mg_2Si precipitate which is responsible for the irradiation induced strengthening.

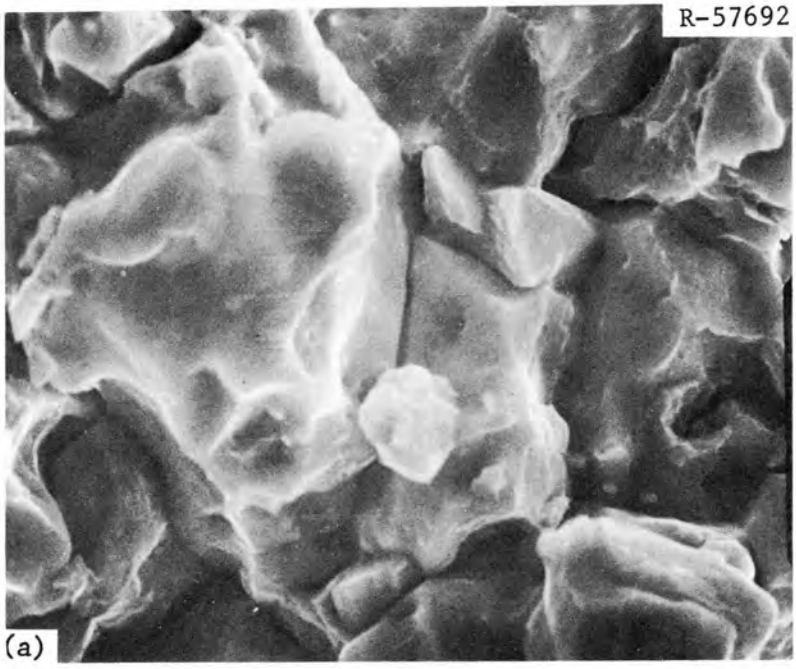

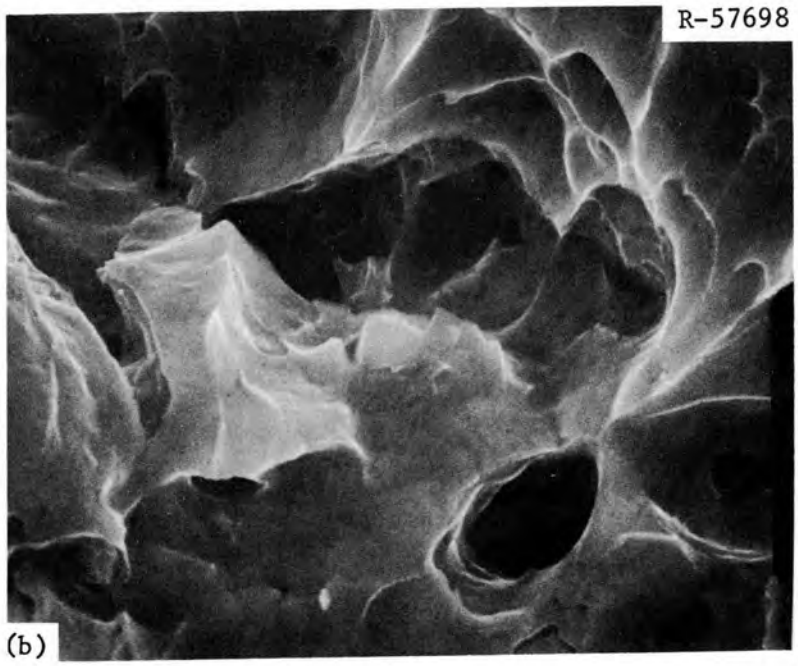

Fig. 4.25. Closeup View of (a) Intergranular Fracture Region and (b) Ductile Fracture Region of Irradiated 5052-0 Aluminum Specimen. 1000×.

Structure and Properties of the Age-Hardened 6061-T6 Aluminum in the Irradiated Condition

R. T. King K. Farrell A. Jostsons

Preliminary microstructural analyses and mechanical properties of 6061 aluminum irradiated in the High Flux Isotope Reactor (HFIR) have been reported previously.[23,24] The Mg_2Si precipitate-hardened 6061 alloy in the fully age-hardened (-T6) condition was included in the HFIR 3 and 4 aluminum experiments, in which it was irradiated in helium at temperatures ranging from 160 to 175°C (Ref. 25). Both irradiated specimens and unirradiated control specimens were then tested in uniaxial creep-rupture tests at 100 and 150°C. In this report, the data for all 6061-T6 specimens included in those experiments is summarized.

In addition, other 6061-T6 aluminum specimens were irradiated in contact with water at 60°C in the HFIR 5 aluminum experiment. These specimens were tested in uniaxial creep rupture at 50°C.

Figure 26 shows the stress-rupture time results for the tests performed on both irradiated and unirradiated specimens. Frequently, the stress chosen for the testing of irradiated specimens was not large enough to produce rupture in a reasonable time; for such tests, the stress that produced the greatest amount of deformation is plotted together with the deformation that occurred under that stress with arrows to indicate that longer test times or large strains might have resulted had the test been conducted entirely at that stress. Because the

---

[23]R. T. King, Fuels and Materials Development Program Quart. Progr. Rept. March 31, 1971, ORNL-TM-3416, p. 104.

[24]R. T. King, Fuels and Materials Development Program Quart. Progr. Rept. December 31, 1970, ORNL-TM-3300, p. 277.

[25]See the discussion of the irradiation temperatures in "The Effect of Irradiation and Test Temperature on the Structure and Properties of an Annealed Solid-Solution Aluminum Alloy," this chapter.

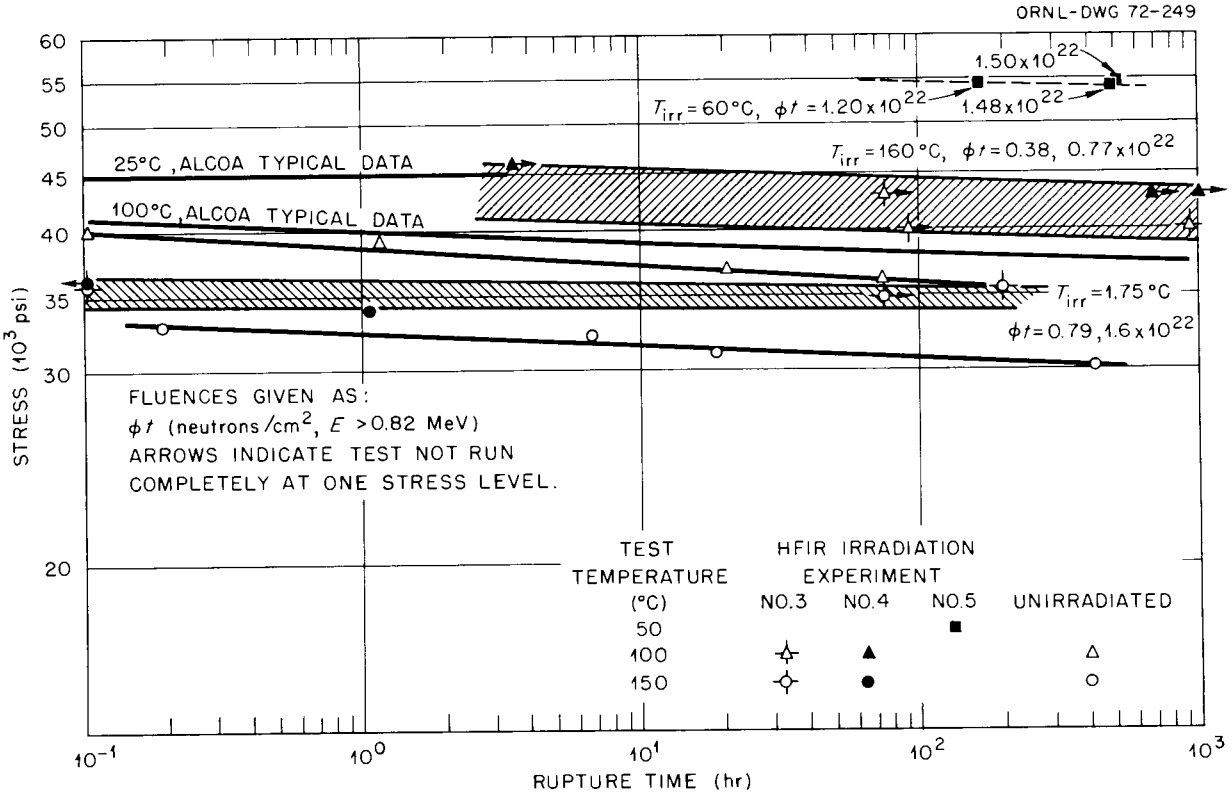

Fig. 4.26. Stress-Rupture Properties of 6061-T6 Aluminum.

neutron fluences for experiment 3 were half the fluences for the specimens in the corresponding positions of experiment 4, it is a straightforward task to assign the proper neutron fluence for each datum on the graph from the information given on the graph. Alcoa data[26] is being used for 50°C control data until our own testing program is complete.

Figure 26 shows that for all the combinations of irradiation and test temperatures employed irradiation-induced strengthening occurred. Electron microscopy investigations of specimens irradiated at even the higher temperatures have shown that the Mg_2Si precipitate structure

---

[26] Alcoa Research Laboratories Typical Mechanical Properties at Various Temperatures for 6061-T6, -T651, and -T611, Elevated Temperature Data Sheet, June 18, 1970.

responsible for strengthening in the unirradiated alloy is stable during irradiation. In addition, transmutation-produced silicon precipitates form during irradiation, together with possible but undefined changes in the dislocation structure. The combined effects of these irradiation-induced structural changes are currently thought to be responsible for the strength increases which occur in this alloy.

The effect of irradiation on the strain to fracture of irradiated and unirradiated specimens is shown in Fig. 4.27. In both cases, the fracture strains tend to decrease with increasing rupture time in tests

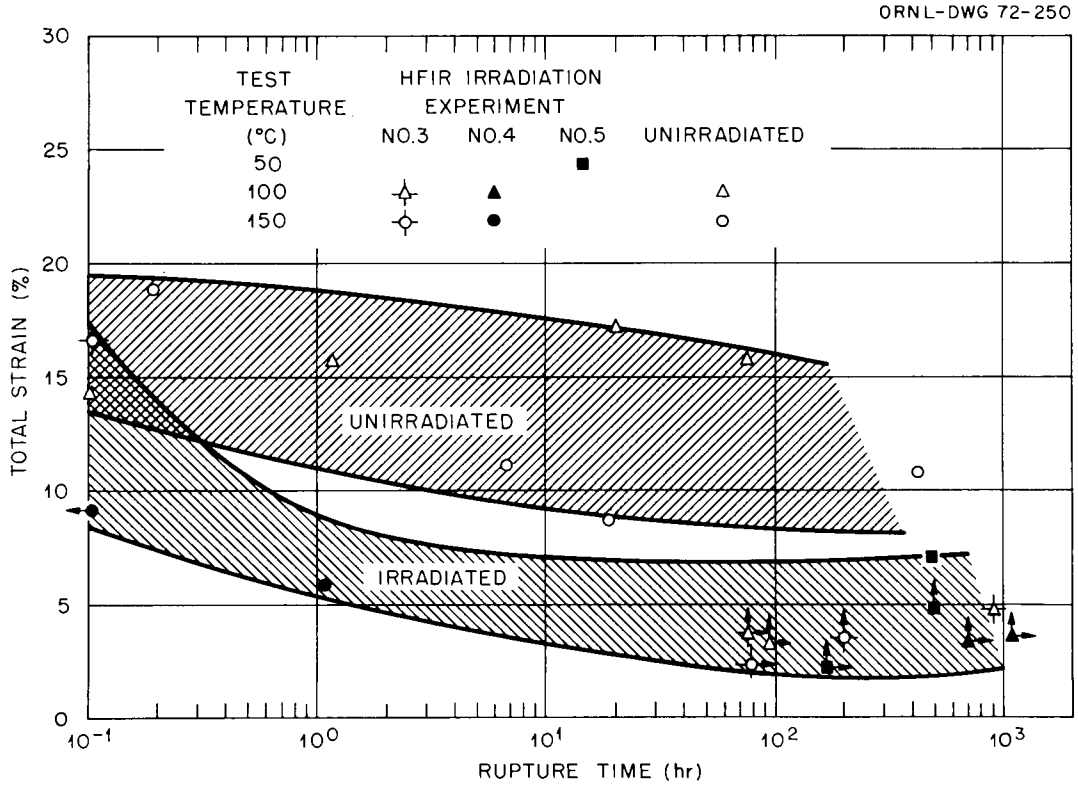

Fig. 4.27. Fracture Strain of 6061-T6 Aluminum.

approaching 1000 hr duration. However, the fracture strains of the irradiated specimens tend to be greater than 10%, and those of the unirradiated specimens tend to be smaller than 5% except in short-term tests. The most important fact, however, is that the fracture strains

are always greater than 2%, even for specimens irradiated to fluences in excess of 1×10^{22} neutrons/cm^2 (> 0.82 MeV). Because of the widespread use of 6061 aluminum in modern water-cooled reactors, it is of great interest to reactor safety personnel to find that major 6061-T6 aluminum reactor structural components should be able to deform small amounts plastically without fracturing under these conditions.

The Influence of Irradiation on the Structure and Properties of an Annealed Solid-Solution Aluminum Alloy

R. T. King A. Jostsons K. Farrell

We have previously reported[27] preliminary results on the effect of irradiation in the High Flux Isotope Reactor (HFIR) upon the microstructure and properties of the solid-solution 8001 aluminum alloy in the annealed or "0" temper.[28] This work has been extended by further testing of specimens from the same experiments, the HFIR 3 and 4 aluminum experiments. The irradiation conditions for those experiments were discussed in the earlier report. The environment was helium, and the specimen irradiation temperatures ranged between approximately 140 and 175°C. These specimens were tested under uniaxial creep-rupture conditions in an argon atmosphere at test temperatures of 100 and 150°C. (It was originally planned to test specimens at nearly the same temperatures at which they were irradiated, based on the calculated irradiation temperatures.) The irradiation-induced microstructural changes observed by transmission electron microscopy indicated that the calculated temperatures were too low by as much as 50°C. (The temperatures reported here are 50°C higher than the calculated temperatures.)

---

[27]R. T. King, Fuels and Materials Development Program Quart. Progr. Rept. March 31, 1971, ORNL-TM-3416, p. 104.

[28]Aluminum Standards and Data, 1968–1969, The Aluminum Association, New York, April 1968, p. 51. Treatment recommended for 1100-grade aluminum.

A second series of experiments, the HFIR 5, 6, 7, and 8 experiments, has yielded 8001 aluminum alloy specimens which were irradiated in water at 55°C. Some of these specimens have been returned to the reactor for further irradiation; however, one specimen was uniaxially tested in creep rupture to yield data for irradiation and test temperatures below those investigated in the HFIR 3 and 4 experiments.

The stress-rupture time results for all of the tests that have been run are summarized in Fig. 4.28. Irradiation-induced strengthening was always observed for irradiation at neutron fluences in excess of

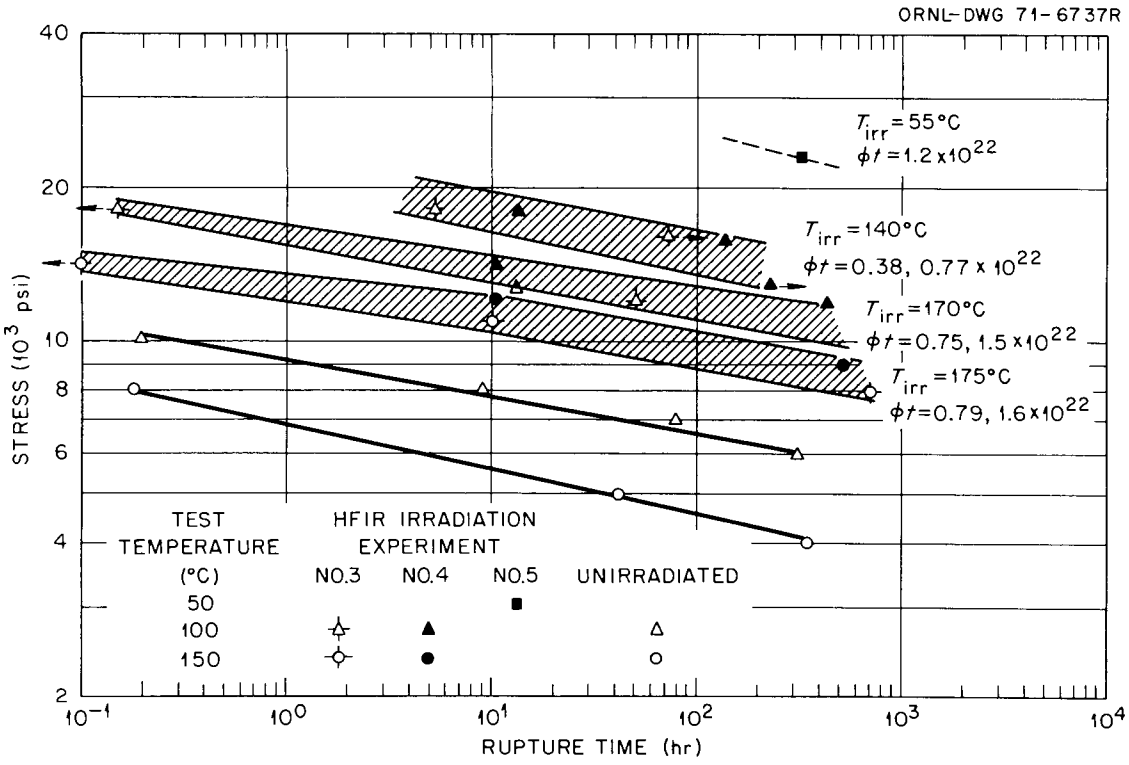

Fig. 4.28. Creep Rupture of Annealed 8001 Aluminum.

0.38 × 10^{22} neutrons/cm^2 (> 0.82 MeV). For any given irradiation temperature, doubling the neutron fluence produced relatively small increases in the rupture time compared to the changes related to irradiation and test temperature. The results are, therefore, represented by scatterbands

for each irradiation temperature. In general, the results show that as the combination of irradiation temperature and test temperature is decreased in the range 50 to 175°C, the rupture times for irradiated specimens increase.

The effect of irradiation on the fracture strain is shown in Fig. 4.29. The unirradiated 8001 aluminum alloy exhibits ductilities exceeding 50% total elongation in tests lasting up to several hundreds of hours.

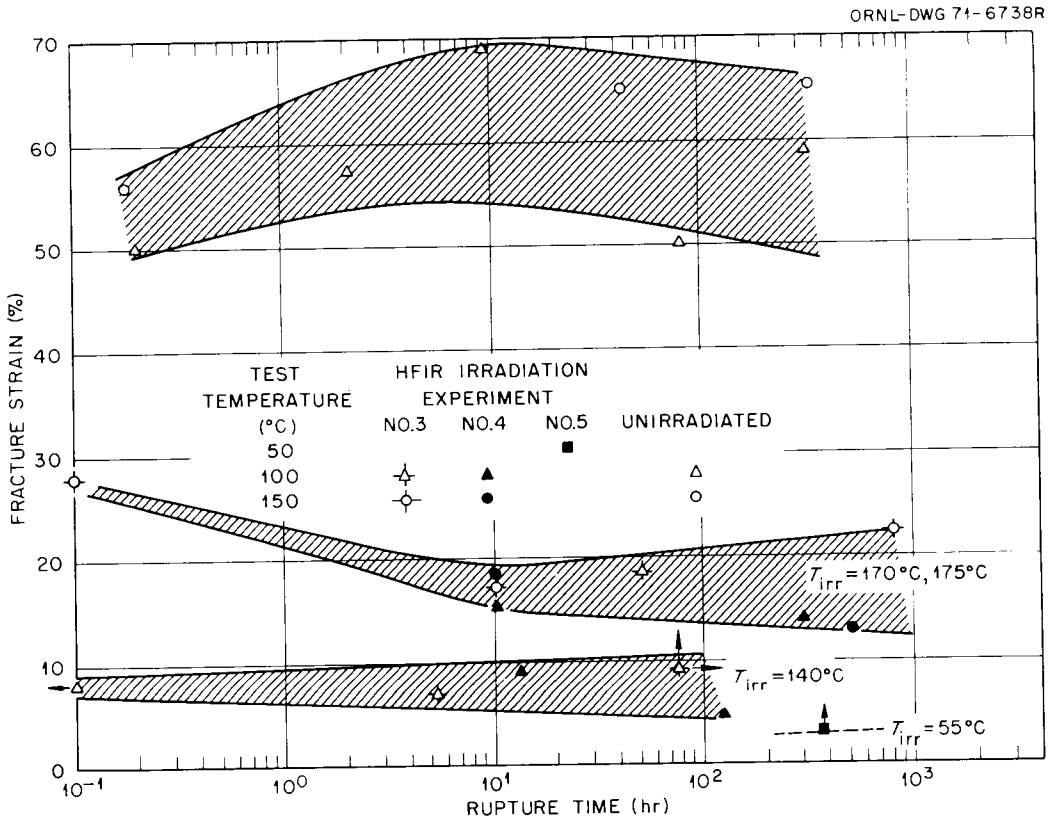

Fig. 4.29. Fracture Strain of Annealed 8001 Aluminum.

Irradiation at 170 or 175°C reduced the ductility measured at 100 and 150°C test temperatures to the 12 to 28% range. Irradiation at 140°C reduced the fracture strain measured at 100°C to the 4 to 10% range. The specimen irradiated at 55°C and tested at 50°C exhibited only 2.9% strain to fracture. The arrow on the figure indicates that the

specimen was first subjected to smaller stresses than the 23,500 psi stress under which it fractured; it strained about 1% under those smaller stresses. Thus, with decreasing irradiation and testing temperature over the range investigated, there is a pronounced reduction in the fracture strain of 8001 aluminum.

In Fig. 4.30, the stress required to cause a given minimum strain rate during second-stage creep is shown to be increased by neutron irradiation. In general, the greatest increases in strength occur for the lower irradiation temperatures and test temperatures.

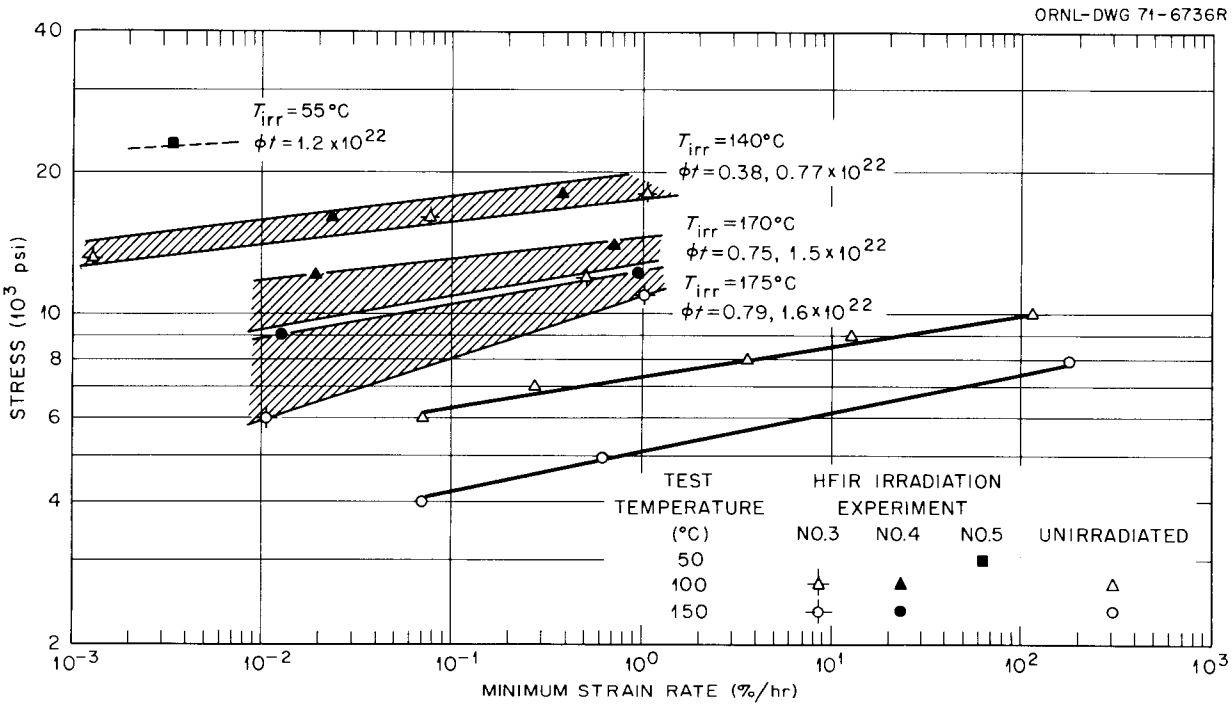

Fig. 4.30. Minimum Strain Rate of Annealed 8001 Aluminum.

These results are consistent with the hypotheses which we presented earlier to explain the effects of neutron irradiation on the properties of solid solution alloys in this range of irradiation and test temperatures.[27] Transmutation-produced silicon precipitate particles appear to be responsible for most of the strengthening which is observed.

Dislocation loops formed during irradiation may also contribute to strengthening. In the 140 to 170°C irradiation temperature range, voids do not form readily at the neutron fluences investigated. However, it is likely that voids were formed during the 50°C irradiations, and this is being investigated by transmission electron microscopy. The precipitate particles form during neutron irradiation, and their number density and size are strongly governed by the irradiation temperature. Increasing the irradiation temperature produces coarser distributions of larger particles which are less effective obstacles to dislocation motion. Hence, the minimum strain rate generally tends to be decreased by decreasing the irradiation temperature. Comparing the results for specimens irradiated at 170 to 175°C, but tested at either 100 or 150°C, demonstrates that the strain rate of irradiated 8001 aluminum is increased by increasing the test temperature as one might expect. Although only a limited amount of metallography has been performed on these specimens, there is no indication that other than transgranular fracture occurs for these irradiation and test conditions. Hence, it seems unlikely that helium is important in reducing the ductility under these conditions by its usual role of promoting intergranular fracture. The loss of ductility after irradiation is most probably linked to the increased strength and irradiation-induced changes in the work-hardening characteristics of the alloy.

5. FABRICATION DEVELOPMENT FOR FBR CLADDING

G. M. Adamson, Jr. A. C. Schaffhauser W. R. Martin

Our effort is currently directed toward a better evaluation of the effects of defects on the properties of unirradiated and irradiated type 316 stainless steel tubing.

Effect of Fabrication Variables

Biaxial Stress-Rupture Properties of 20% Cold-Worked Type 316 Stainless Steel Tubing Containing Altered Notches (R. T. King, K. V. Cook, G. A. Reimann)

The process of making sharp (approx 0.1 mil wide) longitudinal notches in tubing by electrodischarge machining notches into a tube shell and then drawing the tube shell to tubing has been detailed previously.[1] We have tested batch BA1-6 20% cold-worked type 316 stainless steel tubing containing 0.25-in.-long × 0.0001-in.-wide altered notches fabricated in this manner; some early test results were reported in the last quarterly report.[2] Nearly all of the specimens fabricated for this study have now been tested at 650°C under biaxial stress-rupture conditions. The tubing specimens were 4 in. long with a 0.25-in. OD × 0.0155-in. wall thickness. Before testing, they were sealed with trepanned stainless steel end plugs which were welded to the tubes. Included in this study are control specimens and specimens bearing 0.0002-, 0.0005-, and 0.0014-in.-deep altered notches. The 0.0002-in.-deep notches are below the resolution limit of the ultrasonic-detection equipment, and their presence is assumed on the basis of larger size defects which were introduced into the tube shell. All tests were performed in a He–1% O_2 atm with helium or argon as a pressurizing agent.

The results of the tests are presented in Table 5.1. The control specimens were tested at internal presssures calculated to produce nominal

---

[1]K. V. Cook, G. A. Reimann, and R. W. McClung, Fuels and Materials Development Program Quart. Progr. Rept. June 30, 1971, ORNL-TM-3540, p. 80.

[2]R. T. King, G. A. Reimann, and K. V. Cook, Fuels and Materials Development Program Quart. Progr. Rept. Dec. 31, 1971, ORNL-TM-3703, p. 138.

Table 5.1. Tests on 20% Cold-Worked Type 316 Stainless Steel Tubing with 0.25-in.-Long Altered Notches and Control Tubing Without Notches (Tests at 650°C)

Specimen Number	Notch Depth (in.)	Nominal Hoop Stress (psi)	Rupture Time (hr)	Circumferential Strain		Note
				Near Fracture (%)	Failed Specimens At Weld or Near End Cap (%)	
X-7		30,000	608.4	0.8		Pinhole 3/16 in. from weld
X-8		35,000	297.5		2.8	Failure point not obvious
X-9		40,000	60.8	6.4		Split open
X-10		Not tested yet				
Y-6		Not tested yet				
Y-7		35,000	a			
Y-8		32,500	>316.2		1.6	End cap leak
Y-9		35,000	>70.9		0.8	Pinhold near botton end
Y-10		30,000	>133.8	3.2		Failed in gage near bottom end
Z-6		Not tested yet				
Z-7		40,000	>9.9		0.4	Weld failure
Z-8		30,000	a		1.2	
Z-9		35,000	69.1	6.8		Good rupture
Z-10		Not tested yet				
X-1	0.0002	40,000	2.6		0.8	End cap weld
X-2	0.0002	30,000	822.4[a]			
X-3	0.0002	35,000	377.9 (+282?)[a]	3.6		Failed at notch
X-4	0.0002	35,000	>144.7	3.2		Failed ~1/4 in. from weld
X-5	0.0002	Not tested yet				
X-6	0.0002	37,500	>167.5	2.8		Failed ~1/4 in. from weld
Y-1	0.0005	32,500	82.4	~1.5		Failed at notch
Y-2	0.0005	35,000	>40.1		0.6	Failed under end ring
Y-3	0.0005	30,000	548.9	3.0		Failed at notch
Y-4	0.0005	40,000	>1.7		0.6	Failed at weld
Y-5	0.0005	Not tested yet				

Table 5.1 (continued)

Specimen Number	Notch Depth (in.)	Nominal Hoop Stress (psi)	Rupture Time (hr)	Circumferential Strain		Note
				Near Fracture (%)	Failed Specimens At Weld or Near End Cap (%)	
Z-1	0.0014	30,000	a			Failed near weld
Z-2	0.0014	35,000	a		0.9	Split near end cap
Z-3	0.0014	Not tested yet				
Z-4	0.0014	40,000	>2.3		0.9	Failed at weld
Z-5	0.0014	Not tested yet				

[a]Because of frequent bleed-downs and repressurization, the failure time is not well characterized.

hoop stresses ranging from 30,000 to 40,000 psi. The rupture times are recorded in Table 5.1. Several specimens leaked slowly, so that they spent a large fraction of the test period at stresses of less than 90% of the nominal hoop stress; these specimens are identified in Table 5.1. The circumferential strain was always measured a short distance away from the fracture for specimens which failed in the gage length away from the end-cap region. Specimens which failed at the end-cap region and specimens which failed at the end-cap weldment were sampled along their length to assess the maximum circumferential strain which occurred anywhere along the length of the specimen. Because many specimens failed at or near the end cap, we have noted the type or location of failure which occurred for each specimen. These premature failures are caused by either deviations from specified previous welding practices, which cause large heat-affected zones to occur in the tubing, or by damage to the tubing during the insertion of the end plugs. Some of these specimens were tested with a tight-fitting 0.75-in.-long sleeve at the ends of the specimen to reduce bending stresses at the welds and prevent failure at the welds. Nearly all of the specimens were restrained from longitudinal deformation by a yoke-and-collar device. Neither of these devices was satisfactory in preventing specimens from failing near weld joints or end caps.

The rupture time versus stress data are plotted in Fig. 5.1. Arrows indicate tests which might have lasted longer had failure occurred in the center of the specimen gage length. The data may be used to indicate roughly where a strain-versus-rupture-time curve might lie in the absence of the experimental difficulties mentioned above. Rupture times for central specimens might range from about 70 hr at 40,000 psi to about 700 hr at 30,000 psi. There is no well-defined effect of notches on rupture life because of the premature failures which occurred away from the notches. Specimen X-3 with its predicted 0.0002-in.-deep notch lasted longer than the comparable control specimen, but specimens Y-3 (0.0005-in.-deep notch) and Y-1 (0.0005-in.-deep notch) failed after shorter times than comparable control specimens. We plan to reseal and retest several of the specimens which failed near end caps or welds; some tubes are presently ready for retesting.

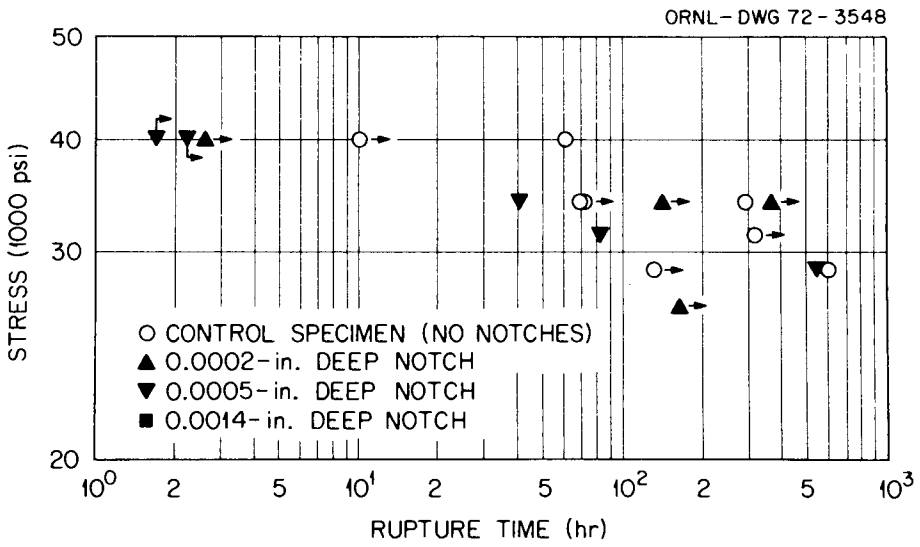

Fig. 5.1. Stress-Rupture Behavior of 20% Cold-Worked Type 316 Stainless Steel Tubing from Altered Notch Study.

Despite the experimental difficulties which have beset this program, there is evidence that the sharp notches should be effective in degrading the properties of this tubing. Clearly, specimens X-3 (0.0002-in.-deep notch), Y-3 (0.0005-in.-deep notch), and Y-1 (0.0005-in.-deep notch) failed at these artificially induced defects. We showed a photomacrograph as evidence for the mode of failure of specimen X-3 in the last quarterly report, and specimen Y-3 failed in an identical manner. Specimen Y-1 leaked gas from a pinhole rupture at the notch location when it was repressurized after the tests. We discontinued the test on specimen Z-1 after testing for 800 hr at pressures below 30,000 psi (the specimen leaked gas constantly). The location of the 0.0014-in.-deep notch in this specimen was determined ultrasonically and the specimen was sectioned for metallographic examination within the 0.25-in. length of the notch. Figure 5.2 shows that the original 0.0001-in.-wide notch has separated extensively, and more extensive intergranular separation has occurred beneath the notch than elsewhere in the specimens. There is every reason to believe that such rapid local deformation would have led to a premature fracture at the notch in the absence of the testing problems.

Fig. 5.2. Cross Section Showing Notch in Specimen Z-1; the Specimen Failed Near Weld Rather Than at the Altered-Notch Region Shown Here.

As-Machined Notch Studies (K. V. Cook, R. W. McClung)

The primary objective of the as-machined notch study is to establish the effects of flaws of various sizes [simulated by electrodischarge machined (EDM) notches] on the mechanical properties of 1/4-in.-OD type 316 stainless steel tubing. Notches such as these are normally used to establish test sensitivity for both ultrasonic and eddy-current tests and are as narrow as we can machine them at the present time (0.0023 in.).

Further work on three tubes designated 065219-4A of ultrafine grain was deleted because of program direction changes.

Fifty-eight, 4-in.-long, tube-burst specimens were prepared from four 1/4-in.-diam, 8-ft-long, ORNL fabricated tubes labeled BA1-2-20, -21, BA1-3-32, and -33. Inner surface longitudinal notches 0.030 in. long were machined in BA1-2 tubes; however, the notch length was increased to 0.250 in. for the BA1-3 material. Inspection data and charts are stored in Room D-54, Building 4500S, in file cabinet USAEC-OE-3840.

Altered-Notch Studies (K. V. Cook and R. W. McClung)

The primary objective of the altered-notch study is to establish methods for fabricating artificially produced flaws in tubing to resemble natural defects. These simulated flaws are being used in studies involving the fabrication, inspection, and mechanical properties groups to evaluate and upgrade tubing fabrication and inspection methods as well as to establish the effect of the simulated flaws on mechanical properties.

The mechanical properties group has two different batches of altered-notch specimens which we prepared. The first batch was prepared by tube drawing on a BA1-1 schedule and consists of a total of thirty 4-in. specimens. Three different depth notch specimens are included in the first batch. These are nominally 0.0002, 0.0005, and 0.0015 in. Figure 5.3 shows in cross section one of the nominal 0.0005-in.-deep altered notches (which had been placed on the tube inner surface). This

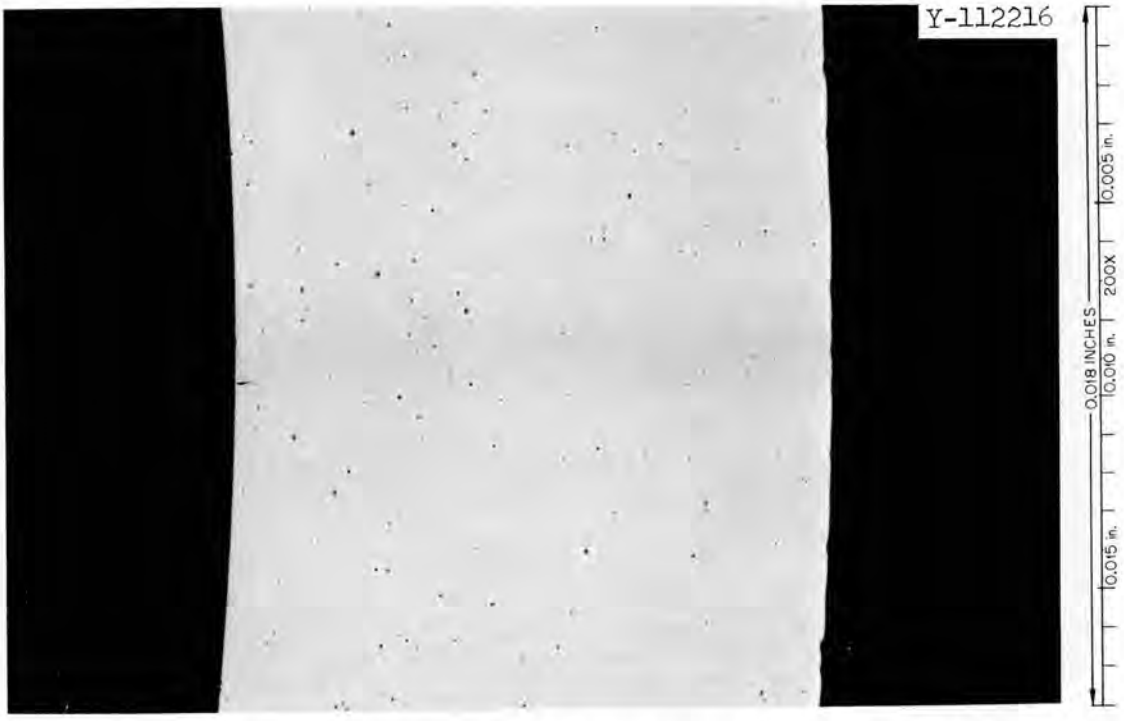

Fig. 5.3. Cross Section of a Nominal 0.0005-in.-Deep Altered Notch Placed on the Inner Surface of a Tube Drawn on a BA1-1 Schedule.

notch certainly simulates a natural flaw since the width is less than 0.0001 in. and the depth is approximately 0.0007 in. In fact, the notch width is so narrow that it was only marginally detectable by a high-sensitivity, fluorescent-penetrant inspection.

Figure 5.4 shows one of the 0.0014-in.-deep-ID notches in cross section that had been partially tested to failure. Note that the notch is much wider than that of Fig. 5.3, and that the inner surface has noticeably deformed. The notch depth has also increased due to the pressure test. Unfortunately our metallographic specimen of a 0.0014-in.-deep altered notch (which had not been pressure tested) was lost in the cutting operation. This loss was apparently caused when the notch, which was initially placed on the thin-wall side of the tube, was not in the thin section after the tube-drawing procedure.

A second batch of 22 altered-notch specimens has been prepared and nondestructively evaluated to locate the exact linear notch positions and their relation to the wall thickness. Part of the notches was found to be as much as 135° around the tube from the thin side Fourteen of the specimens were prepared with a tube-drawing schedule BA2-1. The other eight were prepared by sinking a 0.295-in.-OD × 0.015-in.-wall tube to a 0.250-in.-OD × 0.015-in.-wall tube. All of the notches in this batch are located on the inner surface, and are approximately 0.0015-in. deep.

Fig. 5.4. Cross Section of an Altered Notch Placed on the Inner Surface of a Tube Drawn on a BA1-1 Schedule. The notch was originally 0.0014-in. deep, but the depth is increased due to partial failure during tube-burst testing. 100×.

6. COMPATIBILITY OF STEAM GENERATOR MATERIALS

P. Patriarca J. R. Weir, Jr.

Steam Corrosion of Advanced Steam Generator Materials

G. M. Slaughter

The purpose of this program is to investigate the corrosion behavior of steam generator alloy weldments. Special emphasis is placed upon materials for LMFBR steam generator use and stress corrosion as the mode of failure.

The program currently includes two areas of investigation: (1) general corrosion (uniform scaling, including internal oxidation and localized attack at weld-fusion lines) at 480 and 595°C (900 and 1100°F), and (2) stress-corrosion cracking (induced by chloride or caustic as contaminants) in steam environments that include superheated conditions and cycling between the superheated and water-saturated states.

Stress-Corrosion Cracking (J. P. Hammond)

Construction and Operation of Loops. — Southern Nuclear Engineering, Inc., recently began fabrication of the Inconel 625 corrosion loop developed for investigating stress corrosion with caustic as the contaminant. Manual welding of Inconel 625 by the gas tungsten-arc process proved to require a higher degree of process control than had been needed for type 316 stainless steel and Incoloy 800, materials of construction employed for the first and second corrosion loops. Welding operations were facilitated by developing a weld insert of rectangular cross section for the root passes and performing all of the welding operations in the horizontal (pipe axis vertical) position. We now contemplate that the caustic-injection corrosion loop can be completed and readied for stress-corrosion testing by the end of September, 1972.

After completion of run 7 in the Incoloy-800 chloride-injection corrosion loop,[1] a loop-environmental analysis was made of the conditions that exist in the autoclaves during testing. The results of this analysis are discussed subsequently. Upon termination of this analysis, another crack was discovered in the loop. Whereas the first crack, discovered approximately nine months earlier, occurred in a transverse position between two welds adjacent to the second "U" fitting,[2] this one occurred longitudinally between two welds in the first "U" fitting approximately 5 ft downstream from the point of chloride injection. Repairs were accomplished in a manner similar to that used for the first crack (filing out the crack with a rotary file and welding with an Incoweld-A stick electrode). Stress relief of the weld area was done by prolonged heating at 693°C (1280°F).

After only one week of run 8 in this facility a third crack was found. It was in the last "U" fitting of the loop and, being very small, was repaired easily by previous techniques.

Pipe and fittings of 9 Cr–1 Mo steel for fabrication of a backup loop for the chloride-corrosion program are on hand at Southern Nuclear Engineering, Inc. Fabrication of this loop is anticipated after termination of the present corrosion run 8. At this time the replaced loop will be subjected to a destructive analysis for determination of the character of corrosion attack prevailing within it.

Test conditions employed in run 8 of the chloride-injection loop are as for runs 6 and 7 with 20 ppm O and 10 ppm NaCl as the contaminants. Test specimens include both the usual U-bend strip specimens and a more limited quantity of the tubular test specimens presently being developed for more closely simulating the geometry of steam-generator components. Included in the latter category of specimens are welded and nonwelded tubes in several prominent heat-exchanger alloys as well as a number of commercially-furnished test specimens.

---

[1]J. P. Hammond, Fuels and Materials Development Program Quart. Progr. Rept. Dec. 31, 1971, ORNL-TM-3703, pp 142–150.

[2]J. P. Hammond, Fuels and Materials Development Program Quart. Progr. Rept. Sept. 30, 1971, ORNL-TM-3550, pp. 136–137.

These commercial specimens represent demonstration tube-to-tube sheet joints of Incoloy-800 tubing to an Inconel-82 tube-sheet overlay. The U-bend specimens include a number of new alloys together with a series devised to examine the significance of such experimental variables as the amount of work, whether or not it is welded, and the orientation of the metal-working directions.

Environmental Analysis on Chloride-Injection Steam-Corrosion Loop. — The primary purpose of the environmental analysis conducted on the chloride loop was to determine the amount and location of moisture in the two test autoclaves of the loop as functions of time during the saturation phase of the cyclic testing. Other objectives were to determine the water levels accumulating in the bottom of the autoclaves and to assess the sodium chloride concentrations in both the steam and the entrained water. A schematic of the chloride-injection, steam-corrosion loop is shown as Fig. 6.1.

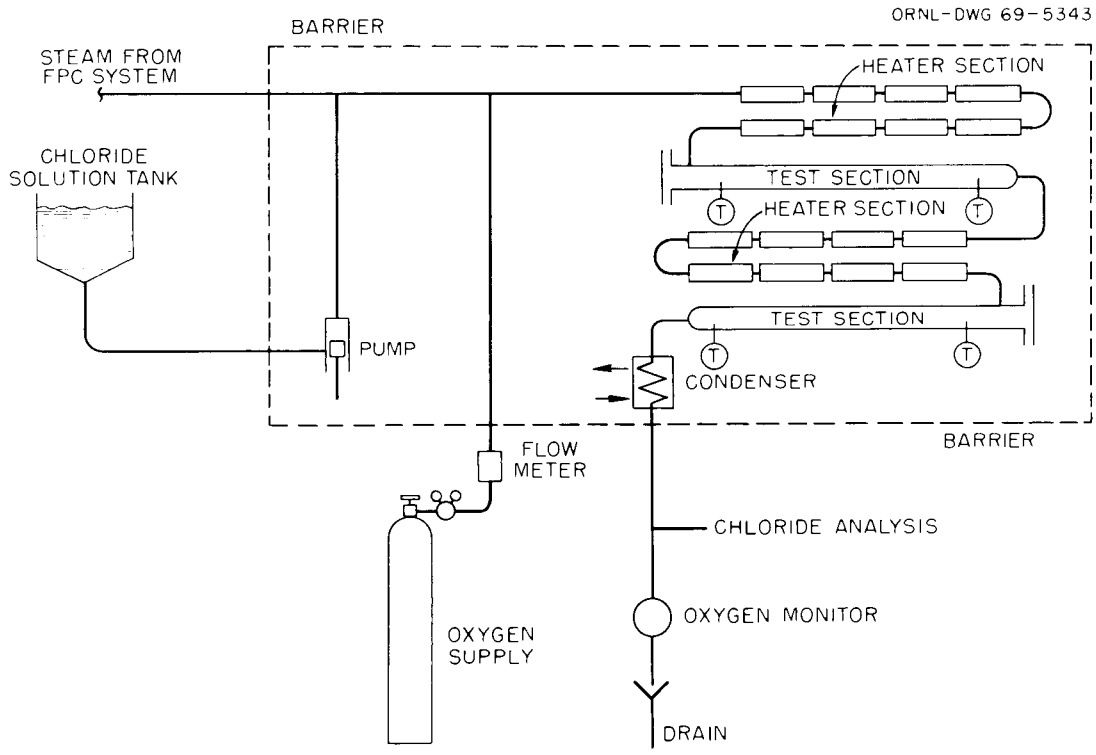

Fig. 6.1. Chloride and Oxygen "Additive" Loop-Schematic.

Since the last three test runs (6–8) were conducted under identical operating conditions and since they contained a large variety of test materials, the environmental analysis was conducted under comparable conditions. These conditions are described as follows:

Steam flow (at saturation temperature)	100 lb/hr
Loop pressure	900 psig
Superheat temperature	427°C (800°F)
Steam-saturation temperature	282°C (540°F)
Oxygen content (continuous)	20 ppm
Sodium-chloride content (during saturation phase of cycle only)	10 ppm
Testing cycles (at saturation)	Three per week of 24-hr duration followed by 24 hr at superheat (except 48 hr at superheat on weekends)

The 100-lb/hr steam flow at the saturation temperature consists of 84.2 lb/hr of steam introduced continuously as superheated [370°C (700°F)] makeup steam (routed from a superheater at the power installation) plus 15.8 lb/hr of saline water introduced into the loop at the time of temperature decrease to saturation for the purpose of introducing dissolved sodium chloride in the steam. During the superheat phase of cycling, saline water is not injected (sodium chloride in the steam during this phase results from dissolution of any solids that may exist on the walls of the loop) and the flow here is 84.2 lb/hr. Oxygen at the indicated concentration is injected for the entirety of the test cycle.

In determination of the amount of moisture in the steam at saturation, two basic assumptions were made: (1) the water phase of the steam-water mixture contains practically all of the input sodium chloride, and (2) the water concentrates almost entirely at the bottom of the autoclaves. The latter view is reasonable since the velocity of the fluid flow was judged to be not more than about 2 ft/sec.

Samples of 150 ml volume were taken from the autoclave (5 lb/hr rate) at various times during the saturation sojourn. These were condensed and analyzed for sodium chloride content by the mercurimetric titration

method. The samples were taken at a distance 4 ft into the interior of the autoclave, first at a position one-third of the diametrical distance from the top of the autoclave and then at the bottom of the autoclave. After gathering data on the top autoclave, the procedure was repeated for the bottom one. A sketch of the apparatus used for taking samples is shown in Fig. 6.2.

The percentage of moisture contained in an autoclave was calculated by making two additional assumptions: (1) samples taken from the autoclaves at the bottom position consists solely of liquid, and (2) the chloride content of samples taken represents equilibrium conditions, that is, they would not contain chloride originating from previously deposited solid salt. The moisture content in an autoclave at a given time during the saturation phase of cycling then was obtained from the following equation:

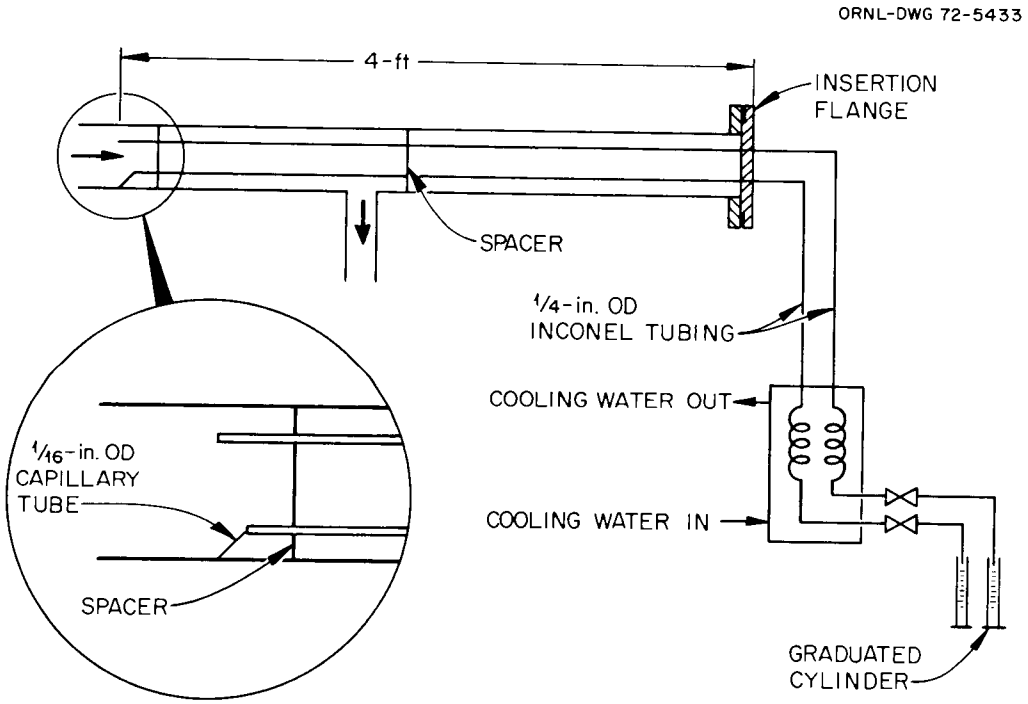

Fig. 6.2. Sketch of Apparatus Used for Collecting Samples from Autoclaves.

$$\text{Moisture Content (wt \%)} = \frac{\text{Water Flow (lb/hr)}}{\text{Total Fluid Flow (lb/hr)}} \times 100$$

$$= \frac{15.8 \text{ lb/hr} \left(\frac{64.2 \text{ ppm}}{\text{NaCl ppm}}\right)}{100 \text{ lb/hr}} \times 100 .$$

where the 64.2-ppm value is the chloride content of the injected saline solution and sodium chloride is the chloride content of the sample taken at the bottom sampling position.

The calculated amounts of moisture (the inverse of steam quality) obtained as a function of time during the saturation phase of cyclic testing are given for the upper and lower autoclaves in graphs as shown in Figs. 6.3 and 6.4, respectively. Superimposed on these curves is a dashed horizontal line representing the quantity of saline water injected into the loop for introducing dissolved sodium chloride. The averaged values of the sodium-chloride concentrations in the upper and lower positions of the autoclaves during the portions of the saturation phase for which saline-equilibrium conditions were judged to be attained are listed below:

Top Autoclave	
Top position,	0.11 ppm
Bottom position,	44.4 ppm
Bottom Autoclave	
Top position,	0.14 ppm
Bottom position,	50.3 ppm

The main purpose for determining the depth of water in the autoclaves was to establish how high the water would stand on the corrosion specimens during the saturation phase of the cycling. The U-bend stress-corrosion specimens are held in fixtures which locate the most highly stressed regions at a distance of 1/16 (0.062) in. from the bottom of the autoclave.

Water levels in the autoclaves were determined as a function of water flow rate by introducing water into a tube arrangement which duplicated the autoclave pipe both in dimensions and slope. The depth of the water was measured with a micrometer head containing a sharp-pointed travel piece. The results of these measurements are listed below.

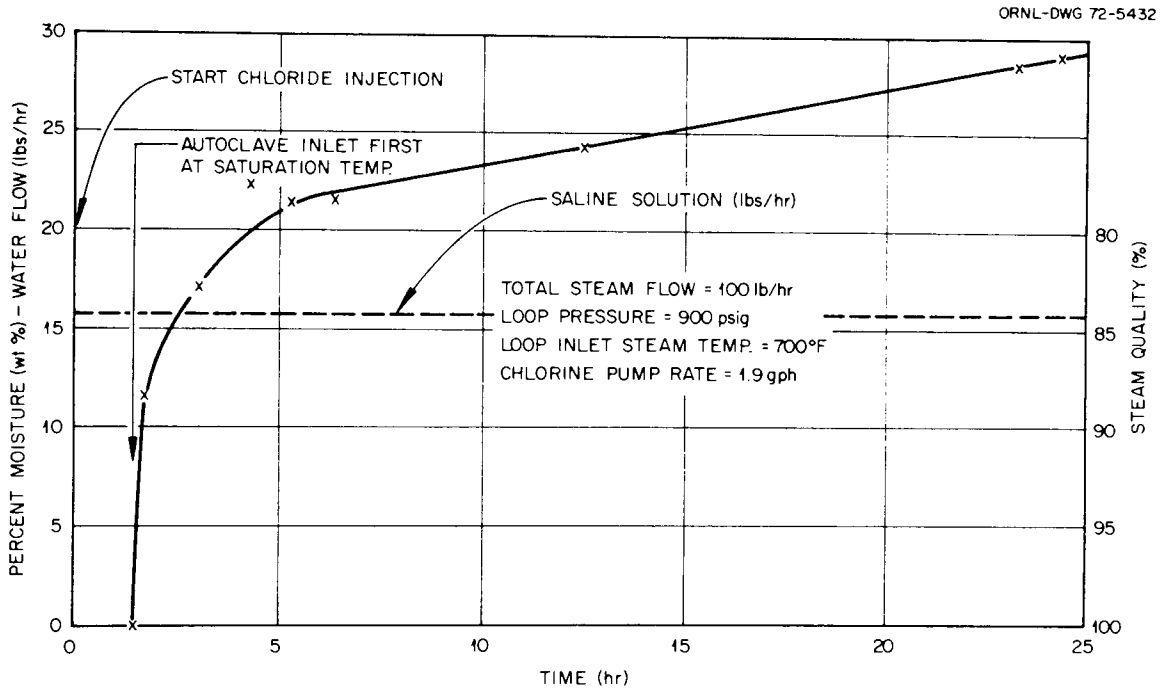

Fig. 6.3. Calculated Moisture Content of Steam in Upper Autoclave as a Function of Time.

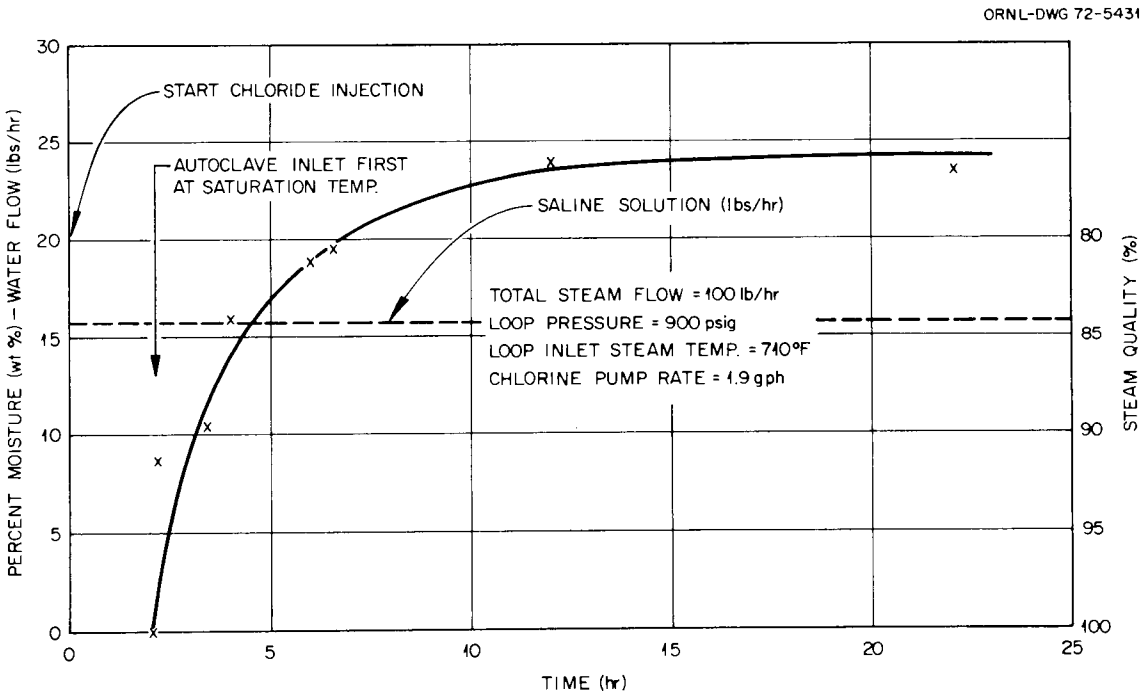

Fig. 6.4. Calculated Moisture Content of Steam in Lower Autoclave as a Function of Time.

Water Flow Rate (lb/hr)	Water Depth in Pipe (in.)
4.8	0.050
10.2	0.07[illegible]
14.9	0.073
19.0	0.090
29.3	0.095
51.4	0.120
97.0	0.129

We have concluded that during the saturation phase of cycling, the moisture content of the steam (Figs. 6.3 and 6.4) goes from zero to around 24–29% (71–76% steam quality). The reason that the top autoclave attains a somewhat higher moisture content than the bottom one may stem from the fact that the makeup steam for the latter was at a slightly higher temperature (see Figs. 6.3 and 6.4). Notwithstanding, the moisture histograms for the two autoclaves are remarkably similar. Since they are, it is assumed that corrosion specimens are subjected to similar environmental exposures irrespective of the autoclave or axial position in which they are placed.

Because the velocity of fluid flow in the autoclaves was quite low, the moisture in them was assumed to condense and quickly collect at the bottom and subsequently flow on through the loop. Since tests simulating the flow conditions indicated that the water level achieved a maximum height of about 3/32 in., the corrosion specimens (located 1/16 in. from the bottom of the autoclave) were definitely wetted during testing. Water-stain markings left on test specimens confirmed the degree of wetting indicated by the simulated tests.

The environmental analysis indicated that for the test conditions employed, the sodium-chloride contaminant concentrates in the moisture or water phase and only a very small concentration resides in the steam. It should be pointed out, however, that the elevated positions in the autoclaves contain a significant amount of moisture along with a high concentration of oxygen. While the concentration of chloride here was quite small, it is sufficient to produce stress-corrosion cracking in some steam generator materials (for example, type 304 stainless steel). By doubling the loop pressure, the solubility of

sodium chloride in the saturated steam could be greatly increased. This, coupled with increasing the velocity of fluid flow, could substantially increase the aggressiveness of the environment in the elevated positions of the autoclaves.

Examination of Alco/BLH Steam Generator

G. M. Slaughter J. H. DeVan

We are examining the Alco/BLH steam generator which failed while under test at the Liquid Metal Engineering Center (LMEC).[3,4] After installation at the Sodium Components Test Installation of the LMEC in 1965, the steam generator operated intermittently with sodium for 7600 hr and with steam for 4100 hr. A water leak on the feedwater chest was found in May 1970, and it was traced to an area of extensive cracking in the lower tube sheet. Extensive corrosion resulting from leakage of steam into sodium was also subsequently observed near the top tube sheet. In view of the vital role of steam generators in the LMFBR demonstration-plant program and the well-documented fabrication and operation history of this unit, it is being examined to determine the mechanisms of failure and to study other metallurgical features of interest.

A progress report covering the work to date has been drafted and is being reviewed. In this quarterly, we will briefly discuss recent activities in several selected areas of work which encompass the rather wide scope of our investigation

Investigation of Tube Failures (J. H. DeVan, B. C. Leslie)

The weld defects apparent in our examination of random tube-to-tube sheet welds[5] suggest a possible mechanism for the three tube failures that occurred during operation of the steam generator. The first of the tube

---

[3]G. M. Slaughter, J. H. DeVan et al., Fuels and Materials Development Program Quart. Progr. Rept. June 30, 1971, ORNL-TM-3540, pp. 97–98.

[4]G. M. Slaughter, J. H. DeVan et al., Fuels and Materials Development Program Quart. Progr. Rept. Sept. 30, 1971, ORNL-3550, pp. 124–133.

[5]G. M. Slaughter et al., Fuels and Materials Development Program Quart. Progr. Rept. Dec. 31, 1971, ORNL-TM-3703, pp. 150–156.

failures was detected after approximately 2000 steaming hours, and the leak was located in Tube 47, row 2, approximately 6 1/4 in. below the upper tube-to-tube sheet weld. The tube was plugged and the unit operated an additional 1100 steaming hours at which time another tube failure was indicated. Leaks were found in Tubes 52 and 53, row 3, both of which were nearest neighbors to the first leaking tube. The leaks in Tubes 52 and 53 were each located approximately 1 1/2 in. below the upper tube-to-tube sheet welds. These latter tubes were plugged by LMEC in the same manner as Tube 47, although the subsequent discovery of cracks in the lower tube sheet precluded further operation of the unit.

The metallographic appearance of Tube 53, row 2, near the tube-to-tube sheet weld is shown in Fig. 6.5. Most of the original tube weld was machined away to provide a seating surface for the Inconel cap used to plug the tube. (The hole now visible in the Inconel cap was drilled at ORNL to permit leak testing of the tube.) Thus, one can only speculate as to the condition of the original weld or its relationship to the leak in this tube. However, there are a number of stress-corrosion cracks near the machined end of the tube (Fig. 6.5), and one of these cracks obviously connects with the missing section of the original tube-to-tube sheet weld. Also the morphology of branching along this crack connotes a downward growth pattern. Assuming that a crack did develop through the weld into the crevice between the tube and tube hole, one could readily explain the tube failure which occurred approximately 1 1/2 in. below the tube-to-tube sheet weld, since steam leaking through the weld into the sodium-filled tube crevice would set up conditions conducive to caustic stress-corrosion cracking. The failed area of the tube wall is pictured in Fig. 6.6, and the high density of transgranular, highly branched cracks strongly suggests stress-corrosion cracking as the cause of failure. However, the water side of the upper tube sheet was dye-checked prior to plugging Tube 53 and showed no evidence of a weld flaw; thus, there is no way of conclusively proving this mode of failure.

Y 112682

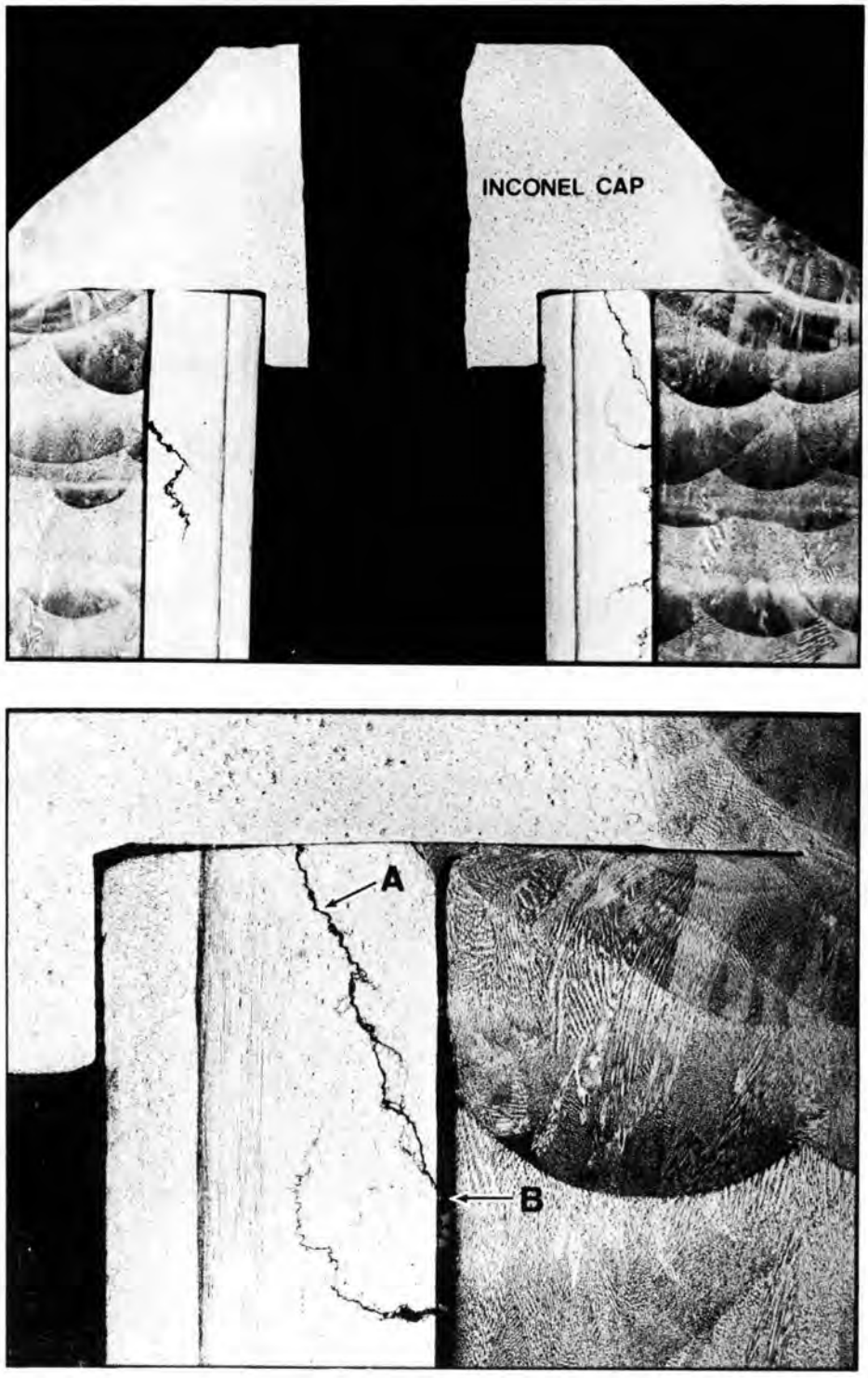

Fig. 6.5. Appearance of Tube 53, Row 3, Near Upper Tube-to-Tube Sheet Weld. Tube leaked during service and was plugged with an Inconel cap. Bottom photo shows crack (A) in tube which connects with the tube-to-tube sheet crevice (B).

Y-112685

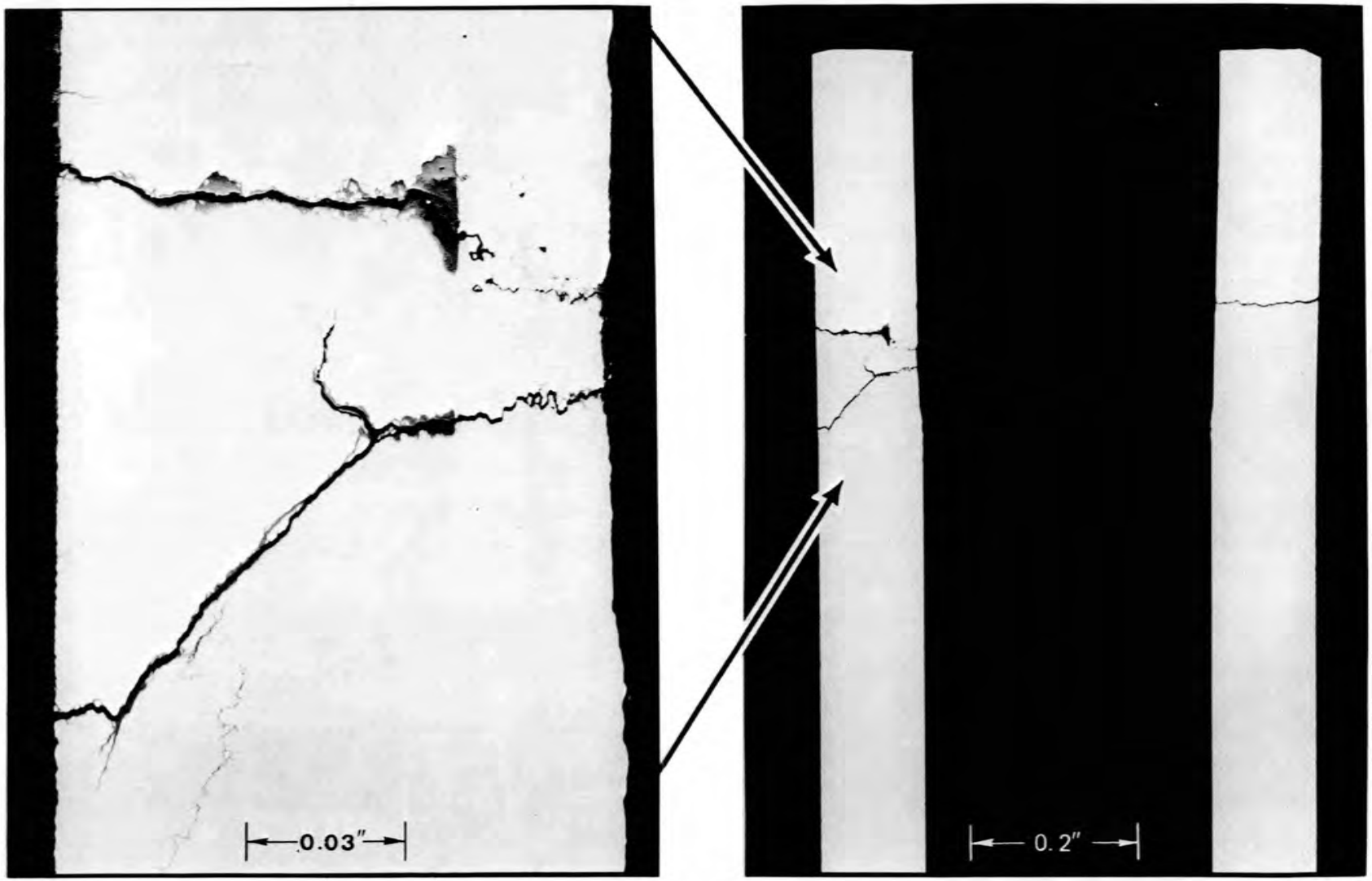

Fig. 6.6. Area of Failure in Tube 53, Row III, Showing Heavy Concentration of Transgranular Cracks.

Corrosion Pattern for Tubes in Argon-Gas Space. (R. H. Jones, G. M. Goodwin, J. H. DeVan) — As reported earlier,[6] steam tubes leading away from the upper tube sheet were heavily corroded by sodium-water reaction products. These products formed in the argon cover-gas space below the tube sheet as a consequence of leaks in three mutually adjacent tubes, which allowed steam to escape into the cover gas. Since previous steam-sodium reaction studies had not indicated gas-space attack of the severity noted here, we investigated the pattern of gas-space attack relative to the location of the steam leaks. Fig. 6.7 shows the maximum wall losses measured for a number of tubes surrounding the three failed tubes. Note that attack increased from the inner row of tubes to the outer row. Attack also decreased rapidly as a function of distance below the tube sheet, and became superficial past the guide ring located 4 1/2 in. below the tube sheet. The maximum wall losses were approximately 0.050 in. and were slightly less than the thickness of the stainless steel portion of the tubes.

Thermocouple Examinations (J. H. DeVan, J. H. Holladay, B. C. Leslie)

The steam generator was originally instrumented with approximately 100 thermocouples to measure surface- and internal-fluid temperatures. The internal thermocouples were sheathed with Inconel on the water (steam) side of the unit and with type 316 stainless steel on the sodium side. There was a mass failure of the sodium temperature-sensing thermocouples during the operating period which followed the first tube leak. Based on our examination of the argon cover-gas region of the steam generator, it appears that the high failure rate stemmed from the corrosion of the thermocouples by sodium-water reaction products in this region. The thermocouple feedthroughs leading into the sodium side of the generator were located just below the top tube sheet, where, as noted before, stainless steel surfaces were heavily corroded. In fact, segments of several of the thermocouples were completely missing behind the feedthrough.[6]

---

[6]J. H. DeVan, G. M. Slaughter, and R. H. Jones, Fuels and Materials Development Program Quart. Progr. Rept. Mar. 31, 1971, ORNL-TM-3416, p. 156.

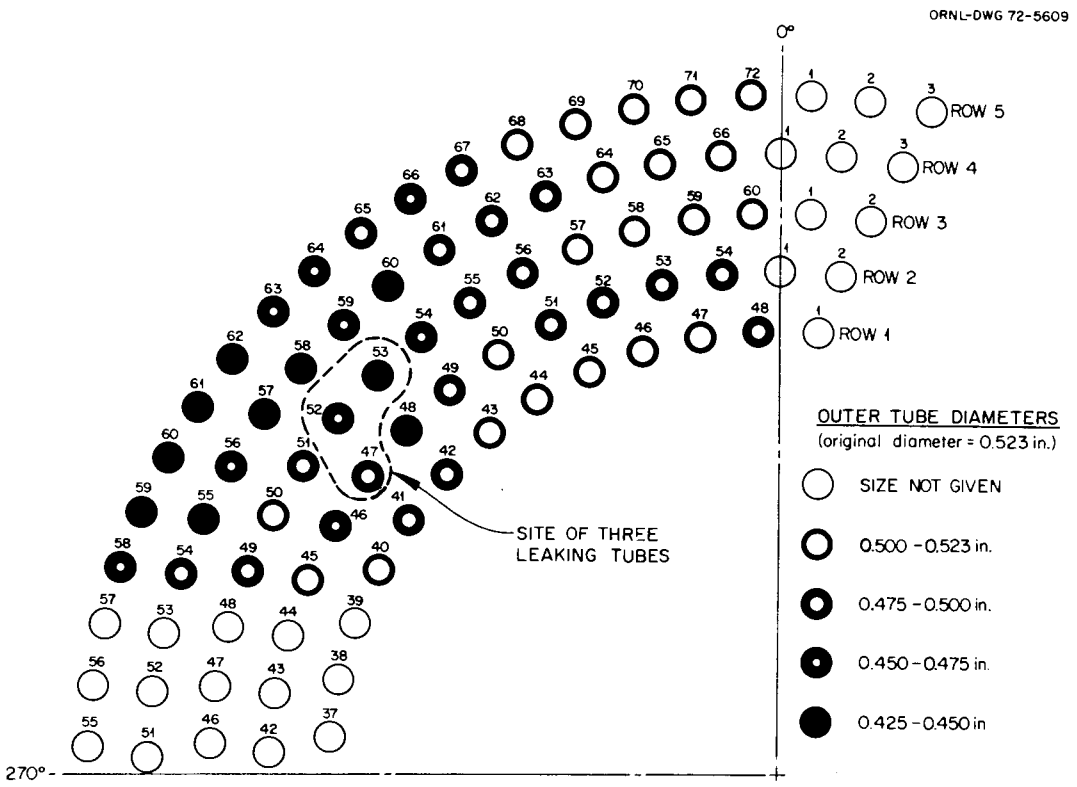

Fig. 6.7. Minimum Tube Diameters Measured in Gas-Space Region Between Upper Tube Sheet and Guide Ring.

Though they did not fail simultaneously, several of the steam-side thermocouples also quit functioning during operation. Three 1/16-in.-diam thermocouples (48, 49, and 53) were removed from the steam chest and examined. Thermocouple 48 was radiographed and an enlarged photographic reproduction of the radiograph showing a section of broken wire near the junction is shown in Fig. 6.8. Radiography of thermocouple 49 revealed weld burnthrough on the sheath, a broken wire, and loss of insulation. The welded junction of thermocouple 53 was also of marginal quality. Metallographic examination of these steam-side thermocouples indicated that the failures were related to the method used to mount the couple junction onto the steam-chest surfaces. The junction ends of the thermocouples were inserted into individual cylindrical pads, and these pads were then tack-welded to the surface being monitored. The thermocouples were secured to the cylindrical pads by means of a weld which ran along a major diameter of the pad and along one side of the thermocouple sheath. A typical weld is shown in Fig. 6.9. Note that the

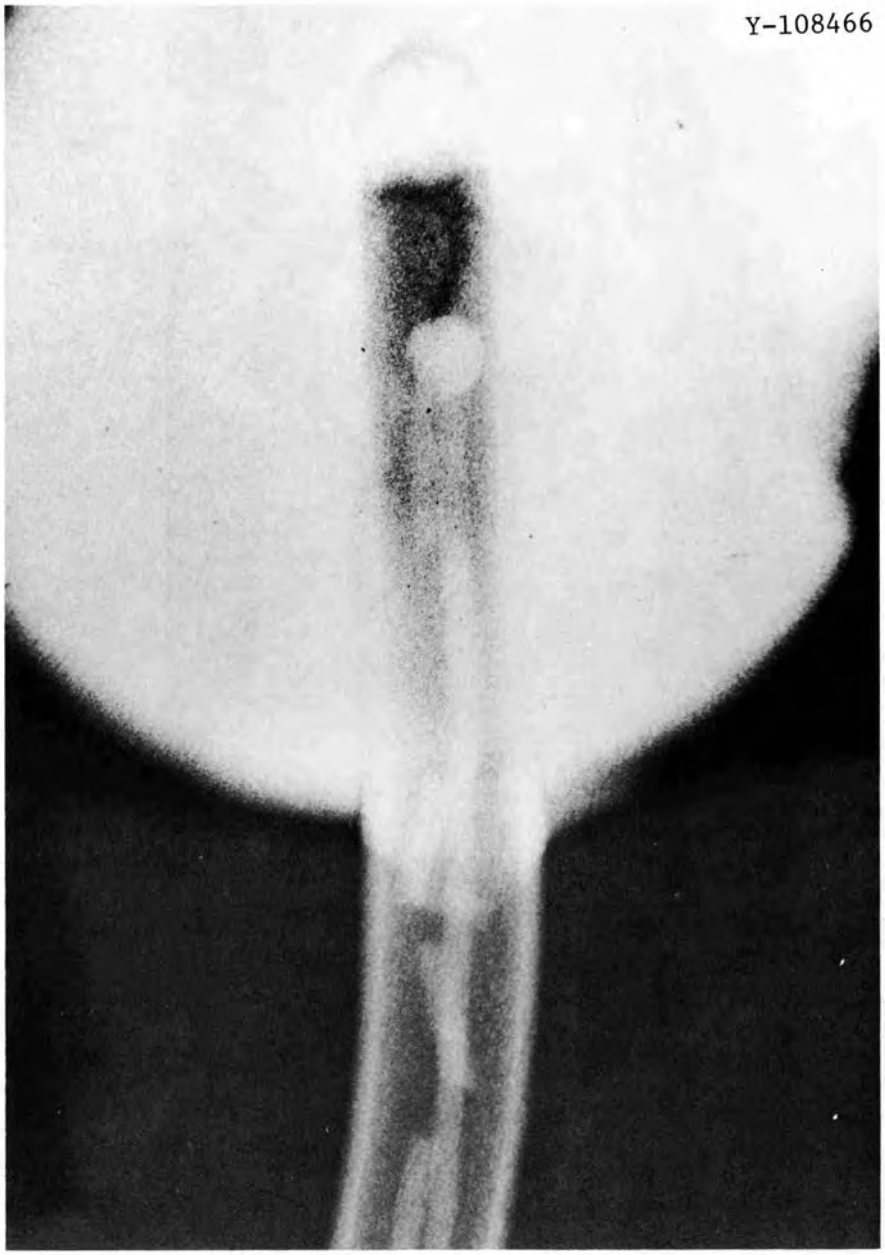

Fig. 6.8. Photographic Reproduction of Radiograph of Thermocouple 48 Showing Broken Wire Near Junction. 9×.

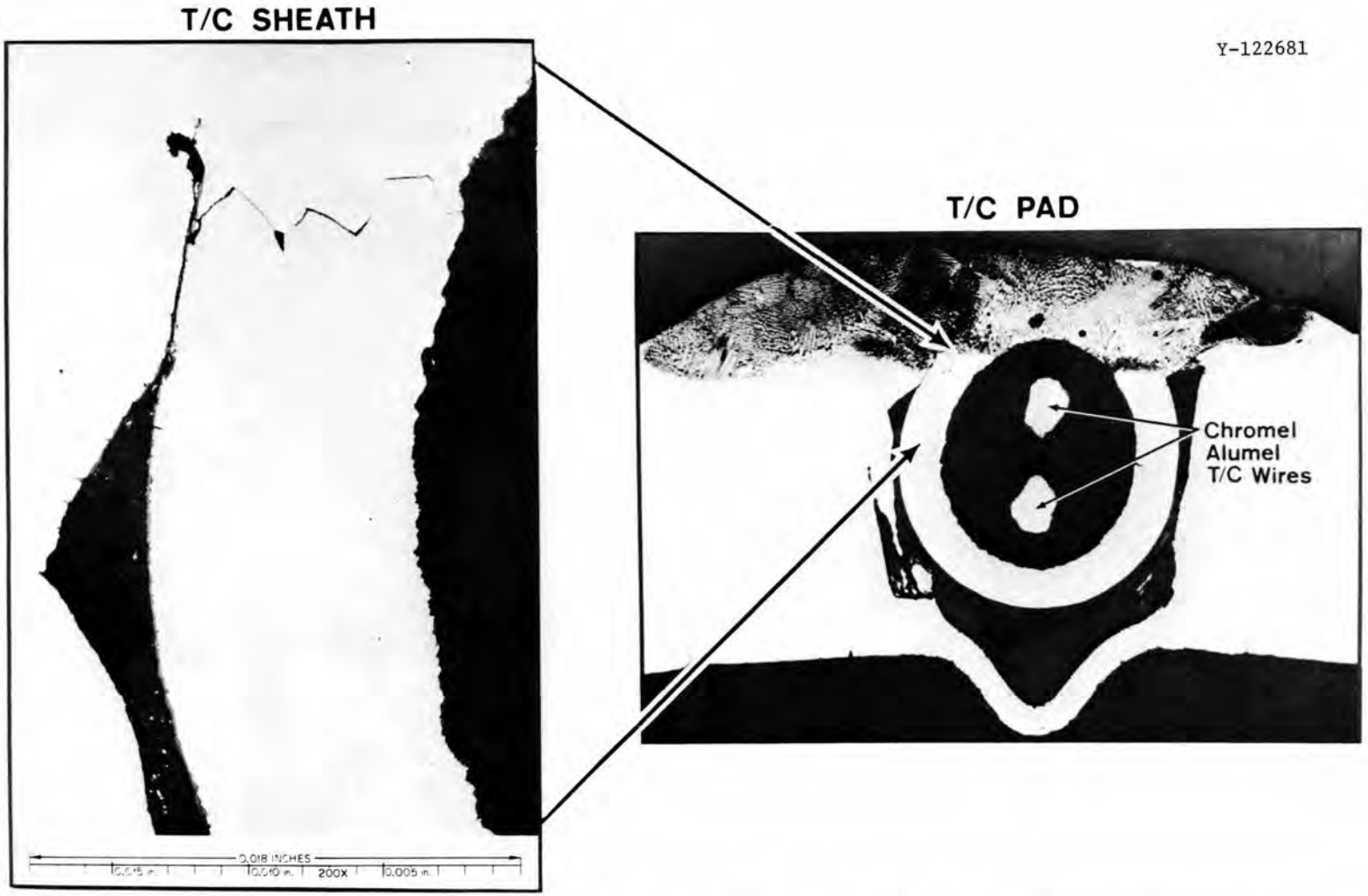

Fig. 6.9. Transverse Section of Thermocouple No. 54 Showing the Thermocouple Assembly Attached to a Pad by Welding the Sheath to the Pad. This pad was then welded to the top tube sheet surface.

sheath has been completely fused over approximately one-fourth of its circumference, and, as shown in Fig. 6.9, a crack runs completely across the heat-affected zone of the sheath on one side of the weld. The crack resulted from too great a heat input into the sheath during welding, which, in turn, resulted from the mismatch in cross section between the sheath and the pad.

Cracks appear to have been present in many of the steam-side thermocouples as a consequence of this poor weld design. These cracks allowed water to penetrate the sheath and resulted in attack of the thermocouple wires and insulation, such as that pictured in Fig. 6.10.

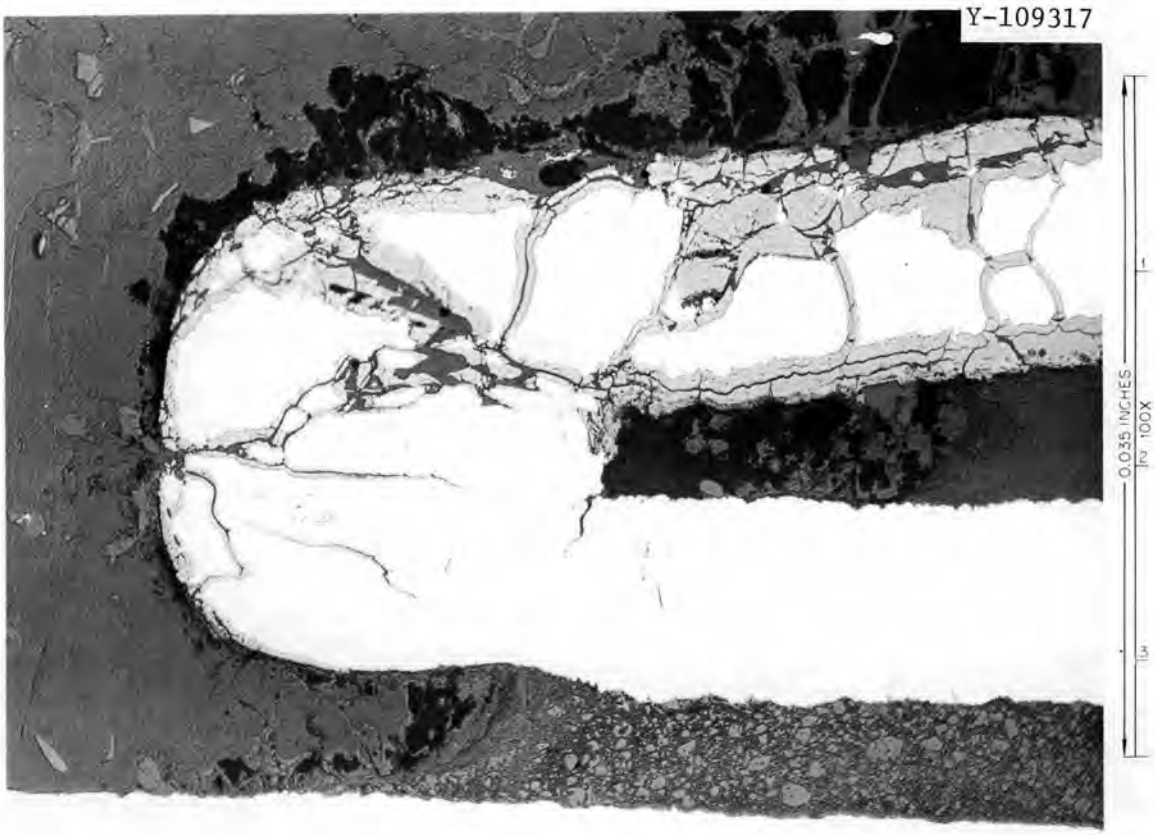

Fig. 6.10. Function of Thermocouple No. 49 from Steam Side of Steam Generator. The Alumel wire shows heavy oxidation.

Microprobe Analyses of Tube-to-Tube Sheet Welds and Overlay Material (H. Mateer, G. M. Goodwin)

Microprobe analyses have been conducted on a section of the bottom tube sheet containing a tube, a tube-to-tube sheet weld, a segment of the tube-sheet forging, and a portion of the Inconel overlay. In general, it appears that there was little dilution of the Inconel-overlay material by type 316 stainless steel forging material. The tube-to-tube sheet weld region, however, showed substantial dilution (approx 30%), particularly in the thin ligament connecting the inner (Inconel) tube wall to the weld fillet.

Measurement of Localized Plastic Strain Using Selected Area-Electron Channeling Patterns (R. S. Crouse, G. M. Goodwin)

Using the recently developed selected area electron channeling techniques, investigators at Westinghouse Research are studing the localized plastic-strain distribution in several typical specimens from the steam generator. Specimens including tube-to-tube sheet welds from both the upper and lower tube sheets, Inconel-overlay material, and tube sheet forging material were delivered to Westinghouse Research during February, 1972, and subsequently ORNL staff members visited there to observe the examination in progress. Westinghouse Research personnel will submit a summary report.

Stress Analysis of Lower Tube Sheet (W. C. Stoddart)

Preliminary calculations were made to determine whether the discontinuity stresses resulting from the 15-in. manway and the concentrated weight load on the tube-sheet extension could have produced high enough stresses to have a major effect on the cracking in this region. The estimated peak stress intensity at the intersection of the lower tube sheet and water chest was 55,000 psi due to pressure alone. Additionally, thermal gradients could contribute an additional 30,000 psi, giving a potential peak-stress intensity of 85,000 psi, nearly twice the allowable design value.

Stresses of this magnitude clearly are sufficient to initiate and sustain stress-corrosion cracking in austenitic stainless steel, provided that the necessary environmental conditions also exist. The preliminary calculations described above, however do not permit correlation of the stress pattern (magnitude and directions) with the location and general contours of the observed major crack systems. In addition, they do not include the complicating influences of residual stresses within the tube sheet (e.g., overlay stresses) and severe thermal shocks during startup.

In view of these considerations, a more detailed stress analysis of the bottom tube-sheet region has been initiated.

7. JOINING OF STRUCTURAL MATERIALS

P. Patriarca G. M. Slaughter

Joining research and development is being carried out on a wide variety of structural materials of interest to the Liquid Metal Fast Breeder Reactor Project. The vessel, primary piping, intermediate heat exchanger, and core support structure of the Fast Flux Test Facility (FFTF) are being made of austenitic stainless steel while steam generators for the demonstration plants will likely contain ferritic steels or Incoloy 800. Inconel 718, on the other hand, is being used or considered for such applications as the Power Burst Facility, the instrument tree for FFTF, and valves and bearing surface components for liquid-metal service.

In view of the diversity of problems associated with those different classes of materials, the progress is reported under the general materials types (i.e., austenitic stainless steels, ferritic steels, and nickel-rich alloys).

AUSTENITIC STAINLESS STEELS

Welding Development for FBR Stainless Steel Components

G. M. Slaughter W. R. Martin

We are evaluating the behavior of weldments in austenitic stainless steel at 370 to 750°C as a function of both welding process and the variables within a process for application to liquid-metal-cooled fast breeder reactor (LMFBR) vessels and components. The solidification substructure of the weld metal markedly influences the mechanical properties of a weldment at elevated temperature; since the size and type of substructure are significantly influenced by factors which the welder can control, our approach is to determine this link between welding variables, the solidification substructure which these variables produce, and the resultant mechanical properties. Also included in the studies are

corrosion behavior, irradiation stability, and the effect of heat treatment, and, of course, deposit composition on structure and properties. A new task involving the use of radioisotopes to study the mechanism of weld cracking is likewise discussed in this report.

Procurement of FFTF Welds (G. M. Goodwin)

Using techniques outlined previously,[1] Combustion Engineering, Inc., Chattanooga, Tennessee, has continued the production of FFTF weld test plates. Electrodes from each of the available production batches used in the vessel plus a control batch without the controlled residual element additions are represented in test plates. As of this date, 64 plates, as outlined in Table 7.1 have been delivered, completing the original

[1]G. M. Goodwin, Fuels and Materials Development Program Quart. Progr. Rept. Sept. 30, 1971, ORNL-TM-3550, pp. 186–187.

Table 7.1. FFTF Vessel Weldment Test Plates: Status as of March 31, 1972

Electrode Designation[a]	Plates Welded[b]	Plate Equivalent of Electrodes Remaining
1 (LOEJ)	3	0
2 (LBHJ)	6	0
4 (CAEA)	8	3
6 (HBEA)	36	14
7 (IBCA)	3	0
9 (JADA)	4	1
10 (JAFA)	4	7
11 (ABHB)	0	c
Total	64	> 25

[a]With the exception of Batch 7 (IBCA), which is a control batch, each batch has identical aim composition.

[b]Each test plate contains a weld 8 in. long × 2 3/8 in. thick with a double "Vee" groove joint preparation.

[c]Batch 11 (ABHB) is a new batch and a large quantity of core wire is available.

purchase order. We plan to procure additional plates to: (1) augment the supply of Batch 6 (HBEA, the reference batch) specimens, (2) to provide an additional control batch since Batch 7 (IBCA) electrodes are no longer available, and (3) to represent any subsequent production batches used in the FFTF vessel.

Investigations of Mechanical Properties (R. G. Berggren, G. M. Goodwin)

Submerged-Arc Welds. – Creep-rupture tests on eight type 308 stainless steel submerged-arc weldments[2] are essentially complete for rupture times to greater than 1000 hr. The results of these series of tests are summarized in Table 7.2. As previously reported,[2] we see no marked property differences between these submerged-arc weldments. The differences that may be noted in Table 7.2 do not indicate a consistent superiority of any weldment over the others.

Shielded Metal-Arc Welds. – No additional data have been obtained.

Electroslag Welds. – A creep-rupture study of two electroslag weldments is now essentially complete. One weld was made on wrought type 304 stainless steel and one was made on cast-type CF8 stainless steel. The filler wire was type 308 stainless steel. The results of these series of tests are summarized in Table 7.3. The electroslag weld (in wrought plate) was weaker than either the wrought or cast base plate but had comparable ductility. Comparison with Table 7.2 shows the electroslag weld to be slightly weaker but of greater ductility than the submerged-arc welds.

Filler Metal Development for Pipe Welding (N. C. Cole, G. M. Goodwin)

We have produced a series of gas tungsten-arc and shielded metal-arc welds in 1/2-in. austenitic stainless steel plates to simulate welds in piping. Types 304 and 316 stainless steel plates were welded using filler metals of standard and special compositions. Many of the filler metals contained minor element additions to improve the creep properties

[2]R. G. Berggren and G. M. Goodwin, Fuels and Materials Development Program Quart. Progr. Rept. Dec. 31, 1971, ORNL-TM-3703, p. 158.

Table 7.2. Summary of Creep Properties: Submerged Arc Welds: Type 308 Stainless Steel
Test Temperature: 650°C (1200°F) (As-Welded Condition)

Weld Number SA-	Description	Stress for $\dot{\varepsilon}_{min} = 10^{-4}$ %/hr (psi)	Stress for Rupture in 10^3 hr (psi)	Stress for 0.5% ε in 10^3 hr (psi)	Stress for Start 3rd Stage in 10^3 hr (psi)	Rupture Strain at 10^3 hr (psi)	Min. Recorded Rupture Strain (%)
2	Arcos flux, sent to WADCO	8,000	13,000	9,000	12,800	13	6.6
3	Arcos flux, low heat input	10,000	14,000	9,200	13,000	5	5.9
4	Arcos flux, medium heat input	8,000	13,200	11,000	12,500	8	6.6
5	Arcos flux, high heat imput	7,600	13,800	8,000	13,600	12	12.0
6	Hobart flux	8,400	15,300	11,000	14,400	11	11.0
7	Arcos flux, duplicate of NRL welds	9,000	13,000	10,000	12,600	7	5.5
8	Linde flux, CR-10	9,600	13,500	12,000	12,600	15	8.8
9,10,11	Arcos flux, 2-in. plate	8,500	13,600	10,000	13,200	13	13.5
		Test Temperature:	1100°F				
2	Arcos flux, sent to WADCO	12,800	20,200	10,000	18,000	13	12.7
3	Arcos flux, low heat input	14,400	22,000	16,000	20,400	12	10.0
4	Arcos flux, medium heat input	12,600	20,400	9,400	18,200	12	10.0
5	Arcos flux, high heat input	11,800	20,400	10,800	19,000	10	10.1
6	Hobart flux	14,000	21,800	15,000	20,000	11	10.2
7	Arcos flux, duplicate of NRL welds	11,800	19,600	11,000	17,600	20	19.2
8	Linde flux, CR-10	13,500	19,200	18,000	16,600	15	15.4
9,10,11	Arcos flux, 2-in. plate	(a)	(a)	(a)	(a)	(a)	(a)

[a]No tests — material not available or tests not scheduled.

Table 7.3. Creep Properties of Electroslag Weldments: As-Welded Condition

Description	Stress for $\dot{\varepsilon}_{min} = 10^{-4}$ %/hr (psi)	Stress in 1000 hr, psi			Rupture Strain at 100 hr (%)	Reduction in Area at 10^3 hr (%)
		Rupture	0.5% Strain	Start of Third Stage		
Test Temperature: 650°C (1200°F)						
Wrought type 340 stainless steel plate	11,600[a]	19,000	13,000[a]	17,300	32	45
Cast type CF8 plate	9,000[a]	15,200	<10,000[a]	14,200	22	45
Electroslag weld metal, type 308 stainless steel transverse weld metal	7,600[a]	12,600	<10,000[a]	12,000	25	45
Test Temperature: 593°C (1100°F)						
Wrought type 304 stainless steel plate	20,000[a]	27,400[b]	20,000[a]	25,600[b]	20[b]	15[b]
Electroslag weld, TW	11,600[a]	18,000	(c)	18,000	15	35

[a]Extrapolated more than one order of magnitude.

[b]Extrapolated less than one order of magnitude.

[c]Insufficient data.

of the welds at high temperatures. The welds are listed and identified in Table 7.4.

Welds V01–V06 represent types 316 and 304 stainless steel plates welded with commercially available filler metals. Welds V07–V16 were gas tungsten-arc welded using special type 308 stainless steel filler metal with minor elements added to the filler wire. Shielded metal-arc welds V17 and V18 were produced with Combustion Engineering's standard 5/32-in.-diam, lime-coated electrodes. The series of welds V19–V23 were made with 5/32-in.-diam, lime-coated electrodes from two different vendors. The electrodes represent each vendors' attempt to reproduce the weld deposit chemistry of the welds being used in the FFTF vessel. Welds V24–V29 were made with filler metals in which the composition was adjusted to produce particular calculated amounts of ferrite. Standard and special type 316 stainless steel coated electrodes have been purchased and they will be welded and tested soon.

Microstructure of Simulated Piping Welds. (N. C. Cole, T. M. Kegley) – Welds V01–V14 have been sectioned and studied metallographically. The ferrite content of selected welds was measured using the Quantitative Television Microscope and we noticed an interesting trend. All welds were made manually by the same welder and under typical field conditions. A recorder was used to monitor the amperage, voltage, and travel speed and the only differences detectable were the ones which reflect the necessary changes between gas tungsten-arc and shielded metal-arc welding.

The ferrite content of the type 316 stainless steel gas tungsten-arc welds averaged about 6–7%, whereas the welds made with commercial type 308 stainless steel filler wire averaged about 4–5% ferrite. The ferrite content of the welds made with filler metals containing minor element additions did not change significantly. However, the weld made with the high purity, no silicon, type 308 stainless steel filler wire only contained about 2–3% ferrite. As expected, the welds with the lowest ferrite content, 1–2%, were the type 316 stainless steel plates shielded metal-arc welded with 16 Cr–8 Ni–2 Mo filler metal. Photomicrographs comparing the welds made with types 316, 308, high purity-no silicon 308, and 16 Cr–8 Ni–2 Mo are shown in Fig. 7.1.

Table 7.4. Stainless Steel Test Welds for Pipe Welding Studies

Number	Process[a]	Base Metal	Filler Wire
V01	GTA	Type 316	Type 316
V02	GTA	Type 316	Type 316
V03	SMA	Type 316	16 Cr—8 Ni—2 Mo
V04	SMA	Type 316	16 Cr—8 Ni—2 Mo
V05	GTA	Type 304	Commercial 308
V06	GTA	Type 304	Commercial 308
V07	GTA	Type 304	Special 308, 1% Ti
V08	GTA	Type 304	Special 308, 0.007% B
V09	GTA	Type 304	Special 308, 0.060% P
V10	GTA	Type 304	High purity 308, no silicon
V11	GTA	Type 304	High purity 308, 0.60% Si added
V12	GTA	Type 304	Special 308, 0.045% P
V13	GTA	Type 304	Special 308, 0.015% B
V14	GTA	Type 304	Special 308, remelted commercial
V15	GTA	Type 304	Special 308, 0.5% Ti.
V16	GTA	Type 304	Special 308, 0.045% P, 0.007% B
V17	SMA	Type 304	Standard lime-coated electrode, CE-KAFA
V18	SMA	Type 304	Standard lime-coated electrode, CE-KAFA
V19	SMA	Type 304	Special 308, F-21 type electrode, Combustion Engineering, Inc., KAGA
V20	SMA	Type 304	Special 308, F-21 type electrode, Combustion Engineering, Inc., KAGA
V21	SMA	Type 304	Special 308, F-21 type electrode, Arcos T8769
V22	SMA	Type 304	Special 308, F-21 type electrode, Arcos T8770
V23	SMA	Type 304	Special 308, F-21 type electrode, Arcos T8771
V24	SMA	Type 304	Special 308, Arcos, 0% ferrite
V25	SMA	Type 304	Special 308, Arcos, 2% ferrite
V26	SMA	Type 304	Special 308, Arcos, 5% ferrite
V27	SMA	Type 304	Special 308, Arcos, 7% ferrite
V28	SMA	Type 304	Special 308, Arcos, 10% ferrite
V29	SMA	Type 304	Special 308, Arcos, 15% ferrite

[a]GTA: gas tungsten-arc; SMA: shelded metal-arc.

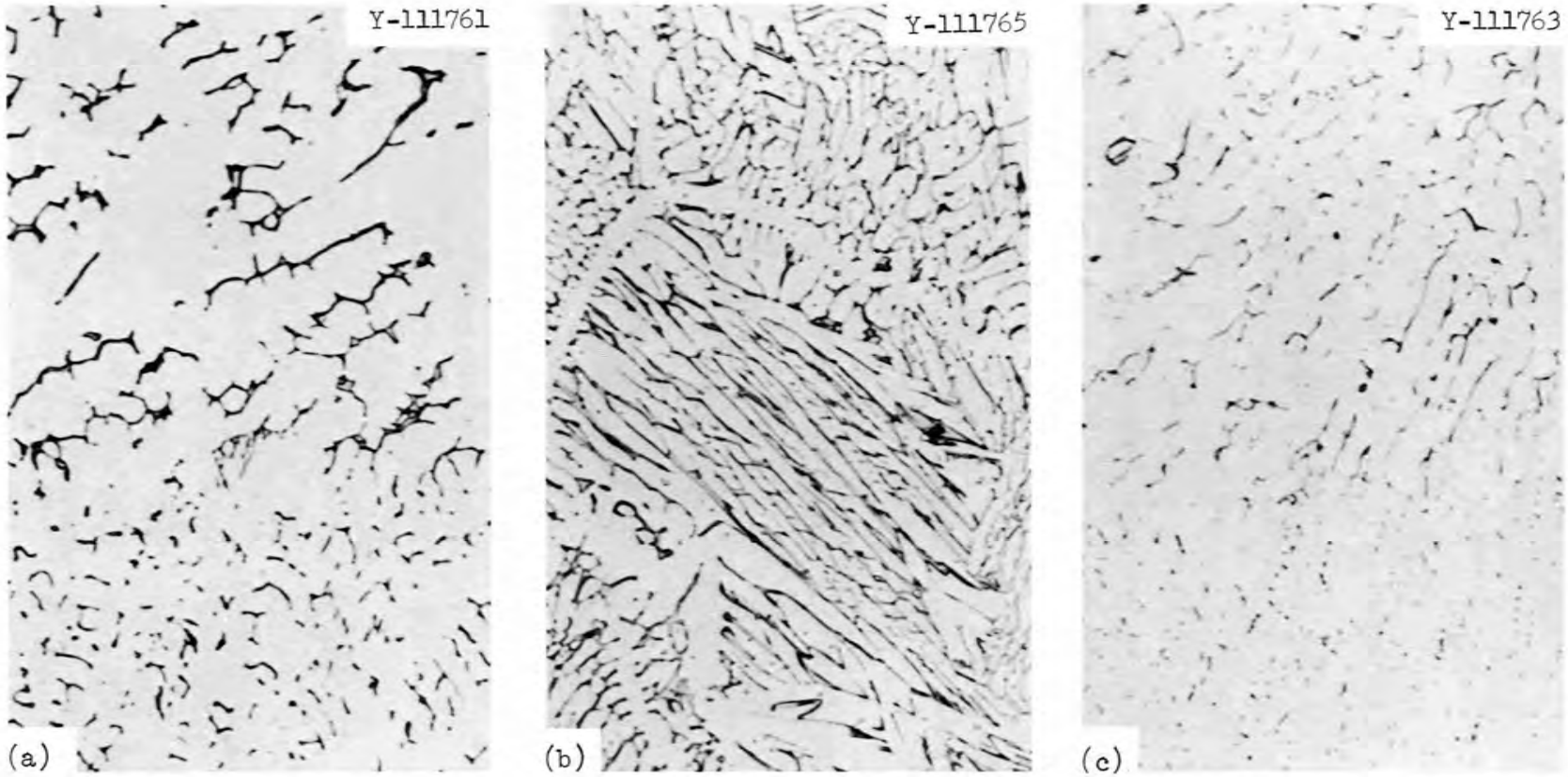

Fig. 7.1. Typical Microstructures of Austenitic Stainless Steel Weld Metal. (a) Type 316 stainless steel. (b) Type 308 stainless steel. (c) 16 Cr–8 Ni–2 Mo. Murakimi etch. 500×.

The microstructures of the welds using various type 308 stainless steel filler metals appeared to be much the same except for weld V07 in which 1% Ti was added. Relatively large precipitates were scattered randomly throughout the microstructure. We assume that they were titanium carbides and we are in the process of identifying them.

Mechanical Properties of Simulated Piping Welds. (R. G. Berggren) — A tensile and creep-rupture test program is in progress on the welds listed in Table 7.4. Twenty-two of these welds have been machined into test specimens and 18 are now in process of testing with some tests already completed for rupture times of about 1000 hr. As expected, the type 316 stainless steel and 16 Cr–8 Ni–2 Mo welds (V01–V04) exhibit lower minimum creep rates and greater rupture lives than any of the type 308 stainless steel welds. On the basis of the presently available data, it appears that titanium and boron additions in the type 308 stainless steel welds increase creep-rupture strength but data on ductilities are insufficient to draw definite conclusions. Test results presently available are presented in Table 7.5.

Use of Radioisotopes to Study Welding

G. M. Slaughter

A study has been initiated to investigate weld cracking in stainless steels using microautoradiography as the main investigative tool. Susceptibility to hot cracking will be determined by the spot Varestraint Test. By introducing radicactive tracers in welding wires, the roles of various microconstituents and such factors as alloy mixing during welding can be examined and correlated with propensity toward cracking.

Fabrication of Weldments with Nickel-63 Impounded Filler Metal Wires and Their Evaluation (J. P. Hammond)

The results of the autoradiographic and metallographic examinations made on weldments of type 347 stainless steel base metal welded with type 347 stainless steel filler metal were reported in the last quarterly

Table 7.5. Creep-Rupture Data for Gas Tungsten-Arc Welds at 650°C (1200°F)

Weld Number	Stress (psi)	Time to: 0.5% Strain (hr)	Time to: Start of Third Stage (hr)	Time to: Rupture (hr)	Total Elongation (%)	Reduction of Area (%)	Minimum Strain Rate (%/hr)
V01	25,000	180	260	451	6.5	23	1.6×10^{-3}
V01	22,000	540	840	1078	4.3	25	6.4×10^{-4}
V02	25,000	90	240	409	4.7	26	1.5×10^{-3}
V03	25,000	21	31	115	25	65	1.5×10^{-2}
V03	20,000	700	1600	(a)	(a)	(a)	2.4×10^{-4}
V04	25,000	6	16	113	30	61	4.2×10^{-2}
V04	22,000	(a)	(a)	357	36	56	(a)
V05	25,000	1	7	27	19	29	2.6×10^{-1}
V05	20,000	2	30	115	12	15	4.3×10^{-2}
V05	16,000	50	430	517	2.8	4.4	2.9×10^{-3}
V06	25,000	1	6	24	21	24	3.4×10^{-1}
V06	20,000	4	70	144	7.9	21	3.0×10^{-2}
V07	25,000	1	15	62	52	81	1.4×10^{-1}
V07	20,000	25	75	322	22	52	2.6×10^{-2}
V07	16,000	29	1000	(a)	(a)	(a)	5.1×10^{-3}
V08	25,000	1	6	40	39	48	3.3×10^{-1}
V08	20,000	5	82	262	19	24	3.4×10^{-2}
V08	16,000	200	900	1199	4.6	11	1.8×10^{-3}
V09	25,000	1	4	26	28	43	4.0×10^{-1}
V09	20,000	3	70	190	13	22	3.5×10^{-2}
V09	16,000	150	720	1092	6.4	6.7	1.7×10^{-3}
V10	25,000	0.2	4	11	38	81	1.8×10^{0}
V10	20,000	1	7	25	14	40	2.7×10^{-1}
V10	14,000	27	560	937	25	37	1.7×10^{-2}
V09	20,000	3	70	190	13	22	3.5×10^{-2}
V09	16,000	150	720	1092	6.4	6.7	1.7×10^{-3}
V10	25,000	0.2	4	11	38	81	1.8×10^{0}
V10	20,000	1	7	25	14	40	2.7×10^{-1}
V10	14,000	27	560	937	25	37	1.7×10^{-2}
V11	25,000	0.4	4	16	33	62	1.0×10^{0}
V12	20,000	10	130	215	10	22	2.8×10^{-2}
V12	16,000	150	670	922	4.3	9	2.2×10^{-3}
V13	20,000	50	300	495	6.3	15	5.4×10^{-3}
V14	20,000	(a)	(a)	432	12	25	(a)

[a]Results not yet available.

report.[3] These weldments, incorporating three different designs of increasing restraint, displayed varying extents of weld inhomogeneity but none showed any form of weld cracking. In addition, a total of 108 lin in. of 1/16-in.-diam Inconel 82 filler metal wire was fabricated by the methods previously described[3] for this purpose. This batch of wire contained approximately 1 mc/cm^3 of metal activity, and isotopic analyses made on arc-melted, drop castings of the alloy indicated that approximately 95% of ^{63}Ni was retained during processing. A preliminary autoradiographic examination of the filler wire showed it to have excellent isotopic homogeneity.

Evaluation of Incoloy 800 Welds. — Three weldability test specimens of the TIGAMAJIG type[4] were prepared from Incoloy 800 for conducting weld-cracking experiments with ^{63}Ni-impounded Inconel 82 filler wire (Inconel 82 is the filler metal conventionally used to weld Incoloy 800). These tests await modifications to be made in the TIGAMAJIG test apparatus. However, several dissimilar metal welds were made joining Incoloy 800 to Inconel 625 with the impounded Inconel 82 welding wire, and it was found that autoradiography in conjunction with the ^{63}Ni tracer provides an excellent tool for studying weld imperfections. The test welds included those made with only root passes and one made with multipass techniques. The 1/2-in.-thick base plates were machined with a 100-deg V-groove and a 0.010-in. root face and were welded with no root spacing. Previously established welding parameters were used to give an approximate 50% dilution factor.

An autoradiographic study of these welds coupled with a routine metallographic examination revealed several features that could prove important to weld integrity. These features are of three categories and are possibly interrelated: (1) weld cracking, (2) inhomogeneity of mixing between base and filler metal in the weld deposit, and (3) dross or crust formation on the weld surfaces.

---

[3]G. M. Slaughter, Fuels and Materials Development Program Quart. Progr. Rept. Dec. 31, 1971, ORNL-TM-3703, pp. 162–169.

[4]P. W. Turner, Effect of Iron on Fissuring of Uranium Weld Metal, Y-1678 (Aug. 11, 1969), pp. 17–19.

Figure 7.2 shows one of these experimental weldments as observed from the face side. It contains both root pass and multi-pass regions. Figure 7.3 shows photographs of the face and root sides of a single-pass weld along with an autoradiograph of a cross section across the weld (location in photographs indicated by arrows). Figure 7.4 is a similar illustration for the multi-pass weld. Figure 7.5 shows still another autoradiograph of the multi-pass weld and depicts the individual weld passes comprising the weld.

The foregoing autoradiographs reveal vividly the character of weld cracks and show them in perspective with the features of alloy mixing and dross formation (Figs. 7.3 and 7.5). The most noteworthy feature disclosed by the autoradiographs was the nonuniformity of alloy mixing in the root passes. Rather than consisting of a homogeneous mixture of base metal and filler metal as is often assumed, observe that the root pass, on the contrary, is quite heterogeneous. In addition to a layering effect similar to that obtained in type 347 stainless steel,[3] relatively heavy and frequently nonsymmetrical segregates of the filler metal are noted (Figs. 7.3–7.4). Most pertinent of all, autoradiographs often showed a severe impoverishment with respect to filler metal in the vicinity of the root surface. Since cracking frequently initiates in this region and special effort is often made to enrich the root pass in

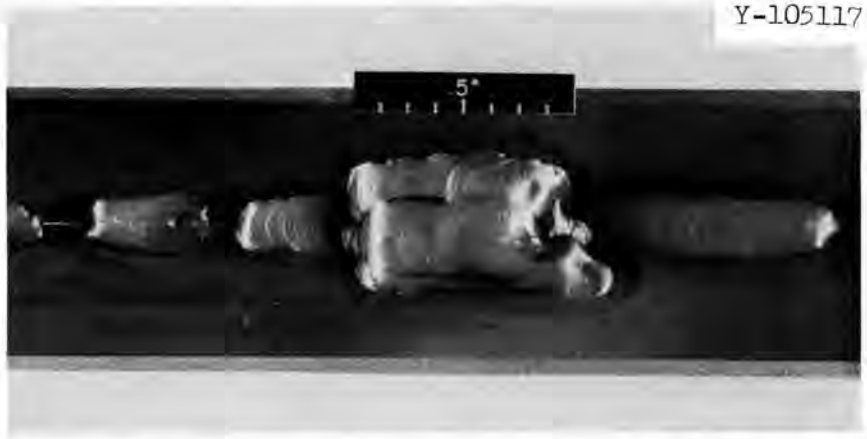

Fig. 7.2. Root Passes and a Multi-Pass Weld Made with the Tracer-Impounded Inconel 82 Filler Wire. Base metals are Incoloy 800 (bottom) and Inconel 625 (top).

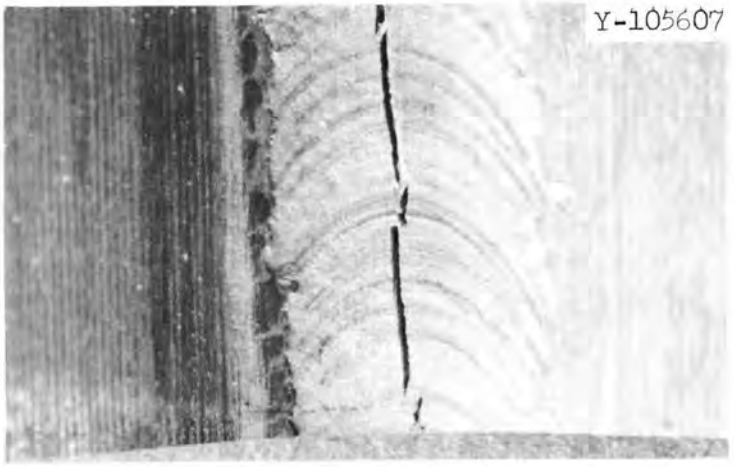

Inconel 625 Incoloy 800

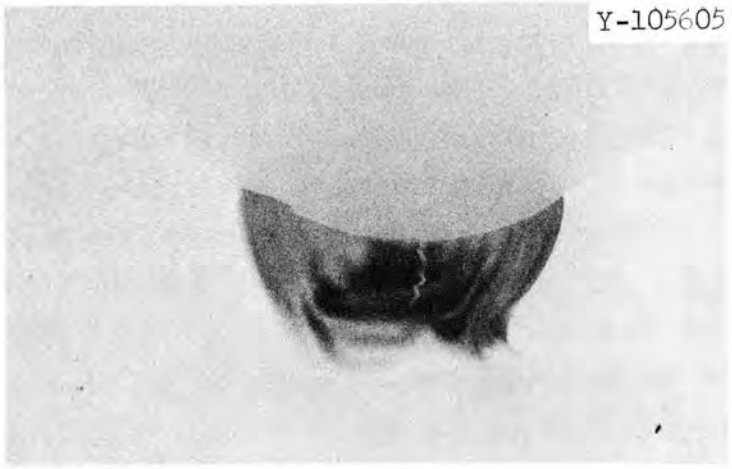

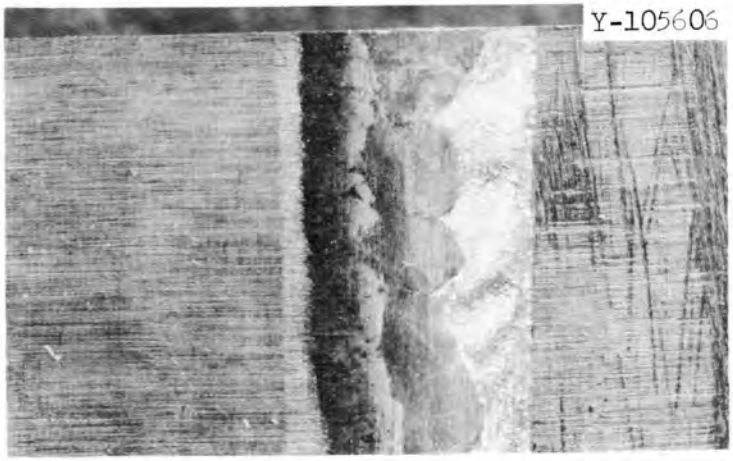

Inconel 625 Incoloy 800

Fig. 7.3. Surface Photographs (Top is Face Side and Bottom is Root Side) and Autoradiograph of Weld Cross Section (Middle) of a Root Pass Made Between Incoloy 800 and Inconel 625 with Tracer-Containing Inconel 82 Filler Metal. Evidence of a weld crack (surface on the face side of the weld) is seen in the autoradiograph along inhomogeneity of base- and filler-metal mixing. 5×.

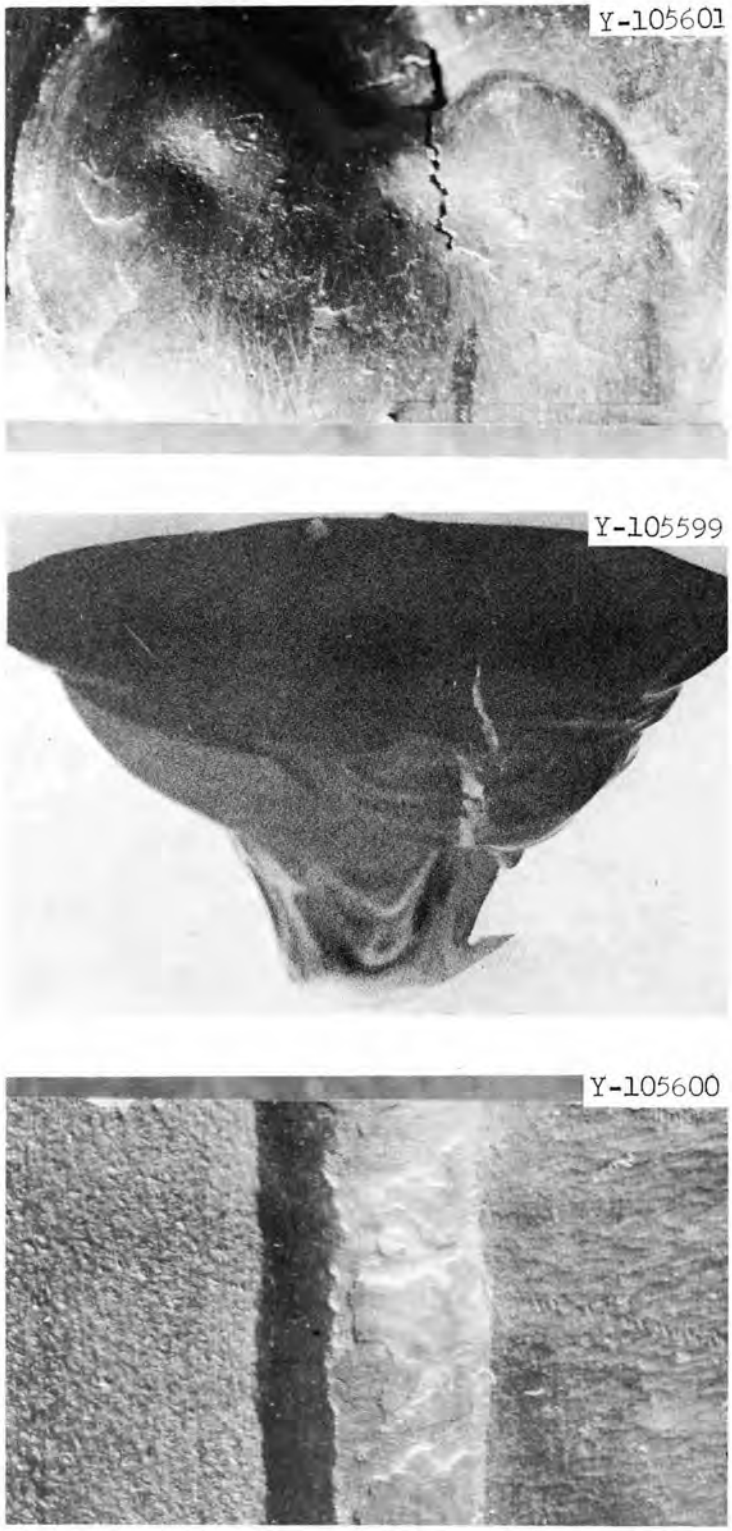

Fig. 7.4. Surface Photographs (Top is Face Side and Bottom is Root Side) and Autoradiograph of Weld Cross Section (Middle) of Multi-Pass Weld Made Between Incoloy 800 and Inconel 625 with Tracer-Containing Inconel 82 Filler Metal. 5X.

Y-105687

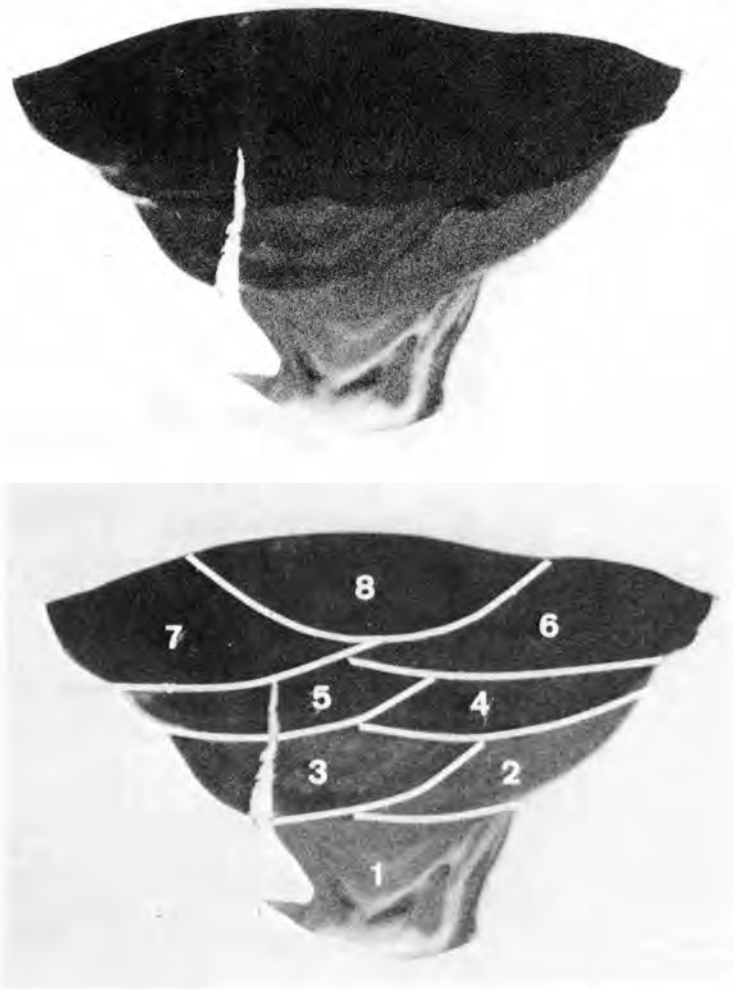

Fig. 7.5. Autoradiograph of Another Cross-Section Through the Multi-Pass Weld Made with Nickel-63-Containing Filler Metal. At the bottom, the confines of the individual passes are superimposed on the autoradiograph. 5X. The disruption extending through pass 4 on into 6 is a weld crack.

filler metal (low base-metal dilution) to discourage cracking, this observation is significant indeed. It is desirable to further study factors promoting alloy inhomogeneity in root-pass welding.

An analysis of the autoradiographs taken of the multi-pass weld (Figs. 7.4 and 7.5) provides a pattern with respect to filler metal distribution. The greatest inhomogeneity of composition occurs in the root pass, as might be expected. Also, base-metal dilution is greatest here. Progressively decreased base-metal alloying is present in the second and third layers of weld metal, with subsequent layers appearing to be very high in filler-metal content. In weld passes adjoining fusion lines, modest base dilution is seen along with isolated instances of base-metal "washing" into the weld deposit. Occasionally, the photographic contrast was quite high, indicating a high concentration of base metal.

Several interesting features were disclosed in examining the character of dross formation. First, it was noted that the encrustation was most often associated with the Inconel 625 side of the dissimilar metal welds (Figs. 7.3 and 7.4), and while it appeared both on the root and face side of root passes, it generally was much more prominent on the root side. The dross invariably was in relief with respect to the remainder of the weld metal surface, which featured the usual ripples and cellular weld metal solidification markings.

The surface character and internal microstructure of the crust formed on the root side of the root passes suggest that it may be a remnant of the original bottom surface of the Inconel 625 plate which had not become completely molten and appreciably mixed with the remainder of the weld pool. Whereas it had been supposed that the region void of dross (containing solidification markings) adjacent to the Inconel 800 base metal consisted of a homogeneous alloy mixture rich in filler metal, evidence of the tracer was not always found in a very substantial amount in this dross-free region (Fig. 7.3). Where the filler metal did appear to a significant degree on the root face, it appeared to show little preference for either the dross-free or the dross-covered region. For face sides of root passes, the dross, as a rule, contained a substantial

concentration of the filler metal as did also the region of the surface free of dross (Fig. 7.3).

Finally, it is interesting to note that the weld metal deposited on the Incoloy 800 side of the dissimilar-metal weld always overlapped (wetted) the base metal. As noted previously, on the Inconel 625 side, the Inconel 82 appeared to extend out over the weld (Figs. 7.4 and 7.5).

Experiments are presently being devised to discern whether the appearance of the dross in the present alloy system can be correlated with the degree to which the metal deposit is contaminated with elements of the air. Also, further studies of the characteristics of alloying between base and filler metal during welding and its association with flaw formation, is planned. A variety of base metal and filler metal alloys will be examined using weld design and power input as experimental variables.

NICKEL-RICH ALLOYS

G. M. Slaughter

Incoloy 800

D. A. Canonico

Previously[5] we discussed the intergranular microfissuring sensitivity of various experimental Incoloy 800 alloys when they were used as filler metals in welding studies. We compared these welds to those produced when Inconel 82, a commercial filler metal recommended for joining Incoloy 800, was employed. The difference in cracking sensitivity was attributed to the solidification morphology of the experimental Incoloy 800 filler metal. These welds, regardless of the fineness of the base-metal grain size, contained large columnar grains and the fissuring was totally in the grain boundaries.

---

[5]D. A. Canonico, Fuels and Materials Development Program Quart. Progr. Rept. Sept. 30, 1971, ORNL-TM-3550, p. 153.

Recent efforts have apparently eliminated the tendency of the filler metals to form large columnar grains. Figure 7.6(a) contains a photomicrograph of a weld made with an experimental Incoloy 800 filler metal. Note the absence of large columnar grains extending epitaxially from the commercial Incoloy 800 base metal. For comparative purposes we have included a photomicrograph of a weld made with identical parameters and Inconel 82T filler metal. Note the similarity in microstructure. We have not completely eliminated the cracking sensitivity of the experimental Incoloy 800 filler metal; however, we have achieved our first milestone, that of a microstructure similar to that of the currently employed Inconel 82T. Our experimental Incoloy 800 alloy contains controlled amounts of silicon, titanium, aluminum, carbon, phosphorus, sulfur, and manganese. In addition, we have added small amounts of niobium. We are continuing our alloy-development studies in an effort to eliminate the cracking sensitivity that still prevails.

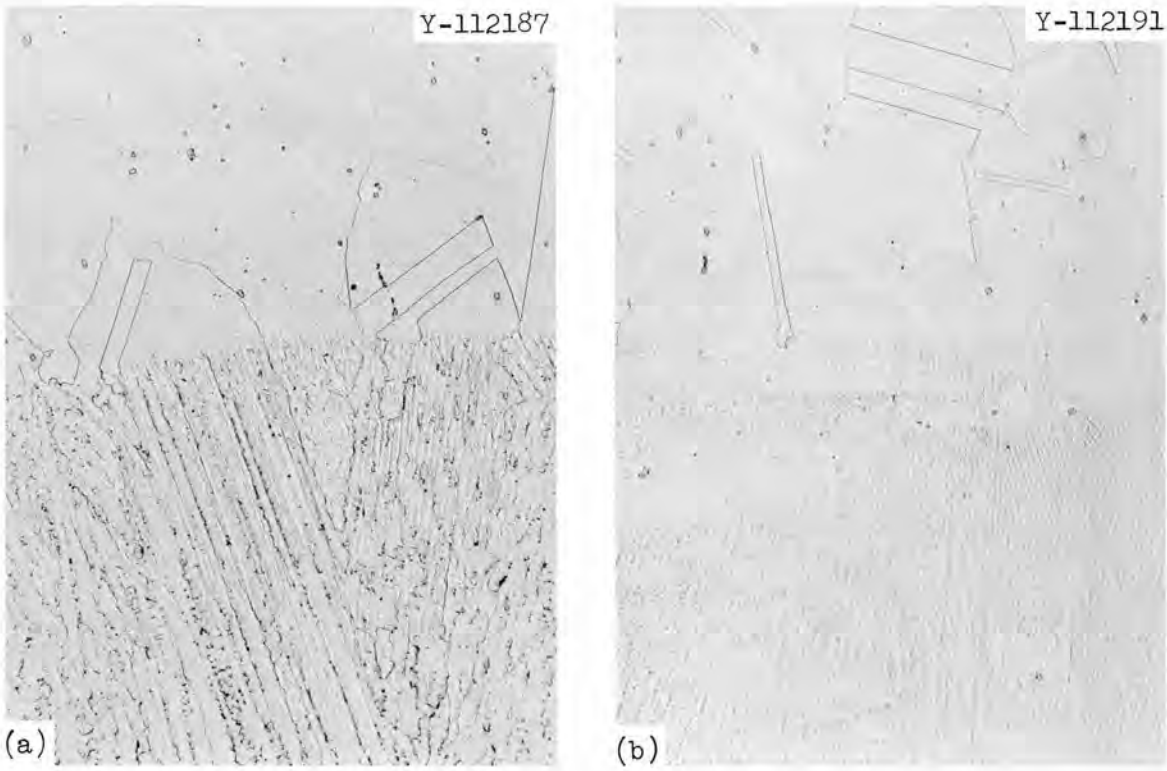

Fig. 7.6. Photomicrographs of Incoloy 800 Weld Fusion Lines. (a) Experimental Incoloy 800 filler metal. (b) Inconel 82T, a commercial filler metal. Identical welding conditions were used.

FERRITIC STEELS

G. M. Slaughter

Stabilized Grades

D. A. Canonico

Samples of the niobium-stabilized 2 1/4 Cr–1 Mo welds that were previously[6] discussed were postweld heat-treated at 700°C (1290°F) for 1 hr. Charpy V-notch (C_V) specimens were prepared where notches were placed in the areas of the weld metal, fusion line, and heat-affected zones. The toughness results obtained with these specimens at 5°C (40°F) were excellent.

The heat-affected zone area, because of the difficulty of notch location, provided test results that more closely represented the exceptionally tough properties. Table 7.6 contains the results of the C_V tests. Note that the heat-affected zone specimen from Heat 450543

[6]D. A. Canonico, Fuels and Materials Development Program Quart. Progr. Rept. Dec. 31, 1971, ORNL-TM-3703, p. 171.

Table 7.6. Results of Charpy V-Notch Tests on 1/2-in.-thick Niobium-Stabilized 2 1/4 Cr–1 Mo–1/2 Ni Welds Postweld Heat Treated at 700°C (1290°F) for 1 hr Test Temperature 5°C (40°F)

Heat Number	Notch Location	Absorbed Energy (ft-lb)	Lateral Expansion (in.)
450543	Weld Metal	54, 65	0.046, 0.053
	Fusion Line	237, 239	0.084,[a] 0.085[a]
	Heat-Affected Zone	239, 202	0.096,[a] 0.084[a]
403150	Weld Metal	53 1/2, 58 1/2	0.027, 0.047
	Fusion Line	128, 120	0.094, 0.087
	Heat-Affected Zone	160, 120 1/2	0.095, 0.082

[a]Specimen not completely broken.

nearly stopped the 240 ft-lb testing arm. All of the specimens exhibited good toughness as measured by the lateral expansion criterion.

A metallographic study of the initiation site for fracture (at the root of the machined notch) showed a considerable amount of plastic deformation. The grain-boundary film seen in the heat-affected zone of the base metal and in the weld metal that has been previously identified as a Fe_2Nb-delta iron eutectic was not brittle. Indeed it is capable of a great degree of deformation and has proven to be tough. Figure 7.7 contains two photomicrographs from the base of the C_V notch in the weld metal. The notch location in the specimen is also shown.

Low-Carbon Grades

D. A. Canonico

Delivery of a commercial heat of low-carbon (0.027%) 2 1/4 Cr—1 Mo has been scheduled for late May 1972. This material will be included in the weldability and mechanical properties evaluations of steam generator materials.

Tube-to-Tube Sheet Welding Studies

D. A. Canonico

We are currently simulating tube-to-tube sheet weldments by the technique described in a previous[7] report. The parameters employed for the 2 1/4 Cr—1 Mo welds are nearly identical to those supplied to us during a recent visit to Foster Wheeler Corporation in Livingston, New Jersey. The technique works well and specimens for mechanical properties testing are being prepared.

We have also developed a double-torch technique that will allow us to simulate, across an entire weldment, that area that may be most critical in a tube-to-tube sheet weld, namely, the overlap region.

---

[7]D. A. Canonico, Fuels and Materials Development Program Quart. Progr. Rept. Sept. 30, 1971, ORNL-TM-3550, p. 159.

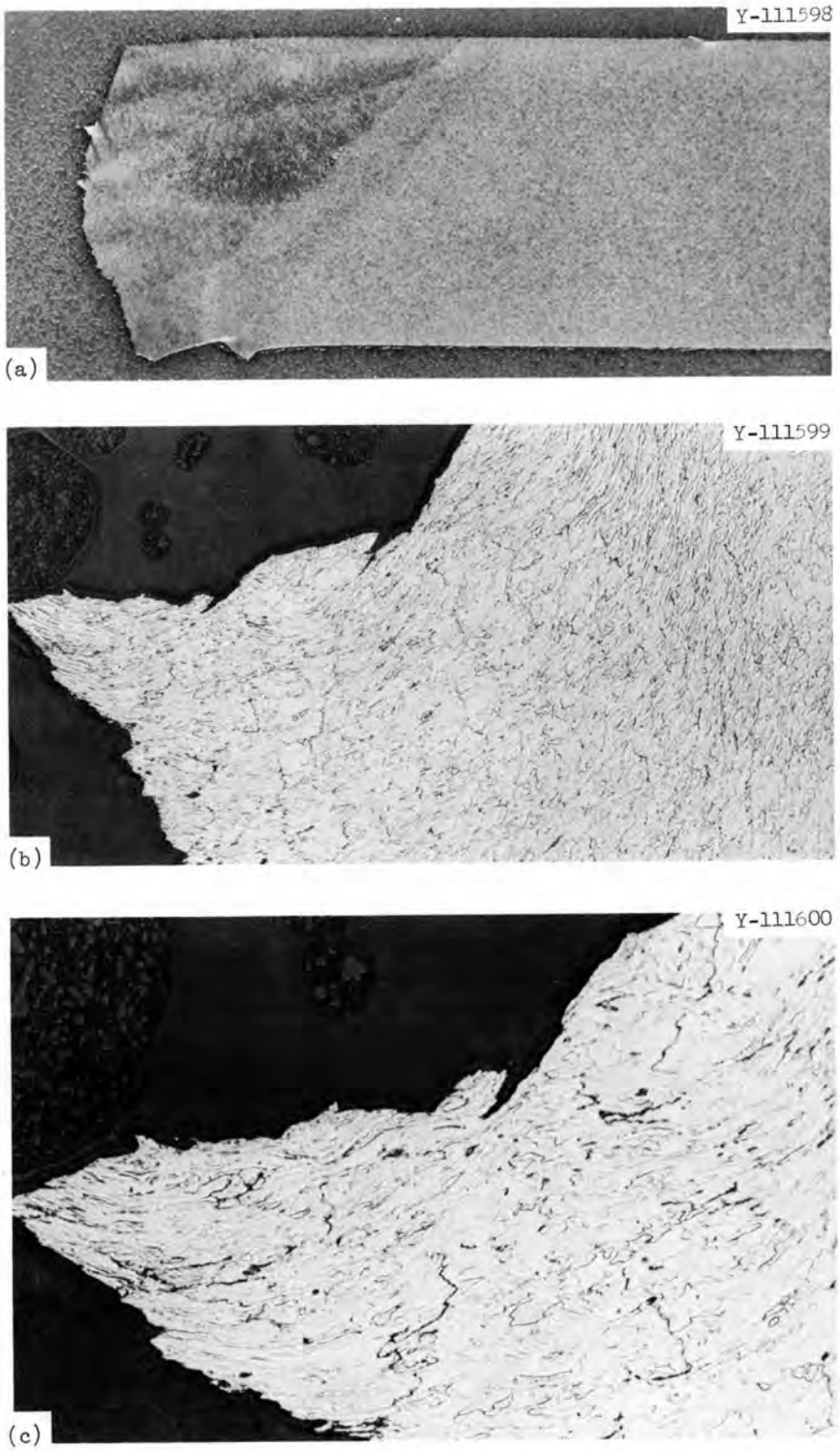

Fig. 7.7. Metallographic Evidence of Superior Toughness of the Niobium-Stabilized 2 1/4 Cr–1 Mo–1/2 Ni Weld Metal. (a) Location of notch in Charpy V-notch specimen. 5.5× (b) High magnification photomicrographs of the weld metal, 200×, and (c) 500×. Note the large amount of plastic deformation which occurred. Etchant: 4% Picral–1% HCl–Alcohol.

Figure 7.8 contains a photograph of the weld-torch arrangement. The spacing between the two torches can be varied to simulate various tube sizes. Simulated tube-to-tube sheet welds are currently being made using the two-torch technique.

It is important to understand the influence of microstructure on the heat-affected zone properties of 2 1/4 Cr—1 Mo steel weldments. We have made calculations whereby we can predict the maximum temperature and cooling rate that a given heat-affected zone region is exposed to as a consequence of welding. These calculations were based on a heat input similar to that employed in the preparation of the 1/2-in.-thick plate welds currently under test. The heat cycles were synthesized on the Duffer's Gleeble. We found that the conventional 1/4-in.-diam specimen did not cool fast enough to simulate the calculated rates. To avoid the cooling-rate problem, we prepared new copper clamps and used 0.156 and 0.094-in.-diam steel rods. The smaller samples permitted close matching of the cooling rate that is encountered in the heat-affected zone of a weld.

This technique was employed to study peak temperatures of 1150, 930, 815, 760, 705, 595, and 480°C. These temperatures span the range that could have an effect on the mechanical properties of the weldments. These specimens are being evaluated thoroughly and will serve as standards for comparison.

We have also begun work on the simulation of Incoloy 800 tube-to-tube sheet weldments. Toward that end we have purchased seven heats of Incoloy 800 Grade 1 sheet and one heat of Incoloy 800 Grade 2 plate. The sheet material measures 4 × 10 ft and the plate is 4 × 4 ft. The analysis of these heats and their mechanical properties as reported by the mill are given in Table 7.7.

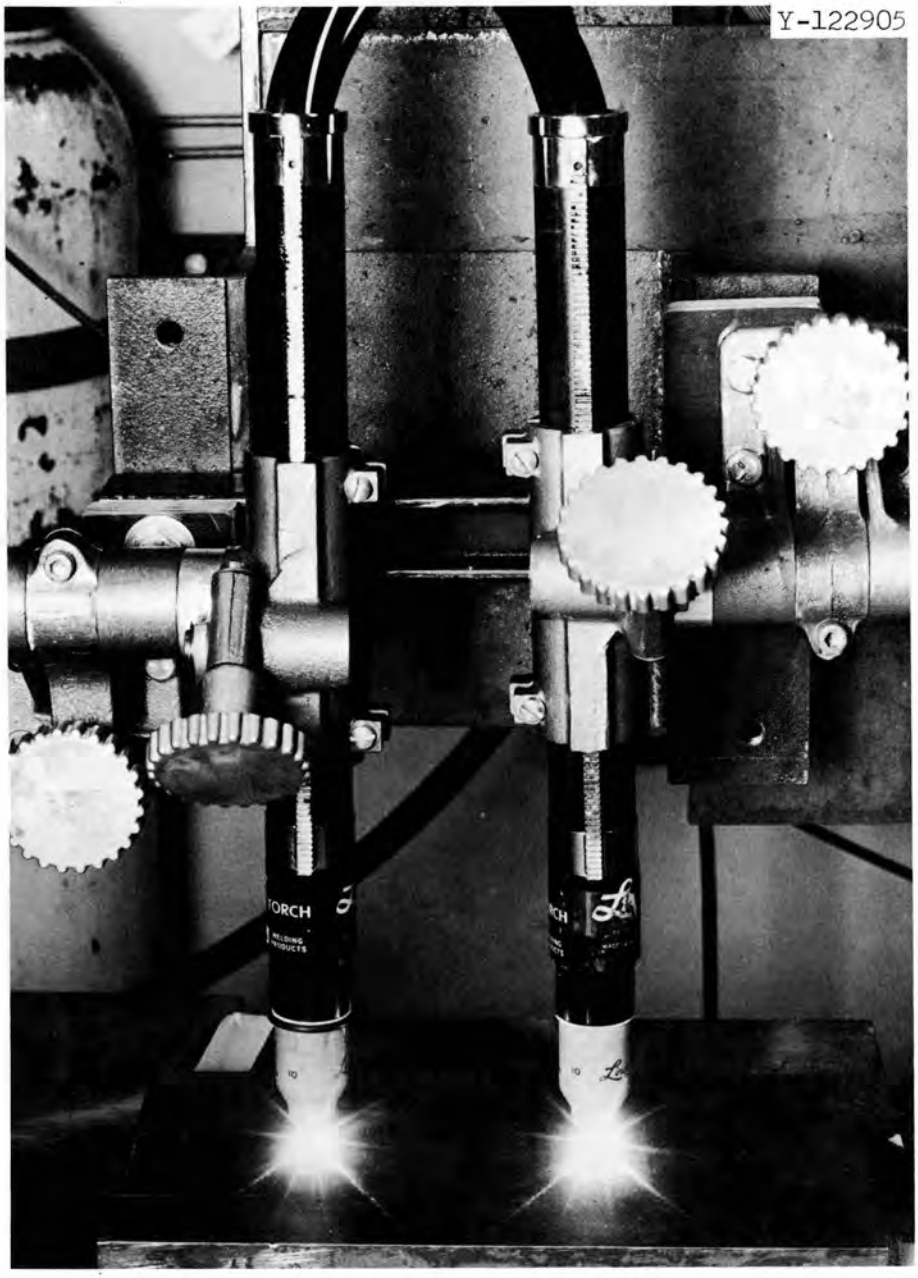

Fig. 7.8. Photograph of the Double-Torch Setup for Simulating the Overlap Region in Tube-to-Tube Sheet Welds.

Table 7.7. Heats of Incoloy 800 Available at ORNL[a]

Heat Number	Thickness (in.)	Heat Treatment[b]	Hardness (R_B)	Yield (ksi)	Ultimate (ksi)	EL (%)	R.A. (%)	Chemical Composition, wt %									
								C	Mn	Fe	S	Si	Cu	Ni	Cr	Al	Ti
HH8561A	2.5	S.A.	62	25	76	55	71	0.03	0.99	45.46	0.007	0.34	0.56	30.6	21.99	N.R.	N.R.
HH3593A	0.109	M.A.	74	37.5	81	44	N.R.	0.04	0.94	45.18	0.007	0.31	0.38	31.8	20.65	0.35	0.32
HH4060A	0.109	M.A.	80	46	85.5	41	N.R.	0.05	0.92	45.20	0.007	0.33	0.19	32.63	19.74	0.42	0.49
HH4101A	0.109	M.A.	71	36	76.5	46	N.R.	0.05	0.95	45.29	0.007	0.41	0.20	32.01	20.30	0.34	0.42
HH4198A	0.109	M.A.	70	37	83.5	45	N.R.	0.04	1.08	44.45	0.008	0.26	0.11	31.89	21.09	0.58	0.47
HH3572A	0.093	M.A.	79	45	85.5	40	N.R.	0.03	1.05	45.54	0.007	0.27	0.08	32.24	20.13	0.28	0.35
HH3603A	0.093	M.A.	82	47.5	85.5	39	N.R.	0.05	0.96	44.83	0.007	0.29	0.30	32.53	20.25	0.46	0.30
HH9691A	0.125	M.A.	80	33.5	78	46	N.R.	0.05	0.93	44.09	0.007	0.29	0.44	31.09	22.15	0.44	0.49

[a]Data are from mill reports.

[b]S.A equals solution anneal; N.R. equals not reported; M.A. equals mill anneal.

8. NONDESTRUCTIVE TESTING DEVELOPMENT

P. Patriarca R. W. McClung

This program is designed to develop new and improved methods of examining LMFBR materials and components. Among the methods being studied are electromagnetic induction, ultrasonics, and penetrating radiation. Special emphasis is being given to developing techniques for inspection problems related to the steam generator.

Electromagnetic Inspection Methods

C. V. Dodd, W. A. Simpson, C. C. Cheng,[1] C. W. Nestor,[2] and W. E. Deeds[1]

We continued research and development of electromagnetic inspection methods on both theoretical and experimental bases.

We have completed a report, "Thickness Measurements Using Eddy-Current Techniques" which was presented at the Spring Conference of the American Society for Nondestructive Testing, and published as ORNL-TM-3712. The report discusses the results of recent computer-based and experimental studies related to the design of optimum test conditions for measuring both the thickness of a single conductor and the thickness of one conductor clad on another. The various graphs in the report provide insight on the effects on thickness measurement of such variables as frequency, coil size, specimen conductivity, coil-to-conductor spacing and coil resistance allowing simple design of optimum test parameters and prediction of attainable results.

We are also investigating the effects of specimen curvature on response when using a probe coil. The measured parameter in the current study is electrical conductivity. We have machined 20 disks each of brass and Inconel, ranging from 4 to 0.2 in. in diameter. These will be

---

[1] Consultant, from the University of Tennessee.

[2] Mathematics Division.

annealed and then measured on both the curved and flat surfaces with various size coils.

We used our computer programs to design an attenuator to minimize the temperature drifts of a reflection type coil. An attenuator based on the computer design was constructed and tested, using a coil and sample in an oven. The calculated drift for a temperature variation of 30°C was approximately 0.0003/°C while the measured drift was 0.003/°C. This measured drift was about two orders of magnitude below that normally encountered in eddy current tests and negligible for practical considerations. This new advanced concept will be extremely important for the performance of eddy current examination of specimens at other than controlled laboratory conditions (e.g., on hot or cold specimens or in field or shop-floor conditions).

Ultrasonic Inspection Methods

H. L. Whaley K. V. Cook Laszlo Adler[1]

Ultrasonic Frequency Analysis

We continued our basic studies of frequency effects in ultrasonic testing by means of spectral analysis. We are employing a special electronic system developed for these studies to learn more about the effects of frequency on conventional ultrasonic techniques and to develop new test techniques based upon principles derived from these studies.

We are studying the spectral variations in broadbanded ultrasonic pulses as a function of the acoustical discontinuity with which they have interacted. Such a study will lead to improvements in the characterization of hidden flaws in materials and components by ultrasonic inspection.

The instruments composing the frequency analysis system were consolidated into a mobile rack mount to conserve space, simplify setup, and allow use conveniently at any location in the laboratory (see Fig. 8.1). Only two coaxial cable connections are required to connect into any ultrasonic test setup. Instrument power is obtained by plugging one large power cable into a voltage regulator. The system shown in Fig. 8.1 is for amplification, gating, and display of the signal

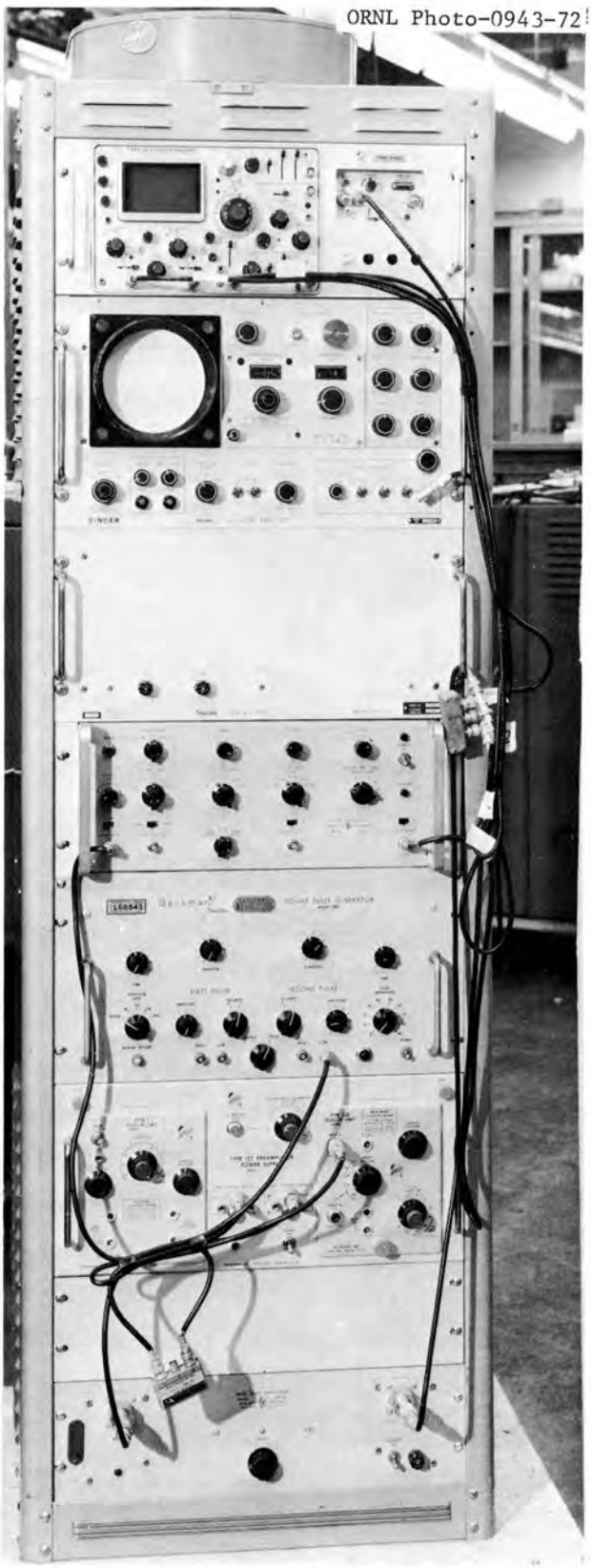

Fig. 8.1. Rack-Mounted Mobile Frequency Analysis System.

pulse of interest and presentation of its frequency spectrum. Its operation is quite similar to a system reported earlier.[3] A second pulse generator was added to improve the flexibility and stability of the gating network. An ultrasonic pulser was not included since various types can be used to drive the transducer in general frequency studies, and if this system is used to monitor a conventional ultrasonic inspection for increased information, the setup would already include an ultrasonic pulser.

The mobile frequency analysis system was "debugged" and used to test the effectiveness of the two-transducer technique for determination of reflector size[4] by consideration of the spectra of ultrasonic pulses interacting with the reflector. This study will increase our ability to characterize flaws in materials. The reflectors were cut from brass shim stock and had circular, elliptical and irregular shapes. Some were flat and others had irregular surface contour. They were mounted on small diameter pedestals in a water tank at random angles with respect to the surface of the water (shown in Fig. 8.2). Spectral data was taken in two orthogonal planes to determine the dimension of the reflector lying in each of these planes. These dimensions were assumed to be the average long and short dimensions of the reflector. The effectiveness of this method of ultrasonic size determination of a reflector is illustrated in Fig. 8.3 for the experimentally determined and actual dimensions of five of the ten reflectors, which are numbered the same as in Fig. 8.2. These results are encouraging for the characterization of actual flaws of random shape, contour, and orientation in materials

Ultrasonic Imaging

Optical techniques are useful to gain an understanding of ultrasonic interactions that are difficult to analyze by conventional methods employing electronic equipment only. Schlieren techniques image the sound itself, while Bragg diffraction and volume holography display any acoustical discontinuity with which the ultrasound field has interacted. We

---

[3] H. L. Whaley and K. V. Cook, Fuels and Materials Development Program Quart. Progr. Rept. December 31, 1968, ORNL-4390, p. 187.

[4] H. L. Whaley, K. V. Cook, and L. Adler, Fuels and Materials Development Program Quart. Progr. Rept. December 31, 1971, ORNL-TM-3703, p. 185.

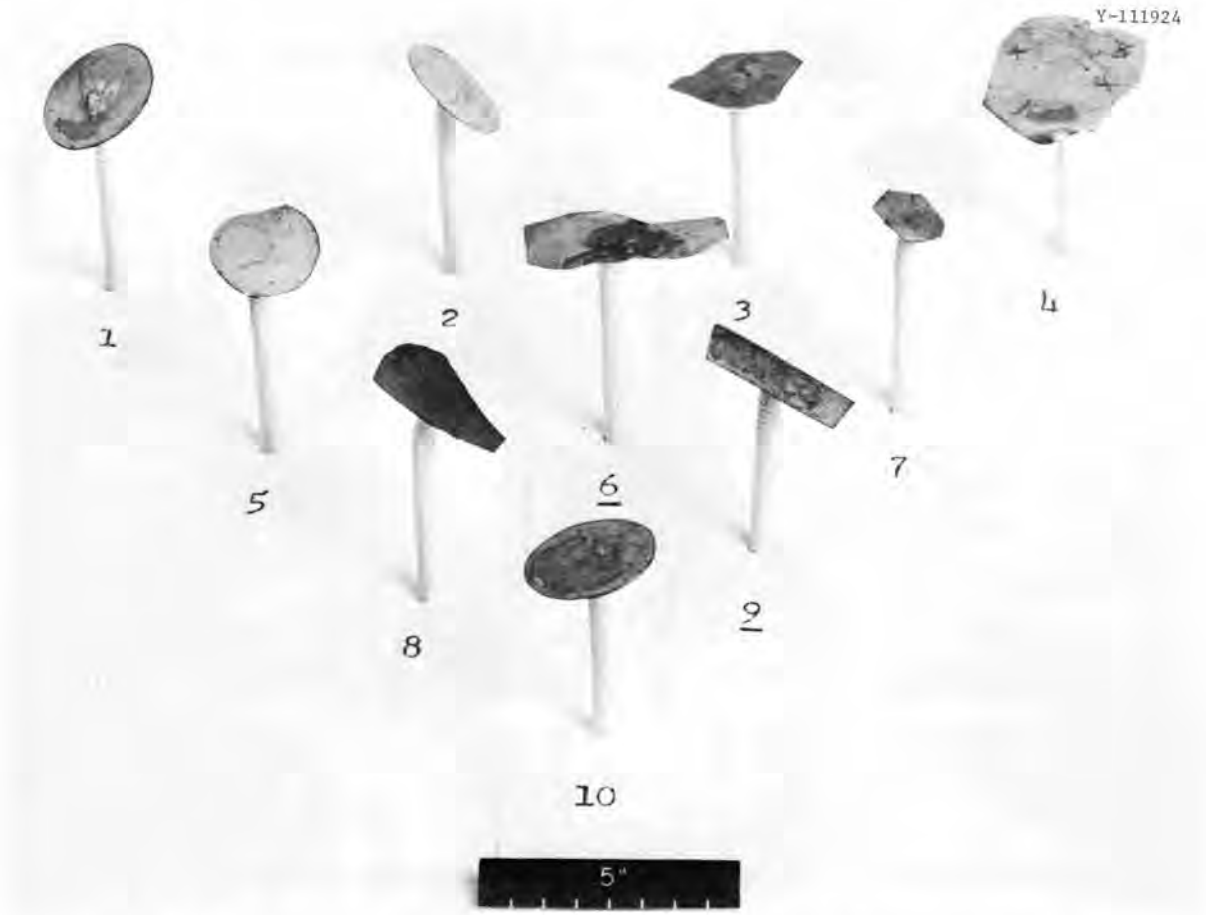

Fig. 8.2. Brass Shim Reflectors Used for Size Determination by Frequency Analysis. Reflectors had random orientation and various shapes and surface contours.

are interested in all such techniques and have developed a flexible optical system for various studies. The basic system is a mirror schlieren system with both continuous and pulsed light sources, a 6-in.-diam field of view and a television display. We have added a video tape system for data recording. Further experiments were done in the development of the Bragg diffraction system in order to determine the advantages and disadvantages of various arrangements of optical components. Figure 8.4 is a photograph of a representative setup using the auxiliary optical table and components which have proved useful for temporary setups although lacking sufficient stability for optimum results. We determined from this elementary arrangement some of the necessary improvements in mechanical rigidity, stability, and ease of adjustment of optical components that are necessary for efficient use. We are now designing an

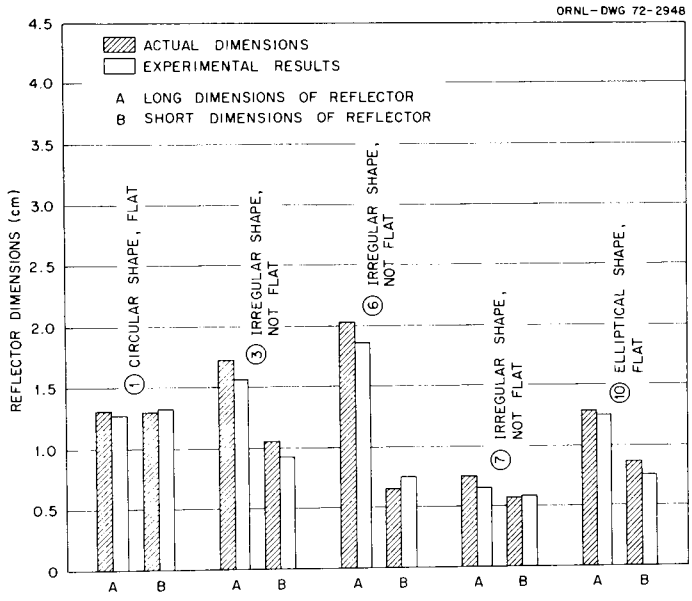

Fig. 8.3. Comparison of Actual Specimen Dimensions with Those Determined by Ultrasonic Frequency Analysis.

improved system. We are building the support structure and necessary optical benches, and other optical components such as long focal length cylindrical lenses and a precision pin hole positioner have been ordered. A new sample holder has been constructed which allows precise adjustment of sample position relative to the transducer.

Penetrating Radiation Inspection Methods

B. E. Foster S. D. Snyder

We continued our development of a closed-circuit television system[5] for enhancing and interpreting radiographs.

We have used a radiograph of 400-mesh screen on a high-resolution plate as a standard for assessing resolution capability of the system. The maximum magnification from subject to monitor screen that we have used is approximately 700X. This is achieved with a 40X microscope lens on the camera. Thus our optical magnification is only 40X, however, an additional magnification of 17.5X is obtained electronically from the vidicon mosaic to the monitor screen for the 700X total enlargement.

---

[5]B. E. Foster and S. D. Snyder, Fuels and Materials Development Program Quart. Progr. Rept. December 31, 1971, ORNL-TM-3703, p. 187.

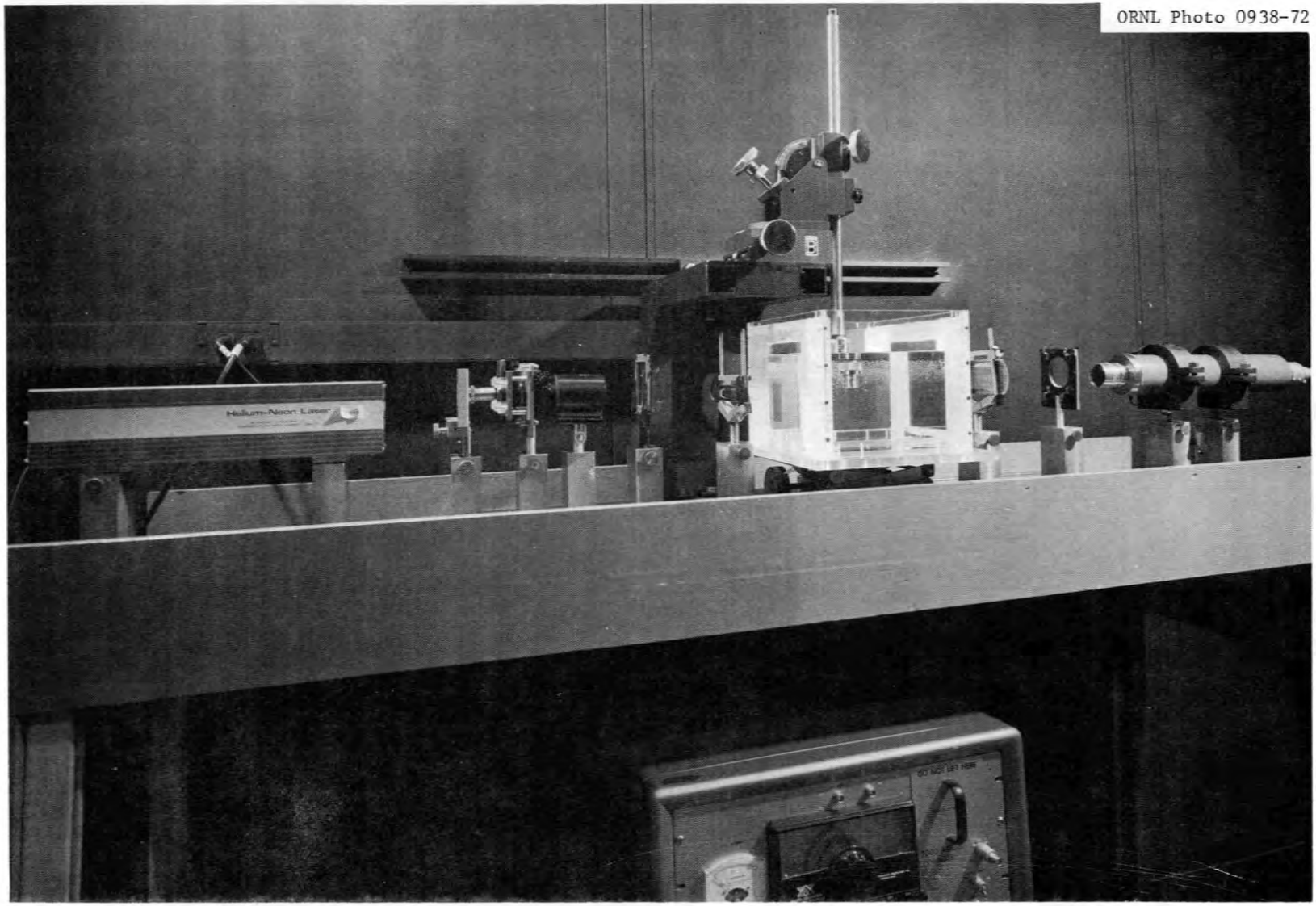

Fig. 8.4. Temporary Setup for Bragg Diffraction Experiments.

An optical magnification of only 2.3X (total magnification of 40X) has enabled us to image a crack or break in a single wire of the 400 mesh screen where the wire is only 30 μ in diameter. Expansion of the time base sweep on the sampling oscilloscope allows additional magnification of the extracted video signal to the x-y recorder. The normal time base sweep is 5 μ sec per line of video which is identical to the sweep of the TV monitor. This time base sweep of the sampling unit can be expanded to 1 μ sec/cm thus producing an additional 5X magnification to the x-y recorder. Therefore, with a 40X optical magnification, we have achieved 700X enlargement to the monitor screen, an additional 5X enlargement to the recorder for a total enlargement of 3500X.

An interesting and promising observation was made with this system using a radiograph of an aluminum step wedge on type M x-ray film. With an initial optical magnification of 6X (and an attendant 100X enlargement on the television monitor) no interference was observed due to film graininess. This was subsequently enlarged to 500X on a single line basis on the x-y recorder.

The system allows selection of one or more of the 500 lines of video on the monitor for evaluation as well as any section of any of the lines. This selected region can be recorded on a strip chart or x-y recorder for further evaluation, magnification, or other comparison.

Any region of the radiograph on the monitor screen can be selected, shaded (darkened or lightened) for more contrast or more comfortable viewing. This is achieved by utilizing two pulse generators. One of the generators is used to inject a pulse directly into the video system while the other generator serves as a pulse gate (controls height on monitor screen). The amplitude of the injected pulse controls the lightness or darkness of that area on the monitor. This effect is quite similar to the split screen viewing on a home television receiver except that in that case the studio is using multiple cameras. Of course, the remaining portion of the screen can be blanked out to prevent interference in the interpretation by the surrounding areas.

NDT Development for Steam Generators

R. W. McClung

We are developing nondestructive testing techniques to solve specific problems of nondestructive testing of steam generators for LMFBR. Emphasis is being given to the inspection of bore-side tube-to-tube sheet welded joints although other problems such as welded overlay for tube sheets and in-place inspection of tubing will also receive attention.

Radiography (B. E. Foster and R. W. McClung)

Because of the potential capabilities of both x-ray and radioisotopic sources for radiography of bore-side tube-to-tube sheet welds and the conflicting reports on which is the better we are planning studies on both. For x-ray studies we have borrowed a small rod anode x-ray tube and generator from the Los Alamos Scientific Laboratory (LASL). The x-ray tube is an HSZ-169 unit fabricated by the Dunlee Corporation, and it has an insertion rod 0.380 in. diam by 8.5 in. long. The tube is capable of operation at 80 kvp and 50 μ amp with a reported focal spot size of 0.25 mm. The power supply for the unit was fabricated by Universal Voltronics.

For preliminary checkout of the x-ray machine, radiographs were made of a 0.100-in.-thick stainless steel plate containing electro-discharge machined (EDM) notches varying in depth from 0.001 to 0.010 in. The smallest notch that could be readily observed was 0.002 in. deep and had a width of 0.002 in. From the radiographs it was evident that the x-ray beam was very nonuniform. Experiments performed to measure the focal spot of the x-ray tube demonstrated that an out-of-focus condition was present with a focal spot much larger than desired. Subsequent telephone conversations with personnel of both LASL and Dunlee revealed that the x-ray tube was new and had never been focussed.

Because of reported needs for occasional (to frequent) refocussing of the small rod anode x-ray tube, we had begun development of techniques for refocussing the x-ray tube without radiation hazard to personnel. A lead (Pb) box with 1/8 in.-thick walls and a 2 in. × 2 in. viewing port

covered with high density lead glass was fabricated to fit over the rod anode. A thin fluorescent screen was placed to encircle the rod anode. On energizing the x-ray tube only a very low level of diffuse illumination was observed and adjustment of the position of the focussing coil was extremely difficult. Because of these problems and the near term need to achieve an optimum focus to allow our radiographic studies to proceed, we temporarily set aside the shielded box approach. A series of radiographs were made on Polaroid film placed in an annular position around the rod anode, with trial-and-error adjustments made on the relative alignment of the focussing coil. The adjustments are difficult to make with precision since the coil is both clamped and adjusted on the rod anode by two sets of three set screws at 120° intervals (one set on each end of the coil assembly). However after a number of adjustments, a uniform 360° beam was achieved. We are fabricating a 0.020 in.-thick concentric ring of Pb containing 8 pinholes approximately 0.005 in. in diameter for measurement of the focal spot at 8 positions around the 360° radiation beam. This will allow optimizing the position of the focussing coil and calibrating the unit for proper coil current at the desired x-ray energies.

Liquid Penetrants (K. V. Cook and B. E. Foster)

We are developing techniques for the performance of liquid penetrant inspection of the tube-to-tube sheet weld joints. Because of the inadequate illumination for viewing when using fluorescent penetrants, a blacklight borescope and closed circuit television, we are investigating the use of red dye visible penetrants. Preliminary investigations with a 3/8-in.-diam, 28-in.-long borescope demonstrated adequate but marginal illumination and good sensitivity. The available borescope requires frequent replacement of bulbs since it is necessary to use voltages higher than those recommended. We are gathering data on other commercial borescope systems that are available in industry to determine the best way to resolve this problem.

Eddy Currents (C. V. Dodd and W. A. Simpson, Jr.)

We are continuing our research into the design parameters of an eddy-current system for the detection of defects in tubular sections.

This is the initial phase of a study to develop techniques for detection of flaws in tube-to-tube sheet welds and will also be applicable for inspection of installed tubing. We are presently investigating two avenues of approach - the first utilizes a dual encircling coil bridge technique and the second a reflection-type encircling coil which is compatible with existing equipment; viz, the phase sensitive eddy current instrument.

We have completed the computer design and have ordered a prototype reflection-type coil. These studies indicate that this type of coil has the same inherent discrimination against diametral and conductivity variations as the bridge configuration and is less affected by d.c. drifts in the driving circuit. In addition the reflection coil system appears to have slightly greater sensitivity to defects than the bridge design. Still another advantage is that defects near the surface are not discriminated against in the reflection coil configuration, a disadvantage of the unbalanced bridge.

Figure 8.5 shows the calculated response of the reflection coil to defects located on the inner and outer surfaces and midway through the tubular wall. From this it can be seen that the orientation of the characteristic figure-eight loop is determined by the depth of the defect; the size of the loop depends on the defect size. Thus the system should allow one to determine both the size and depth of the defect.

Ultrasonics (K. V. Cook and H. L. Whaley)

As a first step in the development of ultrasonic techniques for tube-to-tube sheet joints we have obtained four flat weld specimens simulating a typical joint. We modified a small hand drill to accept a thin small-diameter saw blade to allow rapid cutting of preliminary calibration notches in the thin-plate section of the welds. Such a notched specimen has been used to establish preliminary scanning techniques for evaluation of various transducer arrays to determine the optimum for subsequent design of in-bore probes. We have designed and are constructing an instrument module that will allow x-y-y′ plan view recordings of inspected areas. This will permit continuous, simultaneous, quantitative recording of the analogue amplitude of the discontinuity as well as its

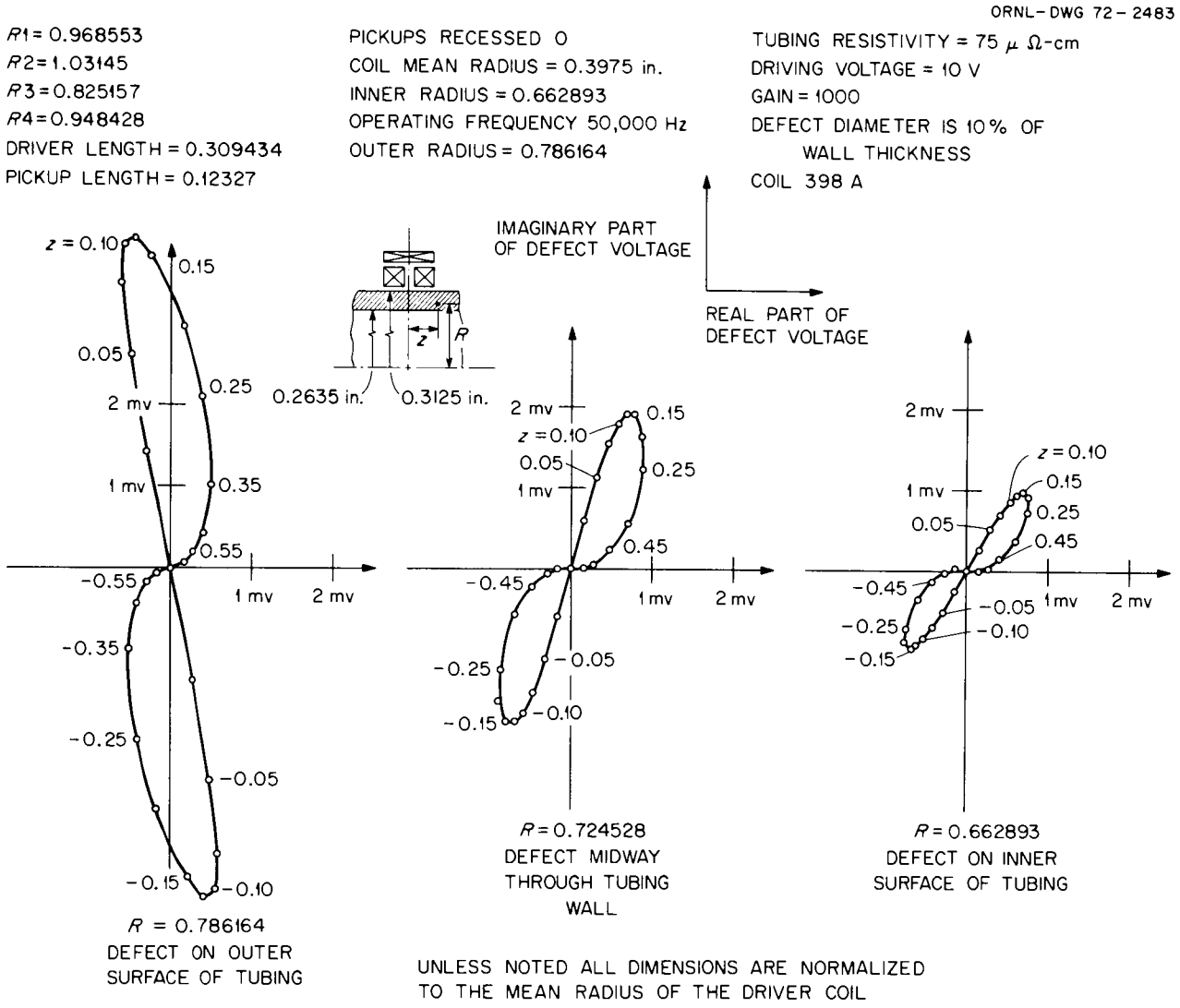

Fig. 8.5. Magnitude in Phase of the Defect Voltage Induced in a Typical Eddy-Current Coil.

x-y position within the specimen. This approach will not only enhance the amount of information that can be obtained from a scan but will also reduce the number of required recordings.

9. MECHANICAL PROPERTIES OF STRUCTURAL MATERIALS

W. R. Martin J. R. Weir, Jr.

The use of structural materials in nuclear reactors at progressively higher temperatures requires that we improve design methods to insure dependable and safe operation of such systems. The improved design methods involve the procurement of mechanical property data under various possible service conditions and that analytical methods be developed for using these materials properties to design complex structures. ORNL is currently active in both of these areas, but the present report will be concerned only with the mechanical properties information.

Although many of the methods that will be developed will be universally applicable for high temperature design, the current work is concerned primarily with LMFBR's. The materials being studied include types 304 and 316 stainless steel, types 304 and 316 stainless steel weldments prepared by different welding processes, and base metal and weldments of chromium-molybdenum steels of various compositions.

Mechanical Properties of Types 304 and 316 Stainless Steel

R. W. Swindeman R. D. Waddell, Jr.

We have now received 17 heats of type 304 and 3 heats of type 316 stainless steel to be used in our investigations of the heat-to-heat variations of the mechanical behavior of austenitic stainless steel. At this time we are working with 11 heats of type 304 stainless steel and the remaining 6 heats, along with the 3 heats of type 316 stainless steel, are in the process of being machined into specimens.

All the heats that have been received are listed in Table 9.1 along with vendor chemistry. The last five heats of type 304 were part of a large group originally purchased by the Maritime Service and have since been transferred to ORNL for use on LMFBR programs. Heat No. 9T2797 was originally purchased by Liquid Metal Engineering Company. The three heats of type 316 stainless steel were purchased by ORNL.

Table 9.1. Vendor Chemistry for Several of the Heats of Types 304 and 316 Stainless Steel Being Evaluated by ORNL

Source	Type	Heat Number	Size	Chemistry[a]							
				C	Mn	P	S	Si	Ni	Cr	N_2(b)
USS	304	9T2796	5/8-in. bar	0.048	1.22	0.028	0.015	0.48	9.70	18.6	0.031
Republic	304	8043813	1-in. plate	0.063	1.79	0.036	0.007	0.5	9.1	18.24	0.033
Carlson	304	600414	2 3/8-in. plate	0.061	1.48	0.016	0.014	0.64	9.56	18.88	0.054
Carlson	304	300380	2 3/8-in. plate	0.058	1.60	0.016	0.011	0.55	8.44	18.68	0.068
Carlson	304	K44086	1-in. plate	0.048	1.48	0.025	0.015	0.52	9.45	18.57	0.045
Allegheny	304	55697	5/8-in. bar	0.051	0.83	0.020	0.012	0.47	9.5	18.3	0.052[c]
Allegheny	304	346544	2-in. plate	0.07	1.06	0.022	0.012	0.45	9.68	18.42	
Allegheny	304	337330	1 1/8-in. plate	0.063	1.99	0.02	0.01	0.6	9.3	18.24	0.031
Allegheny	304	337187	1 1/2-in. plate	0.057	0.99	0.022	0.013	0.39	9.73	18.23	0.034
Allegheny	304	345866	3-in. plate	0.047	1.60	0.019	0.011	0.5	9.30	18.65	
USS	304	X22926	2-in. plate	0.05	1.43	0.029	0.024	0.71	9.7	18.96	0.041
USS	304	9T2797	1-in. plate	0.058	1.44	0.028	0.012	0.51	9.63	18.28	
USS	304	X23634	2-in. plate	0.05	1.54	0.021	0.022	0.53	9.5	18.31	
USS	304	X22807	2 1/2-in. plate	0.03	1.31	0.03	0.021	0.52	9.5	19	
USS	304	X23283	3/4-in. plate	0.06	1.42	0.024	0.024	0.54	9.5	18.9	
Allegheny	304	346779	3 3/4-in. plate	0.059	1.01	0.018	0.015	0.48	9.58	18.18	
Allegheny	304	346845	2 3/4-in. plate	0.06	0.99	0.015	0.01	0.52	9.36	18.55	
Allegheny	316	327686	1/2-in. plate	0.056	1.70	0.02	0.009	0.55	13	17.5	
USS	316	2P3212	1/2-in. plate	0.055	1.48	0.026	0.015	0.62	13.36	17.72	
Carlson	316	500613	1/2-in. plate	0.059	1.72	0.02	0.023	0.7	12.78	16.83	

[a]Weight percent.

[b]ORNL analysis.

[c]HEDL analysis.

Data from tests conducted during this report period, showing the effect of reannealing on grain size, 0.2% offset yield, and ultimate tensile strengths, for both room temperature and 427°C test temperatures, are given in Table 9.2. In a couple of cases the reannealed yield strengths are below the 30,000 psi minimum expected value at room temperature, and, in special cases, are below the 16,850 psi minimum expected at 427°C. There is also a significant difference in the shape of the yield curves of these heats, and, as was the case for the tensile data reported previously, the main difference appears to be the rate of hardening between the proportional limit and the 0.2% offset yield. The slopes of curves for all heats are essentially the same beyond the 0.2% offset yield stress.

We are beginning to generate strength data on several heats of type 304 stainless steel for 100 and 1000 hr rupture and for time to 1/2% creep strain at 17,000 psi stress. Figure 9.1 compares time to rupture for eight heats at 593°C and 30,000 psi stress in both the as-received (A-240 or A-479) and reannealed conditions. The range in rupture times is from about 120 to 2750 hr for the as-received materials and from 93 to about 3100 hr for the reannealed material. Comparison is shown in Fig. 9.2 for the same eight heats tested at 593°C and at a stress of 35,000 psi. The rupture times range from 18 to 325 hr in the as-received condition, and from 25 to 300 hr in the reannealed condition.

Figures 9.3, 9.4, 9.5, and 9.6 show creep curves for both as-received and reannealed materials tested at 593°C and at 30,000 and 35,000 psi for several of the heats of type 304 stainless steel. It is evident from the curves that there is a significant variation in creep behavior of these heats and that reannealing did not appreciably reduce this variation. Note that the strain indicated here is creep strain and not total strain, the strain on loading can vary considerably from weak to strong heats. Tests are now under way on a single heat at 593°C and 35,000 psi (Heat No. X22926) to determine what degree of variation might be expected within a single heat. This type of information should be very helpful in judging the significance of the variation we see from heat-to-heat.

Table 9.2. Comparison of Yield and Ultimate Strengths for Several Heats of Type 304 Stainless Steel at a Strain Rate of 0.05 in.-in.$^{-1}$-min^{-1} in the As-Received and Reannealed Conditions

Heat Number	Condition	Grain Size[b]	Test Temperature (°C)	0.2% Offset Yield Strength (ksi)	Ultimate Strength (ksi)
600414	A240	2–3	(a)	36.8	82.0
	A240	2–3	427	19.6	65.4
	1065°C (annealed)	2–3	(a)	32.9	84.3
	1065°C (annealed)	2–3	427	16.0	63.2
300380	A240	3–4	(a)	39.8	91.4
	1065°C (annealed)	2–4	427	17.5	63.9
8043813	A240	3–5	(a)	33.4	89.4
	A240	3–5	427	20.7	62.1
K44086	A240	3–4	(a)	37.4	89.9
	A240	3–4	427	23.3	64.1
	1065°C (annealed)	2–3	(a)	31.7	88.5
	1065°C (annealed)	2–3	427	15.8	63.3
55697	A479	1–2	(a)	30.0	87.0
	A479	1–2	427	20.5	59.5
	1065°C (annealed)	1–3	(a)	28.0	84.4
	1065°C (annealed)	1–3	427	15.2	59.8
9T2796	A479	3–5	427	27.0	62.9
337187	A240	1–3	(a)	34.7	86.7
	A240	1–3	427	22.0	60.4
	1065°C (annealed)	1–2	(a)	28.4	84.4
	1065°C (annealed)	1–2	427	13.5	63.9
337330	A240	3–4	(a)	40.0	
	A240	3–4	427	25.6	64.4
	1065°C (annealed)	5–6	(a)	33.3	89.7
	1065°C (annealed)	5–6	427	17.4	63.0
X22926	A240	3–4	(a)	39.0	86.4
	A240	3–4	427	22.2	62.0
	1065°C (annealed)	3–4	(a)	31.6	85.2
	1065°C (annealed)	3–4	427	15.4	60.2

[a]Room temperature.

[b]ASTM grain size number.

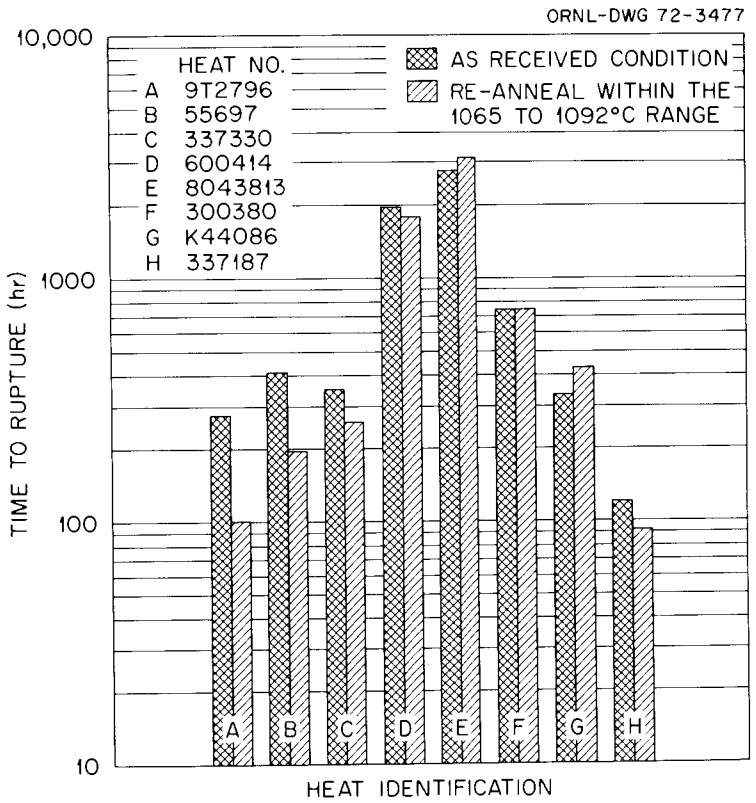

Fig. 9.1. Time to Rupture at 593°C for Eight Heats of Type 304 Stainless Steel Tested at 30,000 psi.

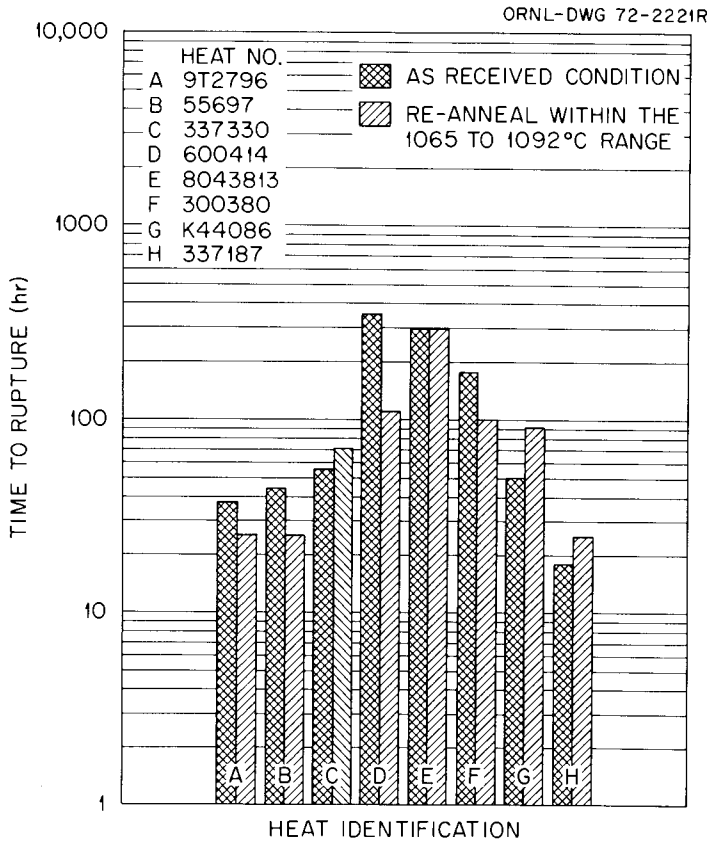

Fig. 9.2. Time to Rupture at 593°C for Eight Heats of Type 304 Stainless Steel Tested at 35,000 psi.

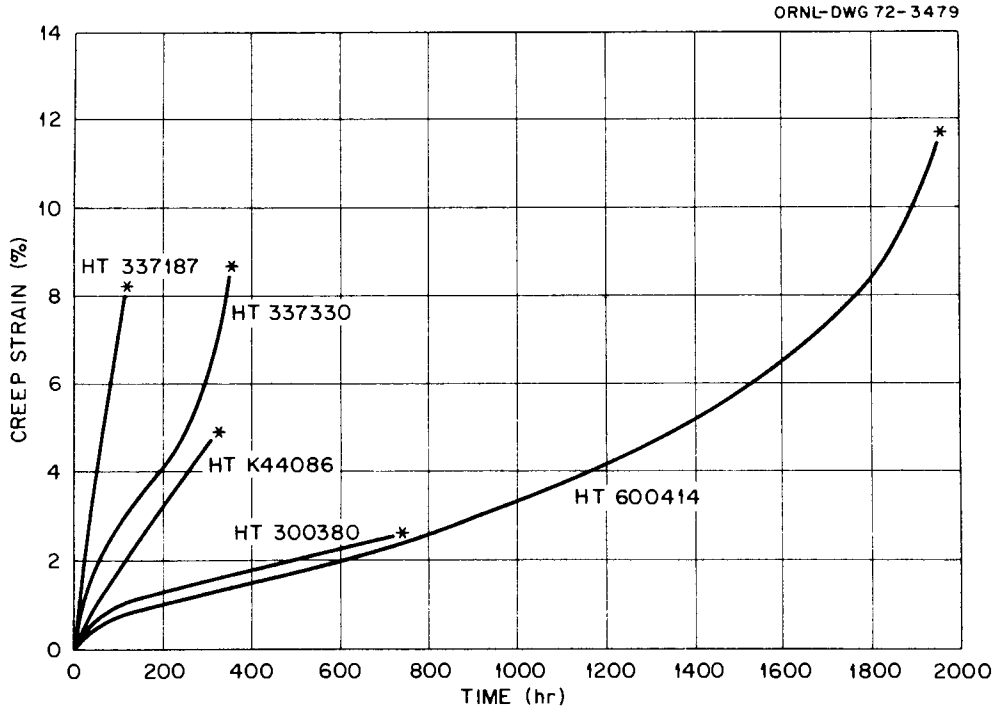

Fig. 9.3. Comparison of Creep Curves at 593°C and 30,000 psi for Five Heats of Type 304 Stainless Steel.

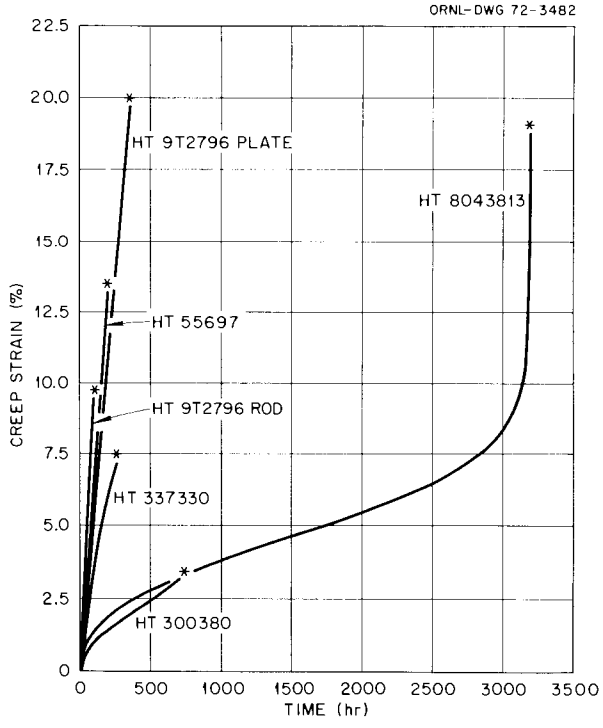

Fig. 9.4. Comparison of Creep Curves at 593°C and 30,000 psi for Five Heats of Type 304 Stainless Steel Annealed in the 1065 to 1092°C Range.

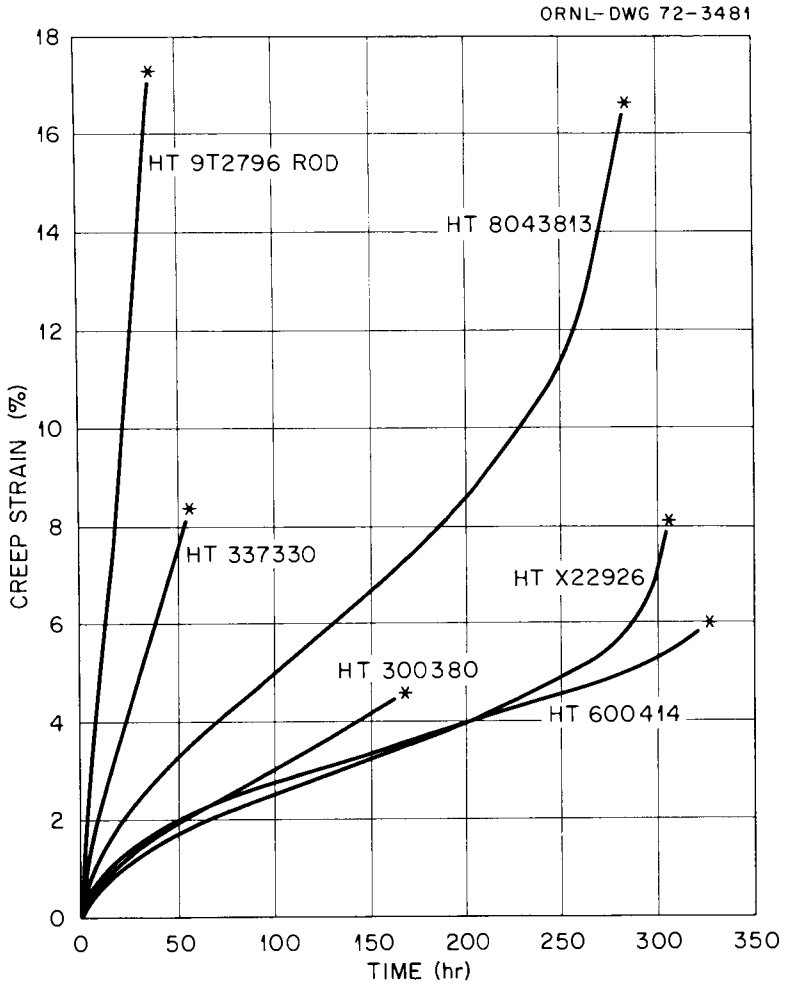

Fig. 9.5. Comparison of Creep Curves at 593°C and 35,000 psi for Six Heats of Type 304 Stainless Steel.

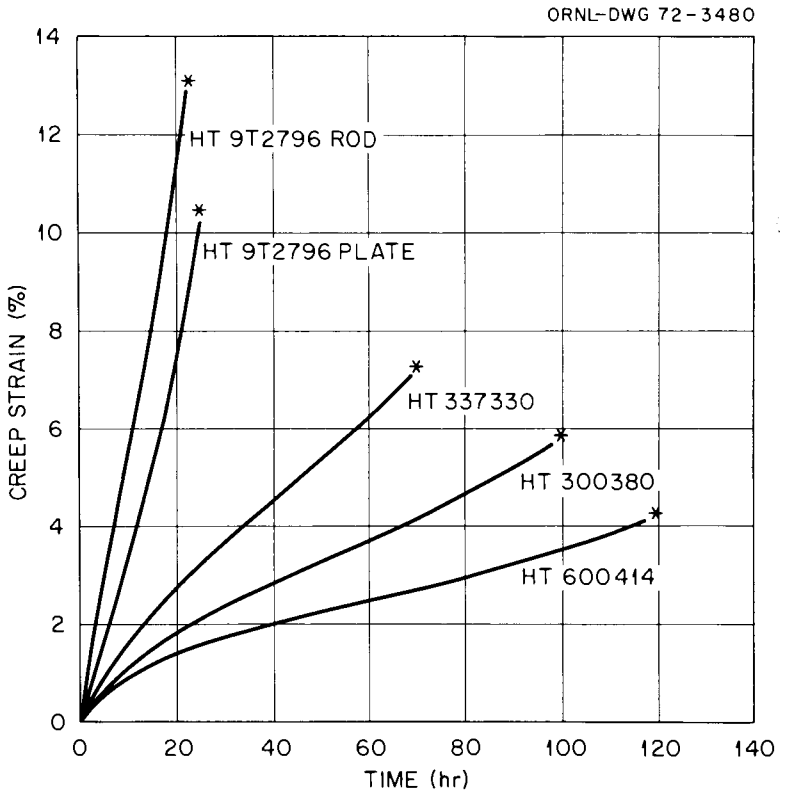

Fig. 9.6. Comparison of Creep Curves at 593°C and 35,000 psi for Four Heats of Type 304 Stainless Steel Annealed in the 1065 to 1092°C Range.

Figure 9.7 indicates time to 1/2% creep strain for nine heats of type 304 stainless steel and compares this to the expected time for an average heat as given by code case 1331-5.

Figures 9.8 through 9.11 are photomicrographs showing grain size for both the as-received and reannealed samples from eight of the heats now being studied.

At this time no attempt has been made to correlate tensile and creep properties with heat treatment, chemistry, or thermal aging; however, this will be done after all heats to be studied are incorporated into the program.

As mentioned earlier three heats of type 316 stainless steel have been received and are now being machined into specimens. Testing of these heats will begin as soon as the inspected specimens have been received.

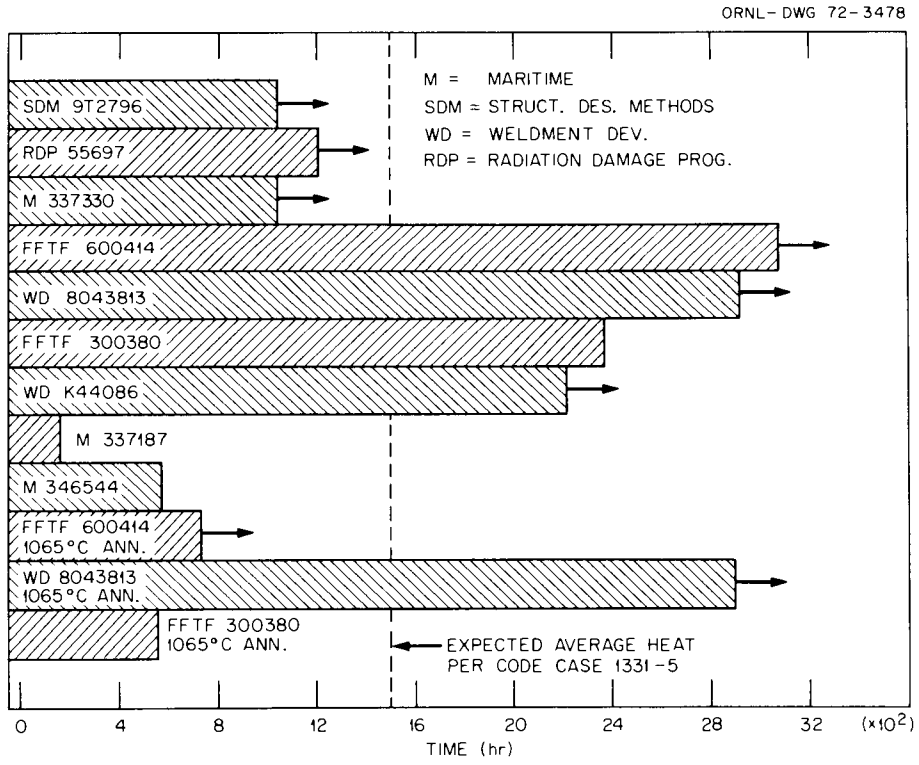

Fig. 9.7. Time to 1/2% Creep Strain at 17,000 psi Stress and 592°C.

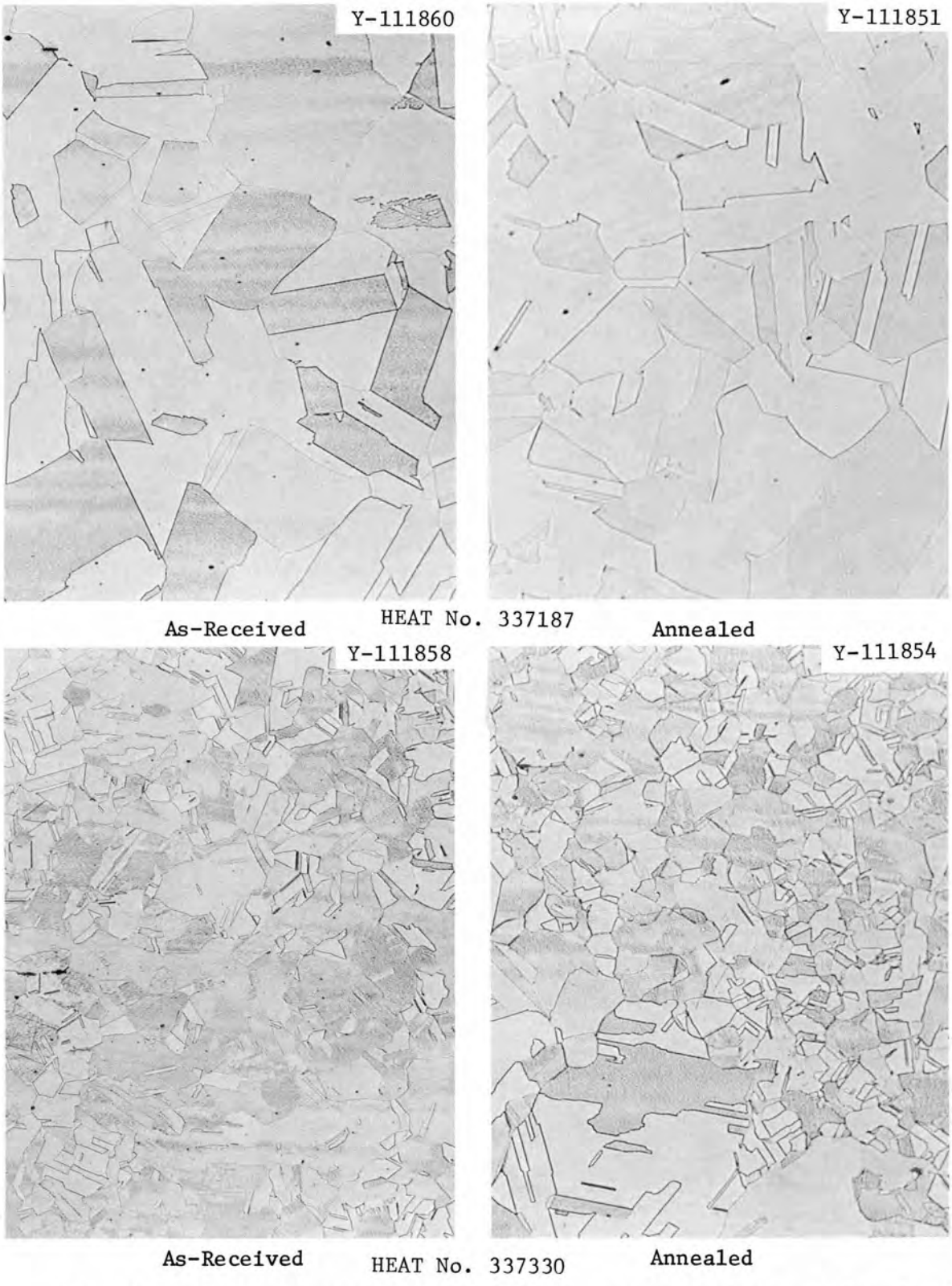

Fig. 9.8. Photomicrograph Showing Grain Size in Both the As-Received Condition and After Annealed in the 1065 to 1092°C Range. 100×.

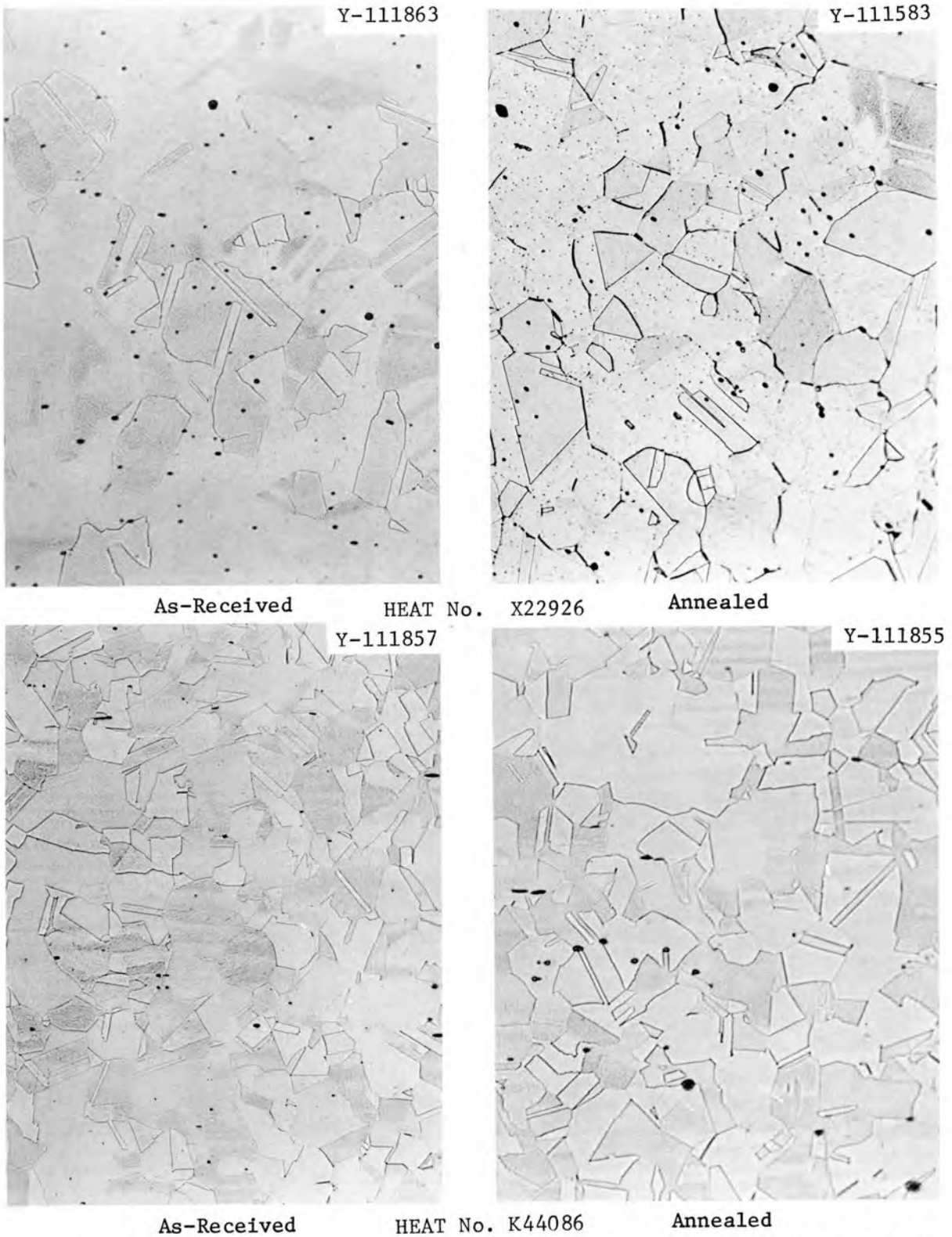

Fig. 9.9. Photomicrograph Showing Grain Size in Both the As-Received Condition and After Annealed in the 1065 to 1092°C Range. 100×.

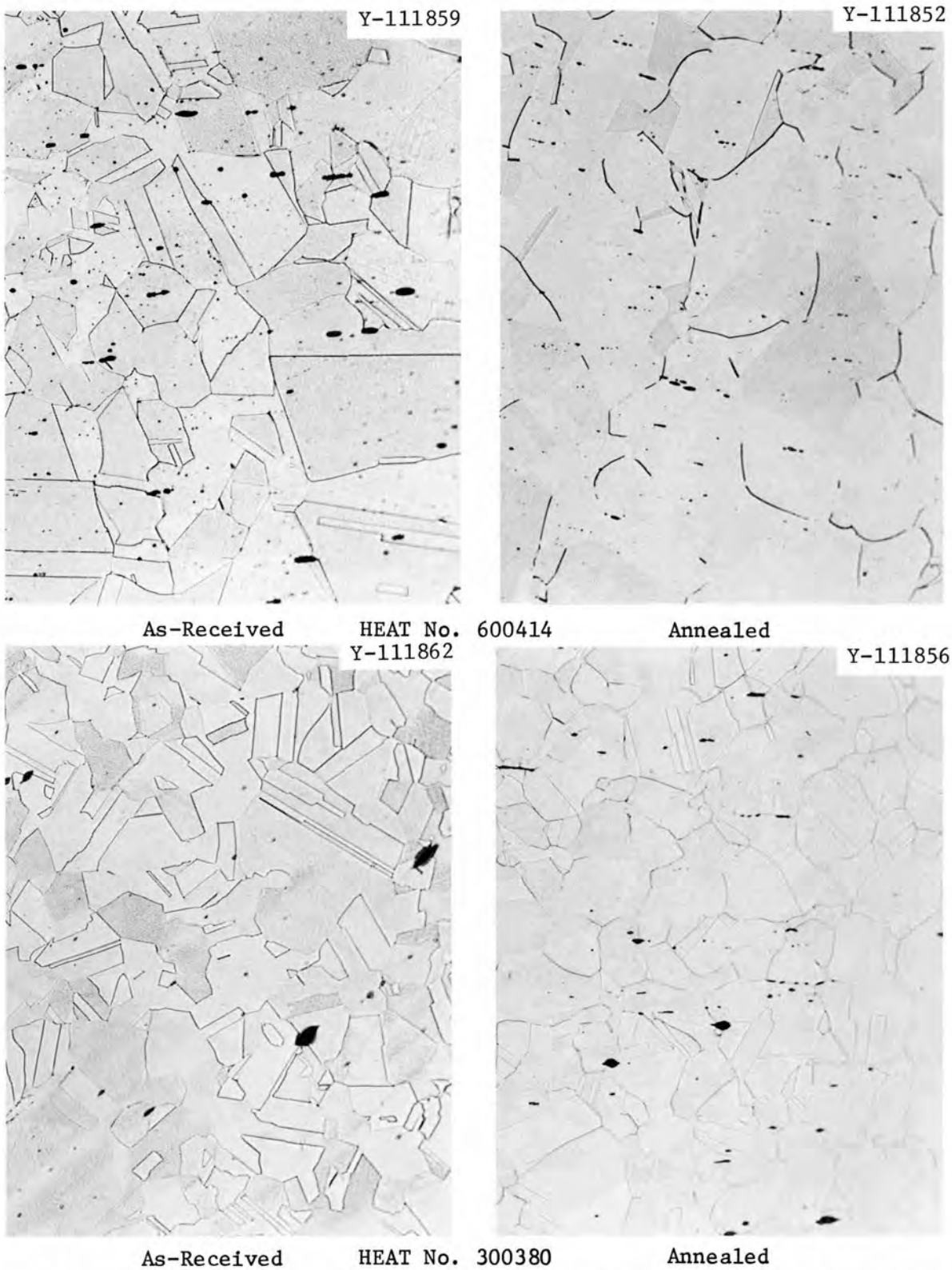

Fig. 9.10. Photomicrograph Showing Grain Size in Both the As-Received Condition and After Annealed in the 1065 to 1092°C Range. 100×.

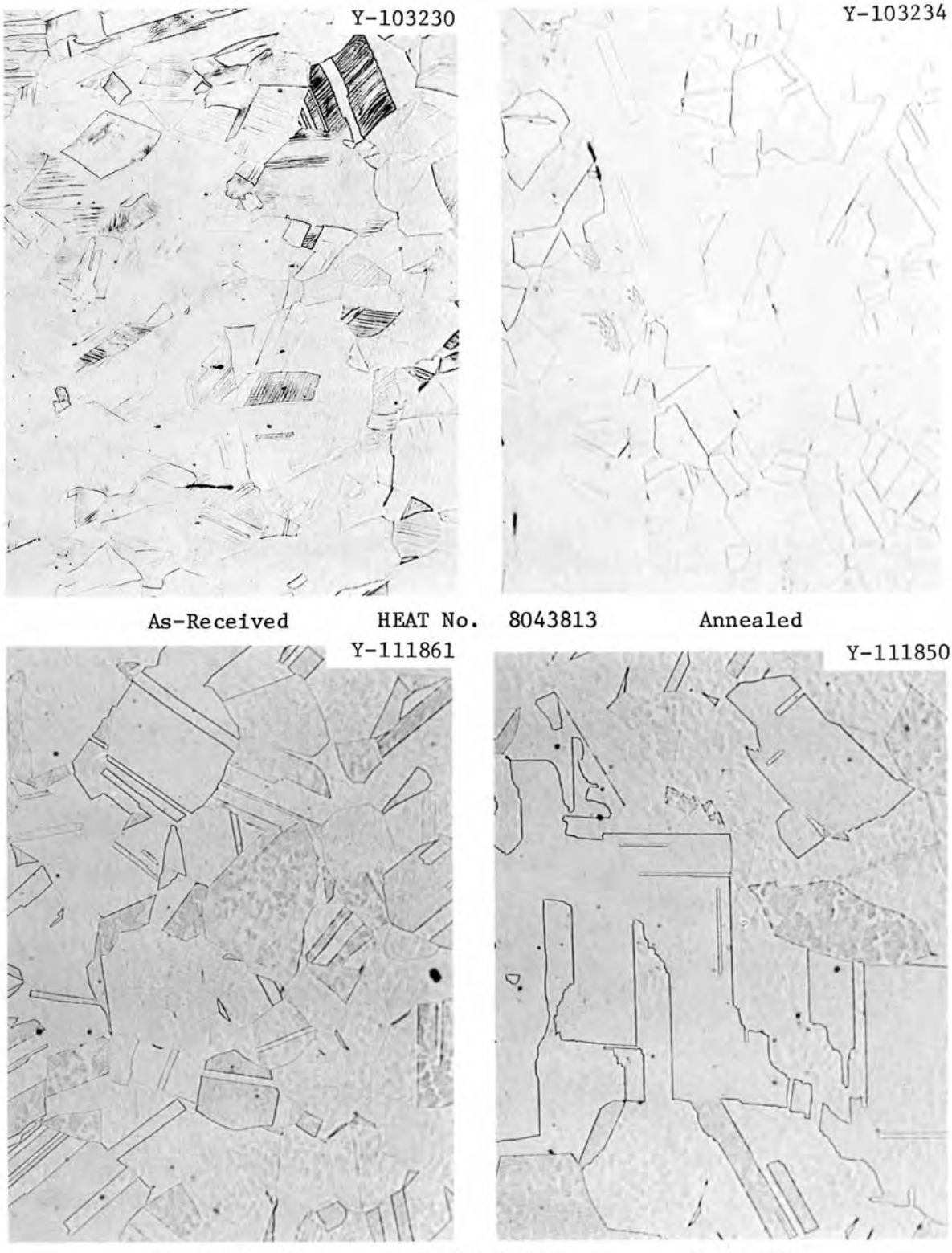

Fig. 9.11. Photomicrograph Showing Grain Size in Both the As-Received Condition and After Annealed in the 1065 to 1092°C Range. 100×.

A problem of immediate concern to us is how best to represent the creep data we are producing. The usual methods, tables and graphs, often lack the detail which is important to anyone trying to use the information to develop strain-time-stress-temperature correlations. We see two methods of handling data. The first is to store everything on magnetic tapes which then could be loaned to users. The second is to develop a generalized equation, such as a polynomial, which would smooth short-time perturbations in data yet preserve the essential shape and provide statistics pertaining to the scatter. Presently, we store all of our data on IBM cards so the magnetic tape approach is quite feasible. The polynomial has some attractive features, however, and we are investigating this approach.

Figure 9.12 shows the fit of two five-term polynomial equations to creep data for type 304 stainless steel at 20,000 psi and 621°C. Both equations are of the form:

$$\varepsilon = A_0 + A_1 t^{n_1} + A_2 t^{n_2} + A_3 t^{n_3} + A_4 t^{n_4} \qquad (1)$$

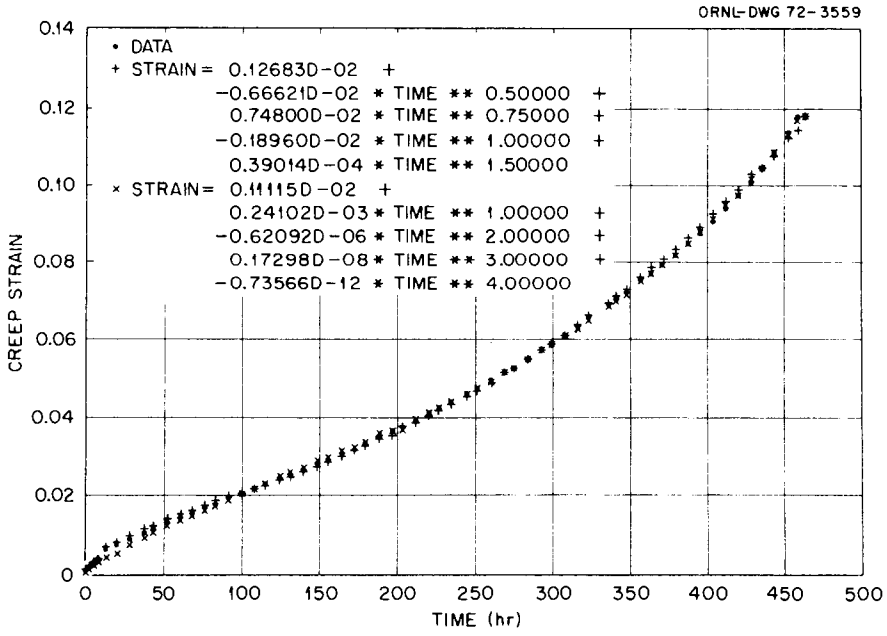

Fig. 9.12. The Fit of Two Polynomial Equations to Creep Data for Type 304 Stainless Steel Obtained at 20,000 psi and 621°C (Heat 9T2796 annealed).

where ε is creep strain and t is time. The values of the exponents, n_i, are selected according to the general shape of the creep curve while the values of A_i are calculated by a least squares method. In Fig. 9.12 it appears that the equation which includes fractional exponents, 0.5, 0.75, 1, and 1.5, provides a better fit to the data in the primary creep period than the equation having the exponents 1, 2, 3, and 4. Neither equation is completely satisfactory, and, in our opinion, a more accurate representation could be developed by expanding the polynomial to more than five terms. We are still using the five-term equation to fit the primary portion of the creep curve, however, and the results we have obtained for a number of tests are summarized in Table 9.3 while a graphical comparison to one test is shown in Fig. 9.13. We think it is significant that the standard error of estimate, S,* decreases with

*We define S by:

$$S = \left(\frac{\Sigma (\varepsilon_{meas} - \varepsilon_{calculated})^2}{\text{Number Data} - 5} \right)^{1/2} .$$

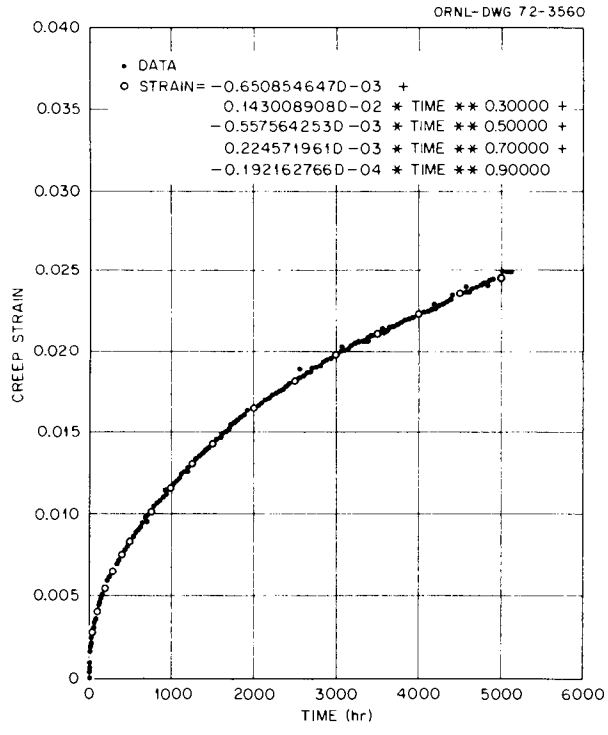

Fig. 9.13. The Fit of a Five Term Polynomial Equation to Creep Data for Type 304 Stainless Steel Obtained at 17,500 psi and 593°C (Heat 9T2796 annealed).

Table 9.3. A Comparison of the Fit of Polynomial and Exponential Creep Equations to Data Generated on Type 304 Stainless Steel

Heat Number	Specimen Number	Temperature (°C)	Stress (ksi)	Time (hr)	Creep Strain (in./in.)	Primary[a] Strain (in./in.)	Minimum[a] Rate (in./in./hr)	S_{poly}[b] (in./in.)	$S_{\beta=1}$[c] (in./in.)	$S_{\beta=3/4}$[c] (in./in.)	$S_{\beta=1/2}$[c] (in./in.)	$r_{\beta=1}$ (1/hr)	$r_{\beta=3/4}$ $(1/hr)^{3/4}$	$r_{\beta=1/2}$ $(1/hr)^{1/2}$
9T2796	RP9	538	35	346	0.0167	0.0046	3.45×10^{-5}	0.00020	0.00038	0.00059	0.00086	0.01003	0.03627	0.1273
9T2796	RP24	538	30	1171	0.0125	0.0055	4.93×10^{-6}	0.00012	0.00012	0.00032	0.00072	0.00365	0.01757	0.08192
9T2796	RP26	538	20	5040	0.0031	0.0036	-1.04×10^{-7}	0.00009	0.00009	0.00019	0.00039	0.000835	0.00578	0.00387
9T2796	RP31	538	10	5035	0.00046	0.00046	-1.69×10^{-9}	0.00004	0.00006	0.00005	0.000038	0.00119	0.00798	0.0517
9T2796	RP54	593	25	202	0.0276	0.0088	9.16×10^{-5}	0.00020	0.00048	0.00022	0.0011	0.0244	0.0755	0.223
9T2796	RP7	593	25	201	0.0294	0.0097	9.65×10^{-5}	0.00019	0.00048	0.00021	0.00098	0.0245	0.0755	0.224
9T2796	RP32	593	22.5	352	0.0179	0.0067	3.11×10^{-5}	0.00011	0.00045	0.00012	0.00050	0.0169	0.0581	0.192
9T2796	RP58	593	20	3500	0.042	0.022	5.72×10^{-6}	0.00034	0.00099	0.00088	0.0018	0.0012	0.00756	0.0471
9T2796	RP40	593	17.5	5131	0.025	0.015	1.95×10^{-6}	0.00012	0.00083	0.00037	0.00091	0.000932	0.00642	0.0430
9T2796	RP62	593	12.5	5660	0.0077	0.0073	5.9×10^{-8}	0.00007	0.00032	0.00022	0.00058	0.000776	0.00552	0.0380
8043813	P4[d]	649	28	21	0.182	0.02	7.6×10^{-3}	0.0013	0.0016	0.0017	0.0031	0.415	0.631	0.901
8043813	P1[d]	649	25	70	0.139	0.014	1.77×10^{-3}	0.00059	0.0012	0.00052	0.0018	0.0973	0.221	0.462
8043813	P2[d]	649	22	351	0.075	0.031	1.24×10^{-4}	0.0005	0.0023	0.00091	0.0014	0.0258	0.0811	0.246
8043813	P3[d]	649	20	604	0.044	0.019	3.99×10^{-5}	0.00022	0.0013	0.0006	0.0006	0.0221	0.0719	0.224
8043813	P5[d]	649	17	5025	0.028	0.017	2.23×10^{-6}	0.00040	0.0019	0.0012	0.00048	0.00189	0.0115	0.0680
8043813	P15	649	15	2000	0.0087	0.0073	6.46×10^{-7}	0.00012	0.00041	0.00019	0.00019	0.00999	0.0393	0.149
8043813	P16	649	12.5	2010	0.0057	0.0052	2.34×10^{-7}	0.00006	0.00038	0.00014	0.00020	0.00538	0.0248	0.110
8043813	P17	649	10	2003	0.0037	0.0035	7.93×10^{-8}	0.00010	0.00021	0.00009	0.00022	0.00268	0.0143	0.0744
8043813	P32	649	8	2000	0.0015	0.0014	1.15×10^{-8}	0.00005	0.00011	0.00007	0.00009	0.00271	0.0145	0.0752

[a] The primary and minimum creep-rate data were obtained by fitting a five-term polynomial through the creep data. This equation is of the form: $\epsilon = A_0 + A_1 t^{0.3} + A_2 t^{0.5} + A_3 t^{0.7} + A_4 t^{0.9}$.

[b] Standard error of estimate for the polynomial.

[c] Standard error of estimate for the exponential equation $\epsilon = \epsilon_t(1-\exp-rt^{\beta}) + \dot{\epsilon}_{min} t$ where $\beta = 1$, $3/4$, or $1/2$.

[d] Extension obtained from the load train.

decreasing creep strain. This behavior implies that the polynomial has not been optimized. For tests which did not produce large creep strains, the polynomial fits the data with a value for S better than the accuracy expected from the extensometer ($\pm$0.000125 in./in.).

We have used the polynomial to calculate the minimum creep rate, $\dot{\varepsilon}_{min}$, and the primary creep strain, ε_t for each test listed in Table 9.3. These data are reported in Table 9.3. The values were generally in good agreement with those calculated by visual methods.[1]

Assuming the equation:

$$\varepsilon = \varepsilon_t[1 - \exp(-rt^{\beta})] + \dot{\varepsilon}_{min}t \ , \qquad (2)$$

We calculated r by a least squares method using just the data between 5 and 95% of ε_t. Calculations were performed assuming values for β of 1, 3/4, and 1/2. The results of these calculations are included in Table 9.3. In most instances the exponential creep Eq. (2) does not fit the creep data as well as the polynomial. Thus, insofar as data representation is concerned the polynomial is still favored. Because the exponential creep equation, assuming $\beta = 1$, has only three constants which must be evaluated in terms of the stress and temperature dependency it is still more desirable from a correlation viewpoint. On the other hand, it presents problems to the experimentalists working with type 304 stainless steel in the temperature range from 450 to 650°C. The difficulty rests with the assumption that the primary creep component, ε_t, is reached at the point in time where the minimum creep rate occurs. The minimum can only be determined after observing the initiation of tertiary creep. Thus, at meaningful stresses and temperatures, extremely long times are required to establish the values of ε_t and r. Other equation forms exist which do not assume exhaustion of primary creep and in some ways these are more convenient. As an example, we have taken

---

[1] Fuels and Materials Development Program Quart. Progr. Rept. September 30, 1971, ORNL-TM-3550, Table 9.2, p. 179.

creep data for type 304 stainless steel (heat No. 8043813) at 649°C and used two points from each curve to determine the constants, t_c and ε_c in the equation:

$$\frac{t}{t_c} = \sinh \left(\frac{\varepsilon}{\varepsilon_c}\right)^2 \tag{3}$$

where t is time and ε is creep strain. The fit of the data to the equation is indicated in Fig. 9.14. There are a number of similar equations which might prove more promising. The important point is that equations such as (3) do not require a breakdown of the creep strain into two components as in Eq. (2) and this could prove advantageous in some instances.

No matter what type of strain-time relationship one proposes, there still exists the problem of describing the stress and temperature dependency of creep. As a result of Garofalo's[2] studies of the creep of type 316 stainless steel under true stress conditions, the hyperbolic sine stress dependency has become popular, even for constant load creep conditions. The equation is of the form:

$$\text{rate} = A[\sinh\alpha\sigma]^n \tag{4}$$

where σ is the stress and A, α, and n are constants which depend on temperature. We attempted to fit our minimum creep rate data at 649°C for type 304 stainless steel (Heat No. 8043813) to this equation and obtained the results summarized in Fig. 9.15. The upper plot compares minimum creep rate data, $\dot{\varepsilon}_{min}$, measured visually with the values we determined using the five-term polynomial equation described previously. These show excellent agreement with one another. There appears to be downward curvature in the data trend with decreasing $\dot{\varepsilon}_{min}$. This trend is expected when the hyperbolic sine, Eq. (4), is applicable. The line in the upper Fig. 9.15 corresponds to a fit of Eq (4) to the data.

---

[2]F. Garofalo, C. Richmond, W. F. Domis, and F. von Gemmingen, "Strain-Time, Rate-Stress, and Rate-Temperature Relations During Large Deformations in Creep," Joint International Conference on Creep, The Inst. of Mech. Engr., London (1963), pp. 1–31.

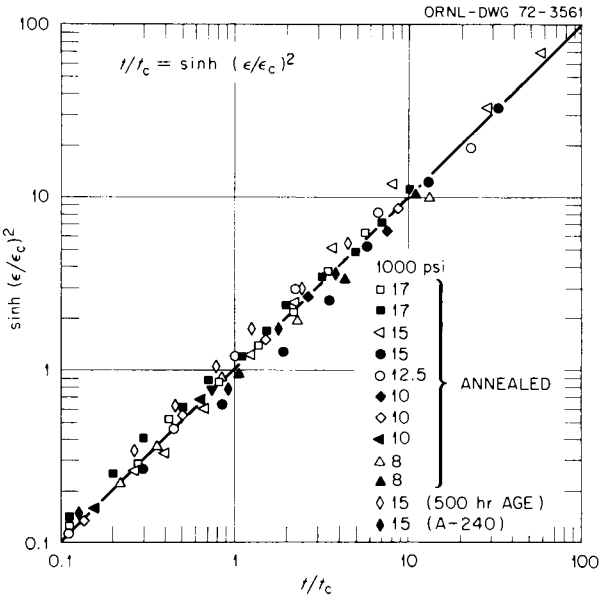

Fig. 9.14. The Fit of a Creep Equation Describing Time as Dependent on Strain to Creep Data for Type 304 Stainless Steel at 649°C and Several Stresses (Heat 8043813 annealed except where noted).

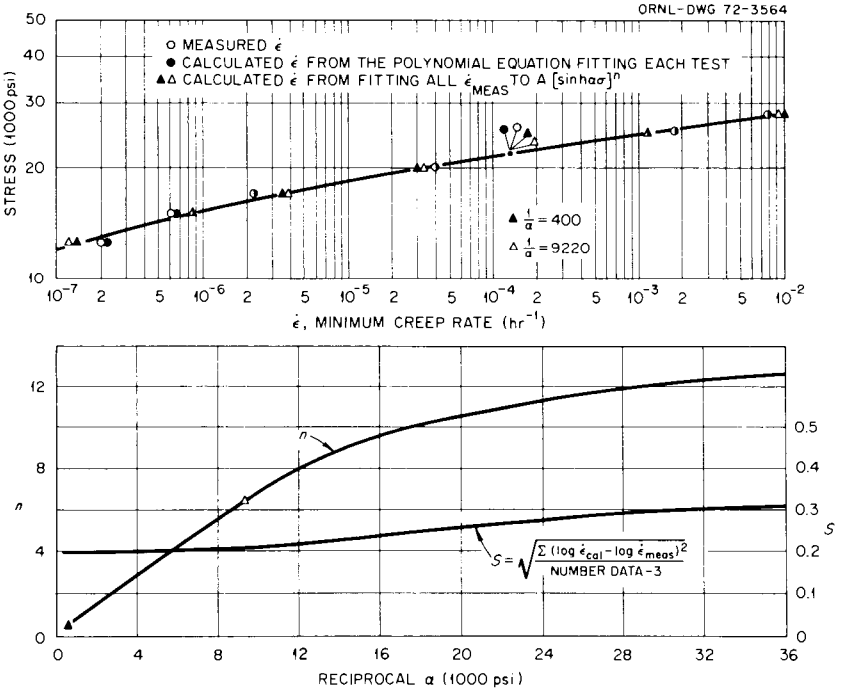

Fig. 9.15. Comparison of the Minimum Creep Rates Measured for Type 304 Stainless Steel (Heat 8043813 annealed) at 649°C with (1) Values Calculated by Fitting a Polynomial Through Each Test and (2) Values Calculated by Fitting a Hyperbolic Stress Dependency to the Measured Data. Lower figure shows how the exponent n and the standard error of estimate vary with the α term in the hyperbolic sine.

The picture is complicated however by the fact that there does not appear to be a unique solution to the equation. The lower Fig. 9.15 shows that many combinations of n and $1/\alpha$ will result in practially the same standard error of estimate. Furthermore, it is possible that the curvature is even less than indicated, since we cannot guarantee that the test at 12,500 psi really achieved the minimum creep rate in only 2000 hr. We have not found any convincing evidence to support the need for Eq. (4) to describe the minimum creep rate data we have obtained on Heat No. 9T2796. The data at 593°C fall within the range reported by Williams[3] for tests performed to 40,000 hr and it appears that a simple power relationship is adequate providing the stress exponent is between 8 and 10.

Exploratory Tests for Design Methods Program

R. W. Swindeman

The exploratory testing of the material purchased for the Structural Design Methods Program (AEC Activity No. 10556) has been extended to include some step-loading creep tests. The results of two such tests at 593°C are compared to constant load data in Fig. 9.16. In contrast to the behavior exhibited by Heat No. 8043813 at 649°C (ref. 4), this heat (9T2796) yielded plastically each time the stress was incremented by 2.5 ksi. The plastic flow resistance has been significantly increased by the creep exposure, however, as evidenced by the smaller loading strains, relative to virgin specimens, introduced when specimens RP71 and 76 were stepped to 15 ksi after 1500 hr. The creep component of strain showed nearly identical behavior as observed for Heat No. 8043813 at 649°C. The pattern is that at low stresses the strain response after

---

[3]W. L. Williams, "Parameter and Long-Life Creep-Rupture Tests on Type 304 Steel," Time-Temperature Parameters for Creep-Rupture Analysis, ASM Publication No. D8-100.

[4]Fuels and Materials Development Program Quart. Progr. Rept. December 31, 1971, ORNL-TM-3703, p. 200.

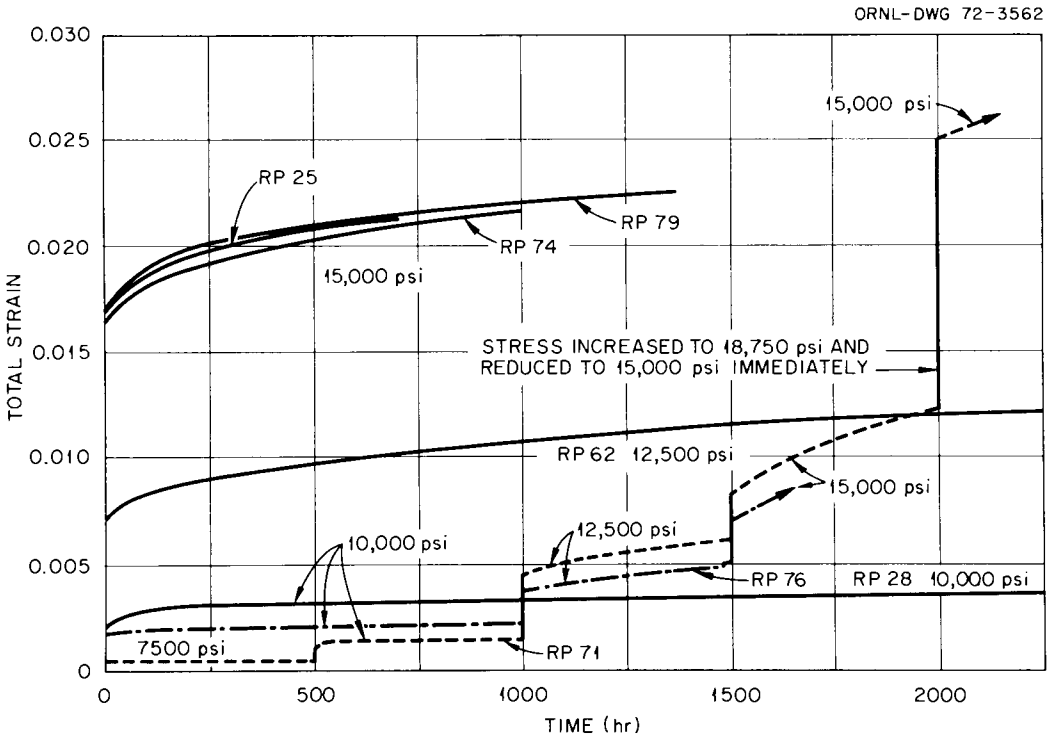

Fig. 9.16. Comparison of Constant Load and Step Load Strain-Time Response for Type 304 Stainless Steel at 593°C (Heat 9T2796 annealed).

step loading falls between the predictions of the strain-hardening and time-hardening rules while at the higher stresses creep is more rapid than would be predicted by either rule.

Relaxation tests to 100 hr were performed on Heat No. 9T2796 at 566 and 621°C holding strain at 0.5%. The results are summarized along with previously reported data[5] in Fig. 9.17. These tests produced greater relaxation in 100 hr than we expected from our earlier results; hence, it will be necessary to continue testing until the trend is more accurately established.

---

[5]Fuels and Materials Development Program Quart. Progr. Rept. December 31, 1971, ORNL-TM-3703, Table 9.4, p. 204.

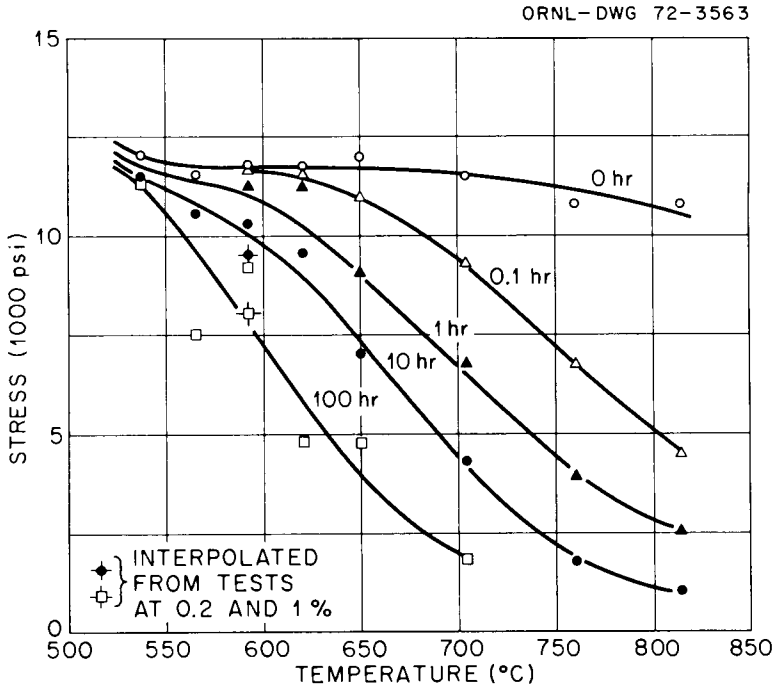

Fig. 9.17. Relaxation Stresses at Several Temperatures and Times. Data were obtained from tests at 0.5% total strain on type 304 stainless steel (Heat 9T2796 annealed).

Our efforts to explore the cyclic hardening behavior of type 304 stainless steel (Heat No. 9T2796) are under way. These tests are in direct support of the Structural Design Methods Program. A few tests have been performed this quarter at room temperature, 427, and 593°C while perfecting our extensometer for axial mode testing. The results are summarized in Table 9.4. We find it interesting to see the rapid hardening that occurs at 427 and 593°C. After ten cycles the tests performed around 0.0095 strain amplitude showed about the same strength at high temperature as at room temperature. This behavior comes as no surprise since stresses greater than reported here have been observed by workers at Argonne National Laboratory[6] in the same temperature range.

---

[6] Reactor Development Program Progress Rept. January 1972, ANL-RDP-1, Table V.5.

Table 9.4. Summary of Several Strain-Cycling Tests Performed on Type 304 Stainless Steel (Heat 9T2796 Reannealed at 1093°C)

Specimen Number	Temperature (°C)	Strain[a] Amplitude	Tensile Stress Amplitude at Indicated Cycle Number (ksi)			
			1/4	1 1/4	2 1/4	10 1/4
FRP-2	Room	0.0045	27	29.2	30.2	33.2
FRP-4	427	0.0045	15.5	17.7	19.2	25
FRP-3	Room	0.0092	29.5	34.5	36.8	42.2
FRP-5	427	0.0095	16.5	21.5	25.5	40
FRP-6	593	0.0097	12.8	18.8	23.5	40.2

[a]Axial control over 0.5-in. gage length at 0.05/min strain rate.

Microstructural Characterization of Type 308 Stainless Steel Welds

R. E. Gehlbach

Our microstructural characterization studies of type 308 stainless steel welds have dealt primarily with comparisons of as-welded microstructures during this reporting period. In addition, we have performed several x-ray diffraction analyses of precipitates electrolytically extracted from welds and the FFTF base plate. Electron microprobe analysis was also employed to identify inclusions in the type 304 stainless steel base metal.

Microstructural studies on the FFTF welds will be carried out on a single test weld, made at Combustion Engineering with Lot HBEA weld wire in Carlson Heat No. 600414-1A type 304 stainless steel base plate. The CE-2 test weld has been cut to provide sections 0.25 in. thick, each containing one-half of the weld and both base plates. These sections have been radiographed and found to contain no resolvable defects; they are now being heat treated to study the effects of heat treatment on microstructural changes.

We have examined the as-welded microstructures of several portions of the CE-2 FFTF test weld and its laboratory counterpart, F21, by transmission electron microscopy. These welds are microstructurally very similar to each other but quite different from that of the F-01 weld reported previously[7] made with standard lime-coated electrodes. Figure 9.18, a typical microstructure of the F21 weld, shows fine $M_{23}C_6$ carbides (identified by selected area electron diffraction) along the periphery of the ferrite. The presence of carbides around ferrite in the F21 and FFTF welds occurs generally, in contrast to the F-01 weld which exhibited no precipitation at the ferrite-austenite interface, in the as-welded condition.

Our transmission electron microscopy studies of the as-welded CE-2 plate have included specimens from both the inner and outer portions of the weld and in three directions. No significant differences are

---

[7]R. E. Gehlbach, Fuels and Materials Development Program Quart. Progr. Rept. September 30, 1971, ORNL-TM-3550, pp. 183–86.

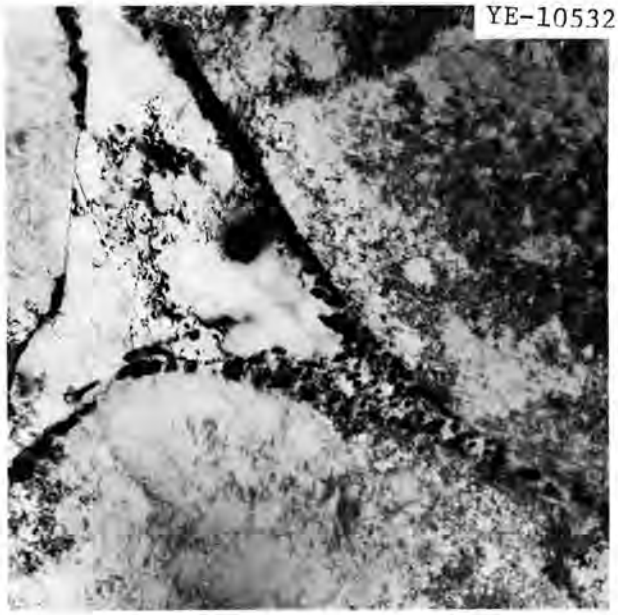

Fig. 9.18. Transmission Electron Micrograph of Typical Structure of As-Welded Type 308 Stainless Steel Weld Metal. Precipitation of $M_{23}C_6$ carbides occurs around ferrite in this weld containing additions of ferrotitanium, boron, and phosphorous. 10,000×.

observed by transmission electron microscopy apart from expected heterogeneity of the weldment. Additional work on these particular sections is planned.

The austenite in all of the weld metal examined to date contains a high density of tangled dislocations arranged into a network of subcell boundaries. These subcells are about 0.8 μm in diameter, as reported previously.[7] We have also observed a relatively high density of straight dislocations in the ferrite, as shown in Fig. 9.19, a transmission electron micrograph taken from the inner portion of the CE-2 weld. As before, these observations are general and not confined to a particular area in a weld. From the appearance of the dislocations, severe deformation of the welds occurred at a few hundred degrees centigrade and at a

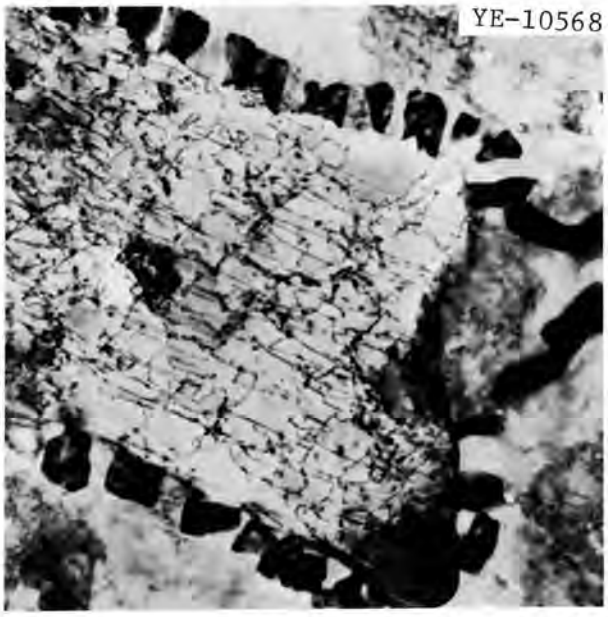

Fig. 9.19. Transmission Electron Micrograph of Typical As-Welded Microstructure in FFTF Test Weld. The specimen is oriented to show dislocations in the ferrite. 25,000×.

fairly high strain rate, probably a result of temperature fluctuations encountered during each weld pass. The welds would be appreciably work hardened as a result.

Precipitates from several specimens have been electrolytically extracted to facilitate identification by x-ray diffraction. The samples of interest were electrolytically etched in 10% HCl-methanol to dissolve the matrix, leaving the precipitates (e.g., carbides, oxides, sulfides, nitrides, and certain intermetallic compounds) as a residue. After these precipitates were collected and washed, x-ray diffraction patterns were obtained.

The detection of sigma phase, which may precipitate in type 308 stainless steel weld metal after appropriate exposure to elevated temperatures, is of particular interest. We extracted phases from a submerged arc weld (SA-S) aged 1000 hr at 800°C (1472°F), which was expected to contain large amounts of sigma phase, to obtain a standard pattern and lattice constants for the sigma. This heat-treated weld contained approximately equal quantities of $M_{23}C_6$ carbide (a = 10.64 Å) and sigma phase (a = 8.786 Å, C = 4.57 Å). We did not detect sigma in preliminary observations of the F-01 weld discussed previously[7] after either 1000 hr at 800°C (1472°F) or 1315 hr at 650°C (1200°F). Analysis of phases extracted from as-welded F-01 revealed $M_{23}C_6$ (a = 10.62 Å) and an additional strong phase, as yet unidentified. Extracted residues from the heat-treated F-01 weld contained large quantities of $M_{23}C_6$, with the unidentified phase being barely detectable. Thus, there is probably no further precipitation of the unidentified phase during aging. No extractions have been made on the CE-2 weld metal at this time.

An extraction was made on the type 304 stainless steel base metal from the CE-1 FFTF weld test plate to identify the inclusions that are present. The only phases detected were α-MnS (ASTM card 6-518) and a spinel, based on $MnFe_2O_4$ (ASTM card 10-319). Electron probe microanalysis confirmed the presence of MnS and revealed two additional phases. Manganese is the primary metallic constituent of both of these phases; in addition, one contained traces of chromium, the other silicon.

No Fe, Ni, Al, or P was detected in any inclusions analyzed. These two phases are most likely spinels of slightly different compositions but having essentially identical lattice parameters as observed by x-ray diffraction analysis.

During the next reporting period we will concentrate primarily on characterizing the FFTF test weld. Sections cut from the CE-2 plate are ready for aging and will be examined as they are available. Additional work is needed to characterize the as-welded condition, particularly with respect to the observed differences in fine carbides around the ferrite in the F-01 vs the F-21 and CE-2 welds.

Tensile Properties of FFTF Vessel Test Weldments

R. T. King, R. E. Adams, and G. M. Goodwin

We are continuing to test longitudinal specimens of all weld metal in the as-welded condition from the type 308 stainless steel FFTF vessel test welds. The acquisition of material[8] and fabrication of test pieces[9] of this controlled residual element (CRE) weldment have already been described. The specimen fabrication process has also been described,[9] and we now use specimens having a 1.25-in. gage length and 0.250 in. in diameter exclusively for longitudinal tensile tests [see Fig. 9.11(b) of ref.9]. It was important that longitudinal all-weld-metal specimens were cut with their centerlines located 0.19, 0.56, and 0.94 in. from the nearest surface of these weldments, for we had already shown both by hardness measurements,[10] preliminary tensile tests,[8] and creep tests[11] that the longitudinal strength properties of the weld metal varied with

---

[8]G. M. Goodwin, Fuels and Materials Development Program Quart. Progr. Rept. September 30, 1971, ORNL-TM-3550, p. 186.

[9]R. T. King and G. M. Goodwin, Fuels and Materials Development Program Quart. Progr. Rept. December 31, 1971, ORNL-TM-3703, p. 210.

[10]R. T. King and R. E. Gehlbach, Fuels and Materials Development Program Quart. Progr. Rept. September 30, 1971, ORNL-TM-3550, p. 187

[11]R. T. King, Fuels and Materials Development Program Quart. Progr. Rept. December 31, 1971, ORNL-TM-3703, p. 215.

depth through the weld. However, because the preliminary tensile tests were performed on an early test specimen design which was not satisfactory, we prefer to disregard those earlier results and deal with the major test matrix results in this quarterly report.

The tensile tests were performed on an Instron tensile testing machine using a system which has the demonstrated capability of holding test temperatures $\pm 3°C$ at 600°C.

Tests have been performed in air at 25°C (75°F), 482°C (900°F), 565°C (1050°F), and 640°C (1200°F). Further testing at these temperatures and a small number of tests at 427°C (1100°F) will be required to complete the longitudinal all-weld-metal test matrix. The 0.004 min^{-1} strain rate receives primary emphasis in the test matrix because it is as close to the 0.005 min^{-1} strain rate requested for ASTM Code Case 1331-5 qualification of materials as can be achieved using the Instron machine and the 1.25-in. gage length needed for extensometer measurements of strain on a 1-in. section of the gage. These measurements are supplemented by other tests at 0.04, 0.016, and 0.0004 min^{-1} to demonstrate the effect of changing strain rate on measured properties.

In addition to obtaining the usual chart of load-vs-crosshead travel from the Instron load cell and drive system, we measured the strain which occurred in a 1-in. section of the gage length using an averaging extensometer fitted with two LVDT sensors. A separate plot of specimen deformation vs load as determined by a second load cell in the loading train was also made on an x-y recorder. As we will show below, the extensometer stress-strain curve is the more useful and accurate at small strains (we use it for strains <0.2%, although it is good to about 2% strain), but because the extensometer does not remain in place at higher strains and because the extensometer electronic system is nonlinear at large strains, we rely on the Instron chart at larger strains.

The data obtained from the averaging extensometer were reduced only to obtain the proportional limit and 0.2% offset yield stress values. These results are given in Table 9.5. We have not yet fit the curves with any parametric equations or stress-strain laws.

Table 9.5. Tensile Properties of FFTF Vessel Test Weldments (Longitudinal, All-Weld Metal)

Test Temperature (°C)	Strain Rate (in./in./min)	Specimen Type and Number	Instron Chart Measurements												Extensometer Measurements	
			Apparent Proportional Limit	0.2% Offset Yield Stress (ksi) (Engr'g/True)	Strength, ksi		Strain		Reduction of Area (%)	Diametral Strain				Gage Mark Elongation (%)	Elastic Limit (ksi)	0.2% Offset Yield (ksi)
					Ultimate (Engr'g/True)	Fracture (Engr'g/True)	Uniform (%) (in./in.) (Engr'g/True)	Fracture (%) (in./in.) (Engr'g/True)		At Fracture (max/min)	(a)	Away from Fracture (max/min)	(a)			
25	0.016	L1 (21-1)	44.87	54.37/54.49	91.51/137.28	87.65/177.58	50.0/0.406	58.0/0.706	50.6	39.7/21.0	1.89	10.9/6.6	1.69	—		
25	0.016	L2 (21-3)	56.12	61.52/61.64	95.30/135.18	91.14/169.90	41.8/0.350	47.8/0.623	46.4	30.9/22.8	1.36	16.9/7.26	2.33	—		
25	0.016	L3 (21-5)	58.44	65.22/65.34	94.96/134.24	88.28/161.99	41.4/0.036	47.7/0.607	45.5	33.6/19.4	1.73	19.3/5.65	3.43	—		
25	0.004	L1 (17-20)	51.40	50.41/50.51	87.98/136.11	81.25/183.83	54.7/0.436	61.2/0.816	55.8	40.7/27.0	1.51	26.8/11.6	2.31	47.0	32.10	49.68
25	0.004	L2 (21.4)	45.29	56.61/56.67	89.44/129.45	88.00/159.41	44.7/0.370	48.8/0.594	44.8	32.8/19.2	1.71	19.6/8.84	2.22	60.6	41.40	55.90
482	0.04	L1 (21-19)	30.22	36.02/36.09	61.38/79.05	45.54/119.33	28.8/0.253	37.3/0.963	61.8	41.5/35.1	1.18	13.3/3.61	3.67	40.0	22.77	34.89
482	0.04	L2 (17-23)	36.23	42.44/42.52	62.52/76.60	50.72/103.88	22.5/0.203	29.9/0.717	51.2	34.3/26.2	1.31	12.0/3.20	3.75	33.0	38.30	41.90
482	0.004	L1 (21-20)	26.29	33.18/33.25	62.92/81.86	51.13/108.97	30.1/0.263	36.7/0.757	53.1	38.5/25.2	1.53	15.7/3.63	4.2	40.0	20.80	32.60
482	0.004	L2 (21-13)	37.3	44.51/44.60	65.21/78.66	52.27/104.56	20.6/0.188	27.4/0.693	50.0	33.9/25.0	1.36	10.4/4.74	2.19	30.0	29.00	44.51
482	0.004	L3 (21-16)	34.93	49/44/49.53	65.54/76.12	50.50/103.90	16.1/0.149	23.4/0.721	51.4	35.8/25.2	1.42	6.93/2.10	2.31	28.0	29.46	48.92
482	0.0004	L1 (21-12)	23.60	33/12/33.19	65.52/84.21	52.48/115.77	28.5/0.251	36.0/0.791	54.7	40.3/25.8	1.56	15.7/4.01	3.90	46.0	20.70	32.50
482	0.0004	L2 (17-28)	37.62	45.73/45.84	62.36/73.54	44.85/98.00	17.9/0.165	25.3/0.696	50.15	36.2/23.2	1.56	10.0/2.82	3.57	30.0	29.10	45.20
565	0.04	L2 (21-14)	31.25	39.59/39.68	53.55/64.01	41.90/97.03	19.5/0.178	27.8/0.838	56.7	40.1/28.8	1.39	11.6/5.58	2.08	29.0	24.60	38.55
565	0.04	L1 (21-9)	26.08	30.97/31.03	52.79/66.86	39.85/103.19	30.4/0.265	38.5/0.951	61.4	40.3/35.5	1.14	14.2/4.47	3.16	40.0	21.74	30.33
565	0.04	L1 (21-2)	22.36	30.85/31.03	52.38/65.95	37.26/81.82	25.9/0.230	38.1/0.787	54.4	42.3/23.9	1.77	15.3/4.86	3.15	38.0	18.10	30.53
565	0.004	L2 (21-8)	30.69	39.02/39.10	50.98/62.02	36.79/90.61	21.7/0.196	34.3/0.901	59.4	43.1/30.1	1.43	16.2/4.86	3.33	47.0	27.33	39.31
565	0.004	L3 (21-6)	29.02	44.58 44.67	52/87/58.67	36.29/88.7	11.0/0.104	22.1/0.898	59.1	39.7/32.6	1.32	7.92/1.89	4.19	24.0	24.90	43.54
565	0.0004	L1 (21-10)	22.36	28.86/28.90	41.20/48.77	22.77/51.20	18.4/0.169	49.3/0.921	60.2	44.4/30.2	1.48	22.2/6.85	3.24	54.0	18.80	29.74
565	0.0004	L3 (21-17)	31.52	37.32/37.39	43.85/49.05	28.51/73.17	11.8/0.112	33.7/0.942	61.0	40.7/34.7	1.17	13.3/3.23	4.13	39.0	28.00	38.15
649	0.04	L1 (17-11)	20.58	26.39/26.46	39.19/47.71	28.00/75.15	21.7/0.197	42.4/0.987	62.7	42.3/35.2	1.20	18.94/6.50	2.91	55.0	12.35	25.32
649	0.004	L1 (21-11)	22.36	28.90/28.96	34.57/36.99	21.94/64.08	7.0/0.068	40.0/1.07	65.8	49.2/34.7	1.42	16.53/5.24	3.15	50.7	17.60	27.32
649	0.0004	L1 (17-21)	22.56	27.95/28.00	30.89/31.82	15.73/49.77	3.0/0.030	46.7/1.15	63.4	48.4/39.5		29.8/17.3			20.70	27.53

[a] Ratio of maximum to minimum.

The data obtained from the Instron are processed by a BASIC-language program, MOD13, on the DEC PDP-10 time-sharing computer at ORNL. The program treats all of the observed elastic deflection as testing stand and load train deflection and computes the engineering and true stress and strain values at the apparent proportional limit, the 0.2% offset yield, the ultimate point, and the fracture point. The true fracture stress is based on an after-test measurement of the fracture diameters. For this anisotropic material, the fracture area is computed as though the projection of the fracture area were an ellipse. As a measure of the anisotropic behavior of the material, we also compute the diametral strain along the major and minor axes of the elliptical fracture surface. Because the deformation which occurs while the specimen necks down locally may differ considerably from uniform deformation, we have also measured the diametral strains at points about 0.5 in. removed from the fracture to compare with the fracture strains. All of these results are recorded in Table 9.5.

Although there are not sufficient data to perform any type of sophisticated statistical analysis, there are several interesting points to be gained from examining the available data.

Perhaps the first comparison should involve the methods used to recover data. The apparent elastic limits from the Instron chart are always considerably greater than those measured directly with the extensometer. Hence, the Instron load-elongation curve should not be relied upon at small strains. However, the greatest difference in the 0.2% offset yield stress measured by the two methods is 2300 psi, and there is at least that much variation in our results due to specimen location problems. Thus, we feel reasonably confident that above the 0.2% offset yield stress, the data from the Instron chart are useful and reasonably accurate.

Nonhomogeneity of properties through the thickness of the weld may become a major factor in analyzing weld behavior in structures. We have therefore plotted much of the data to show how properties vary through the thickness of the weld. Figure 9.20 shows such property variations at room temperature. Tests have been run at both 0.016 and 0.004 min^{-1} strain rate, but there is no significant difference in the results

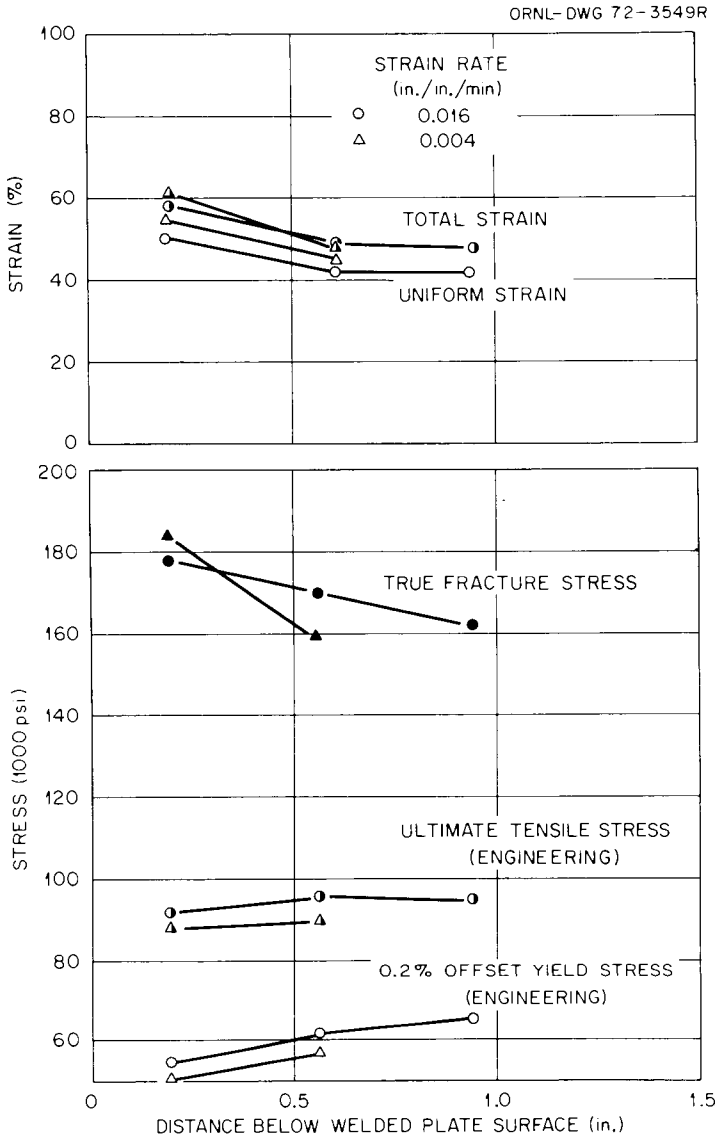

Fig. 9.20. Variation of Properties of FFTF Vessel Test Welds Through the Thickness of the Weld at 25°C (75°F).

obtained at either strain rate. The yield strength increased by approximately 10,000 psi, the ultimate strength increased by about 3000 psi, and the true fracture stress apparently decreased by about 20,000 psi with a 0.75-in. decrease in distance from the nearest weld surface. Both the uniform and total strain decreased by about 10% over the same span.

Similar property variations are shown in Fig. 9.21 for tests performed at 482°C (900°F). Three strain rates were employed, 0.04, 0.004, and 0.0004 min^{-1}, but properties were not found to vary with strain rate at this temperature. Over the same 0.75-in. span, the yield stress increased by about 15,000 psi, the tensile strength increased by perhaps 3000 psi, and the fracture strength apparently decreased by about 10,000 to 15,000 psi. Whereas the uniform and total strains decreased by about 10%, the reduction of area showed a smaller decrease averaging perhaps 5%.

The effect of specimen location on measured properties at 565°C (1050°F) is shown for 0.04, 0.004, and 0.0004 min^{-1} strain rates in Fig. 9.22. The magnitudes of the changes in the yield and ultimate stresses are about the same as those observed at the lower temperatures, but the picture is complicated by a new effect, that of strain rate. The strengths of the specimens tested at 0.0004 min^{-1} are consistently lower than those for specimens tested at 0.004 and 0.04 min^{-1} strain rates, which are quite similar to each other. The fracture strains obtained at the lowest strain rate are greater than those for specimens tested at the higher rates. The reader should note that whereas the uniform and fracture strains decrease with increasing distance from the weld surface, the reduction of area remains about constant; thus, reduction of area should not be used as a measure of ductility in this type of tensile test.

Because only a few specimens have been tested at 649°C (1200°F), we cannot present a clear picture of whether the specimen location effect persists strongly at high temperatures. However, we have investigated the effect of strain rate on measured properties for specimens located 0.19 in. below the weld surface. These data are given in Fig. 9.23. Decreasing the rate of straining from 0.04 to 0.0004 min^{-1} has little effect on the yield strength, fracture strain, and reduction of area.

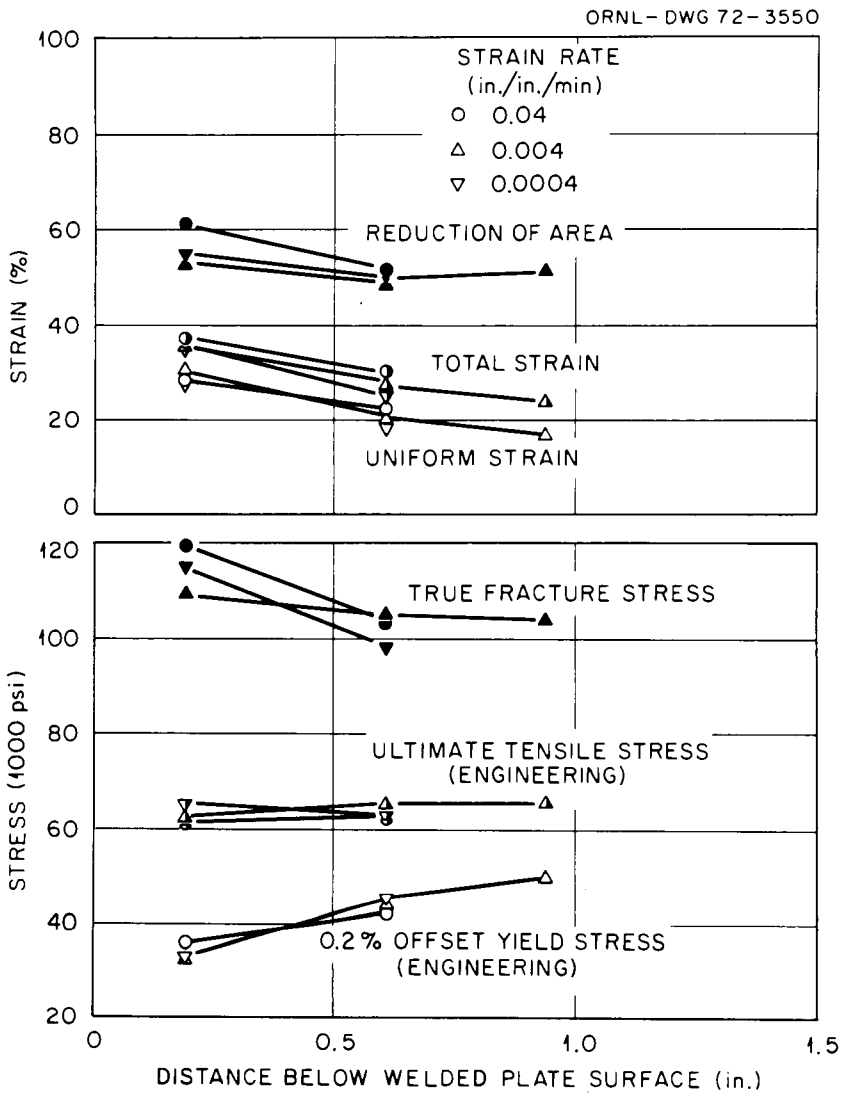

Fig. 9.21. Variation of Properties of FFTF Vessel Test Welds Through the Thickness of the Weld at 482°C (900°F).

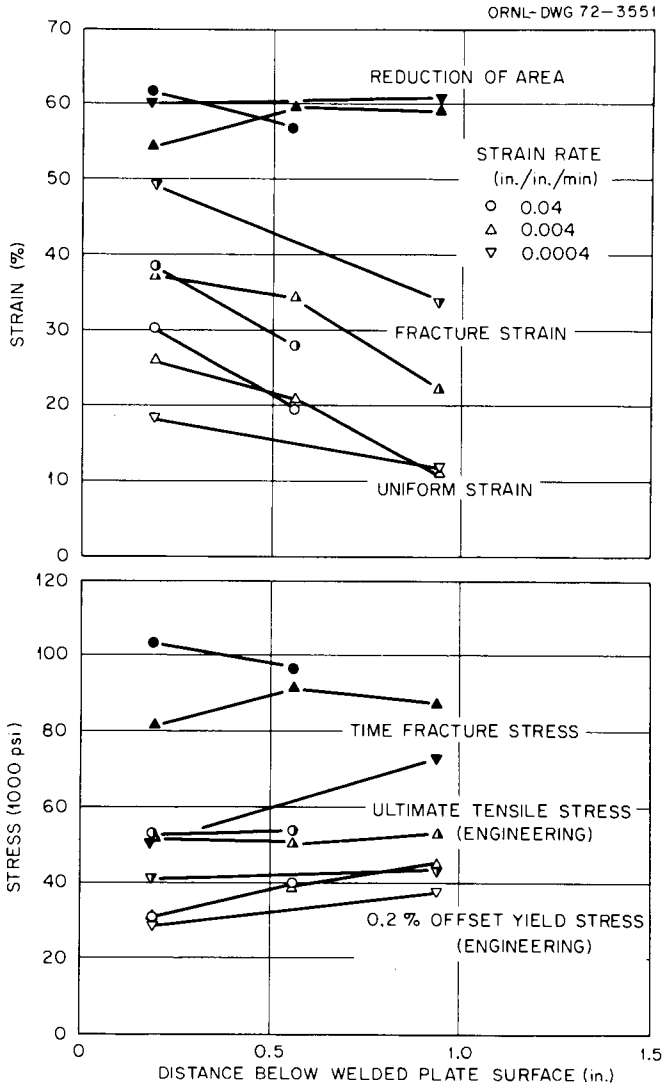

Fig. 9.22. Variation of Properties of FFTF Vessel Test Welds Through the Thickness of the Weld at 565°C (1050°F).

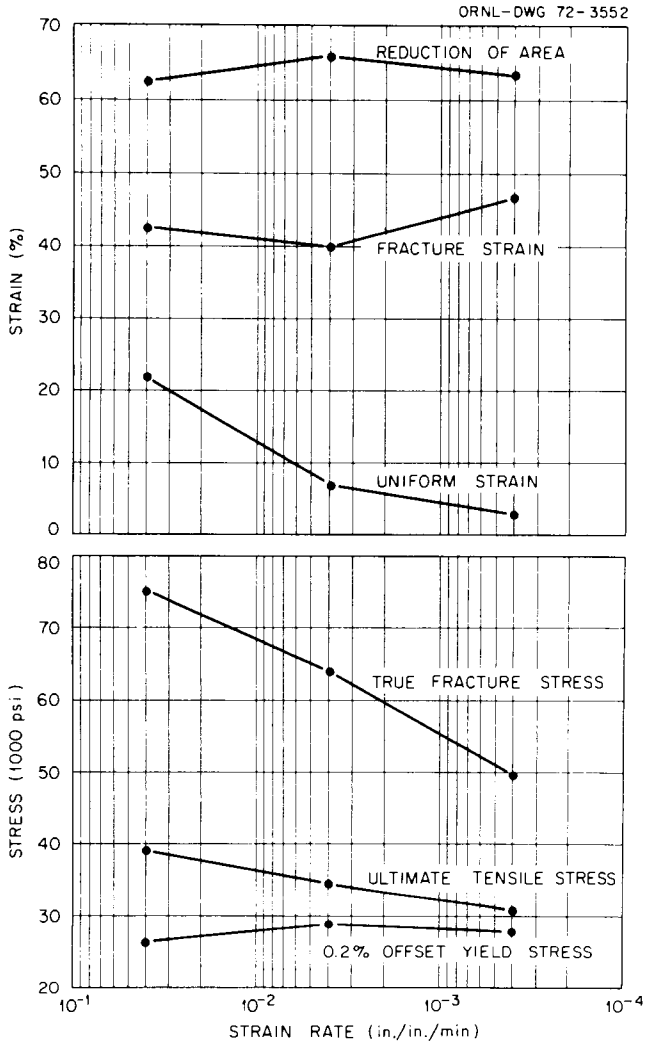

Fig. 9.23. Effect of Strain Rate on Properties of FFTF Vessel Test Weldment Material Taken 0.19 in. Below the Weld Surface at 649°C (1200°F).

However, it causes an 8000 psi drop in the ultimate strength and an apparent 25,000 psi reduction of the true fracture stress, as well as 19% reduction of the uniform strain.

Clearly, the last passes of the weld (near the surface) are weaker and more ductile than the first passes (near the center of the weld). This property variation must be factored into any complete analysis of weldment behavior. Also, there is little effect of strain rate on measured tensile properties at temperatures up to 482°C (900°F), but strain rate should be considered to be an important variable at 1050°F and higher temperatures.

From the designer's standpoint for present code criteria, the most important results are those which show the weld metal to be sufficiently strong that he can design to base-metal specifications. The yield strength, ultimate tensile stress, and true fracture strength are plotted in Fig. 9.24 as a function of test temperature for the weaker regions of the weldment (0.19 and 0.56 in. below the surface) for tests performed at 0.004 min^{-1} strain rate. All these stresses decrease with increasing test temperature. However, they are all considerably above the minimum yield stress for type 304 stainless steel base metal at any given temperature. The total and uniform strains for the same specimens are plotted vs the test temperature in Fig. 9.25. The ductility generally tends to decrease with increasing test temperature, but there is nothing alarming in the results; the lowest total elongation recorded was 22% for type L3 specimen (0.91 in. from the surface). Ductility results taken from the Instron (fracture strain, Table 9.5) agree reasonably well with the after-test gage measurements (gage mark elongation, Table 9.5).

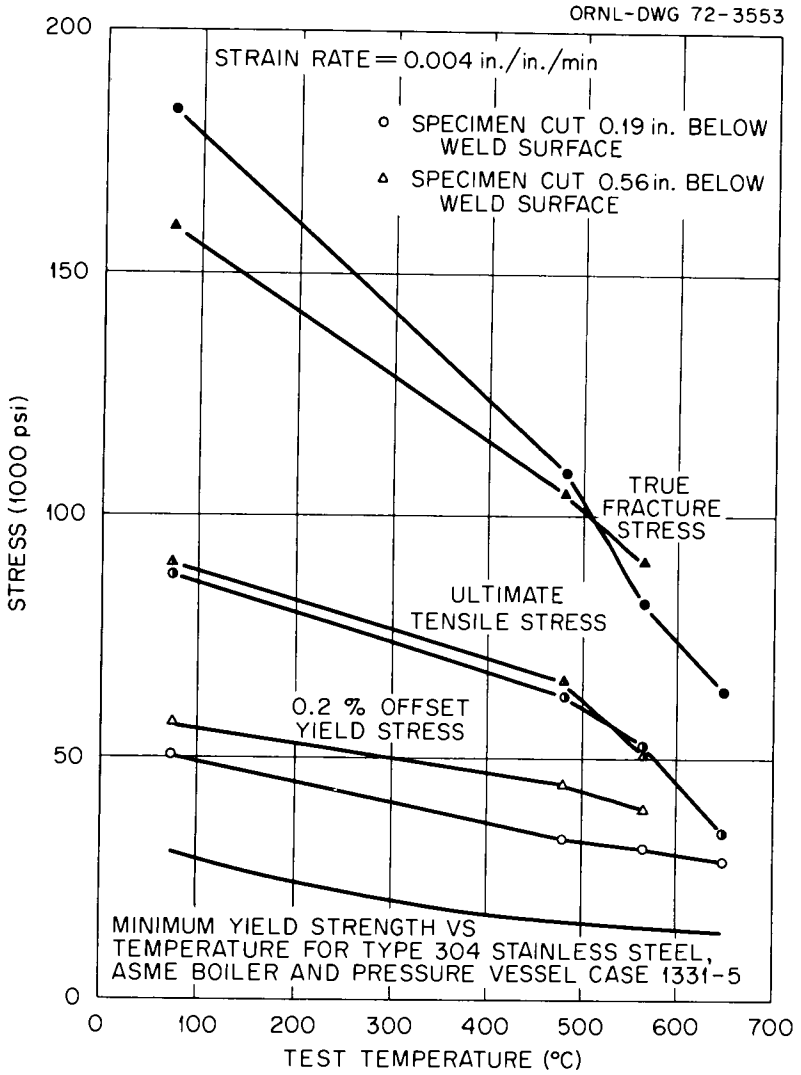

Fig. 9.24. Effect of Test Temperature on the 0.2% Offset Yield Stress, Ultimate Tensile Stress, and True Fracture Stress of FFTF Vessel Test Welds.

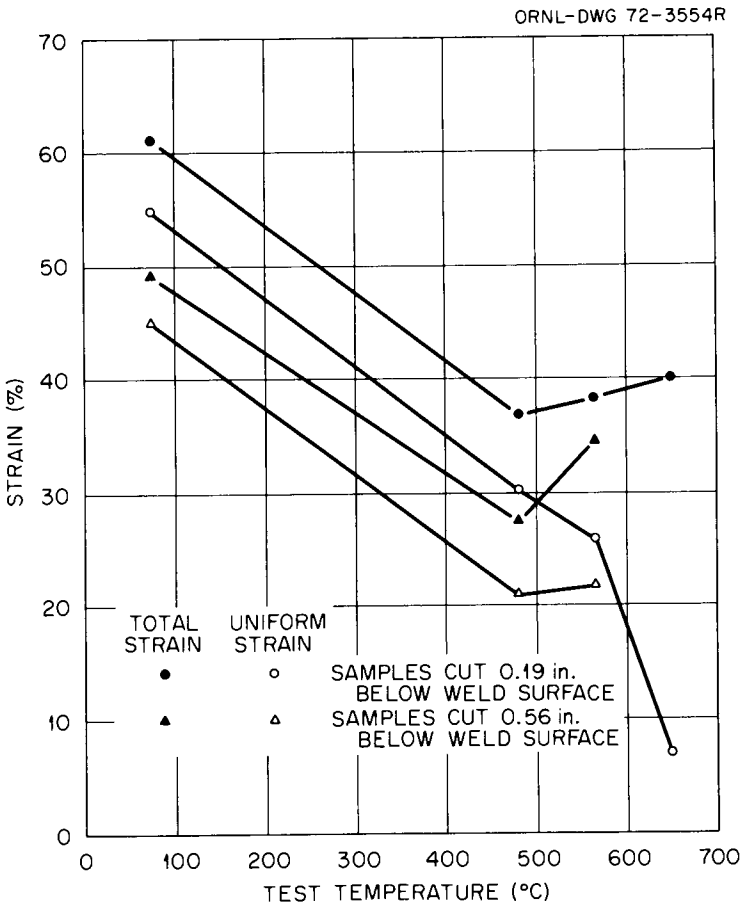

Fig. 9.25. Effect of Test Temperature on the Straining of FFTF Vessel Test Welds at 0.004 in./in./min Strain Rate.

Strain-Hardening Properties of FFTF Vessel Test Weldments

R. T. King and R. E. Adams

Although it is important that weld metal be sufficiently strong and ductile to withstand service conditions, in the final analysis the overall performance of a weld joint relates to differences in the stress-strain properties between weld and base metal. If weld metal work hardens differently than the surrounding base metal, local stress and strain concentrations may develop which adversely affect the performance of the joint. A sophisticated stress-strain analysis of a welded joint must therefore require strain-hardening properties for both the weld and surrounding base metal.

While the MOD13 program does the computation of our basic tensile properties data, it has other routines which interact with the operator to select points from the Instron chart for analysis of the strain-hardening characteristics of the test specimen under uniaxial tensile loads. A selected set of points (10 in this case), including the 0.2% offset yield point and the ultimate point as limits, is spaced out such that the points are uniformly spaced in $\ln \varepsilon$, where ε_i are true strain values. True stresses, σ_i, are then calculated at each point. A standard least-squares fit is then obtained according to the following three equations for the constant $S = 0$:

$$\ln (\sigma - S) = \ln k_1 + 0.5 \ln \varepsilon \ , \tag{5}$$

$$\ln (\sigma - S) = \ln k + n \ln \varepsilon \ , \tag{6}$$

$$\ln (\sigma - S) = a + b \ln \varepsilon + c (\ln \varepsilon)^2 \ . \tag{7}$$

Where k_1, k, n, a, b, and c are constants for each test. Equation (5) is just the familiar exponential strain-hardening law with an exponent of 0.5, Eq (6) is exponential strain-hardening with a variable exponent, and Eq. (7) is a second-order polynomial in $\ln (\sigma - S)$ vs $\ln \varepsilon$ space.

The error, e, is taken to be

$$e = \sum_{i=1}^{10} \left\{ \frac{[\ln(\sigma - S)_{measured} - \ln(\sigma - S)_{calculated}]^2}{10} \right\}^{1/2} \qquad (8)$$

where the calculated stresses were obtained from Eqs. (5) through (7). The computer then calculates the constants in Eqs. (5) through (7) for different values of S in 500 psi increments of S, $0 \leq S \leq \sigma_y$, (where σ_y is the measured yield stress) to find the values of S which minimize the standard error for each of the three stress-strain laws. A subscript "0" indicates the constants computed for the value of S ($\neq 0$) which minimized the error for each equation: the values k_o, n_o, a_o, b_o, and c_o mentioned below were for such best fits. These results are summarized in Table 9.6. Two points are worthy of note: (1) Eq. (5) was always such a poor fit to the data that it was immediately discarded, and no results are reported for Eq. (5); further, (2) the value of S which minimized the error was almost invariably S = 0. The improvement in data fit obtained for a nonzero value of S is usually sufficiently marginal that we feel that setting S = 0 provides an adequate representation of all of our available data. For specimens in which the computer found a minimum standard error for $S \neq 0$, the values of k_o and n_o, or of a_o, b_o, and c_o are recorded as footnotes together with the standard error e_o in Table 9.6.

The strain hardening exponent from Eq. (6), n, is plotted vs distance from the weld surface in Fig. 9.26 for tests performed at various temperatures. It is always in the range $0.09 \leq n \leq 0.211$. Over the range of parameters for which there are data, n clearly decreases with increasing distance from the weld specimen surface. At room temperature and 482°C, there is no effect of strain rate upon n, but at 565 and 649°C, there is a tendency for n to decrease with decreasing strain rate for specimens taken near the weld surface.

Table 9.6. Strain Hardening Behavior of FFTF Vessel Test Weldments (Longitudinal, All-Weld Metal)

Test Temperature (°C)	Strain Rate (in./in./min)	Specimen Type and Number	$\sigma = k\varepsilon^n$ $\sigma - \sigma_o = k_o\varepsilon^{n_o}$, best fit $0 \leq \sigma_{yield}$				$\ln \sigma = a + b \ln \varepsilon + c(\ln\varepsilon)^2$ $\ln(\sigma - \sigma_o) = a_o + b_o \ln \varepsilon + C_o(\ln \varepsilon)^2$, best fit $0 \leq \sigma_o \leq \sigma_{yield}$				
			Standard Error e/e_o	σ_o	k	n	Standard Error $\varepsilon/\varepsilon_o$	σ_o	a	b	c
25	0.016	L1(21-1)	0.160/0.160	0	11.92	0.196	0.038/0.038	0	12.22	0.487	0.0458
25	0.016	L2(21-3)	0.139/0.139	0	11.92	0.165	0.030/0.030	0	12.21	0.425	0.039
25	0.016	L3(21-5)	0.137/0.137	0	11.88	0.150	0.039/0.039	0	12.17	0.406	0.039
25	0.004	L1(17-20)	0.175/0.175	0	11.90	0.175	0.039/0.038	34,000[a]	12.19	0.491	0.045
25	0.004	L2(21-4)	0.161/0.161	0	11.83	0.157	0.040/0.032	45,000[b]	12.15	0.428	0.0378
482	0.04	L1(21-19)	0.129/0.129	0	11.53	0.186	0.074/0.074	0	11.70	0.356	0.0264
482	0.04	L2(17-23)	0.087/0.073	36,000[c]	11.47	0.147	0.012/0.012	0	11.65	0.305	0.0236
482	0.004	L1(21-20)	0.122/0.117	0	11.50	0.198	0.035/0.035	0	11.74	0.409	0.032
482	0.004	L2(21-13)	0.067/0.064	36,500[d]	11.51	0.143	0.0217/0.0217	0	11.65	0.265	0.0182
482	0.004	L3(21-16)	0.067/0.065	36,500[e]	11.51	0.143	0.0217/0.0217	0	11.51	0.143	0.0675
482	0.0004	L1(21-12)	0.149/0.149	0	11.54	0.211	0.049/0.049	0	11.54	0.458	0.0376
482	0.0004	L2(17-28)	0.069/0.069	0	11.43	0.129	0.013/0.013	0	11.59	0.259	0.0198
565	0.04	L1(21-9)	0.129/0.105	26,000[f]	11.36	0.186	0.019/0.019	0	11.33	0.596	0.024
565	0.004	L2(21-14)	0.104/0.104	0	11.34	0.142	0.014/0.014	0	11.53	0.320	0.0276
565	0.004	L1(21-2)	0.044/0.044	0	11.34	0.200	0.033/0.033	0	11.40	0.263	0.0115
565	0.004	L2(21-8)	0.095/0.095	0	11.27	0.132	0.0145/0.0145	0	11.44	0.288	0.0246
565	0.004	L3(21-6)	0.075/0.075	0	11.28	0.104	0.0166/0.0166	0	11.41	0.222	0.0183
565	0.0004	L1(21-10)	0.039/0.039	0	10.94	0.111	0.028/0.028	0	10.99	0.152	0.0061
565	0.0004	L3(21-17)	0.072/0.072	0	11.09	0.102	0.013/0.013	0	11.21	0.211	0.0168
649	0.04	L1(17-11)	0.072/0.034	20,500[g]	11.10	0.167	0.015/0.015	0	11.22	0.284	0.019
649	0.004	L1(21-11)	0.076/0.076	0	10.94	0.121	0.0198/0.0198	0	11.04	0.228	0.0173
649	0.004	L3(21-16)	0.070/0.070	0	11.47	0.118	0.0118/0.0118	0	11.62	0.241	0.0181
649	0.0004	L1(17-12)	0.0457/0.0457	0	10.75	0.090	0.0098/0.0098	0	10.79	0.155	0.011

[a] $a_o = 12.05$, $b_o = 0.709$, $c_o = 0.038$.

[b] $a_o = 12.03$, $b_o = 0.773$, $c_o = 0.0568$.

[c] $k_o = 11.19$, $n_o = 0.401$.

[d] $k_o = 11.22$, $n_o = 0.367$.

[e] $k_o = 11.22$, $n_o = 0.367$.

[f] $k_o = 11.17$, $n_o = 0.442$.

[g] $k_o = 10.86$, $n_o = 0.36$.

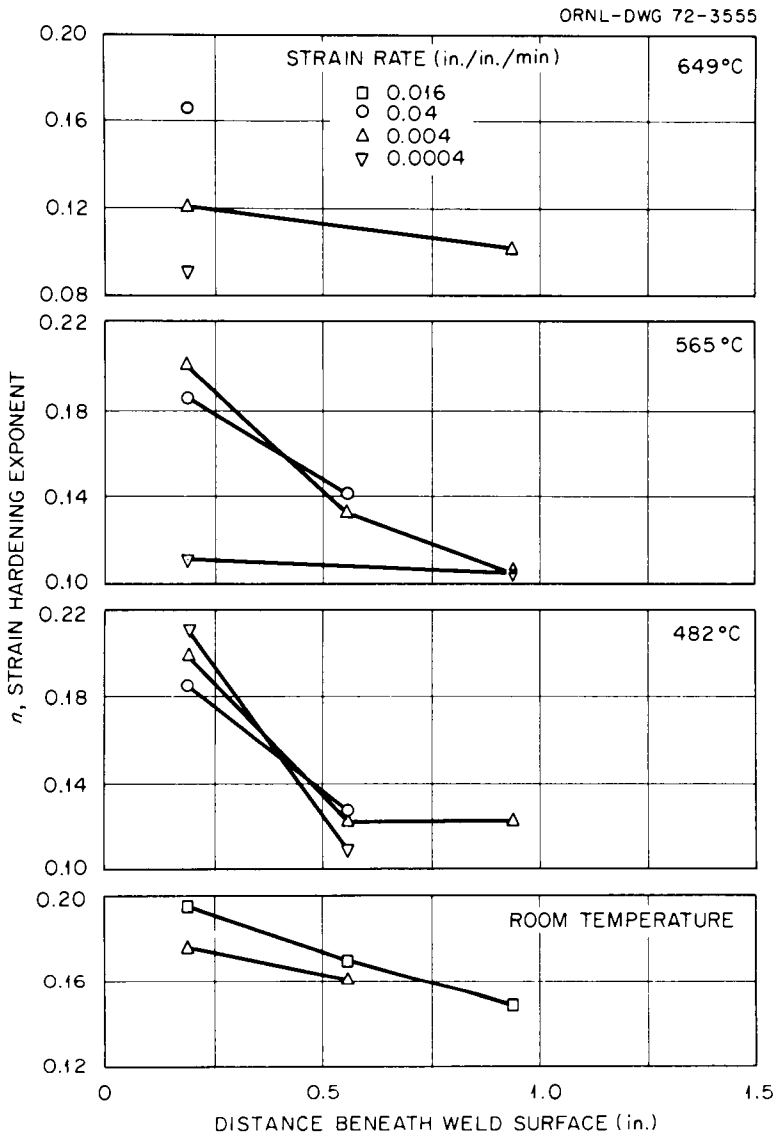

Fig. 9.26. Variation of Strain Hardening Coefficient n with Distance Beneath Weld Surface.

The reader will note that Eq. (6) is a straight line on a ln σ vs ln ε graph, whereas Eq. (7) is a second order curve. Because of this, Eq. (7) always provided a better fit to the data than did Eq. (6), and Eq. (7) should be employed whenever possible. Although we omit plots for the sake of brevity, (b + 2c ln ε) is the analog of n. Quite obviously, b and c could be treated in the same manner as n, and with similar results.

Although structural design analysts are presently using equations of the form

$$\sigma = a_1 + b_1 \varepsilon \ , \tag{9}$$

where a_1 and b_1 are constants, we feel that such simple straight-line representations of stress-strain data are generally not as desirable as Eq. (6) or Eq. (7). We present our data in a form which allows realistic plots of stress vs strain to be reconstructed, and the user may then approximate these curves by straight line segments wherever he deems such action appropriate.

Status of Stress-Rupture Tests on Longitudinal All-Weld-Metal FFTF Vessel Test Weld Specimens

R. T. King and E. Bolling

Stress-rupture testing of longitudinal all-weld-metal specimens of the type 304 stainless steel FFTF vessel test welds is in progress. We reported the status of the program in the last quarterly report,[12] and the results are brought up to date in this report.

The stress vs rupture time data for the tests which have been completed and some tests in progress are plotted in Fig. 9.27. The observation that specimens from near the surface of the weld are weaker than specimens cut near the center of the weld in creep-rupture tests at

---

[12]R. T. King, Fuels and Materials Development Quart. Progr. Rept. December 31, 1971, ORNL-TM-3703, p. 215.

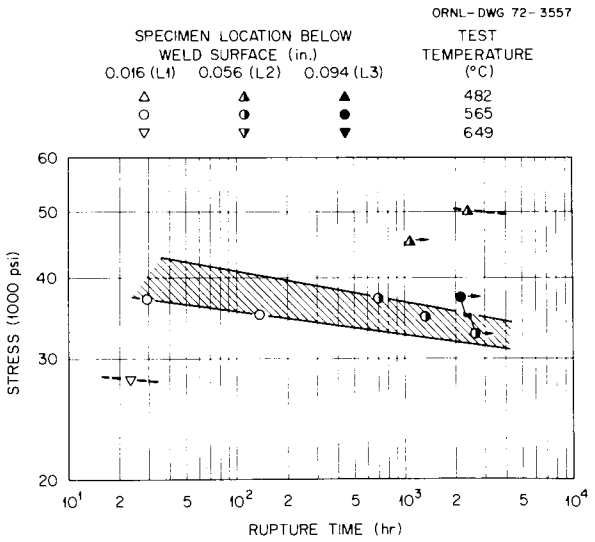

Fig. 9.27. Creep-Rupture Behavior of FFTF Vessel Test Welds.

565°C (1050°F) remains valid. The ductility of specimens tested to failure and the strains accumulated to date for specimens which are currently being tested are shown in Fig. 9.28. The points denote the last extensometer strain readings taken before the specimen failed, whereas aftertest measurements on the overall specimen elongation are shown by lines and bars. For tests which ruptured in short times in the absence of an operator to take strain readings during third-stage creep, the latter are the preferred measurements. The fracture ductility of all specimens tested to failure exceeded 15% even in tests lasting more than 1000 hr.

Anisotropy of FFTF Vessel Test Weldments

R. T. King, E. Bolling, and T. N. Jones

In order to investigate the anisotropy of plastic deformation in the weldment, we prepared a set of transverse specimens having the same geometry as the longitudinal specimens but with the weld metal test section transverse to the weld (Fig. 9.29). The specimens were of types denoted T1, T2, and T3 their centers were located 0.19, 0.56, and 0.94 in. below the surface of the weld. These specimens were tensile tested on the Instron tensile testing machine at 0.004 min^{-1} at room temperature.

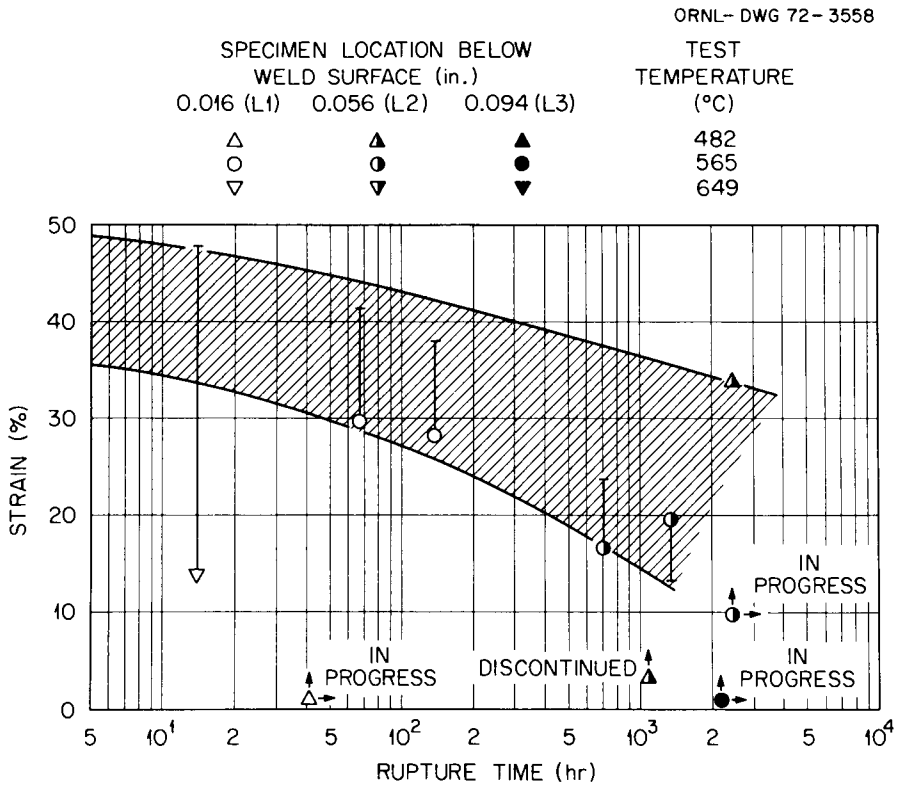

Fig. 9.28. Ductility of FFTF Vessel Test Welds.

Tested specimens all exhibited anisotropic deformation which varied in character across the width of the weld. Figure 9.30 shows the T1 specimen which was tested to fracture at room temperature. The orientation of the specimen in Fig. 9.30(a) is the same as the view to be had in Fig. 9.29, except that the unsectioned half of the specimen had been rotated 180°. Figure 9.30(b) shows the specimen looking down from the top of the welded plate. The punch marks on the shoulder of the section shown in Fig. 9.30(b) were orientation marks to identify the vertical direction in the weld. The left half of the specimen has been sectioned and macroetched to reveal the base metal near the shoulder and the darker weld metal. The solidification direction is clearly denoted by the columnar grain structure which formed during freezing. Surface rumpling of the unetched half of the specimen exhibits a pattern quite similar to the solidification pattern. It is interesting to note that wherever the

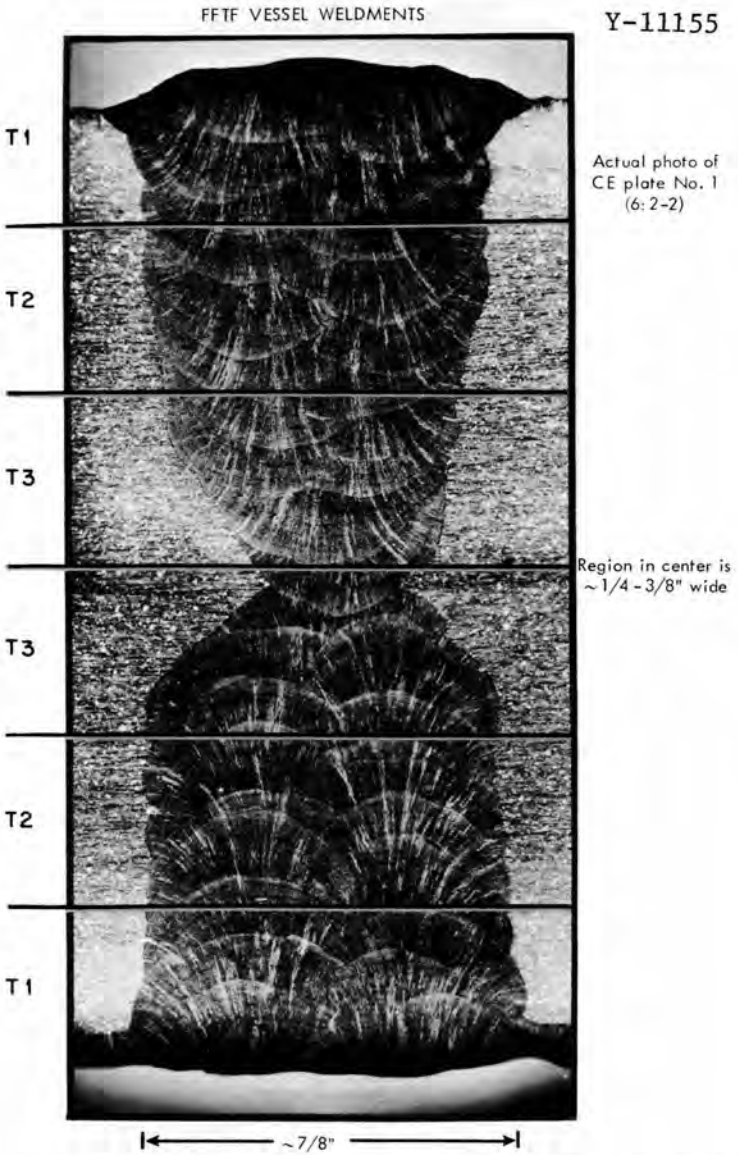

Fig. 9.29. Location of T1, T2, and T3 Specimens in the FFTF Vessel Test Weld. Note that the solidification direction in this multipass weld can be detected from the columnar grain structure.

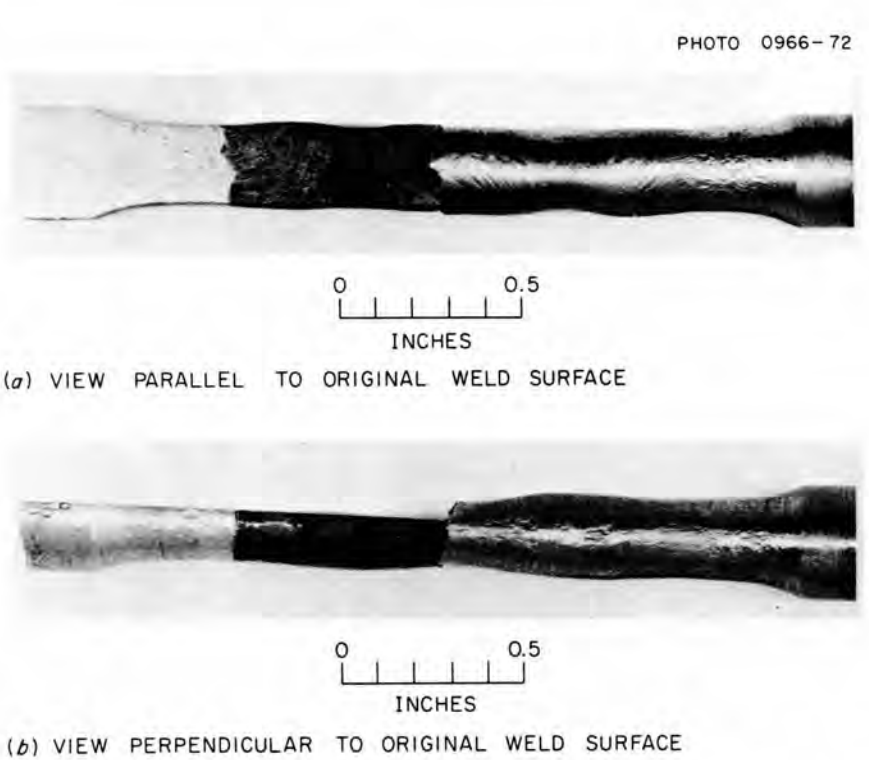

Fig. 9.30. Two Views of the Gage Section of a Transverse Weld Specimen Taken 0.19 in. Below the Weld Surface, Pulled at Room Temperature at 0.004 in./in./min. Left side has been cut, polished, and macroetched (2 parts HNO_3, 1 part H_2SO_4). Left side is rotated by 180° relative to right side.

solidification direction is normal to the tensil axis, the greatest reduction occurs normal to the surface of the welded plate, but that elsewhere the greatest reduction is parallel to the plate surface. The principal axes of anisotropy change orientation from location to location across the weld, and the specimen geometry after testing is similar to a soda straw which has been pinched in first one direction and then another. Our observations to date on this specimen and other specimens are consistent with the notion that one of the principal axes of anisotropy is parallel to the welding direction (normal to the section of Fig. 9.29), and that the other two principal axes of anisotropy are orthogonal with one axis alway parallel to the local direction of solidification. However, much remains to be done to substantiate this hypothesis.

The yield strengths of the transverse weld metal specimens were measured using the averaging extensometer located on weld metal only. (The weld fusion zone had been revealed by light macroetching.) The engineering ultimate stress was computed from the Instron chart and represents a maximum value for the entire gage length, including weld metal and base metal. The strains are summed over the entire 1.25-in. gage length and hence are not an accurate measure of the deformation sustained by the weld metal proper. These results are given in Table 9.7 together with comparable L1 specimen results. The transverse yield stresses and ultimate strengths for the T1 and T2 specimens are greater than the stresses for L1 and L2 specimens taken at the same distance below the weld surface. However the L3 specimen was slightly stronger than the T3 specimen. Comparisons of strains have little value because of the mixture of metal types involved in the transverse specimens. Both of the transverse specimens which fractured at room temperature broke in the weld metal, and the total strains for weld metal and base metal are in excess of 40%.

We had observed earlier in preliminary tensile tests of longitudinal all-weld-metal specimens[13] that deformation occurred most rapidly in the direction normal to the welded plate surface. This occurred because all

---

[13]R. T. King, Fuels and Materials Development Program Quart. Progr. Rept. December 31, 1971, ORNL-TM-3703, p. 214.

Table 9.7. Instron Chart Tensile Properties of Transverse Specimens of FFTF Vessel Test Weldments at Room Temperature

Specimen	0.2% Offset Yield Stress (psi)	Ultimate Stress (psi)	True Fracture Stress (psi)	Uniform Strain (%)	Total Strain (%)
T1	58,800	94,900	155,800	87.5	88.2
(L1)	(54,370 and 50,410)	(91,510 and 87,980)			
T2[a]	62,900	96,900		37.6	>43.2
(L2)	(61,500 and 50,410)	(95,300 and 89,400)			
T3	63,500	93,750	154,000	46.4	56.7
(L3)	(65,200)	(94,960)			

[a]Specimen was not tested to failure.

of the specimens which were investigated were cut from regions where the solidification direction was normal to the original welded plate surface.

The ratio of maximum to minimum diametral strain for a nearly homogeneous test specimen gives a measure of the plastic deformation occurring along two of the axes of anisotropy when the third axis coincides with the uniaxial tensile axis. Since this condition may be met for tests performed on longitudinal specimens if one of the principal axes of anisotropy parallels the welding direction, we recorded the diametral engineering strain at the point at which the fracture occurred in Table 9.5. A ratio was devised by dividing the maximum strain at the minimum strain. However, the maximum and minimum diametral strains which had occurred away from fracture where the gage length was not severely necked down were also measured, and the ratios of these strains were computed. Both strain ratios are listed in Table 9.5. Clearly, the ratio of maximum to minimum diametral strain at fracture differed from that measured away from the fracture. In fact, the two ratios are not simply correlated in any fashion that can be deduced from these tests. The ratios are plotted vs one another in Fig. 9.31 for the various test temperatures, but there are no consistent trends except that the fracture strain ratios tend to be smaller than those measured where necking had occurred.

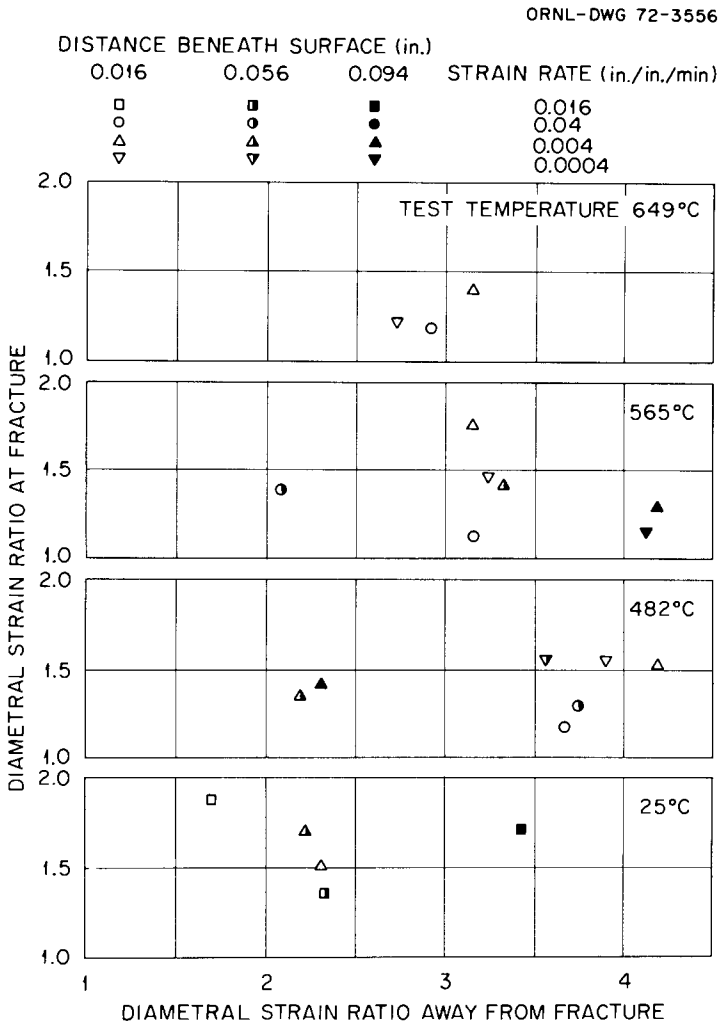

Fig. 9.31. Correlation of Strain Ratio at Fracture with Strain Ratio Away from Fracture.

Mechanical Properties of 2 1/4% Cr—1% Mo Steel

R. L. Klueh

We are studying the mechanical properties of 2 1/4% Cr—1% Mo steel as a function of the carbon content. Three steels were melted by the Bureau of Mines, Albany, Oregon, with desired carbon levels of 0.01, 0.04, and 0.10 wt %. The steels were fabricated into 1/2-in. plate, 3/4-in. tubing, and 7/8-in. rod. Previously, the chemistry of the 1/2-in. plate was reported,[14] and for the low carbon steel a value of 0.003% C has been used in subsequent discussion[14—16] regardless of the product form.

Analytical chemistry on the tube and rod material, however, shows that the carbon contents more closely approached the 0.01% C level desired. Table 9.8 lists the chemistry for all materials. With the exception of

[14]D. A. Canonico and H. E. McCoy, Fuels and Materials Development Program Quart. Progr. Rept. March 31, 1971, ORNL-TM-3416, pp. 143—146.

[15]R. L. Klueh and H. E. McCoy, Fuels and Materials Development Program Quart. Progr. Rept. September 30, 1971, ORNL-TM-3550, pp. 193—203.

[16]R. L. Klueh, Fuels and Materials Development Program Quart. Progr. Rept. December 31, 1971, ORNL-TM-3703, pp. 222—234.

Table 9.8. Chemical Analysis of 2 1/4% Cr—1% Mo Steels Being Tested

Material Identification	Chemical Composition (wt %)							
	C	Mn	Si	Cr	Mo	Ni	S	P
A[a]	0.003	0.33	0.41	2.6	1.14	<0.02	0.008	0.002
AT[b]	0.008	0.50	0.58	2.5	0.98	<0.05	0.008	0.006
AR[c]	0.009	0.51	0.58	2.3	0.98	0.05	0.009	0.002
B	0.035	0.30	0.20	2.4	1.17	<0.02	0.016	0.022
BT	0.03	0.39	0.22	2.4	1.1	<0.05	0.019	0.022
BR	0.03	0.38	0.27	2.4	1.14	<0.05	0.025	0.019
C	0.11	0.33	0.27	2.4	0.97	0.24	0.011	0.0095
CT	0.105	0.45	0.34	2.3	0.87	0.28	0.011	0.018
CR	0.12	0.44	0.40	2.2	0.91	0.21	0.015	0.0096
Standard Croloy[d]	0.135	0.57	0.37	2.2	0.92	0.16	0.016	0.012

[a]Single letter is 1/2-in. plate.

[b]T refers to tubular product.

[c]R refers to rod product.

[d]1-in. plate from B & W.

the 0.003% C, the chemistry from a given heat agrees well for the various products; these chemistry values will be used in future discussions. Also listed in Table 9.8 is the analytical chemistry for the 1-in. plate of standard Croloy procured from Babcock & Wilcox.

Annealing Studies

Our mechanical properties studies are conducted on normalized and tempered material: 1 hr at 927°C (1700°F), air cooled; 1 hr at 704°C (1300°F), air cooled. We previously reported on the tempering characteristics (as measured by hardness changes) of the modified carbon steels, but gave no metallography. Figures 9.32, 9.33, and 9.34 show the normalized and normalized-and-tempered microstructures of the 0.009, 0.030, and 0.120% C steels, respectively. The photomicrographs are from the center of 7/8-in.-long specimens from the 7/8-in.-diam rod. There was little change in microstructure or hardness through the cross section, except near the edge, which was decarburized during heat treatment at the Bureau of Mines.

The low and medium carbon materials have a two-phase structure after normalization [Figs. 9.32(a) and 9.33(a)]. Only a few percent of the second phase is present in the low carbon steel, whereas the medium carbon steel contains 10 to 20% austenite decomposition products (bainite and pearlite). After tempering for 1 hr at 704°C, the low carbon steel appears completely ferritic. The amount of decomposition products in the medium carbon steel after tempering, however, is relatively unchanged, although comparison of the two microstructures at higher magnification, Fig. 9.33(b) and (d), shows that tempering has changed the appearance of the decomposition products.

The high carbon steel (0.120%) was almost entirely bainite after normalization, and after tempering a difference in microstructure was only observed at high magnification, Fig. 9.34(b) and (d). The microstructure for a similar specimen of the 1-in. plate of standard Croloy (0.135% C) was the same as the high carbon steel shown in Fig. 9.34.

Table 9.9 compares hardnesses for these materials. Note the small difference between the low and medium carbon steels after tempering,

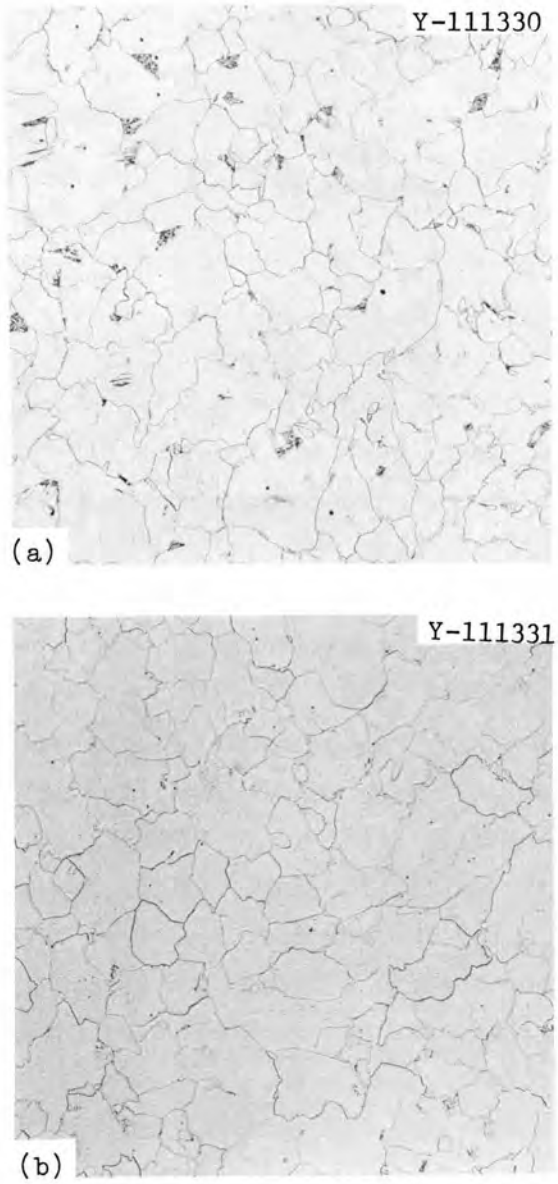

Fig. 9.32. Low Carbon (0.009%) 2 1/4% Cr—1% Mo Steel. 100×.
(a) Normalized. (b) Normalized and tempered.

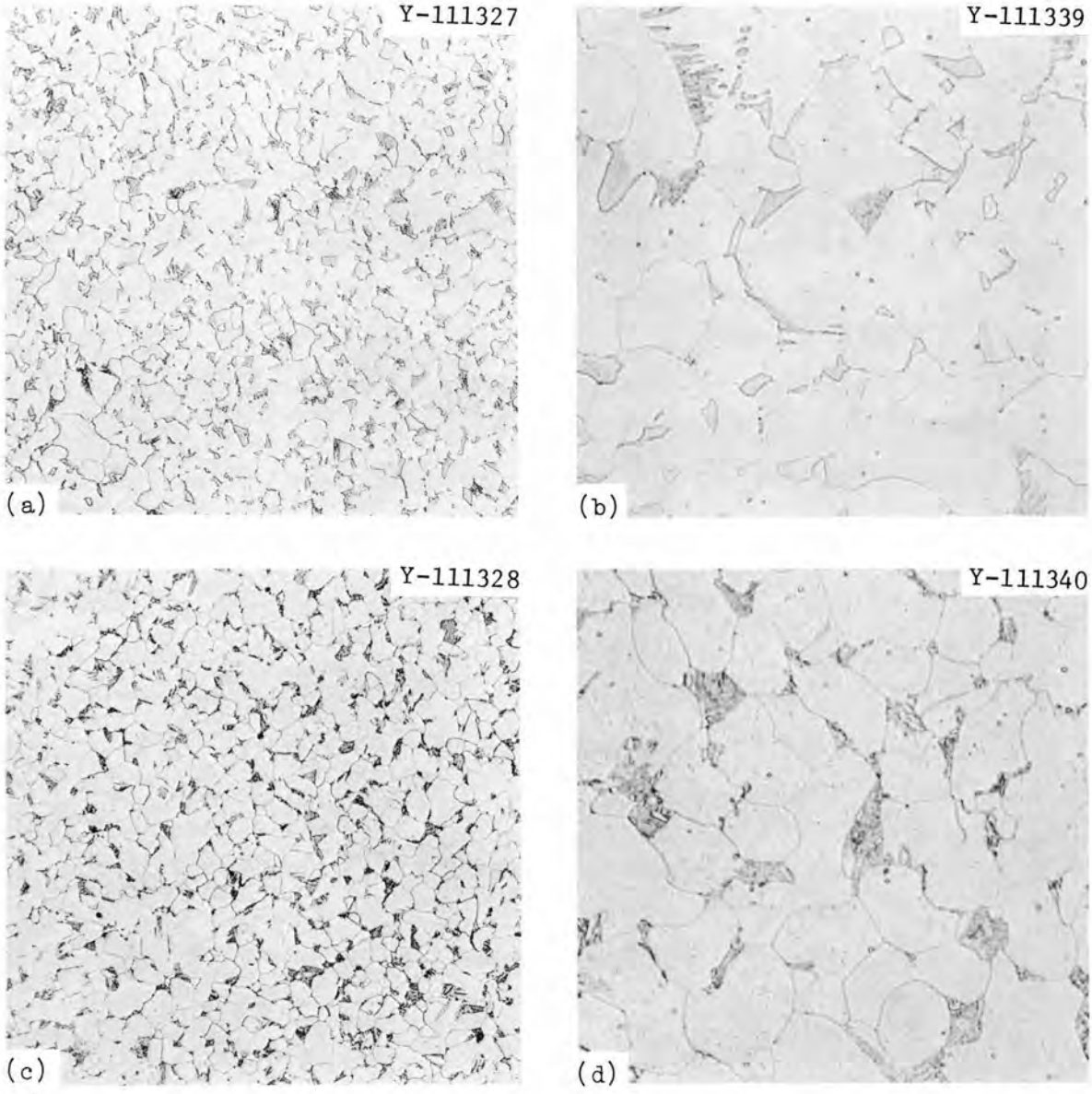

Fig. 9.33. Medium Carbon (0.030%) 2 1/4% Cr—1% Mo Steel.
(a) Normalized, 100×. (b) Normalized, 500×. (c) Normalized and tempered, 100×. (d) Normalized and tempered, 500×.

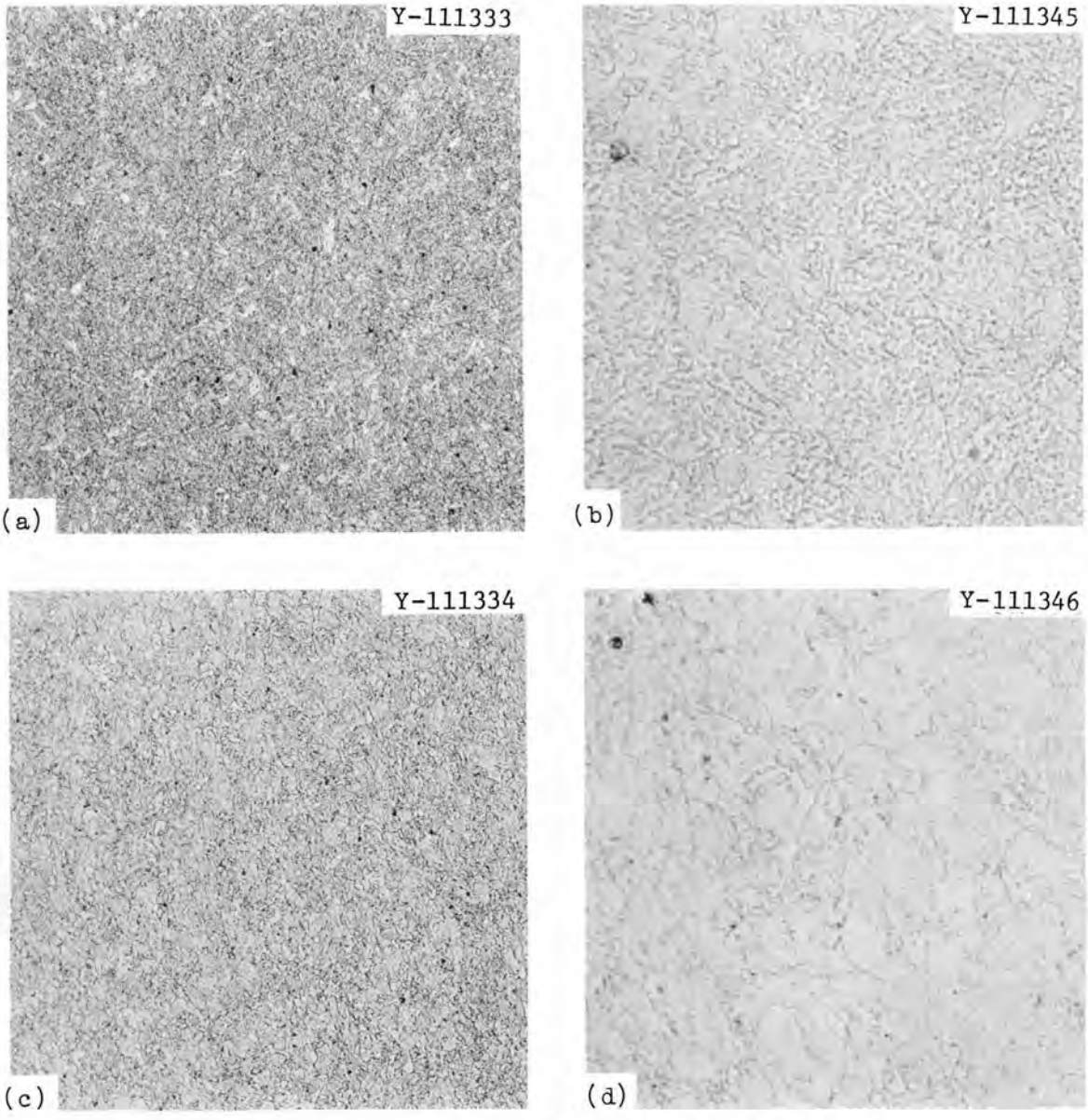

Fig. 9.34. High Carbon (0.120%) 2 1/4% Cr—1% Mo Steel.
(a) Normalized, 100×. (b) Normalized, 500×. (c) Normalized and tempered, 100×. (d) Normalized and tempered, 500×.

Table 9.9. Hardness of 2 1/4% Cr—1% Mo Steel After Heat Treatment

Carbon (wt %)	Heat Treatment	Hardness (DPH)
0.009[a]	N[b]	115
	N&T[c]	100
0.030[a]	N	135
	N&T	110
0.120[a]	N	304
	N&T	215
0.135[c]	N	305
	N&T	215

[a]Hardness determined at the center of a 7/8-in. length of 7/8-in.-diam rod.

[b]Normalized: 1 hr at 927°C (1700°F) and air-cooled.

[c]Normalized then tempered: 1 hr at 704°C (1300°F) and air-cooled.

[d]Hardness determined at center of a 7/8-in. length of 1/2-in.-diam rod removed from 1-in. plate.

despite the difference in microstructure [Fig. 9.32(b) and 9.33(b)]. The similarity of the high carbon steel and the 1-in. plate is also obvious.

We are presently thinning specimens of these materials for examination by electron microscopy.

Creep-Rupture Properties of Weldments

We continued creep-rupture studies of weld metal and transverse welds and to date have generated curves for the modified carbon steels at 565°C (1050°F) and have begun tests at 510°C (950°F). The 565°C data for the weld metal and transverse welds are given in Tables 9.10 and 9.11, respectively; creep-rupture curves are shown in Figs. 9.35 and 9.36, and in Figs. 9.37 and 9.38 the minimum creep rates are shown as a function of stress.

Tabe 9.10. Creep-Rupture Properties of 2 1/4% Cr—1% Mo Steel Weld Metal at 565°C (1050°F)[a]

Carbon (wt %)	Stress (psi)	Rupture Life (hr)	Strain (%)	Reduction in Area (%)	Minimum Creep Rate (%/hr)
0.003	30,000	11.2	30.2	91.7	0.62
	20,000	182.0	31.6	82.6	0.018
	15,000	2244.1	26.9	84.0	
0.035	35,000	7.6	31.6	86.8	0.66
	25,000	148.9	23.1	86.9	0.043
	20,000	723.9	40.7	86.2	0.015
	18,000	990.1	14.3	65.7	0.0045
0.110	40,000	14.5	15.9	83.2	0.32
	30,000	137.0	16.1	79.0	0.027
	20,000	2017.2	11.1	30.5	0.00093

[a]Specimens were tempered for 1 hr at 704°C (1300°F).

Table 9.11. Creep-Rupture Properties of 2 1/4% Cr—1% Mo Steel Transverse Welds at 565°C (1050°F)[a]

Carbon (wt %)	Stress (psi)	Rupture Life (hr)	Strain (%)	Reduction in Area (%)	Minimum Creep Rate (%/hr)
0.003	30,000[b]	16.4	15.2	89.6	0.1
	20,000	51.1	21.5	81.0	0.42
	15,000	150.9	23.5	94.1	0.028
	10,000[c]	>3095			
0.035	30,000[b]	11.7	15.1	83.1	0.058
	25,000	13.6	20.9	83.8	0.15
	20,000	46.8	28.3	92.4	0.30
	15,000	362.5	20.3	86.6	0.055
	12,000	1739.2	29.8	90.7	0.011
	9,500[c]	>2270			
0.110	30,000[b]	35.0	19.2	85.7	0.05
	30,000	12.8	20.0	86.9	0.5
	25,000	75.4	24.8	87.7	0.067
	25,000	105.8	16.5	83.7	0.05
	20,000	591.9	21.2	81.8	0.011
	15,000	2839.0	12.9	70.8	0.0001

[a]The 1/2-in. plates were normalized and tempered before welding.

[b]Specimen tested as welded; all other specimens were tempered 1 hr at 704°C (1300°F).

[c]Test in progress.

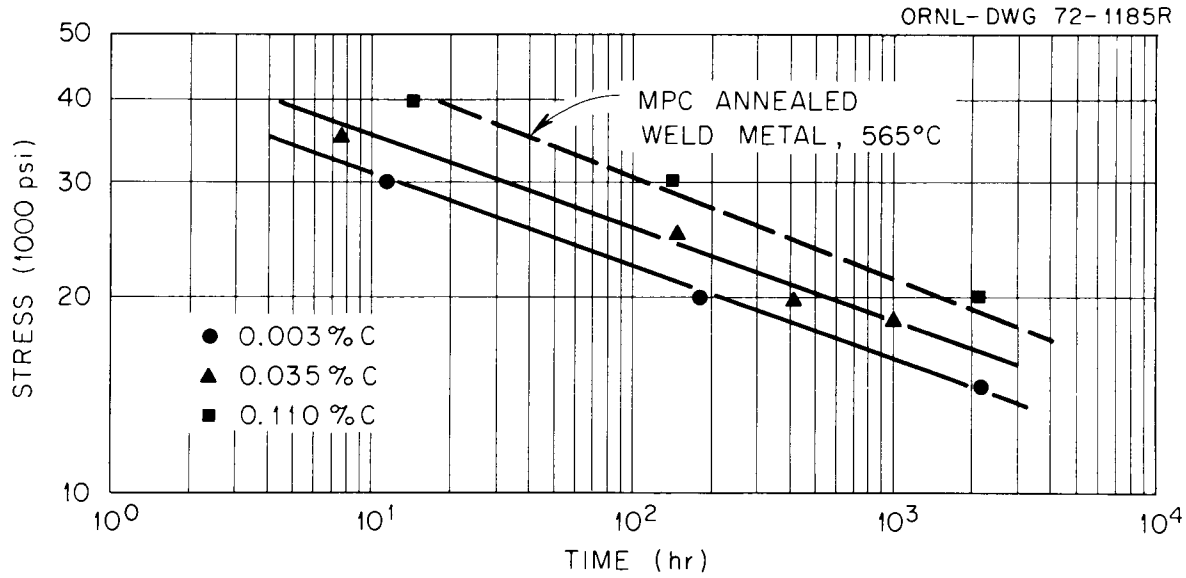

Fig. 9.35. Creep-Rupture Properties of 2 1/4% Cr—1% Mo Weld Metal with Varying Carbon Contents at 565°C. Specimens were tempered for 1 hr at 704°C.

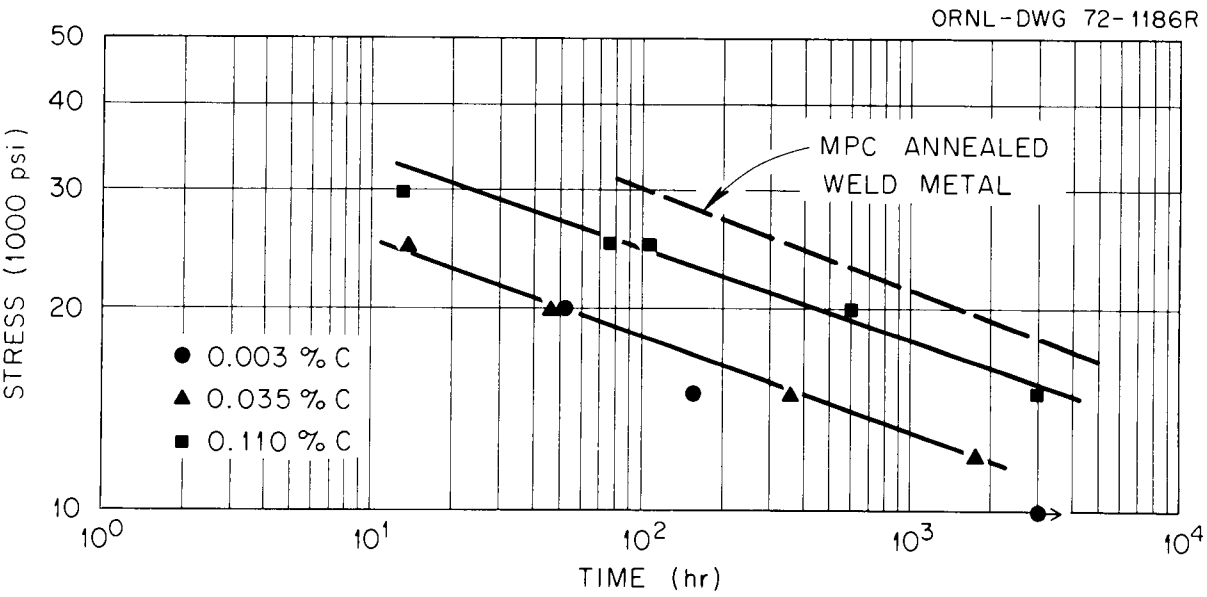

Fig. 9.36. Creep-Rupture Properties of 2 1/4% Cr—1% Mo Transverse Weldments with Varying Carbon Contents at 565°C. The plates were normalized and tempered before welding and the specimens were tempered after welding.

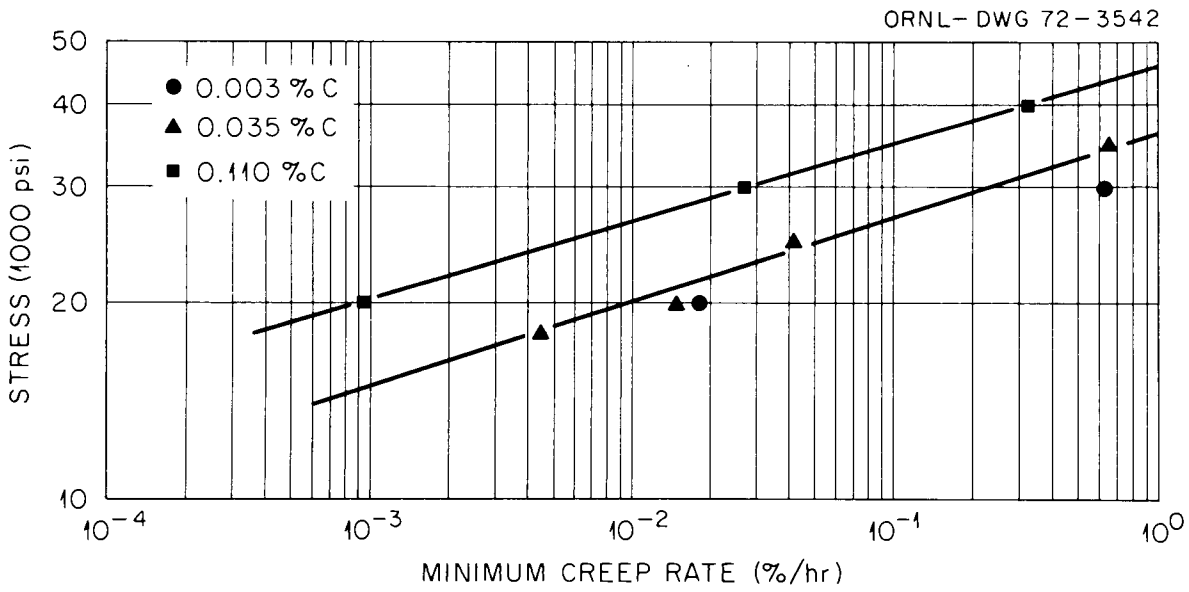

Fig. 9.37. Minimum Creep Rate Vs Stress for 2 1/4% Cr—1% Mo Weld Metal at 565°C.

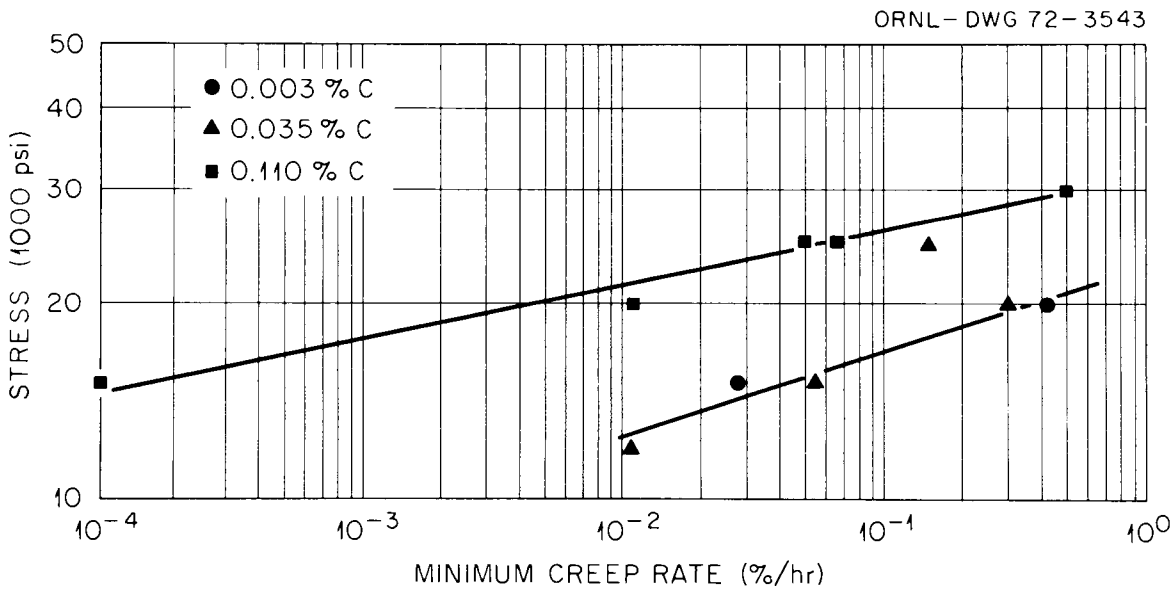

Fig. 9.38. Minimum Creep Rate Vs Stress for 2 1/4% Cr—1% Mo Transverse Weldments at 565°C.

Examination of Figs. 9.36 and 9.38 for the transverse welds shows that there is little difference in the stress-rupture properties for the low (0.003%) and medium (0.035%) carbon steels (only one curve has been drawn for both materials). There appears to be separate curves for the three weld metals (Fig. 9.35), although the difference in rates is small (Fig. 9.37). In Figs. 9.35 and 9.36 a creep-rupture curve for tempered weld metal, taken from Smith's[17] compilation of elevated temperature properties for standard Croloy, is also shown. The weld metal data for the high carbon alloy seem to lie on this curve. In all cases, the weld metal curves of Fig. 9.35 fall above (longer rupture time for a given stress) those for the transverse welds of Fig. 9.36.

Creep-Rupture Properties of Base Metal

Creep-rupture data for the three variable carbon steels (7/8-in. rod) and the 1-in. plate of standard Croloy at 565°C are given in Table 9.12. Creep-rupture curves are shown in Fig. 9.39, along with a curve for normalized-and-tempered bar taken from Smith.[17] Figure 9.40 shows the minimum creep rates as a function of stress (Smith has only two minimum creep-rate data points at 565°C, and they are in agreement with the data for the high carbon rod and standard Croloy plate).

The low and medium carbon steels show similar properties, especially the rate data in Fig. 9.40 (the rate data for the low carbon steel shows more scatter than the other materials). Likewise, the high carbon rod and the 1-in. plate of standard Croloy have similar properties.

We previously stated[18] that the transverse weld specimens failed in base metal that was unaffected by welding. When Figs. 9.35 and 9.39 are compared, it is seen that the creep-rupture properties for the low and medium carbon steels agree quite well with those for the transverse welds. The creep-rupture curve for the high carbon base metal is somewhat above

---

[17]G. V. Smith, An Evaluation of the Elevated Temperature Tensile and Creep-Rupture Properties of 2 1/4% Cr–1% Mo Steel (to be published).

[18]R. L. Klueh, Fuels and Materials Development Program Quart. Progr. Rept. December 31, 1971, ORNL-TM-3703, pp. 222–234.

Table 9.12. Creep-Rupture Properties of Normalized and Tempered 2 1/4% Cr–1% Mo Steel at 565°C (1050°F)

Carbon (wt %)	Stress (psi)	Rupture Life (hr)	Strain (%)	Reduction in Area (%)	Minimum Creep Rate (%/hr)
0.009[a]	25,000	5.6	23.0	87.3	1.65
0.009[a]	25,000	1.9	34.2	90.7	8.75
0.009[a]	22,500[b]	8.7	38.2	84.1	1.35
0.009[a]	20,000[b]	48.6	20.8	90.3	0.010
0.009[a]	20,000[b]	59.6	20.3	91.2	0.010
0.009[a]	20,000	33.6	19.5	90.0	0.065
0.009[a]	17,500	60.9	28.2	83.9	
0.009[a]	15,000	429.2	27.0	91.0	0.014
0.009[a]	12,500	797.7	31.0	90.4	
0.030[a]	25,000	10.1	43	90.3	1.75
0.030[a]	20,000[b]	424.1	33.9	89.2	0.145
0.030[a]	20,000[b]	214.5	45.6	83.8	0.060
0.030[a]	20,000	221.8	43.6	90.5	0.080
0.030[a]	17,000	511.1	41.6	90.0	0.025
0.030[a]	17,000	536.3	47.8	89.3	0.030
0.030[a]	15,000	675	37.1	89.5	0.023
0.120[a]	50,000[b]	0.2	18.1	86.7	
0.120[a]	45,000[b]	1.3	24.1	87.8	
0.120[a]	35,000[b]	32.4	25.1	83.9	0.137
0.120[a]	35,000	25.0	28.1	87.0	0.18
0.120[a]	30,000	194.5	25.2	78.8	0.026
0.120[a]	25,000	435.9	24.2	71.2	0.008
0.120[a]	20,000	2519.5	14.9	33.9	0.0016
0.135[c]	45,000	3.8	18.5	85.3	1.25
0.135[c]	40,000	15.4[b]	21.0	84.9	0.31
0.135[c]	40,000	22.0	23.1	84.5	0.20
0.135[c]	35,000	86.1	22.1	74.4	0.08
0.135[c]	30,000	362.2	15.7	37.8	0.0102
0.135[c]	25,000	>720[d]			

[a]Specimens were made from 7/8-in.-diam rod.

[b]Tests were step loaded.

[c]Specimens were made from 1-in. plate.

[d]Test still in progress.

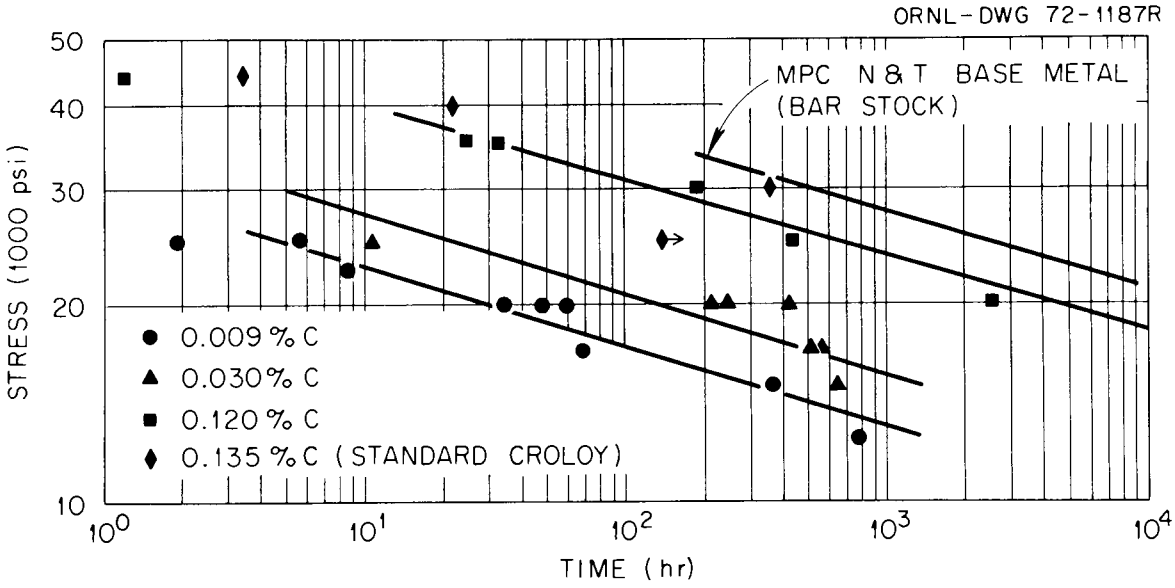

Fig. 9.39. Creep-Rupture Properties of Normalized-and-Tempered 2 1/4% Cr—1% Mo Steel with Varying Carbon Contents at 565°C.

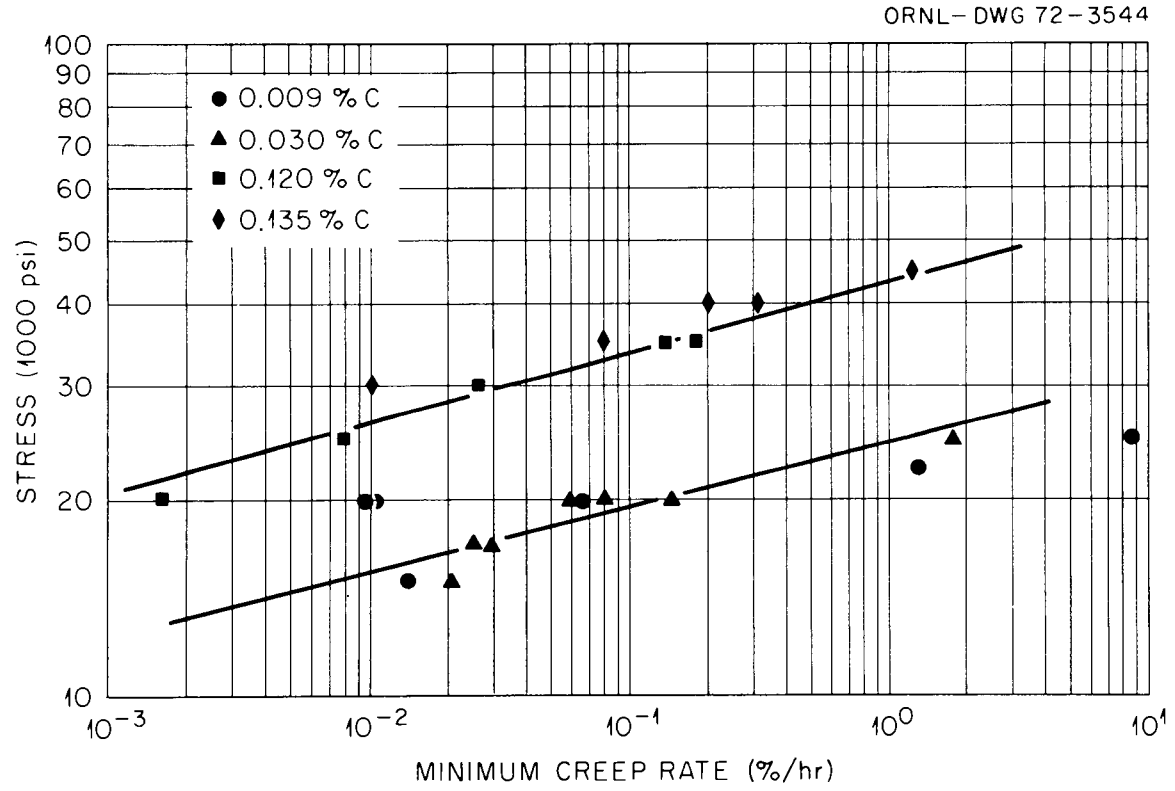

Fig. 9.40. Minimum Creep Rate Vs Stress for Normalized-and-Tempered 2 1/4% Cr—1% Mo Steel at 565°C.

that for the transverse welds with similar carbon content. It should be pointed out, however, that the base metal properties were determined for 7/8-in. rod, while the transverse welds were made in 1/2-in. plate. To allow for a more direct comparison, we are determining the creep-rupture properties of base metal taken from the 1/2-in. plate.

Tensile Properties of Base Metal

We began our tensile program on the 7/8-in.-diam rod with variable carbon content and the 1-in. plate of standard Croloy. Tests were made in the temperature range 25 to 565°C on normalized-and-tempered material; tests at 25 and 565°C were also done on normalized and as-received specimens [the as-received material was specified by the vendor to be in an "annealed" condition (i.e., furnace cooled from the austenitizing temperature)].

The results for a crosshead speed of 0.05 in./min (strain rate approximately 0.02 min^{-1}) are given in Table 9.13. In Figs. 9.41, 9.42, and 9.43, respectively, the yield stress, tensile stress, and ductility parameters (elongation and reduction in area) are given as a function of temperature. In each figure, a scatterband from Smith's compilation[17] is also shown. A definite yield point was observed at room temperature for the three normalized-and-tempered rod materials, and both the upper and lower yield points are given in Table 9.13.

The results for the high carbon rod and the standard Croloy plate — both comparable to the materials in Smith's compilation — fall at the top of the scatterband for strength (Figs. 9.41 and 9.42) and just below the elongation band (Fig. 9.43). These results are for specimens (0.25 in. in diameter) that were normalized and tempered. Therefore, while these results will be closer to the properties of the thin-wall tubes to be used for steam generators, they are expected to be stronger than the material used in Smith's compilation where slower cooling rates were encountered because the heat treatment was carried out on a given product (i.e., the rod or plate). Slower cooling rates affect the austenite decomposition and thus the strength and ductility. In order to check this, we are heat treating some plates and rod prior to machining the specimens.

Table 9.13. Tensile Properties of 2 1/4% Cr–1% Mo Steels of Varying Carbon Centents[a]

Carbon (wt %)	Temperature (°C)	Heat Treatment	Yield Strength (ksi)	Tensile Strength (ksi)	Elongation (%)	Reduction in Area (%)
0.009[b]	25	A[c]	31.7	53.2	31.0	87.6
0.009[b]	25	N[d]	32.7	64.4	19.4	83.9
0.009[b]	25	N&T[e]	40.8[f] 36.8[g]	60.2	23.2	87.0
0.009[b]	95	N&T	34.8	55.2	21.3	87.3
0.009[b]	204	N&T	33.8	61.4	16.8	86.1
0.009[b]	316	N&T	32.9	59.6	16.4	81.2
0.009[b]	371	N&T	28.6	58.3	20.2	82.7
0.009[b]	454	N&T	29.2	62.1	16.6	82.3
0.009[b]	510	N&T	23.6	49.5	22.4	85.3
0.009[b]	565	N&T	21.4	40.2	30.4	88.5
0.009[b]	565	N	27.4	56.9	19.0	80.2
0.009[b]	565	A	16.4	39.7	29.0	88.8
0.030[b]	25	A	27.6	56.3	31.6	81.6
0.030[b]	25	N	26.6	65.6	29.0	75.0
0.030[b]	25	N&T	45.5[f] 42.3[g]	61.4	29.3	82.9
0.030[b]	95	N&T	39.9	69.6	21.7	81.6
0.030[b]	204	N&T	34.9	63.7	19.0	81.3
0.030[b]	316	N&T	32.7	65.2	15.6	77.8
0.030[b]	371	N&T	28.6	63.5	15.6	78.9
0.030[b]	454	N&T	26.0	62.7	16.5	80.6
0.030[b]	510	N&T	25.6	61.0	19.0	81.9
0.030[b]	565	N&T	20.5	45.6	23.6	85.5
0.030[b]	565	N	23.5	65.5	26.1	76.3
0.030[b]	565	A	15.3	32.7	36.8	88.5
0.120[b]	25	A	40.5	69.8	25.8	70.6
0.120[b]	25	N	100.0	151.0	11.0	63.5
0.120[b]	25	N&T	83.1[f] 77.9[g]	94.3	16.6	75.3
0.120[b]	95	N&T	68.6	86.1	15.6	72.8
0.120[b]	204	N&T	68.4	86.2	14.0	76.9
0.120[b]	316	N&T	63.7	90.4	14.0	66.6
0.120[b]	371	N&T	67.0	92.8	13.8	73.0
0.120[b]	454	N&T	58.3	82.0	16.2	75.0
0.120[b]	510	N&T	58.3	74.2	14.2	77.2
0.120[b]	565	N&T	54.7	61.4	20.4	86.4
0.120[b]	565	N	89.0	113.3	10.8	67.8
0.120[b]	565	A	19.4	43.8	36.0	86.4
0.135[h]	25	A[i]	62.3	115.8	17.6	57.2
0.135[h]	25	N	92.0	153.4	11.0	61.5
0.135[h]	25	N&T	83.9	100.7	16.0	67.3

Table 9.13 (Continued)

Carbon (wt %)	Temperature (°C)	Heat Treatment	Yield Strength (ksi)	Tensile Strength (ksi)	Elongation (%)	Reduction in Area (%)
0.135[h]	95	N&T	86.4	101.4	14.4	74.7
0.135[h]	204	N&T	76.5	92.6	12.3	73.1
0.135[h]	316	N&T	81.8	102.9	12.4	69.6
0.135[h]	371	N&T	70.6	93.1	12.2	74.5
0.135[h]	454	N&T	67.4	84.8	12.6	72.9
0.135[h]	510	N&T	71.2	82.8	13.2	78.0
0.135[h]	565	N&T	57.8	62.5	16.3	85.5
0.135[h]	565	N	88.9	119.0	10.4	64.8
0.135[h]	565	A	45.0	92.9	22.5	80.1

[a]Crosshead speed: 0.05 in./min.

[b]Specimens made from 7/8-in. rods.

[c]Specimens in annealed condition; furnace cooled from 870°C.

[d]Specimens in normalized condition; annealed 1 hr at 927°C and air cooled.

[e]Specimens in normalized and tempered conditions; tempered 1 hr at 704°C and air cooled.

[f]Upper yield point.

[g]Lower yield point.

[h]Specimens made from 1-in. plate.

[i]Specimens in annealed condition; furnace cooled from 900–425°C, then air cooled.

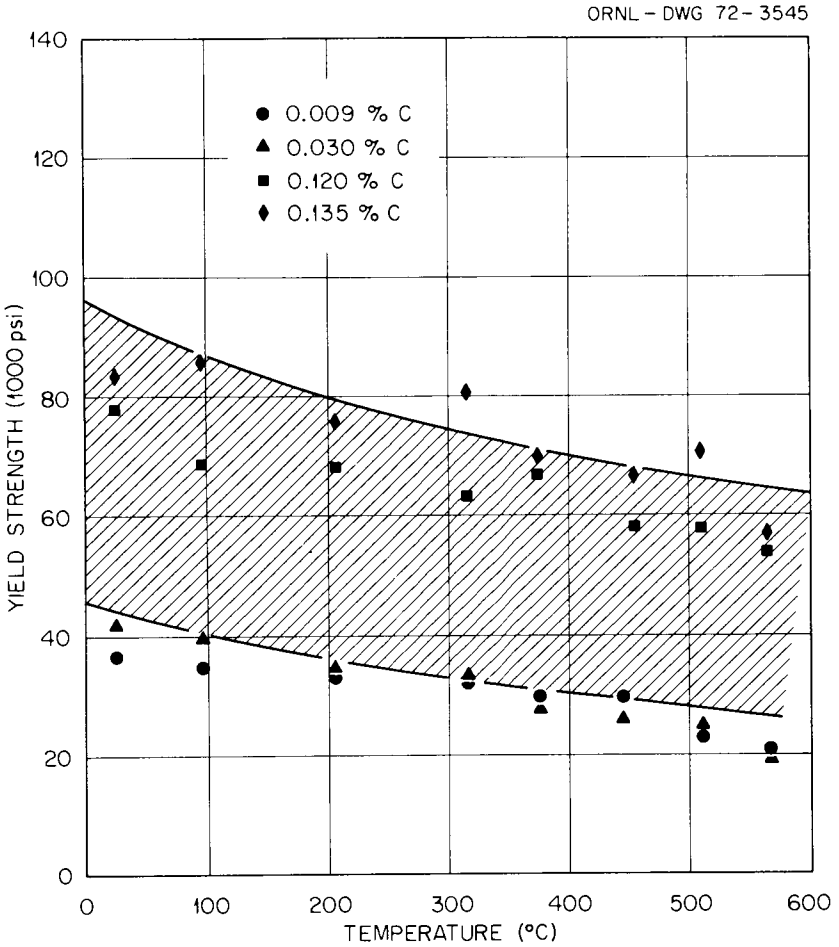

Fig. 9.41. Yield Strength Vs Temperature for Normalized-and-Tempered 2 1/4% Cr—1% Mo Steel. The data are compared with data taken from G. V. Smith, "An Evaluation of the Elevated Temperature Tensile and Creep-Rupture Properties of 2 1/4% Cr—1% Mo Steel" (to be published).

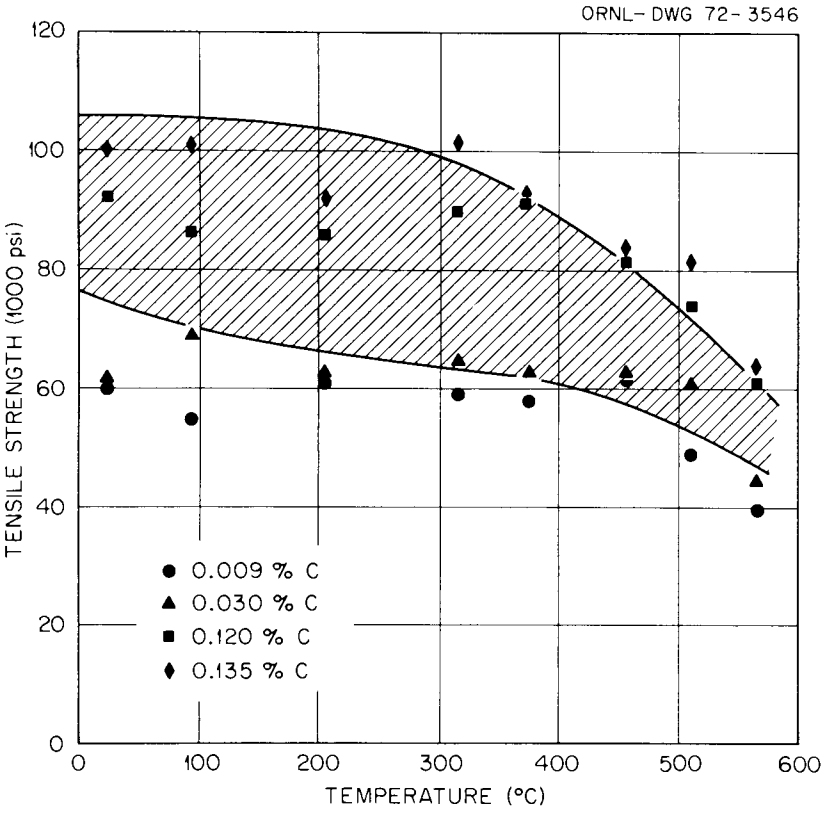

Fig. 9.42. Tensile Strength Vs Temperature for Normalized-and-Tempered 2 1/4% Cr—1% Mo Steel. The data are compared with data taken from G. V. Smith, "An Evaluation of the Elevated Temperature Tensile and Creep-Rupture Properties of 2 1/4% Cr—1% Mo Steel" (to be published).

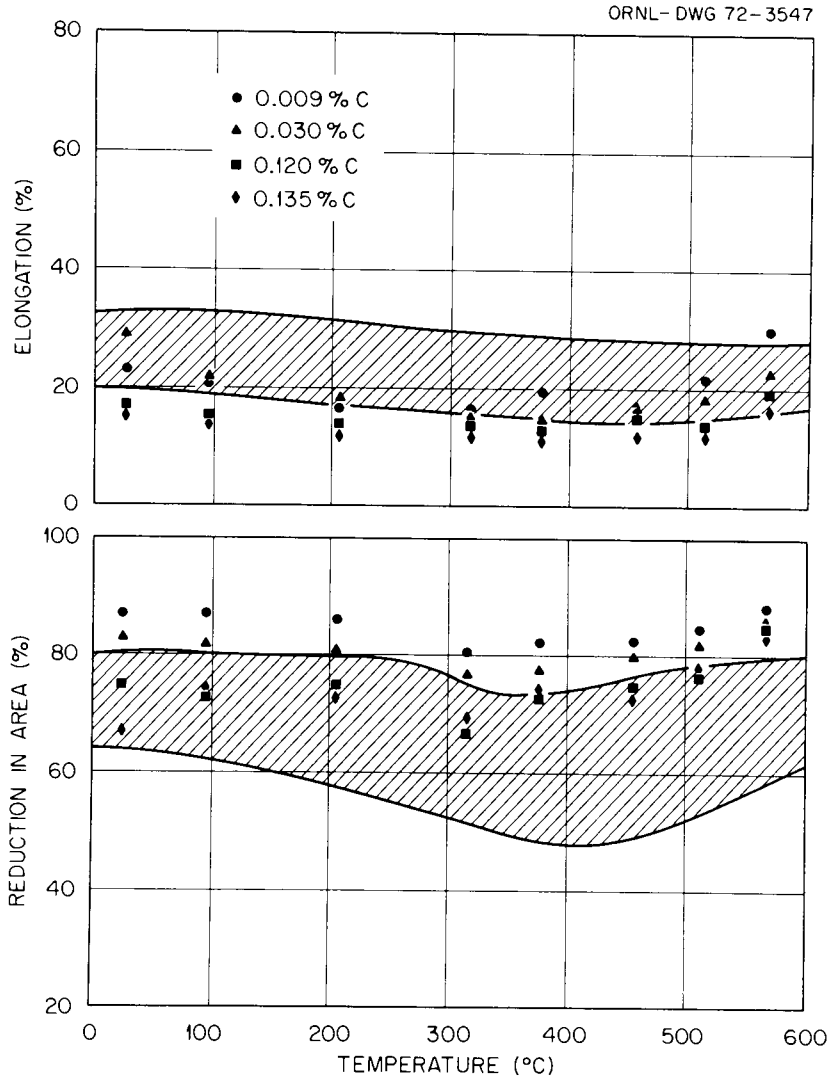

Fig. 9.43. Elongation and Reduction in Area Vs Temperature for Normalized-and-Tempered 2 1/4% Cr—1% Mo Steel. The data are compared with data taken from G. V. Smith, "An Evaluation of the Elevated Temperature Tensile and Creep-Rupture Properties of 2 1/4% Cr—1% Mo Steel" (to be published).

From the tensile data it is again obvious that the low and medium carbon rods have similar properties, especially yield stress. They work harden at different rates, and as seen in Fig. 9.42, the tensile stress for the medium carbon alloy is somewhat larger than that of the low carbon material.

Since the low carbon steel contains only ferrite, the similarities in strength for the low and medium carbon steels must mean the yield strength is primarily determined by the ferrite. Although the amount of dissolved carbon in the medium carbon ferrite is unknown (precipitates are present), the results must also reflect the relatively small strengthening effect of dissolved carbon at elevated temperatures. These conclusions are substantiated when the strengths of the "annealed" (as-received) rods at 565°C are compared (Table 9.13). The low and medium carbon steels were both single phase, while the high carbon rod contained the large dispersed carbides shown in Fig. 9.44. At room temperature, the high carbon rod is stronger and has less ductility than the other two rods. At 565°C, however, all three steels have about the same strength and ductility. From these limited data, therefore, we conclude that at 565°C the tensile properties of single-phase ferrite or ferrite with large dispersed carbides are not greatly affected by carbon content in the range 0.009 to 0.120% C. To show the effect of microstructure, and thus history (i.e., cooling rates, etc.), we can compare the data for the "annealed" (specified by the vendor to be furnace cooled from 900 to 425°C, then air cooled) standard Croloy plate with that of the three modified carbon rods, Table 9.13. At 565°C, the strength of the standard Croloy is over twice that of the modified carbon alloys. The microstructure, in this case, consists of a blocky proeutectoid ferrite and localized carbides (Fig. 9.45). Hence, the term "annealed" is of little value without a knowledge of the history and microstructure of the steel in question.

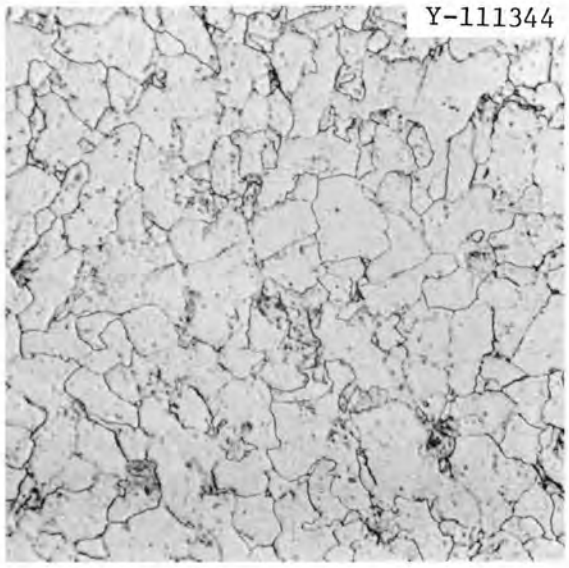

Fig. 9.44. Microstructure of Annealed (Furnace Cooled from 870°C) 2 1/4% Cr—1% Mo Steel (0.120% C). 500×.

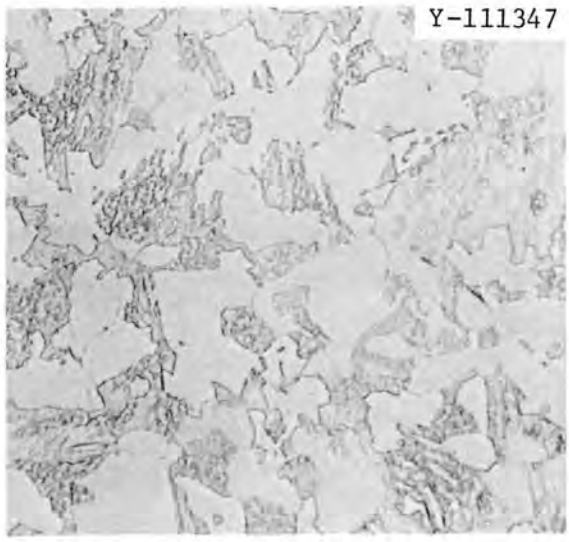

Fig. 9.45. Microstructure of Annealed (Furnace Cooled from 900 to 425°C then Air Cooled) Standard Croloy Plate (0.135% C). 500×.

PART II. SPACE POWER TECHNOLOGY

10. DEVELOPMENT OF URANIUM MONONITRIDE FUELS

J. L. Scott P. Patriarca

The objective of the ORNL program for irradiation testing of uranium mononitride (UN) is to obtain basic information on fuel swelling, fission-gas release, and compatibility with cladding materials at fuel temperatures from 1000 to 1500°C, cladding outside surface temperatures of 900 to 1400°C, and linear heat ratings of 5 to 10 kW/ft. Detailed descriptions of our capsule design[1] and previous test results[2,3,4] have been reported.

Thermal Simulation Tests

B. Fleischer, J. H. DeVan, and T. N. Washburn

Thermal simulation testing of UN-4, -5, and -6 type fuel pins is continuing in accordance with the schedule outlined previously.[5] The status and conditions of these tests through April 3, 1972, are reported in Table 10.1.

---

[1]V. A. DeCarlo, F. R. McQuilkin, R. L. Senn, K. R. Thoms, and S. C. Weaver, Design of a Capsule for Irradiation Testing of Uranium Nitride Fuel, ORNL-TM-2363 (February 1969).

[2]T. N. Washburn, D. R. Cuneo, and E. L. Long, Jr., "Irradiation Performance of Uranium Nitride at 1500°C," Am. Ceram. Soc. Bull. 50, 427 (1971).

[3]T. N. Washburn, K. R. Thoms, S. C. Weaver, D. R. Cuneo, and E. L. Long, Jr., "Examination of UN-Fueled Pins Irradiated at 1400°C Cladding Temperature," Trans. Amer. Nucl. Soc. 13, 101 (1971).

[4]S. C. Weaver, K. R. Thoms, and V. A. DeCarlo, "Irradiation Testing of UN in ORR," Trans. Amer. Nucl. Soc. 12, 547 (1969).

[5]B. Fleischer et al., Fuels and Materials Development Program Quart. Progr. Rept. Dec. 1971, ORNL-TM-3703, pp. 238–9.

Table 10.1. Status of Thermal Simulation Tests for UN-4, UN-5, and UN-6

Operating Conditions	Pin Type	
	UN-4 and UN-5	UN-6
Pin Temperature (°C)		
Top	1006	1010
Bottom	962	976
Cumulative Test Time (hr)	2996	2588
Number of Cycles	12	11
Vacuum at Exterior of Pins (torr)	5.8×10^{-9}	5.8×10^{-9}

Operation of Capsules

B. Fleischer, K. R. Thoms,* and T. N. Washburn

UN-4. This capsule was installed in the ORR on February 9, 1971, and has operated 8280 hr above 800°C cladding temperature through March 27, 1972.

The heat generation rate at the middle fuel pin has been increased from 10.2 to 10.8 kW/ft to achieve 1000°C thermocouple history as a function of heat generation rate and time revealed that the temperatures were about 50°C lower than desired.

Neutron radiographs of the capsule were made after about 7000 hr of operation. These films showed that there was no swelling of the fuel pins and little or no swelling of the fuel; however, some questionable evidence of cladding failure was present in the middle and bottom fuel pins. Analysis of cover gas samples has shown only minor quantities of fission gases and therefore does not correlate with the other large defects indicated on these radiographs. We are continuing our study of these radiographs. The radiographs also confirm our theory that the NaK capsule is off center with respect to the primary container. The

*Reactor Division

two containers appear to be in contact at the level of the top and bottom fuel pins and about 5 mils off center at the middle fuel pin. These conditions agree well with heat flow analysis made prior to radiography.

The calculated fission heat generation rates have been adjusted to take into account more recent information regarding higher gamma heat generation rates. This correction reduces the previously reported fission rates to about 96.5% of the previous values. A current summary of operating conditions and burnups for the three fuel pins is reported in Table 10.2.

UN-5. This capsule was installed in the ORR on March 1, 1971, and has operated 7955 hr above 800°C cladding temperature through March 27, 1972.

Table 10.2. Average Operating Conditions and Estimated Fuel Burnup for the Three Fuel Pins of Capsule UN-4 after 7975 hr of Irradiation

Fuel Pin	Average Cladding Temperature (°C)	Average Heat Generation Rate (kW/ft)	Estimated Burnup (% FIMA)
Top	973	10.0	2.19
Middle	972	9.8	2.14
Bottom	929	9.8	2.14

A current summary of the burnup and operating conditions for each fuel pin is presented in Table 10.3. The heat generation values have also been adjusted for the recent gamma heat information as described in the previous section for UN-4.

Table 10.3. Average Operating Conditions and Estimated Fuel Burnup for the Three Fuel Pins of Capsule UN-5 After 7650 hr of Irradiation

Fuel Pin	Average Cladding Temperature (°C)	Average Heat Generation Rate (kW/ft)	Estimated Burnup (% FIMA)
Top	1006	10.0	2.10
Middle	990	9.6	2.01
Bottom	974	9.9	2.08

UN-6. This capsule was installed in the ORR on August 3, 1971, and has operated 5000 hr above 800°C cladding temperature through March 27, 1972.

A current summary of the burnup and operating conditions for each of the fuel pins is presented in Table 10.4.

Table 10.4. Average Operating Conditions and Estimated Fuel Burnup for the Three Fuel Pins of Capsule UN-6 After 4700 hr of Irradiation

Fuel Pin	Period Covering First 1550 hr		Period from 1550 to 4700 hr		Estimated Burnup (% FIMA)
	Average Cladding Temperature (°C)	Average Heat Generation Rate (kW/ft)	Average Cladding Temperature (°C)	Average Heat Generation Rate (kW/ft)	
Top	860	4.1	979	4.5	0.84
Middle	845	4.6	938	4.8	0.90
Bottom	895	5.1	989	5.5	0.96

11. TUNGSTEN METALLURGY

A. C. Schaffhauser

The objective of this program is to provide the base technology on tungsten materials for advanced space power applications. We are developing fabrication processes for tungsten alloys based on chemical vapor deposition (CVD) and high-temperature extrusion techniques. Since a primary criterion for use of tungsten materials for fuel cladding is based on the creep properties, we are conducting extensive long-time tests at the temperatures of interest and determining the mechanisms that control creep behavior. The effects of decomposition products from a reactor fuel on creep properties are being determined. We are also evaluating the effects of high-temperature fast-neutron irradiation on the structure and physical properties of tungsten alloys.

Creep Properties of Tungsten Materials

J. O. Stiegler H. E. McCoy

Variations in The Creep Properties of Fluoride CVD Tungsten

Previously we showed that the high-temperature creep properties of fluoride CVD tungsten deposited from WF_6 and duplex deposits of fluoride and chloride CVD tungsten could be correlated with the fluorine impurity content of the deposits.[1,2] At 1650°C and stresses between 3500 and 10,000 psi, material high in fluorine (15–25 ppm) has a lower minimum creep rate, longer rupture life, and lower fracture strain (except for the duplex deposits) than material containing less than 9 ppm F. Data showing

---

[1]H. E. McCoy, Fuels and Materials Development Program Quart. Progr. Rept. Sept. 30, 1971, ORNL-TM-3550, pp. 216–19.

[2]J. O. Stiegler and H. E. McCoy, Fuels and Materials Development Program Quart. Progr. Rept. Dec. 31, 1971, ORNL-TM-3703, pp. 241–56.

this correlation are summarized in Table 11.1 and Figs. 11.1 and 11.2. Except as noted in Fig. 11.2 all of the specimens were annealed at the test temperature (1650°C) 2 to 4 hr before applying the test stress.

Recent data obtained at 2000 psi and 1650°C show a large decrease in the relative creep strength of the high fluorine material compared to the higher stress data (Fig. 11.2). However, annealing this material for 20 hr at 1800°C before test decreased the minimum creep rate at 2000 psi by more than a factor of 20. The 1800°C pretest annealing treatment appears to have little effect on the strength of the low fluorine material.

It should be noted that most of the data in Fig. 11.2 were obtained in externally loaded creep machines with strain measurements obtained from dial gage readings of movement of the load strain. This equipment was designed primarily for creep-rupture testing. Because of the low loads and small strains (<1%) in the tests below about 3000 psi significant inaccuracies could exist and the data should only be compared on a relative basis. However, the tests at 2000 psi on deposit WF-55 and GGA-D2 annealed 20 hr at 1800°C were performed with internally loaded ultrahigh vacuum creep

Table 11.1 Relation Between the Fluorine Content and Creep Properties of CVD Tungsten at 1650°C

Lot Number	Fluorine Content (ppm)	Minimum Creep Rate at 5000 psi (% hr^{-1})	Rupture Life at 5000 psi (hr)	Fracture Strain (%)
WF-1	17 to 25	0.015	172	1 to 7
WF-2	13 to 23	0.0093	270	3 to 6
WF-55	15 to 25	0.0046	380	1 to 12
WF-5	3 to 6	0.075	126	19
WF-6	2 to 7	0.16	108	30 to 45
WF-9	2 to 7	0.22 to 0.31	77.6	12 to 46
GGA-D1[a]	14	0.015	1686	6 to 51

[a]Duplex CVD tungsten supplied by Gulf General Atomic, San Diego, Calif.

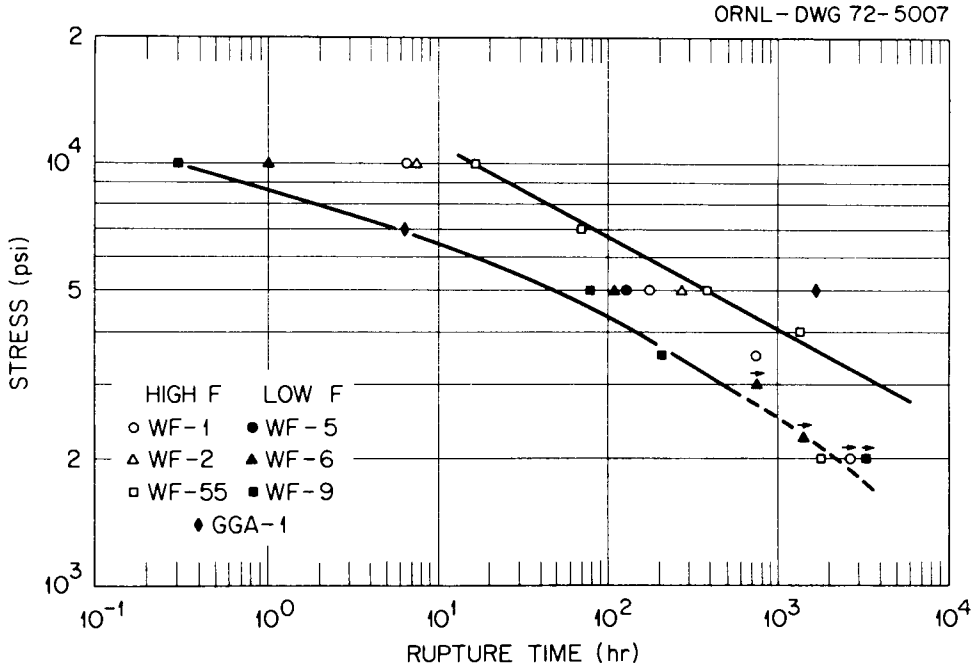

Fig. 11.1. Comparative Stress-Rupture Properties of Several Lots of CVD Tungsten at 1650°C. (Low fluorine is 2–7 ppm high fluorine is 13–25 ppm.)

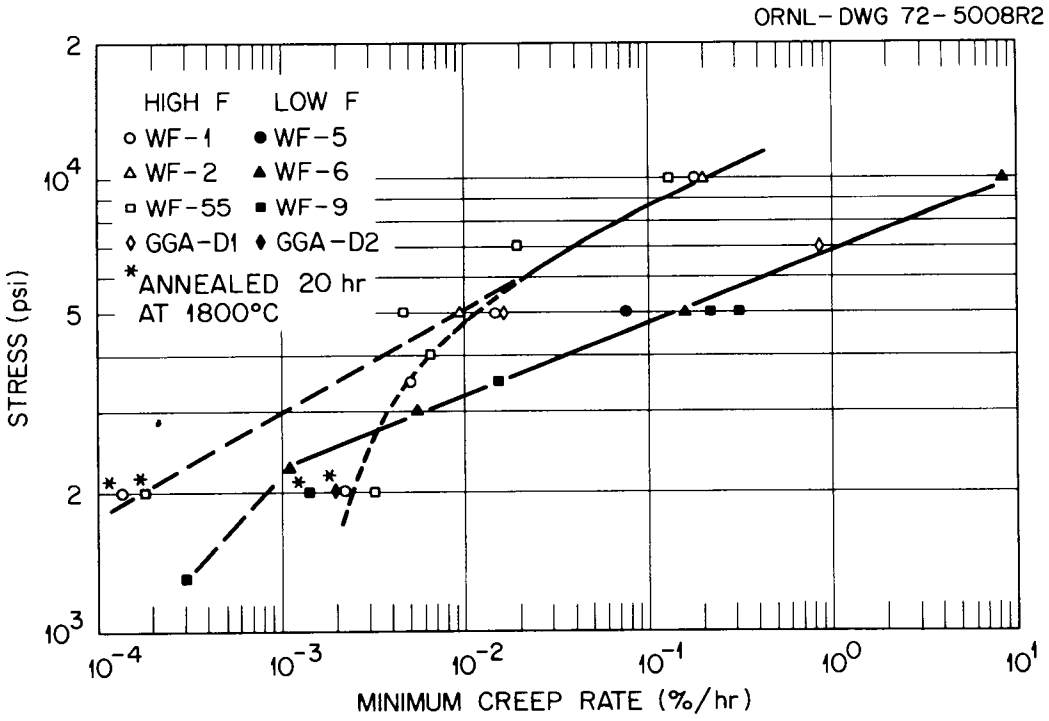

Fig. 11.2. Comparative Creep Rates of Several Lots of CVD Tungsten at 1650°C. (Low fluorine is 2–7 ppm, high fluorine is 13–25 ppm.)

machines with optical strain measurement having an accuracy of about ±0.02% strain. These data, which are discussed further in the next section, confirm the data obtained with the creep-rupture machines.

At this time we can only postulate that the large decrease in the relative creep strength of the 1650°C annealed high fluorine material below about 3500 psi is due to an instability of the microstructure. The fact that annealing at 1800°C before testing results in a large decrease in minimum creep rate indicates that the larger grain boundary bubbles formed at this temperature stabilize the grain boundaries and inhibit deformation of the matrix under stress. Stress induced grain boundary void growth at the higher stresses in the 1650°C annealed material could have the same effect. Optical metallography, transmission electron microscopy, and electron fractography of creep tested specimens are being performed to verify this hypothesis.

Low-Stress Creep Tests on CVD Tungsten

We are obtaining creep data on CVD tungsten at low stresses producing 1% creep in 1000 to 10,000 hr to provide design data needed for the thermionic reactor program. The test matrix and creep testing equipment being used have been described previously.[2] A cooperative testing program with NASA-Lewis Research Center is in progress to accelerate acquisition of data and provide duplicate testing of specimens. The major emphasis is on testing of duplex deposits of CVD tungsten, described previously,[2] supplied by Gulf General Atomic (GGA) which is the reference material for emitters in thermionic fuel elements. Tests on high fluorine (15–25 ppm) fluoride CVD deposits are also under way because of the higher strength exhibited by this material in higher stress screening tests.

Tests at 1000 and 2000 psi at 1650°C are under way on specimens from deposits GGA-D2 and WF-55. Deposit GGA-D2 is a duplex deposit containing 4 to 7 ppm F and WF-55 is a fluoride deposit made at ORNL containing 15 to 25 ppm F. All specimens were annealed 20 hr at 1800°C before testing.

The creep data at 2000 psi for the two deposits is compared in Fig. 11.3. The minimum creep rate of the higher fluorine deposit (WF-55) is more than a factor of 10 lower than the low fluorine duplex deposit for

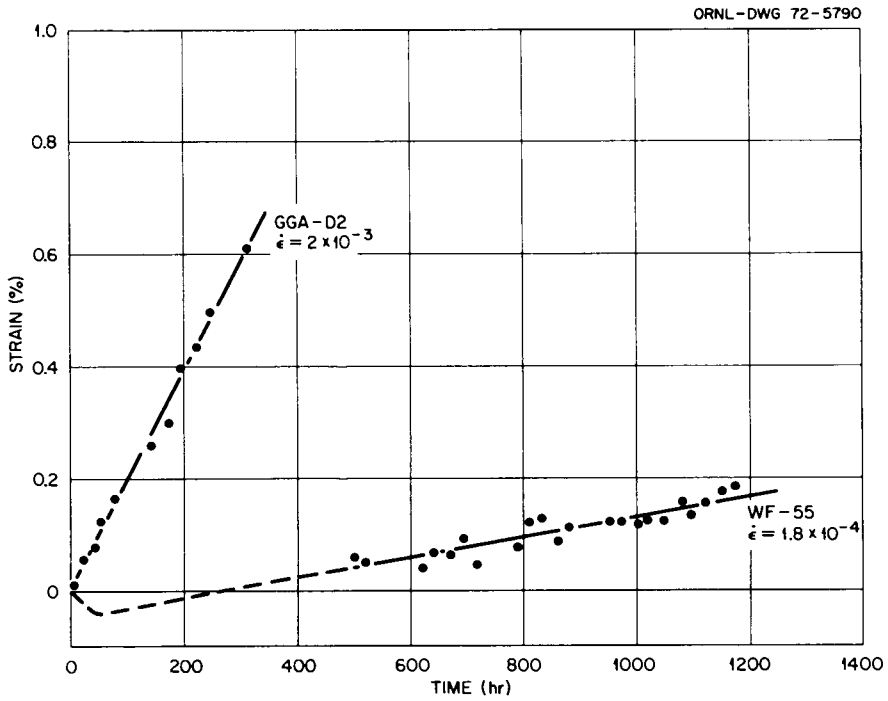

Fig. 11.3. Comparison of the Creep Properties of Duplex CVD Tungsten (GGA-D2, 5 ppm F) and Fluoride CVD Tungsten (WF-55, 20 ppm F) Tested at 2000 psi and 1650°C Annealed 20 hr at 1800°C Before Test.

the test times to date. Inconsistent strain measurements occurred during the first 500 hr of testing on WF-55 due to malfunction of the optical strain measuring device. Measurement of the true elongation after 500 hr and compensation for thermal expansion indicated that the specimen actually decreased in length during the first 100 hr after applying the stress. This behavior has also been observed in low stress creep test on CVD tungsten at TRW.[3] Insufficient strain has occurred in the two specimens under test at 1000 psi to permit comparison.

The two remaining creep specimens from deposit GGA-D2 were sent to NASA-Lewis for testing at 1000 and 500 psi at 1650°C. Also enough sheet material for 16 samples from our deposit WF-56 containing 11–15 ppm F was sent to NASA-Lewis for their creep testing program.

---

[3]K. D. Sheffler, Generation of Long Time Creep Data on Refractory Alloys at Elevated Temperatures, First Semi-Annual Report Nov. 8, 1970, TRW ER-7506.

Two deposits of fluoride CVD tungsten having high and low fluorine contents (GGA-F3, 3 to 5 ppm F and GGA-F4, 18 to 26 ppm F) were received from GGA and are being machined into specimens. Two specimens from each deposit will be tested at ORNL and NASA-Lewis.

Effect of Carburization on the Creep Properties of Tungsten Alloys

H. Inouye

The creep properties of 0.040-in.-diam W wire are being measured while being carburized with CH_4 at thermionic temperatures.

A 1033-hr creep test at 1650°C and 2000 psi was conducted at a CH_4 pressure of 2×10^{-4} torr to determine whether the creep strength continues to increase with the CH_4 pressure. The results of this test are given in Table 11.2 together with data previously reported[4] for comparison purposes. These data show no definite trend as to the effect of the CH_4 pressure; however, in all cases carburized tungsten continues to show more creep resistance than comparably stressed tungsten in vacuum.

An 864-hr test was also run at 1650°C and 1000 psi to determine the influence of carburization at a lower stress. As shown in Table 11.2 carburization at this stress appears to have the greatest effect during the earlier stages of the creep test and has a probable weakening effect on the minimum creep rate, $\dot{\varepsilon}$. It is presently suspected that the graphite cylinder being used as the control for temperature measurement does not give consistent results due to slightly different degrees of contact with the tungsten specimen. Temperature errors of ±40°C are suspected and may account for the scatter in the tests conducted at 2000 psi.

---

[4]H. Inouye, Fuels and Materials Development Program Quart. Progr. Rept. Dec. 31, 1971, ORNL-TM-3703, p. 257.

Table 11.2 Effect of CH_4 on the Creep Properties of Tungsten at 1650°C

Pressure of Environment (torr)	Test Time (hr)	Time (hr) for Strain of					Minimum Creep Rate (hr^{-1})
		0.1%	0.2%	0.5%	1.0%	2.0%	
				2000 psi			
3×10^{-8} (vacuum)	959	—	—	75	188	385	5.0×10^{-5}
3×10^{-5} (CH_4)	721	—	—	232	375	750	2.6×10^{-5}
9×10^{-5} (CH_4)	1007	—	—	52	445	1280	1.2×10^{-5}
2×10^{-4} (CH_4)	1033	—	—	90	245	742	1.6×10^{-5}
				1000 psi			
1×10^{-7} (vacuum)	500	17	80	430	—	—	6.7×10^{-6}
3×10^{-5} (CH_4)	864	85	187	500	—	—	9.7×10^{-6}

Effect of Fast-Neutron Irradiation on the Properties of Tungsten Alloys

E. E. Bloom D. L. McElroy

EBR-II Irradiation Experiment (W. F. Wiffin)

Our high-temperature tungsten irradiation capsule, O-11, has reached its goal exposure and has been removed from EBR-II. The capsule was located in the center position of subassembly X136 and was exposed during runs 51C through 55A. The exposure between September 19, 1971 and March 26, 1972, was 6331 MWd. The subassembly occupied EBR-II grid position 7C1 during its reactor residence. A preliminary estimate of the midplane fluence is $7.8 \pm 2.0 \times 10^{21}$ neutrons/cm^2 ($E > 0.1$ MeV). As only the near-midplane positions of this capsule were used for irradiation of the tungsten specimens, all specimens will have been exposed to a fluence at least 80% of the midplane value.

The design of this experiment was described briefly in an earlier report.[5] The experimental design used to achieve the elevated temperatures (600 to 1500°C) is basically the same as that used in earlier ORNL structural materials experiments in EBR-II. The design balances the heat generated by gamma heating in the cylindrical specimen holder against the width of the argon-filled conduction gap between the specimen holder and the containment tube. This temperature gradient across the gap gives the desired irradiation temperature. A two-dimensional steady-state nodal heat transfer computer program (HEATING3) was used to design the experiment. This program calculates heat transfer as a function of temperature dependent conductivity and radiation. Midplane heating rate assumed was 1.41 W/g for stainless steel. The total hemispherical emittance assumed for tungsten was 0.4 and for gold plated stainless steel was 0.03. Thermal conductivity versus temperature values used are snown in Table 11.3.

---

[5] F. W. Wiffen and D. A. Dyslin, Fuels and Materials Development Program Quart. Progr. Rept. Dec. 31, 1970, ORNL-TM-3300, p. 258.

Table 11.3 Heat Transfer Data Used for Tungsten Irradiation Experiments

Temperature (°F)	Thermal Conductivity (Btu/hr•ft•°F) Stainless Steel	Argon	Tungsten	Tantalum
0	8.25	0.008	75.3	30.0
1000	12.50	0.022	69.7	30.0
2000	16.75	0.030	64.2	30.0
3000	21.00	0.038	58.6	30.0

Specimen holders were designed to operate at irradiation temperatures of 600, 900, 1100, 1300, and 1500°C. The specimen loading in a tungsten specimen holder is shown schematically in Fig. 11.4 and all of the components of a typical holder, assembled prior to loading, are shown in Fig. 11.5. The specimen loading distribution of the tungsten and tungsten-rhenium alloys produced by the various fabrication methods is given in Table 11.4 for the five specimen holders.

Electrical Resistivity Measurements (R. K. Williams)

Room temperature electrical resistivity (ρ) data were obtained on three tungsten and three W–25% Re alloy specimens which had been irradiated in EBR-II subassembly X034 to a fluence of 3.7×10^{22} neutrons/cm^2 ($E > 0.1$ MeV) by General Electric Nuclear Systems Project. The tungsten samples were irradiated at nominal temperatures of 800, 900, and 1000°C and the W–25% Re samples at 700, 800, and 900°C. The results were compared to data on unirradiated control samples and for tungsten the ρ was found to increase by 17, 12, and 12% at 800, 900, and 1000°C respectively. For the W–25% Re alloy, the ρ increments were +6, –10, and –11% at 700, 800, and 900°C respectively. The latter results indicate that irradiation induces a phase change or ordering in the W–25% Re alloy.

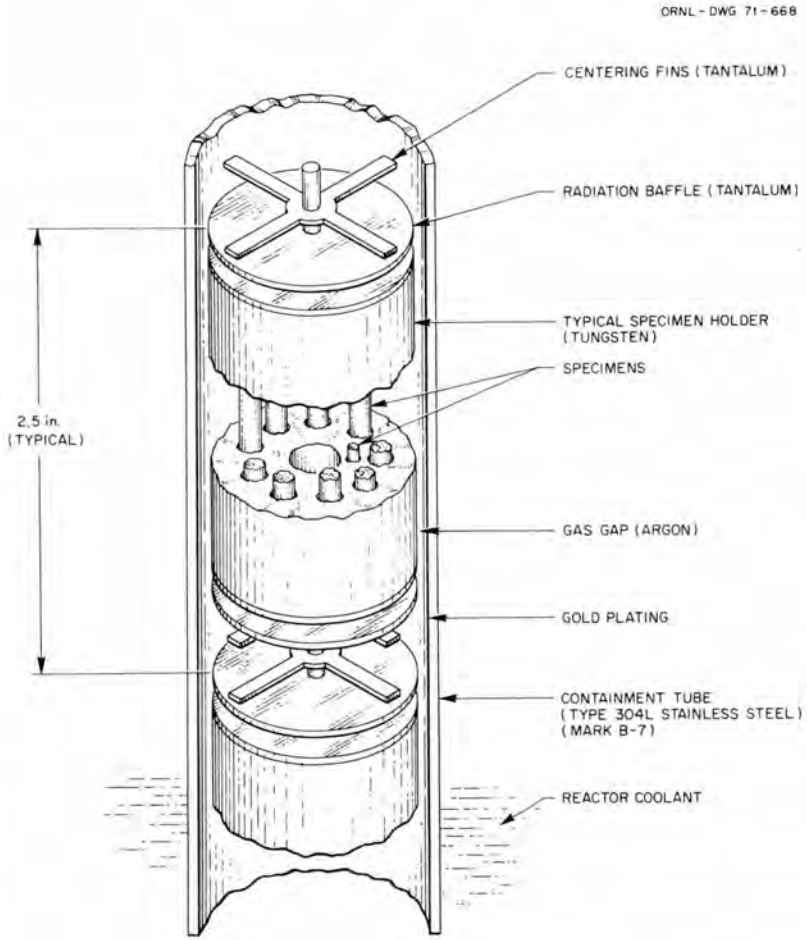

Fig. 11.4. Schematic of Specimen Holder Used in EBR-II Capsule 0-11 Tungsten Irradiation Experiment.

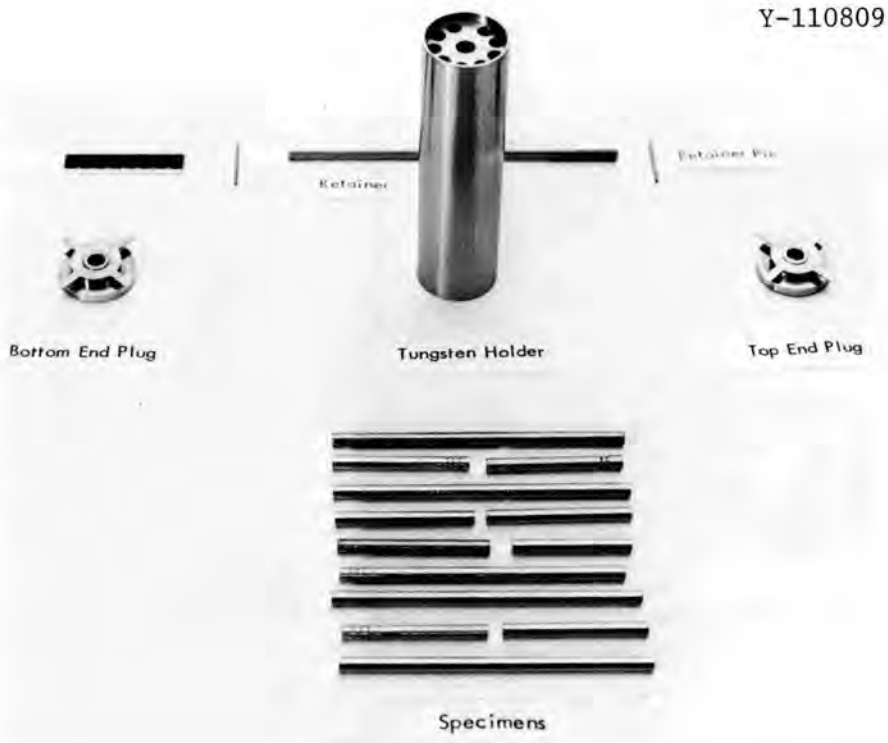

Fig. 11.5. Specimens and Components for a Specimen Holder for EBR-II Capsule 0-11 Shown Before Assembly.

Table 11.4. Specimen Distribution in Tungsten Irradiation Capsule 0-11

Product[a]	CVD-W →					AC-W		PM-W	AC-W-25 Re		PM-W-25 Re		AC-W-5 Re		CVD-W-5 Re
Heat number	GGA-F-1 →				PW69C	W-1046		TECO	WR-1099		W1124-525		SA 25816		WRe 229
Heat treatment	5 hr 1800°C		As deposit		5 hr 1800°C →			1 hr 1600°C	5 hr 1800°C →						
Sample type[b]	RES	TEM	RES	TEM	TEM	RES	TEM	TEM	RES	TEM	RES	TEM	RES	TEM	TEM
Experiment position															
Holder No. 1 1500°C	1	2	0	1	1	1	1	0	1	1	1	1	0	1	1
Holder No. 2 1300°C	1	2	1	1	1	1	1	1	1	1	0	0	0	1	1
Holder No. 3 1100°C	1	1	0	0	0	1	2	1	1	1	1	1	1	0	1
Holder No. 4 900°C	2	1	0	0	1	2	1	0	1	1	0	1	0	1	1
Holder No. 5 600°C	0	1	0	0	0	1	1	1	1	0	0	1	0	0	0

[a] RES = resistivity sample, 0.100 in. in diameter by 2.1 in. long.
TEM = electron microscopy specimen rods, 0.100 in. in diameter by 1.0 in. long.

[b] CVD = chemical vapor deposited.
AC = arc cast.
PM = powder metallurgy.

12. PHYSICAL METALLURGY OF REFRACTORY ALLOYS

R. G. Donnelly P. Patriarca

The purpose of this program is to provide a base technology evaluation of high-temperature materials for use in space applications of radioisotope thermoelectric generators (RTG's). Emphasis is presently on tantalum and molybdenum alloys used as containment materials for $^{238}PuO_2$.

Effect of Oxygen Contamination on the Mechanical Properties of T-111

C. T. Liu

Previous work[1] indicated that T-111 can tolerate 300 and 750 ppm O when contaminated in low oxygen pressure at 825 and 1000°C, respectively. The fractured surfaces of brittle specimens were examined by scanning electron microscopy. The fractograph of a specimen containing 730 ppm O doped at 1000°C (Fig. 12.1) indicates that grain boundary separation (location A) and cleavage (location B) are competitive fracture modes. It is interesting to note that slip traces (location C) are observed on some grain boundary areas. The ductility of the contaminated specimen increases with heat treatment at high temperatures. Figure 12.2 shows the dimple-type ductile fracture surface of a specimen annealed 15 min at 1700°C after doping with 3640 ppm O. Here, HfO_2 precipitates (about 0.3 μm diam) are observed at the bottom of the crests on the fracture surface.

In order to show the effect of a heat pulse during reentry of the Pioneer heat source on the tensile properties of oxygen-contaminated T-111, 20-mil sheet specimens containing 700, 1700, and 3150 ppm O were subjected to the thermal history outlined in Table 12.1, then tested at

---

[1]C. T. Liu, Fuels and Materials Development Program Quart. Progr. Rept. Dec. 31, 1971, ORNL-TM-3703, pp. 259–260.

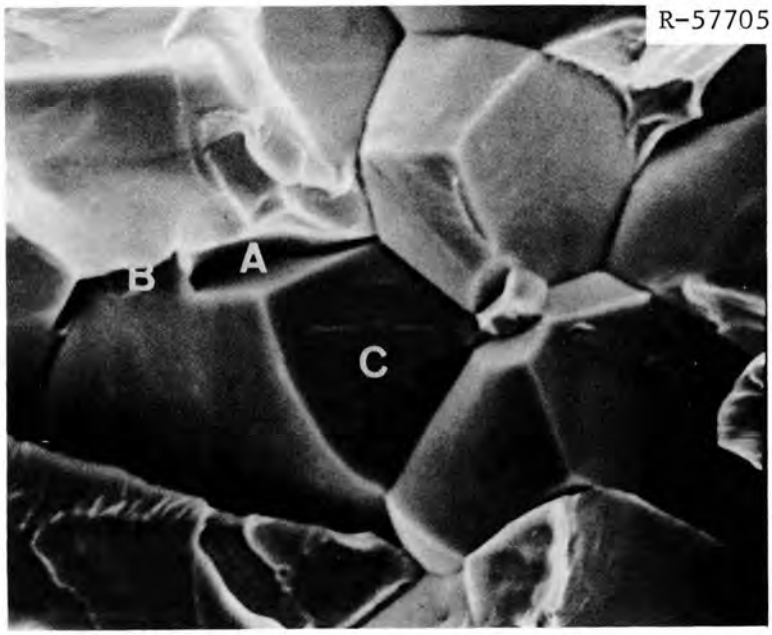

Fig. 12.1. Scanning Electron Microscopy Fractograph of T-111 Doped with 730 ppm O at 1000°C Exhibiting 2.2% Elongation at Room Temperature. 3000X.

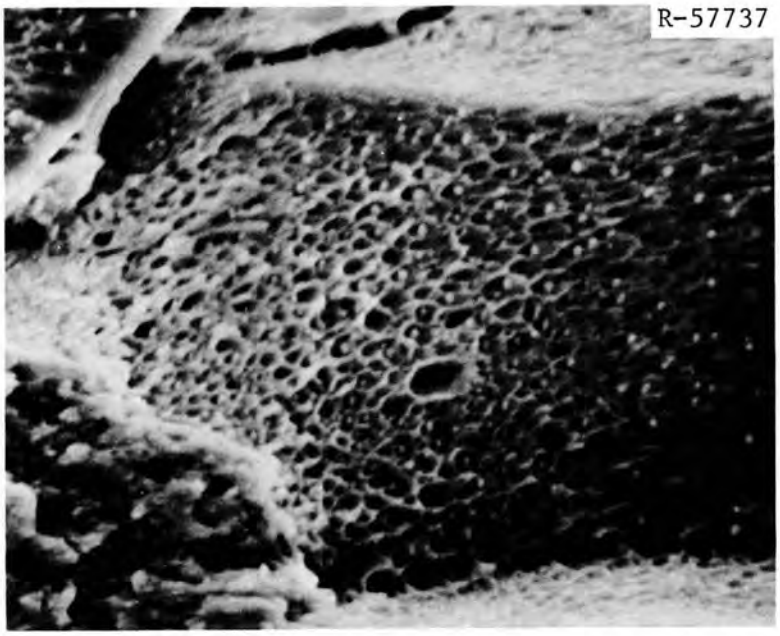

Fig. 12.2. Scanning Electron Microscopy Fractograph of T-111 Doped with 3640 ppm O, Heat Treated 15 min at 1700°C; 10.5% Elongation at 760°C. 3000X.

Table 12.1. A Possible Heat Pulse[a] During Reentry of Pioneer Heat Source

Time Elapsed (sec)	Temperature (°F)
0	1517
1180	2000
1350	2500
1400	2600
1460	2500
1560	2400

[a]Information obtained from A. P. Litman, AEC/SNS, Washington, D. C.

room temperature. As shown in Table 12.2, the simulated heat pulse ductilizes oxygen-embrittled T-111 to the extent that the alloy can now tolerate an oxygen level between 1700 and 3150 ppm. Assuming a linear contamination rate of 1/20 ppm/hr (based on the data of Pioneer test capsules PF-3 and -7), the results in Table 12.2 suggest that the T-111 strength member of the Pioneer heat source can be ductilized effectively by the reentry heat pulse after five years at 825°C.

Table 12.2. Effect of Pioneer Heating Pulse on the Mechanical Properties of Oxygen-Contaminated T-111

Oxygen Amount Doped (ppm)	Heat-Pulse Treatment	Mechanical Properties at Room Temperature		
		Elongation (%)	Tensile Strength (psi)	Fracture Mode
0	No	28	101,000	Ductile
700	No	1	135,000	Brittle
700	Yes	17.3	112,000	Ductile
1700	No	0[a]		Brittle
1700	Yes	10.2	151,000	Ductile
3150	No	0[a]		Brittle
3150	Yes	1.8	234,000	Brittle

[a]Fracture within elastic limit.

The critical condition which ductilizes T-111 during reentry is believed to be the 110 sec (1.83 min) at temperatures between 1371 (2500°F) and 1427°C (2600°F) (see Table 12.1). To verify this, the kinetics of the ductilization of T-111 specimens containing 3000 ppm O at 1400°C was studied. The results in Table 12.3 show that the ductility increases and strength decreases continuously with annealing time. The oxygen-contaminated specimen was only partially ductilized after the 2 min anneal at 1400°C, which is consistent with the results in Table 12.2. Examination by transmission electron microscopy reveals numerous HfO_2 precipitates about 100 A diam [Fig. 12.3(a)]. The ductilization is due to the continuous coarsening of fine precipitates with annealing time [Fig. 12.3(b)].

Table 12.3. Effect of Annealing Time at 1400°C on the Room-Temperature Tensile Properties of T-111 Containing 3000 ppm O

Annealing Time (min)	Elongation (%)	Tensile Strength (psi)
0	0.4	110,000
2	1.7	233,000
5	3.6	220,000
30	10.5	177,000
240	13.0	142,000

Based on these studies we believe that oxygen contamination of T-111 at still higher temperatures can result in significant strengthening with only moderate reduction of ductility. In other words, T-111 can tolerate much higher levels of oxygen when used at higher temperatures. A series of T-111 specimens were thus doped with oxygen at a pressure of 1×10^{-5} torr at 1200°C and tested at room temperature. The results in Table 12.4 show that T-111 can tolerate 4000 to 5000 ppm O, which is more than an order of magnitude higher than the permissible level when doped at 825°C.

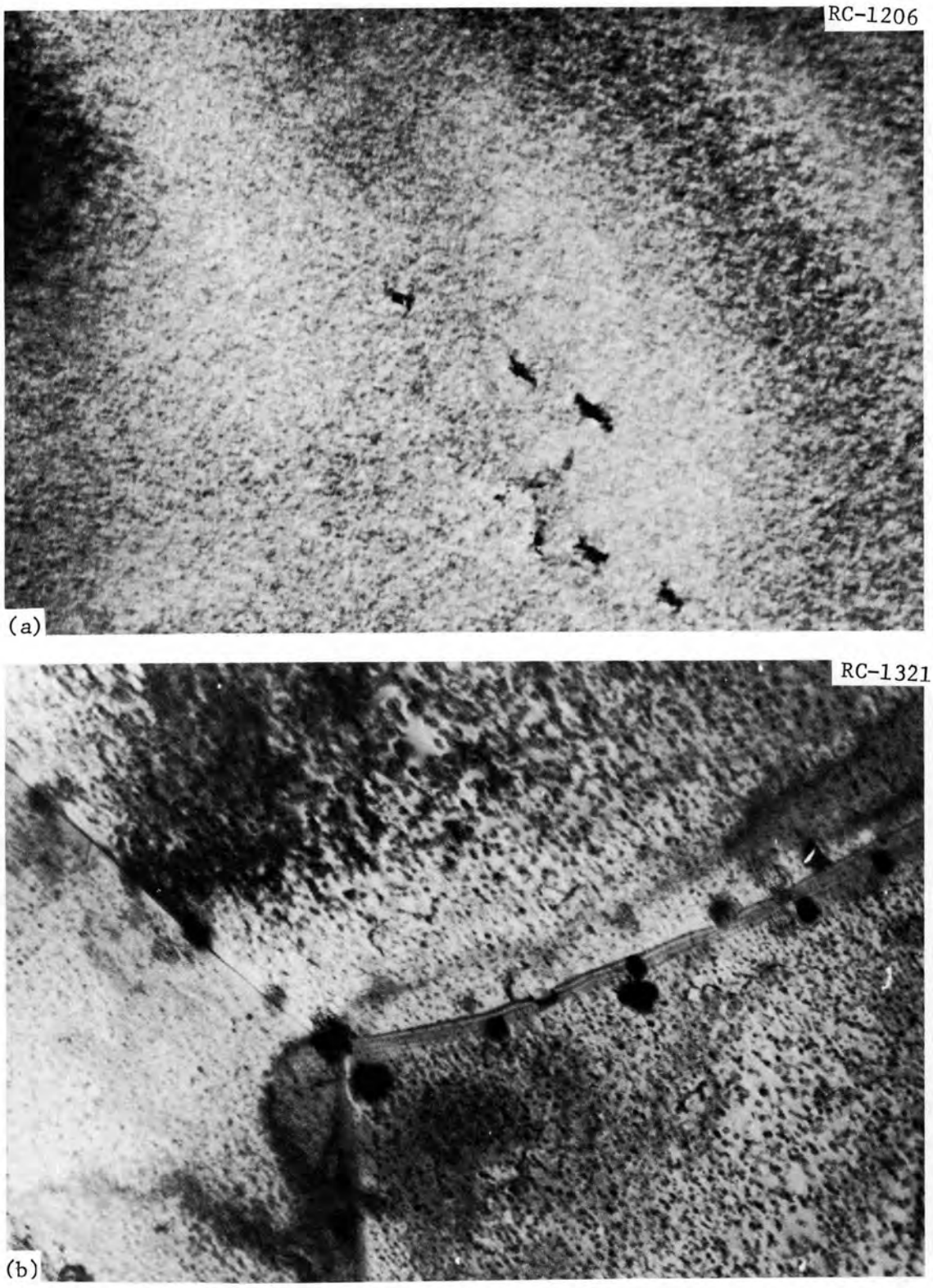

Fig. 12.3. TEM of T-111. (a) As-doped with 2650 ppm O at 1000°C. (b) As-doped at 1000°C with 2650 ppm O and annealed 5 min at 1400°C. 88,750×.

Table 12.4. Room-Temperature Mechanical Properties of T-111 Oxygen Doped at 1200°C

Oxygen Amount Doped (ppm)	Tensile Strength (psi)	Elongation (%)
1375	114,000	18.7
2655	125,000	16.7
3940	147,000	11.0
5120	178,000	2.2
6550	40,000[a]	0[a]

[a]Fractured within elastic limit.

Effect of Oxygen on the Mechanical Properties of 0.090-in.-thick T-111

H. Inouye

The embrittlement of 0.020- and 0.040-in.-thick T-111 by oxygen has been reported to be dependent on the contaminating temperature as well as the specimen thickness.[2] Because of the importance of the relationship between oxygen contamination and the ductility of the strength member in the Pioneer heat source, it was deemed necessary to conduct similar studies on 0.090-in.-thick T-111. The tensile properties of 0.090-in.-thick T-111 at 825°C which were machined from blanks after doping with oxygen at a rate of about 1.5 ppm/hr are summarized in Table 12.5. The data show that the ductility remains constant at about 18% elongation to an oxygen level of at least 290 ppm O, but drops sharply from there to zero ductility between 686 and 1070 ppm. Within experimental scatter, the ductility of T-111 as a function of the oxygen content at 825°C of the 0.090-in.-thick specimen is the same as the ductility of the 0.020-in.-thick specimen. Table 12.6 shows that the ductility of T-111 at room temperature for a given level of oxygen decreased as the specimen thickness increased.

[2]H. Inouye, Fuels and Materials Development Program Quart. Progr. Rept. Dec. 31, 1971, ORNL-TM-3703, pp. 264–265.

Table 12.5. Effect of Oxygen on the Tensile Properties of 90-mil-thick T-111[a] at 825°C

Oxygen Added (ppm)	Tensile Strength (psi)	Elongation (%)
Control[b]	59,200	18.0
185	72,500	20.5
290	77,500	18.5
422	75,500	11.5
560	71,900	5.2
686	74,600	2.8
1070	50,800	0.0

[a]3/4- × 2 1/2- × 0.090-in. blanks doped with oxygen at 1×10^{-6} torr prior to machining tensile specimens.

[b]Annealed 1 hr at 1650°C. Analysis: 10 ppm O, 10 ppm N, 3 ppm H, 24 ppm C.

Table 12.6. Effect of Specimen Thickness on the Room-Temperature Ductility of T-111

Oxygen Added (ppm)	Elongation, %		
	Specimen Thickness, in.		
	0.020	0.040	0.090
170	23	26	16.8
244	21	12	6.0
362	10	1	3.2

Contamination Studies of T-111 and TZM by Impurities Out-Gassed from Graphite and Min-K 1301

H. Inouye

Tensile specimens of bare T-111, molybdenum-coated T-111, and TZM have been exposed at 825°C to gases out-gassed from graphite and Min-K 1301 under conditions that approximate those in the Pioneer radioisotope

thermoelectric generator.[3] The reaction rates of 0.020-in.-thick sheet specimens of T-111 with the impurity gases transported through a 0.020-in.-diam orifice are shown in Table 12.7. These results show that the oxygen contamination varies linearly with the exposure time. The calculated reaction rates of 0.6 to 0.8 ppm/hr for 0.090-in.-thick specimens contaminated from one side are somewhat higher than the 0.16 ppm rate observed for PF-7 (ref. 4) in a 1000-hr test. This difference is attributed mainly to differences in the volume ratios of the test components, to the geometry of the separate systems, and to the use of different out-gassing procedures.

The contamination rate of T-111 decreases as the thickness of molybdenum coating increases as shown in Table 12.8. Table 12.9 shows that the oxygen contamination of T-111 coated with 0.0012 in. of molybdenum is 16 to 27 times lower than the uncoated specimens and that the tensile ductility of the coated specimens is not seriously impaired by the simulated Pioneer environment. The uncoated specimens were

---

[3]Argon at 600 torr plus gases from ATJ graphite and Min-K at 538°C gettered with both bare and palladium-wrapped zirconium foil. Graphite previously vacuum out-gassed 4 hr at 1200°C and Min-K out-gassed 48 hr in air at 400°C plus 2 hr at 600°C in vacuum.

[4]S. E. Bronisz, Los Alamos Scientific Laboratory, personal communication.

Table 12.7. Reaction Kinetics of T-111 in the Simulated Pioneer Heat Source Environment

Exposure (hr)	Contamination Rate for T-111, ppm/hr	
	0.020 in. thick[a]	0.090 in. thick[b]
280	7.21	0.80
506	5.72	0.63
1004	6.57	0.73

[a]Based on weight gain. Specimen contaminated from both sides.

[b]Calculated rate for 90-mil-thick T-111 contaminated from one side.

Table 12.8. Effect of Molybdenum Coating on Contamination of 0.020-in.-thick T-111 in Simulated Pioneer Environment

Exposure (hr)	Thickness of Molybdenum (in.)	Contamination Rate (ppm/hr)
204	None	11.8
534	None	11.1
204	0.0001[a]	4.0
204	0.0002[a]	2.2
534	0.0002[a]	1.5
280	0.0012[b]	0.27
506	0.0012[b]	0.35
1004	0.0012[b]	0.29

[a]Vacuum-evaporated molybdenum.

[b]0.0002-in. vacuum-evaporated molybdenum plus 0.001-in. CVD molybdenum.

Table 12.9. Effect of a 0.0012-in.-thick Molybdenum Coating on the Contamination and Room-Temperature Properties of 0.020-in.-thick T-111

Exposure (hr)	Level of Oxygen Contamination,[a] ppm		Tensile Properties of Coated Specimens	
	Uncoated	Coated	Tensile Strength (psi)	Elongation (%)
280	2020	76	83,300	15.0
506	2900	179	100,000	15.3
1004	6620	293	102,500	10.7

[a]Calculated from weight gain of specimens.

completely brittle as would be expected for specimens containing 2000 to 6600 ppm O.

Table 12.10 summarizes the tensile properties of TZM after 2004 hr exposure to the simulated environment. In general, no significant differences were noted in the tensile strengths; however, the ductility

Table 12.10. Tensile Properties of 0.020-in.-thick TZM at Room Temperature and 825°C After Exposure to Simulated Pioneer Heat Source Environment

Exposure (hr)	Ultimate Tensile Strength (psi)	Elongation (%)
	Room Temperature	
Control	79,600	33.5
534	77,800	35.7
1030	78,400	32.8
2004	79,300	15.0
	825°C	
Control	45,000	24.8
534	43,800	20.0
1030	43,700	21.8
2004	46,300	12.0

decreases steadily with exposure times to values of 12 to 15% elongation. Although chemical analyses have not been obtained yet, the extent of contamination based on the weight change of the specimens was very small. From the standpoint of compatibility with the Pioneer heat source environment, it is concluded that both molybdenum-coated T-111 and TZM would be suitable alternate strength members.

Effect of Oxygen Contamination on the Mechanical Properties of Molybdenum-Base Alloys

C. T. Liu

The mechanical properties of molybdenum-base sheet specimens contaminated with oxygen at 825°C and 1×10^{-5} torr O pressure were determined at various temperatures. The results are presented in Tables 12.11 and 12.12 together with data obtained previously at room temperature and 825°C. Oxygen contamination of TZM at 825°C causes only a small decrease of ductility at room temperature, and the ductility remains at a level of 25% after 2000 hr of exposure. However, as shown in Table 12.11, TZM

Table 12.11. Tensile Properties of 20-mil-thick TZM Sheet Specimens at Various Test Temperatures After Contamination with Oxygen at 1×10^{-5} torr and 825°C

Doping Time (hr)	Tensile Strength (psi)	Elongation (%)
	Room Temperature	
0	79,300	35.3
100	81,200	35.3
500	85,000	29.2
994	84,000	31.0
2000	85,000	24.5
	825°C	
0	45,000	24.8
994	46,800	18.0
2000	51,200	17.7
	1093°C	
0	33,000[a]	24[a]
500	41,000	15.3
994	40,000	12.2
2000	42,000	6.6
	1316°C	
0	22,000[a]	30[a]
500	25,000	23
994	25,500	14.2
2000	28,700	10.0

[a]General Electric Company, Multi-Hundred Watt, Radioisotope Thermoelectric Generator Program, GESP-7034 (March 1970).

suffers a moderate reduction of ductility at 825 and 1316°C and a more serious reduction at 1093°C. These results clearly indicate that increasing the test temperature does not improve the ductility of oxygen-contaminated TZM. The same behavior was found in T-111. The tensile strength of TZM does increase some with doping time.

The response of the Mo–46% Re alloy to an oxygen environment is quite different from TZM. The Mo–46% Re specimens show no change in ductility at room temperature after 1000 hr contamination, but a sharp drop after the 2000-hr exposure assuming that the reported value of

Table 12.12. Tensile Properties of 20-mil-thick Mo–46% Re Sheet Specimens at Room Temperature and 825°C After Contamination with Oxygen at 1×10^{-5} torr

Doping Time (hr)	Tensile Strength (psi)	Elongation (%)
	Room Temperature	
0	195,000	8.2
1000	192,000	9.2
2000	153,000	1.3
	825°C	
1000	116,000	13.7
2000	115,000	9.6

1.3% elongation in Table 12.12 is not due to defects in the specimen. However, increasing the test temperature to 825°C restores the ductility of the specimen contaminated for 2000 hr. The difference in behavior of these two alloys is believed to be due to the retention of oxygen in solution in the Mo-Re alloy, but in TZM oxygen reacts with zirconium and titanium to form oxide precipitates.

Effect of CO Gas Contamination on the Mechanical Properties of Molybdenum-Base Alloys

C. T. Liu

The tensile properties of TZM sheet specimens contaminated with CO at 825°C and 1×10^{-5} torr gas pressure have been determined at elevated temperatures. The results are presented in Table 12.13 together with those obtained previously[5] at room temperature and 825°C. TZM shows a moderate increase in strength and a moderate decrease in ductility with doping time; however, TZM has more than 15% elongation after 2000 hr exposure. We thus believe that TZM is reasonably compatible with CO.

[5]H. Inouye, Fuels and Materials Development Program Quart. Progr. Rept. Dec. 31, 1971, ORNL-TM-3703, pp. 273–274.

Table 12.13. Tensile Properties of 20-mil-thick TZM Sheet Specimens at Various Temperatures After Contamination with CO at 825°C and 1×10^{-5} torr

Doping Time (hr)	Tensile Strength (psi)	Elongation (%)
	Room Temperature	
0	79,000	37.0
0	79,600	33.5
196	79,500	33.2
1000	83,000	30.0
2000	82,000	27.9
	825°C	
0	45,000	24.8
2000	46,300	22.5
	1093°C	
0	33,000[a]	24[a]
1000	38,800	15.2
	1316°C	
0	22,000[a]	30[a]
196	27,600	23.0
1000	30,000	18.0
2000	30,700	15.5

[a]General Electric Company, Multi-Hundred Watt, Radioisotope Thermoelectric Generator Program, GESP-7034 (March 1970).

The effect of CO contamination on the mechanical properties of Mo–46% Re is shown in Table 12.14. The tensile data obtained at room temperature and 825°C indicate that CO at 825°C has no effect whatsoever on the mechanical properties of Mo–46% Re after 2000 hr of exposure.

Table 12.14. Tensile Properties of 20-mil-thick Mo–46% Re Sheet Specimens at Room Temperature and 825°C After Contamination with CO at 825°C and 1×10^{-5} torr

Doping Time (hr)	Tensile Strength (psi)	Elongation (%)
	Room Temperature	
0	195,000	8.2
1004	190,000	10.7
2006	186,000	12.0
	825°C	
1004	115,000	10.5
2006	123,000	9.7

Contamination Studies of TZM by Water Vapor

H. Inouye

Table 12.15 shows the tensile properties of TZM after exposure to 1×10^{-5} torr H_2O at 825°C. The room-temperature tests show only a small decrease in ductility for exposures to 1000 hr; however, after 2000 hr the specimen was completely brittle. The tensile properties at 825°C after exposures to 2000 hr are only slightly different from the control specimen.

Table 12.15. Tensile Properties of 0.020-in.-thick TZM at Room Temperature and 825°C After Exposure to 1×10^{-5} torr H_2O

Exposure (hr)	Ultimate Tensile Strength (psi)	Elongation (%)
	Room Temperature	
Control[a]	79,600	33.5
457	83,200	31.0
1002	80,600	29.3
1995	74,500	0.3
	825°C	
Control	45,000	24.8
457	45,600	20.2
1002	46,000	16.3
1995	44,600	20.0

[a]Recrystallized 1 hr at 1450°C.

13. CLADDING MATERIALS FOR SPACE ISOTOPIC HEAT SOURCES

R. G. Donnelly H. Inouye

The purpose of this program is to develop alloys with a superior combination of properties to better assure reliable containment of radioisotopic fuels such as $^{238}PuO_2$ and $^{244}Cm_2O_3$ under both operating and accident conditions for space thermoelectric generators. Ideally the encapsulating material should be insensitive to the operating environment and capable of surviving launch aborts, reentry heating, and earth impact as well as provide maximum post-impact containment of the fuel. At the same time it must be both fabricable and weldable.

We feel these goals can best be accomplished with high-strength, noble-based alloys having melting points above 2000°C.

Development of Improved Alloys

C. T. Liu

The mechanical properties of hafnium- and titanium-stabilized Pt-Rh-W alloys in the recrystallized condition (1 hr at 1200°C) were determined at 1316°C. A comparison of the tensile properties of the recently developed platinum-base alloys with other candidate alloys at 1316°C is made in Table 13.1. The tensile strength of the Pt-Rh-W alloys increases with tungsten content. Hafnium and titanium additions further improve the strength. Both the ternary and the hafnium- and titanium-modified alloys are stronger than Pt–30% Rh and are comparable to iridium or TZM, but weaker than T-111. In terms of the impact strength (i.e., fracture strain times tensile strength), the Pt–30% Rh–8% W–1% Hf–0.2% Ti alloy is the best among the candidate alloys.

The tensile properties of Pt–30% Rh–8% W–1% Hf–0.2% Ti alloy were determined in the stress-relieved condition (1 hr at 1000°C); these data are presented in Table 13.2 together with the recrystallized data. The hafnium- and titanium-stabilized alloy is very strong in the stress-relieved condition, even up to 1093°C. The ductility of the alloy is

Table 13.1. Comparison of the Tensile Properties of Platinum-Base Alloys[a] with Iridium, TZM, and T-111 at 1316°C (2400°F)

Composition (wt %)	Tensile Strength (psi)	Elongation (%)	Impact Strength (in.-lb/in.^{3})
Pt–30 Rh	10,000	26.5	2,650
Pt–30 Rh–6 W	17,500	55.0	9,600
Pt–26 Rh–8 W	21,200	45.0	9,550
Pt–30 Rh–10 W	25,500	50.5	12,900
Pt–30 Rh–8 W–0.25 Hf–0.1 Ti	21,600	52.0	11,200
Pt–30 Rh–8 W–0.5 Hf–0.2 Ti	25,000	44.5	11,100
Pt–30 Rh–8 W–1.0 Hf–0.2 Ti	27,700	54.5	15,100
Iridium	26,000	38	9,900
TZM	22,000	30	6,600
T-111	37,000	36	13,300

[a]0.020-in.-thick sheet recrystallized 1 hr at 1200°C; strain rate 0.05 in./min.

Table 13.2. Tensile Properties of Pt–30% Rh–8% W–1% Hf–0.2% Ti in Stress-Relieved and Recrystallized Conditions

Testing Temperature (°C)	Tensile Properties			
	Elongation, %		Tensile Strength, psi	
	Stress Relieved[a]	Recrystallized[b]	Stress Relieved[a]	Recrystallized[b]
Room temperature	5.5	11.7	243,000	130,000
760 (1400°F)	5.7	26.3	186,000	108,000
1093 (2000°F)	7.5	28.1	102,000	42,000
1316 (2400°F)	54.5[c]	54.5	27,700[c]	27,700

[a]Stress relieved 1 hr at 1000°C.

[b]Recrystallized 1 hr at 1200°C.

[c]Estimate from the recrystallized value.

lower in the stress-relieved condition and does not increase significantly with temperature below its recrystallization temperature (i.e., 1200°C).

To further qualify the use of the newly developed platinum-base alloys as cladding material for space isotopic heat sources, 23-mil-thick sheet specimens were exposed to oxygen at 1×10^{-5} torr. Table 13.3 shows the tensile properties of Pt-Rh-W alloys after a 253-hr exposure at 1100°C, and Table 13.4 shows the data of Pt-Rh-W-Hf-Ti alloys after a 1000-hr exposure at 1000°C. The Pt-Rh-W alloys show only a small reduction of the room temperature ductility, but no change in the 825°C ductility. It is important to note that this result is independent of the tungsten content. If an activation energy for oxidation of 27.5 kcal/mole (ref. 1) is used to extrapolate the data to a lower

[1]W. L. Phillips, Jr., Trans. Am. Soc. Metals 57, 33 (1964).

Table 13.3. Mechanical Properties of Pt-Rh-W Alloys at Room Temperature and 825°C After Oxygen-Doping at 1100°C and 1×10^{-5} torr for 253 hr

Composition (wt %)	Condition	Elongation (%)	Ultimate Tensile Strength (psi)
	Room Temperature		
Pt–30 Rh–6 W	As recrystallized	26	112,000
	Doped	16.3	88,000
Pt–26 Rh–8 W	As recrystallized	20[a]	115,000[a]
	Doped	13.5	90,000
Pt–30 Rh–10 W	As recrystallized	14.5	118,000
	Doped	10	82,000
	825°C		
Pt–30 Rh–6 W	As recrystallized	30[a]	71,000[a]
	Doped	31.5	52,000
Pt–26 Rh–8 W	As recrystallized	30[a]	76,000[a]
	Doped	30	54,000
Pt–30 Rh–10 W	As recrystallized	30[a]	85,000[a]
	Doped	31	66,000

[a]Data obtained from composition or temperature extrapolation.

Table 13.4. Tensile Ductility of Pt-Rh-W-Hf-Ti Alloys After Oxygen Doping at 1000°C and 1×10^{-5} torr for 1000 hr

Composition (wt %)	Condition	Testing Temperature (°C)	Tensile Elongation (%)
Pt–30 Rh–6 W–0.5 Hf–0.2 Ti	As recrystallized	Room	19.3
	Doped		8.7
Pt–30 Rh–8 W–0.25 Hf–0.1 Ti	As recrystallized	Room	18.5
	Doped		10
Pt–30 Rh–8 W–0.5 Hf–0.2 Ti	As recrystallized	Room	19.3
	Doped		7.3
Pt–30 Rh–6 W–0.5 Hf–0.2 Ti	As recrystallized	825	30[a]
	Doped		21.3
Pt–30 Rh–8 W–0.25 Hf–0.1 Ti	As recrystallized	825	30[a]
	Doped		22
Pt–30 Rh–8 W–0.5 Hf–0.2 Ti	As recrystallized	825	30[a]
	Doped		16

[a]Data estimated from temperature extrapolation.

exposure temperature, the data in Table 13.3 predicts no change of the 825°C ductility of Pt-Rh-W alloys after a 2400-hr exposure at 825°C (the Pioneer service temperature).

As indicated in Table 13.4 the modified alloys show a moderate reduction of ductility at room temperature and a lesser degree of reduction at 825°C. The room-temperature ductility is dependent on the hafnium and titanium level; the alloy containing 0.25 Hf and 0.1 Ti has better ductility after oxygen exposure than the alloys containing 0.5 Hf and 0.2 Ti. However, the latter alloys still have 7 to 9% elongation at room temperature and 16 to 21% at 825°C.

To demonstrate the formability of the alloy, two 2-in.-diam blanks of hafnium- and titanium-stabilized alloys were made from 30-mil-thick sheet stock fabricated by hot rolling at 1230°C, followed by cold rolling at room temperature. After recrystallizing 1 hr at 1200°C, the blank was formed over a 1 1/4-in.-diam mandrel at room temperature. The first blank cracked at the last stage when we attempted to form a complete hemisphere in one pass. With two intermediate anneals at 1200°C, the second blank was fabricated to a 1 1/4-in.-diam hemisphere without cracking (Fig. 13.1).

Fig. 13.1. A Pt–30% Rh–8% W–0.25% Hf–0.1% Ti 1 1/4-in.-diam Hemisphere Formed by Cold Drawing from 2-in.-diam × 0.03-in.-thick Disk with Two Intermediate Anneals at 1200°C.

Preparation of Pt–26% Rh–8% W Sheet

J. H. Erwin

To make the desired encapsulation components for isotopic heat sources, fabricable sheets of a Pt-Rh-W alloy 0.025 to 0.030 in. thick by greater than 8 in. square are required. We have fabricated 1- and 4-lb ingots of the Pt–26% Rh–8% W alloy into sheets 0.030 in. thick by approximately 5 1/2- and 10 1/2-in. square with very little difficulty. Although this initial sheet exhibited low ductility (1 to 5% elongation), we have successfully drawn blanks into 7/8- and 1 1/4-in.-diam hemispheres (see Fig. 13.2) with small increments of reduction between anneals. In this material, failure always appeared to occur at the grain boundaries. Thus, improvement in quality control and fabrication procedures appeared necessary to raise the elongation to 15 to 20% obtained on sheet specimens prepared from small buttons of chemically pure metal ingredients.

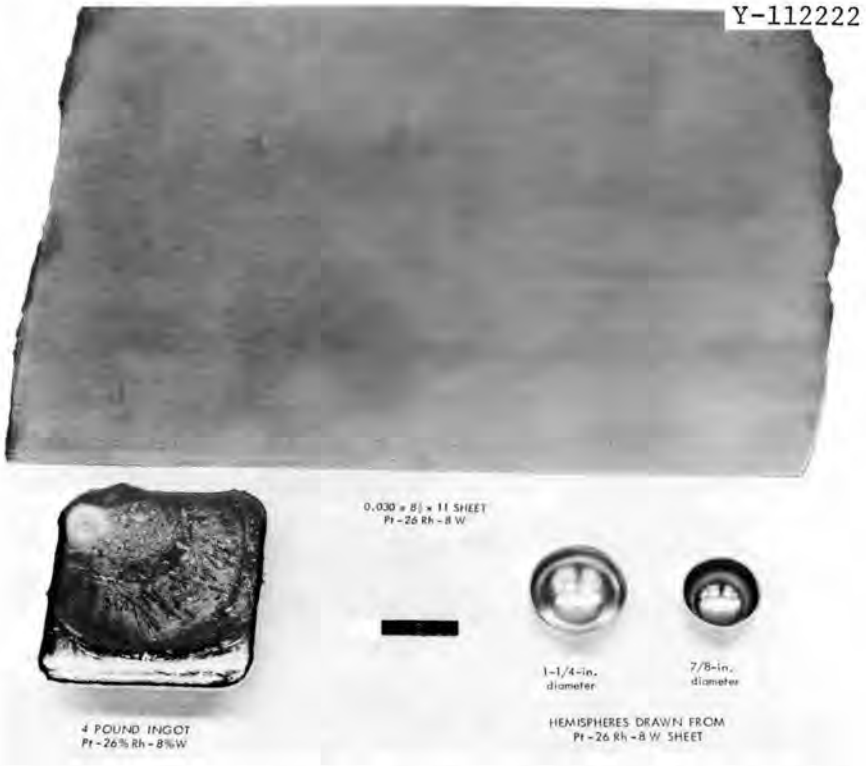

Fig. 13.2. Photograph of Electron-Beam Melted Ingot, Rolled Sheet, and Fabricated Parts from Pt–26% Rh–8% W Alloy.

The alloy ingots have been made by separately electron-beam melting platinum-rhodium scrap (obtained from Mound Laboratory) and virgin rhodium powder and then electron-beam melting these together with arc melted and crushed tungsten. Examination of sheet with poor ductility revealed microporosity near the surface, random contamination (primarily aluminum and silicon) of the grain boundaries, and tungsten segregation. The surface microporosity was eliminated by scalping the hot rolled ingot prior to cold rolling. Repeated melting reduced the aluminum content from 500 to 200 ppm and the silicon content from 300 to 100 ppm. The observed tungsten segregation was in the form of small, undissolved chips at the surface of the hot rolled plate which we expect to overcome by improved melting procedures.

We have fabricated 0.030-in.-thick sheet from 1 lb drop-cast electron-beam melted ingots of both the platinum-rhodium scrap and the scrap with the virgin rhodium added to make up the Pt-Rh base alloy for

Pt–26% Rh–8% W. Blanks from each of these materials were cold drawn without difficulty to make both 7/8- and 1 1/4-in.-diam hemispherical cups. Tensile specimens from each of the alloys, heat treated at 1000 and 1200°C, showed about 37% elongation for the Pt–10% Rh scrap and 43% elongation for the Pt–28.3% Rh base alloy. Published data[2] indicate about 35 and 33% elongation, respectively, for these two alloys in the annealed condition. Therefore, we now feel there is no problem of purity in the alloy constituents.

We are presently preparing another 4-lb ingot. The arc-melted tungsten will be replaced by hydrogen heat-treated tungsten powder and the alloy will be compounded initially as 1-lb buttons in the arc furnace to assure dissolution of the tungsten prior to electron-beam melting. We expect this change in melting procedure along with changes in the fabrication procedure to improve the ductility of the final sheet.

Characterization of Iridium

C. T. Liu

The tensile properties of 20-mil-thick sheet iridium specimens recrystallized 1 hr at 1500°C were determined at 1316°C. The result is presented in Table 13.5 along with low-temperature data reported previously.[3] Although iridium is weak at low temperatures, it has almost the same strength as the Pt–30% Rh–8% W–1% Hf–0.2% Ti alloy (Table 13.1) at 1316°C. Thus, the excellent high-temperature strength of iridium is confirmed.

Recent work[4] on iridium indicates that as-fabricated iridium hemispheres as well as sheet contain numerous inclusions (in stringer and globular forms) and surface microcracks. Silica-type beads were

---

[2] Metals Handbook, Vol. 1, 8th ed., p. 1191, American Society for Metals, Metals Park, Ohio, 1961.

[3] C. T. Liu, Fuels and Materials Development Program Quart. Progr. Rept. December 31, 1971, ORNL-TM-3703, p. 281.

[4] J. Aliotta, Iridium Characterization Program Progress Reports Nos. 1 and 2, Englehard Industries Division, September and November, 1971.

Table 13.5. Room- and Elevated-Temperature Tensile Properties of Iridium Recrystallized 1 hr at 1500°C

Testing Temperature (°C)	Ultimate Tensile Strength (psi)	Elongation (%)
Room temperature	56	5.7
760	56	23.5
1093	35	19.8
1316	26	38.0

also observed on the surface of and in welds. These results indicate the presence of impurities which may be the cause of the low ductility at room temperature (see Table 13.5) and difficulty in fabrication.

In order to improve the physical and mechanical properties of iridium, we are now working on the purification of iridium by a zone-refining technique. Two rectangular specimens 0.05 × 0.125 × 3.5 in. were cut from iridium plate purchased from Englehard Industries, then zone refined without difficulty in ultravacuum. The resulting zone-refined iridium single crystal bar was cold swaged 40% in area without cracking.

Previous reports in this series are:

ORNL-TM-920	Period Ending June 30, 1964
ORNL-TM-960	Period Ending September 30, 1964
ORNL-TM-1000	Period Ending December 31, 1964
ORNL-TM-1100	Period Ending March 31, 1965
ORNL-TM-1200	Period Ending June 30, 1965
ORNL-TM-1270	Period Ending September 30, 1965
ORNL-TM-1400	Period Ending December 31, 1965
ORNL-TM-1500	Period Ending March 31, 1966
ORNL-TM-1570	Period Ending June 30, 1966
ORNL-TM-1700	Period Ending September 30, 1966
ORNL-TM-1720	Period Ending December 31, 1966
ORNL-TM-1825	Period Ending March 31, 1967
ORNL-TM-1941	Period Ending June 30, 1967
ORNL-TM-2020	Period Ending September 30, 1967
ORNL-TM-2090	Period Ending December 31, 1967
ORNL-TM-2217	Period Ending March 31, 1968
ORNL-4330	Period Ending June 30, 1968
ORNL-4350	Period Ending September 30, 1968
ORNL-4390	Period Ending December 31, 1968
ORNL-4420	Period Ending March 31, 1969
ORNL-4440	Period Ending June 30, 1969
ORNL-4480	Period Ending September 30, 1969
ORNL-4520	Period Ending December 31, 1969
ORNL-4560	Period Ending March 31, 1970
ORNL-4600	Period Ending June 30, 1970
ORNL-4630	Period Ending September 30, 1970
ORNL-TM-3300	Period Ending December 31, 1970
ORNL-TM-3416	Period Ending March 31, 1971
ORNL-TM-3540	Period Ending June 30, 1971
ORNL-TM-3550	Period Ending September 30, 1971
ORNL-TM-3703	Period Ending December 31, 1971

INTERNAL DISTRIBUTION

Central Research Library (3)
ORNL — Y-12 Technical Library
Document Reference Section
Laboratory Records Department (10)
Laboratory Records, ORNL RC
ORNL Patent Office
G. M. Adamson, Jr.
M. Bender
S. E. Beall
E. E. Bloom
J. A. Conlin
W. B. Cottrell
J. A. Cox
R. S. Crouse
F. L. Culler, Jr.
J. E. Cunningham
J. H. DeVan
R. G. Donnelly
W. P. Eatherly
D. E. Ferguson
J. H Frye, Jr.
R. J. Gray
B. L. Greenstreet
W. R. Grimes
W. O. Harms
M. R. Hill (3)
F. J. Homan
H. Inouye
P. R. Kasten
E. L. Long, Jr.
A. L. Lotts
T. S. Lundy
R. E. MacPherson
W. R. Martin
R. W. McClung
H. E. McCoy, Jr.
H. C. McCurdy
W. T. McDuffee
D. L. McElroy
J. R. McGuffey
C. J. McHargue
L. C. Oakes
P: Patriarca (20)
S. Peterson
P. L. Rittenhouse
M. W. Rosenthal
A. C. Schaffhauser
J. L. Scott
J. D. Sease
G. M. Slaughter
J. O. Stiegler
D. B. Trauger
J. E. Van Cleve
T. N. Washburn
J. R. Weir, Jr.
G. D. Whitman
R. G. Wymer
H. L. Yakel

EXTERNAL DISTRIBUTION

Manager TIC (17)
Oak Ridge
For transmittal to members of ACRS

AEC DIVISION OF REACTOR DEVELOPMENT AND TECHNOLOGY, Washington, DC 20545

M. Booth
R. W. Cochran
J. W. Crawford
G. W. Cunningham
R. P. Denise
M. D. Dubrow
O. P. Gormley
N. Grossman
P. A. Halpine
W. H. Hannum
P. L. Havenstein
E. E. Hoffman
K. E. Horton
J. R. Hunter
R. H. Jones
E. E. Kintner
R. E. Kosiba
E. C. Kovacic (5)
W. H. Layman
J. E. McEwen

W. H. McVey
J. J. Morabito
J. Morris
E. C. Norman
R. E. Pahler
D. Pollock
A. J. Pressesky
T. C. Reuther
M. A. Rosen
S. Rosen
F. A. Ross
M. Shaw
G. L. Sherwood
J. M. Simmons
B. Singer
E. E. Sinclair
R. W. Sliger
J. F. Smith, Jr.
R. F. Sweek
S. A. Szawlewicz
A. Taboada
A. N. Tardiff
A. Van Echo
C. E. Weber
M. J. Whitman
W. A. Williams

AEC DIVISION OF RESEARCH, Washington, DC 20545

L. C. Ianniello
P. W. McDaniel
D. K. Stevens

AEC DIVISION OF REACTOR LICENSING, Washington, DC 20545

P. A. Morris (2)

AEC DIVISION OF REACTOR STANDARDS, Washington, DC 20545

E. G. Case (2)

AEC TECHNICAL INFORMATION CENTER, Oak Ridge, TN 37830

Director (2)

AEC OAK RIDGE OPERATIONS OFFICE, P.O. Box E, Oak Ridge, TN 37830

Research and Technical Support Division

AEC-RDT SITE REPRESENTATIVES

Mr. Russell H. Ball
RDT Site Representative, GE-AG
U.S. Atomic Energy Commission
310 DeGuigne Drive
Sunnyvale, California 94085

Dr. David F. Cope
RDT Sr. Site Representative, ORNL
U.S. Atomic Energy Commission
P.O. Box X
Oak Ridge, Tennessee 37830

Mr. Theodore Iltis
RDT Sr. Site Representative, W
U.S. Atomic Energy Commission
P.O. Box 154
Madison, Pennsylvania 15663

Mr. Max E. Jackson
RDT Sr. Site Representative, ANL
U.S. Atomic Energy Commission
9800 South Cass Avenue
Argonne, Illinois 60439

Mr. C. L. Matthews
RDT Site Representative, ORNL
U.S. Atomic Energy Commission
P.O. Box X
Oak Ridge, Tennessee 37830

Mr. Robert L. Morgan
RDT Sr. Site Representative, AI
U.S. Atomic Energy Commission
P.O. Box 1446
Canoga Park, California 91304

Mr. DeWitt Moss
RDT Sr. Site Representative, ANL-ID
U.S. Atomic Energy Commission
P.O. Box 2108
Idaho Falls, Idaho 83401

Mr. Thomas A. Nemzek
Assistant Director for Pacific
Northwest Programs, RDT
U.S. Atomic Energy Commission
P.O. Box 550
Richland, Washington 99352

Mr. J. B. Radcliffe
RDT Sr. Site Representative, GGA
U.S. Atomic Energy Commission
P.O. Box 2325
San Diego, California 92112

Mr. J. Sako, Westinghouse Hanford Company, P.O. Box 1970,
Richland, Washington 99352

Atomic Energy Commission Library, Room G-049, Washington,
DC 20545

AEC DIVISION OF NAVAL REACTORS, Washington, DC 20360

R. H. Steele

AIR FORCE MATERIALS LABORATORY, Wright-Patterson Air Force Base, OH 45433

C. H. Armbruster
H. M. Burte
I. Perlmutter

AMES LABORATORY, USAEC, Iowa State University, Ames, IA 50010

M. S. Wechsler

ARGONNE NATIONAL LABORATORY, 9700 S. Cass Avenue, Argonne, IL 60439

B.R.T. Frost
J. H. Kittel
M. V. Nevitt
D. R. O'Boyle
P. G. Shewmon
R. C. Vogel

ATOMIC POWER DEVELOPMENT ASSOCIATES, 1911 First Street, Detroit, MI 48226

A. S. Shoudy, Jr.

ATOMICS INTERNATIONAL, P.O. Box 309, Canoga Park, CA 91304

J. G. Asquith
H. M. Diecamp
T. A. Moss
H. Pearlman
S. Siegel

K. L. Adler
E. Rodwell
Liquid Metal Engineering Center
Atomics International
P.O. Box 1449
Canoga Park, California 91304

BABCOCK & WILCOX COMPANY, Beaver Falls, PA 15010

G. F. Tisinai

BABCOCK & WILCOX COMPANY, Lynchburg, VA 24505

C. J. Baroch
S. P. Grant
C. R. Johnson
L. R. Weissert

BATTELLE COLUMBUS LABORATORIES, 505 King Avenue, Columbus, OH 43201

D. Keller
S. J. Paprocki
Defense Materials Information Center

BROOKHAVEN NATIONAL LABORATORY, 29 Cornell Avenue, Upton, Long Island, NY 11973

D. H. Gurinsky
C. Klamut

BUREAU OF MINES, Albany Metallurgy Research Center, P.O. Box 70, Albany, OR 97321

Haruo Kato

BUREAU OF MINES, Boulder City, NV 89005

T. A. Sullivan

COMBUSTION ENGINEERING, INC., 911 W. Main St., Chattanooga, TN 37402

R. C. Armstrong
D. Vandergriff
C. T. Ward
Librarian, Metallurgy Laboratory

COMBUSTION ENGINEERING, INC., P.O. Box 500, Windsor, CT 06095

M. Andrews
W. P. Chernock
W. P. Staker

FOSTER WHEELER CORPORATION, John Blizard Research Center, Livingston, NJ 07039

W. R. Apblett

GENERAL ELECTRIC COMPANY, Pleasanton, CA 94566

H. W. Alter
Maurice Indig

GENERAL ELECTRIC COMPANY, 175 Curtner Avenue, San Jose, CA 95125

R. R. Asamoto
W. E. Bailey
R. Duncan
J. L. Krankota

GENERAL ELECTRIC COMPANY, 310 DeGuigne Drive, Sunnyvale, CA 94086

J. M. Case
R. E. Skavdahl
C. N. Spalaris
E. L. Zebroski
Technical Library

GEORGE C. MARSHALL SPACE FLIGHT CENTER, Huntsville, AL 35812

R. J. Schwinghamer

GULF GENERAL ATOMIC, P.O. Box 608, San Diego, CA 92112

L. J. Colby
A. J. Goodjohn
J. P. Howe
J. N. Lindgren
J. F. Watson
L. Yang

IDAHO NUCLEAR CORPORATION, P.O. Box 1845, Idaho Falls, ID 83401

W. C. Francis
W. W. Hickman
D. Kaiser
W. A. Yuill

KNOLLS ATOMIC POWER LABORATORY, P.O. Box 1072, Schenectady, NY 12301

R. F. Wojciescak

LMFBR PROGRAM OFFICE, Argonne National Laboratory, 9700 S. Cass Avenue, Argonne, IL 60439

A. Amarosi
G. A. Bennet
P. F. Gast
J. M. McKee
J. T. Venard

LOS ALAMOS SCIENTIFIC LABORATORY, P.O. Box 1663, Los Alamos, NM 87544

R. D. Baker

MINE SAFETY APPLIANCES COMPANY, J. T. Ryan Memorial Laboratory, 100 N. Braddock Avenue, Pittsburgh, PA 15208

Library

MOUND LABORATORY, P.O. Box 32, Miamisburg, OH 45342

W. T. Cave
R. E. Vallée

NASA HEADQUARTERS, Code RN, 600 Independence Avenue, Washington, DC 20545

J. J. Lynch

NASA-LEWIS RESEARCH CENTER, 21000 Brookpark Road, Cleveland, OH 44135

G. M. Ault
J.W.R. Creagh
F. E. Rom
L. Rosenblum
N. T. Saunders
C. M. Scheuermann
Roger Smith

NAVAL RESEARCH LABORATORY, Code 6390, Washington, DC 20360

J. R. Hawthorne

O'DONNELL & ASSOCIATES, INC., 5100 Centre Avenue, Pittsburgh, PA 15232

William J. O'Donnell

SANDIA CORPORATION, Albuquerque, NM 87115

J. R. Holland
P. D. O'Brian

SPACE NUCLEAR SYSTEMS OFFICE, AEC, Washington, DC 20545

R. E. Anderson
D. Beard
J. F. Griffo
H. Jaffe
C. E. Johnson
A. P. Litman
J. J. Lombardo
J. A. Powers
F. C. Schwenk

UNION CARBIDE CORPORATION, 270 Park Avenue, New York, NY 10017

J. A. Swartout

UNITED NUCLEAR CORPORATION, Grasslands Road, Elmsford, NY 10523

A. A. Strasser

UNIVERSITY OF CALIFORNIA, LAWRENCE RADIATION LABORATORY, P.O. Box 808, Livermore, CA 94550

W. R. Holman
L. W. Roberts
A. J. Rothman

U.S. NAVAL AIR SYSTEM COMMAND (AIR-52031B), Washington, DC 20360

I. Machlin

USAEC SCIENTIFIC REPRESENTATIVE, American Embassy, P.O. Box 40, FPO New York, NY 09510

W.L.R. Rice

WESTINGHOUSE ADVANCED REACTORS DIVISION, Waltz Mill Site, P.O. Box 158, Madison, PA 15663

E. C. Bishop
A. Boltax
P. J. Levine
P. Murray
W. E. Ray
J. J. Taylor
G. A. Whitlow

WESTINGHOUSE ADVANCED REACTORS DIVISION, Cheswick Fuel Facility, P.O. Box 217, Cheswick, PA 15024

P. M. French

WESTINGHOUSE ASTRONUCLEAR LABORATORY, P.O. Box 10864, Pittsburgh, PA 15231

D. C. Goldberg

WESTINGHOUSE ATOMIC POWER DIVISION, P.O. Box 355, Pittsburgh, PA 15230

Technical Library

WESTINGHOUSE BETTIS ATOMIC POWER DIVISION, P.O. Box 79, West Mifflin, PA 15122

R. H. Fillnow
P. N. Gustafson
W. Yenascavich
Technical Library

WESTINGHOUSE HANFORD COMPANY, P.O. Box 1970, Richland, WA 99352

E. A. Evans
W. E. Roake (5)
W. F. Sheely (5)

WESTINGHOUSE TAMPA DIVISION, Nuclear Energy Systems, P.O. Box 19218, Tampa, FL 33616

M. E. Eilbeck
D. G. Harmon
B. King